

A MULTI-WAVELENGTH PERSPECTIVE ON
GAMMA-RAY FLARING BLAZARS

Ein Multiwellenlängen-Blickwinkel auf
Gammastrahlungs-Ausbrüche von Blazaren

Der Naturwissenschaftlichen Fakultät
der Friedrich-Alexander-Universität
Erlangen-Nürnberg

zur
Erlangung des Doktorgrades Dr. rer. nat.

vorgelegt von
Andrea Katharina Gokus

Als Dissertation genehmigt
von der Naturwissenschaftlichen Fakultät
der Friedrich-Alexander-Universität Erlangen-Nürnberg

Tag der mündlichen Prüfung: 04.08.2022

Vorsitzender der Promotionsorgans: Prof. Dr. Wolfgang Achtziger

Gutachter: Prof. Dr. Jörn Wilms & Prof. Dr. Matthias Kadler
Prof. Dr. Marcus Brüggem

The cover picture shows an artistic impression of multi-wavelength emission from a blazar reaching the Earth. The emission at different frequencies is represented by a cone of light in the colours of the rainbow.

Image: Andrea Gokus, watercolour painting

Zusammenfassung

In meiner Dissertation verwende ich Beobachtungsdaten des gesamten elektromagnetischen Spektrums, vom Radio- bis hin zum Gamma-Bereich, um die Jets von Blazaren und blazarartigen aktiven Galaxiekernen (engl. *active galactic nuclei*; AGN) zu untersuchen. Mein Fokus liegt dabei im Speziellen auf Zeiträumen, in denen ein AGN einen hellen Gammastrahlungsausbruch zeigt. AGN gewinnen Energie durch den Prozess der Akkretion von Masse, und können die Helligkeit ihrer Galaxie übertreffen, in deren Zentrum sie sich befinden. Ein kleiner Teil der AGN ist in der Lage, große kollimierte Materieströme zu bilden, die Jets genannt werden. In diesen bewegen sich Teilchen mit relativistischen Geschwindigkeiten, also nahe der Lichtgeschwindigkeit, und die Jets können die Größenskalen von Galaxien erreichen. Zeigt ein solcher Jet in unsere Richtung, nennt man solch einen AGN Blazar. Die Emission von Blazaren ist im gesamten elektromagnetischen Spektrum sehr variabel, und es können auch Strahlungsausbrüche, sogenannte Flares, auftreten, bei denen die Helligkeit in einem oder mehreren Wellenlängenbereichen für einen kurzen Zeitraum stark ansteigt. Die dafür verantwortlichen Prozesse sind noch nicht vollständig verstanden. Insbesondere die extrem schnelle Variabilität der Gammastrahlung stellt eine Herausforderung für aktuelle Modelle dar.

Der Blazar Mrk 421 ist einer der hellsten extragalaktischen Objekte, und zeigt oft helle Flares. Als Teil meiner Dissertationsarbeit habe ich Multiwellenlängendaten ausgewertet, die im Rahmen einer kontinuierlichen Überwachung mit dem Gamma-Teleskop FACT und den Instrumenten an Bord des Satelliten *Swift*, sowie während eines Gammastrahlen-Ausbruchs im Juni 2019, genommen wurden. Ich habe optische, UV- und Röntgendaten, inklusive *INTEGRAL*-Daten aus dem harten Röntgenbereich, zu einem Breitband-Spektrum (engl. *broadband spectral energy distribution*; SED) kombiniert. Eine Blazar SED zeigt typischerweise zwei charakteristische ‘‘Höcker’’, wobei die zuvor erwähnten Energiebereiche im Fall von Mrk 421 das Maximum und den Abfall des ersten Höckers sehr gut abdecken. Ich modelliere diese Daten mit einer logarithmischen Parabelfunktion, welche die Daten empirisch ausreichend beschreibt, und Veränderungen des Höckers bzgl. Maximalfluss und -energie leicht bestimmen lässt. Während des Strahlungsausbruchs im Gamma-Bereich ereignete sich auch zeitgleich ein Flare im Röntgenbereich, der zugleich mit einer Verschiebung des Höcker-Maximums zu höheren Energien einherging. Dieses Verhalten spiegelt sich auch in der Beobachtung mit *XMM-Newton* wieder, in der Mrk 421 für einen Zeitraum von etwa 25 Stunden fast durchgehend beobachtet wurde. Ich stelle die Daten in einem Härte-Intensitäts-Diagramm und einer Hystereseurve dar, und finde einen starken und konstanten Anstieg von Photonen im Energiebereich von 4–10 keV, während auch der gemessene Fluss ansteigt. Dieses Verhalten, dass das Spektrum härter wird, wenn die Quelle heller wird, wurde bereits zuvor für Mrk 421 und auch andere Blazare beobachtet. Auf der Suche nach Variabilität auf sehr kurzen Zeitskalen habe ich zwei signifikante ‘Mini-Flares’ in der Lichtkurve im höchsten Energieband (4–10 keV) der *XMM-Newton* Beobachtung entdeckt. Die damit verbundenen Zeitskalen sind kürzer als fünf Minuten, und damit ungefähr so schnell wie die extremste Kurzzeitvariabilität, die im Gammalicht bei anderen Blazaren entdeckt wurden. Ein Prozess, der für die Entstehung dieser in Frage kommt, ist magnetische Rekonnexion. Simulationen zeigen, dass dieser Prozess Röntgenstrahlung in einer bestimmten Art und Weise polarisieren könnte, was im Falle von

besonders hellen Strahlungsausbrüchen von der Mission IXPE zukünftig gemessen werden könnte.

Ein weiteres Projekt meiner Dissertation behandelt die schmallinige Seyfert 1 (engl. *narrow-line Seyfert 1*; NLSy 1) Galaxie PKS 2004–447 und deren ersten beobachteten Gammastrahlungsausbruch. NLSy 1 Objekte sind typischerweise AGN ohne Jet. Allerdings weist ein kleiner Teil von ihnen relativistische Jets auf, von denen wiederum eine kleine Anzahl auch im Gammalicht von *Fermi*/LAT beobachtet wurden. Auch für die Analyse von PKS 2004–447 werte ich Multiwellenlängen-Daten aus. Seit Beginn ihrer Entdeckung im Gammalicht zeigte diese Quelle eine moderate Variabilität, bis sie im Oktober 2019 einen Gammastrahlungsausbruch zeigte, der denen von Blazaren ähnlich war. Mittels schnellen Nachbeobachtungen durchgeführt mit *Swift*, *XMM-Newton* und *NuSTAR* war es möglich, Daten im optischen, UV und Röntgenbereich während und nach dem Flare zu sammeln. Eine gute Abdeckung von Daten in mehreren Wellenlängenbereichen des Spektrums macht es möglich, die verschiedenen Aktivitätsphasen von PKS 2004–447 in zeitaufgelösten SEDs zu analysieren. Die Strahlung wird mit einem einfachen, leptonischen Modell, welches das breitbandige Verhalten der Quelle gut beschreibt, modelliert und man erkennt eine starke Ähnlichkeit zu Blazaren, und im besonderen zu Quasaren mit einem flachen Radiospektrum. Desweiteren analysiere ich die Röntgendaten von *XMM-Newton* und *NuSTAR* in einem kombinierten Spektrum, welches stark von der Jet-Strahlung dominiert ist. Ich kann keine typischen Merkmale von NLSy 1 Galaxien in dem Röntgenspektrum von PKS 2004–447 ausmachen. Diese Quelle zeigt Variabilität auf längeren Zeitskalen im gesamten elektromagnetischen Spektrum, aber auch Kurzzeitvariabilität in der Größenordnung von Stunden im Gammalicht im Zeitraum des Strahlungsausbruchs. Das schwarze Loch im Zentrum von PKS 2004–447 hat vermutlich eine vergleichsweise geringe Masse für AGN, die einen Jet ausbilden ($< 10^8 M_{\odot}$), und die Radiostrahlung von der Quelle ist kompakt. Diese zwei Beobachtungen in Kombination mit der in dieser Arbeit vorgestellten Multiwellenlängenanalyse lassen die berechtigte Frage aufkommen, ob PKS 2004–447 ein junger AGN ist, der sich über die Zeit hinweg zu einem mächtigen Blazar entwickeln wird.

Abstract

In this thesis I use multi-wavelength data from radio up to γ -rays to study emission processes in the jets of flaring blazars and blazar-like active galactic nuclei (AGN). Powered by accretion onto a supermassive black hole, AGN can produce luminosities that outshine their host galaxy. A fraction of AGN form large-scale, collimated outflows of particles moving at relativistic speed, which are called jets. In case such a jet is orientated towards our line of sight at a small angle, the object is called a blazar. Blazars exhibit a variable behaviour across the entire electromagnetic spectrum, and, on occasion, show flares, which are a dramatic increase in luminosity at one or several wavelengths. The processes partaking in flares are not fully understood, and rapid variability detected at γ -ray energies is a challenge for current jet models.

The blazar Mrk 421 is one of the brightest sources in the extragalactic sky, and regularly shows bright flares. I analysed multi-wavelength data obtained as part of a monitoring program with the γ -ray telescope FACT and the optical, UV and X-ray instruments on-board *Swift*, and, in particular, during a γ -ray flare in June 2019. A combined fit of the optical, UV and X-ray data, including hard X-ray data from *INTEGRAL*, with a log-parabola model revealed a shift of the peak position of the low-energy hump in the typical two-hump broadband spectral energy distribution (SED) towards higher energies. This behaviour is also covered by a long (90 ks) *XMM-Newton* observation. I displayed the X-ray data in hardness-intensity diagrams and a hysteresis curve, and found a steady increase of high energy photons in the 4–10 keV band during a general increase of the flux, known as the ‘harder-when-brighter’ trend, which has been observed in Mrk 421 and other blazars before. Searching for signals of variability on very short time scales, I discover two distinct features in the hard (4–10 keV) X-ray band, which resemble ‘mini-flares’ on top of the generally variable emission. The associated time scales are on the order of four to five minutes, and as short as the rapid variability detected at (very high energy) γ -rays in a few other blazars. A process that could explain rapid variability in both energy regimes is magnetic reconnection, which has been predicted to produce certain polarisation characteristics that might be detectable in the future with IXPE.

In this dissertation, I also present a multi-wavelength study of the narrow-line Seyfert 1 (NLSy 1) galaxy PKS 2004–447 in the context of its first γ -ray flare. Typically, NLSy 1s are non-jetted AGN, but a fraction of them have been found to host relativistic jets, and a small number of them was also detected by the γ -ray telescope LAT on-board the *Fermi* satellite. PKS 2004–447 belongs to the latter ones, and showed moderate variability since *Fermi*/LAT began surveying the sky, until it exhibited a blazar-like γ -ray flare in October 2019. Target-of-opportunity observations were conducted with *Swift*, *XMM-Newton*, and *NuSTAR* to study optical, UV, and X-ray emission of the source during and after the flare. Due to good multi-wavelength coverage at different activity phases of the source, it was possible to build time-resolved broadband SEDs with quasi-simultaneous data. A leptonic model describes the flaring behaviour sufficiently well, and reveals a strong resemblance to blazar, and in particular to flat-spectrum radio quasars. Furthermore, I analyse the combined X-ray data from *XMM-Newton* and *NuSTAR*, and find that the X-ray spectrum is strongly dominated by the jet, and lacks typical properties of NLSy 1 X-ray spectra. While PKS 2004–447 shows longer-term variability at all wavelengths, the γ -ray light curve reveals short-term variability

on the order of hours during its state of enhanced γ -ray flux. Based on these findings, and due to its possibly low-mass black hole ($< 10^8 M_{\odot}$) and compact radio emission, PKS 2004–447 might be a powerful blazar in the making.

Contents

1	Introduction to Active Galactic Nuclei	3
1.1	From then until now	3
1.1.1	Discovery	3
1.1.2	A unifying model and its limits	6
1.2	Jetted AGN	9
1.2.1	Jet formation, structure & emission	9
1.2.2	Variability	11
1.2.3	Broadband spectral energy distribution	17
1.3	Plan of my thesis	19
2	Instruments in Astronomy: Detecting Light across the Broadband Spectrum	21
2.1	Gamma-ray astronomy	22
2.1.1	Historical overview	22
2.1.2	The First G-APD Cherenkov Telescope	26
2.1.3	The <i>Fermi Gamma-ray Space Telescope</i>	27
2.2	X-ray astronomy	32
2.2.1	Design of focusing X-ray telescopes	32
2.2.2	Historical overview	37
2.2.3	The <i>X-ray Multi-Mirror Mission</i>	47
2.2.4	The <i>Neil Gehrels Swift Observatory</i>	49
2.2.5	The <i>Nuclear Spectroscopic Telescope Array</i>	49
2.3	Optical astronomy	51
2.3.1	The Optical Monitor	51
2.3.2	The UltraViolet and Optical Telescope	52
2.4	Radio astronomy	53
2.4.1	The Radio Telescope Effelsberg: A giant in the Eifel	55
2.4.2	The Australian Telescope Compact Array	56
3	Multiwavelength Monitoring of the Universe: Motivation, Methods and Examples	57
3.1	Feasibility and limitations of unbiased monitoring	58
3.2	Monitoring programmes dedicated to blazars	60
3.2.1	γ -ray & X-ray monitoring programmes	60
3.2.2	Optical & infrared monitoring programmes	61
3.2.3	Radio monitoring programmes	62
3.3	Performing blazar multi-wavelength monitoring	63
3.3.1	PKS 1510–089: a bright and VHE γ -ray emitting FSRQ	64

3.3.2	TXS 1508+572: a powerful blazar in the early Universe	67
4	Multi-wavelength study of Mrk 421 during a TeV flare	71
4.1	The famous Mrk 421	71
4.2	Multi-wavelength monitoring program	74
4.3	Multi-wavelength observations & data processing	75
4.3.1	FACT	75
4.3.2	<i>Fermi</i> /LAT	75
4.3.3	<i>INTEGRAL</i>	76
4.3.4	<i>XMM-Newton</i>	76
4.3.5	<i>Swift</i> : XRT & UVOT	77
4.3.6	Effelsberg	78
4.4	Outburst in June 2019	79
4.5	Multi-wavelength analysis	81
4.5.1	Variability analysis	82
4.5.2	Low-energy SED evolution	84
4.6	X-ray timing analysis	87
4.6.1	Spectral variability	88
4.6.2	Searching for the shortest variability time scales	93
4.6.3	Physical interpretation of the variability	99
4.7	Outlook	101
5	AGN outside the unification scheme - What is the nature of PKS 2004–447?	103
5.1	Narrow-line Seyfert 1 galaxies	103
5.2	The γ - and radio-loud NLSy1 galaxy PKS 2004–447	105
5.3	Multiwavelength analysis of its first γ -ray flare	107
5.3.1	Observations and data reduction	107
5.3.2	Variability	110
5.3.3	X-ray analysis	116
5.3.4	SED modelling	118
5.4	Discussion of analysis results	121
5.4.1	Variability	121
5.4.2	SED parameters	122
5.4.3	Comparison with other SEDs	124
5.5	Conclusions from our multi-wavelength analysis	126
6	Conclusion and Outlook	129
	Bibliography	133
	Appendix	150
A.1	<i>XMM-Newton</i> observation of Mrk 421 in June 2019	151
A.2	<i>Swift</i> observations of Mrk 421 in 2019	153
A.3	ATCA observations of PKS 2004–447	155
	Acknowledgements	157

“We are a species poised between an awareness of our ultimate insignificance and an ability to reach far beyond our mundane lives, into the void, to solve the most fundamental mysteries of the cosmos.”

Katie Mack, *The End of Everything*

Introduction to Active Galactic Nuclei

“In the beginning the Universe was created. This has made a lot of people very angry and has been widely regarded as a bad move.”

Douglas Adams, *The Restaurant at the End of the Universe*

It is widely accepted that black holes of monstrous size lie at the centre of most galaxies. These supermassive black holes outweigh our sun by a factor of a million up to 10 billion, and can become the central engine of *Active Galactic Nuclei* (AGN) when supplied with enough material to accrete. In this chapter, I will give a broad overview of the discovery and properties of AGN in Sect. 1.1, and dive deeper into the physics and characteristics of jetted AGN in Sect. 1.2. At the end of this chapter, I present my plan of this thesis in Sect. 1.3.

1.1 From then until now

In April 1920, a meeting of the National Academy of Sciences took place in Washington, which would later go down in history as the place of the *Great Debate*. Both Heber D. Curtis and Harlow Shapley presented their version of ‘The scale of the Universe’, which mainly differed by their separate points of view regarding the distance of observed nebulae. While Shapley held the opinion that those nebulae were located in our galaxy, the Milky Way, Curtis argued that they were of extragalactic nature. Their presentations at the meeting led to discussions and an extensive exchange of arguments (Shapley & Curtis, 1921). The conflict was resolved when Edwin Hubble measured the distances to several nebulae using the luminosity-periodicity relationship of δ Cepheids discovered by Leavitt & Pickering (1912), proved their extragalactic origin (Hubble, 1926). At the same time introduced the basic galaxy classifications that we still use today (although later revised and adapted by others, e.g., de Vaucouleurs, 1959). Now, more than 100 years later, we have found a vast amount of galaxies, with estimates that the total number exceeds two trillion (Conselice et al., 2016).

1.1.1 Discovery

After the confirmation that nebulae are extragalactic objects, new research fields in astronomy emerged. The detection of other galaxies opened new possibilities to measure the size of the Universe and created the field of cosmology. Others devoted their time and work to studying

the galaxies themselves. Among these individuals was Carl Seyfert, who performed the first systematic spectral analysis of spiral galaxies, and noticed that some of them showed very bright cores, as well as strong emission lines, which were very broad in a few cases (Seyfert, 1943). Those objects are nowadays referred to as Seyfert galaxies. In retrospect, Seyfert was not the first person to discover these galaxies, because Edward A. Fath had found the same signatures of Seyfert galaxies in the optical spectrum of NGC 1068¹ in 1909 (Fath, 1909). At that time, however, nebulae were considered to lie within the Milky Way and to be irradiated by stars, which was in contradiction with the observation of emission lines.

The detection of radio emission outside of our solar system laid the foundation for radio astronomy (Jansky, 1933, Reber, 1944), which opened a new window through which the Universe could be explored in a completely new energy range. After the second World War, intriguing, large-scale regions of radio emission were detected (e.g., Jennison & Das Gupta, 1953). Mills (1952) and Baade & Minkowski (1954) identified their optical counterparts, which were galaxies for a few of them. In addition, a few very bright radio sources, which appeared point-like, were found, and dubbed ‘quasi-stellar radio sources’ or ‘quasars’. The first of its kind is 3C 273², which was found by Schmidt (1963) and Hazard et al. (1963). Although the source appeared extremely bright, and therefore first suggested close proximity, the optical spectrum of the source revealed a redshift³ of $z = 0.158$ (Schmidt, 1963), which made it one of the most distant objects known at that time.

To explain the extreme luminosity coming from the centre of Seyfert galaxies and quasars, Woltjer (1959) used the established quantity of the mass-luminosity ratio to infer an estimate for the mass of the object responsible, and concluded that only extremely massive objects, i.e., of 10^8 solar masses, can cause this amount of emission. Hoyle & Fowler (1963) suggested the process of accretion as the responsible mechanism for the observed large energy output, but they only considered an accretion process onto a stellar-type object. Zel’dovich & Novikov (1964) and Salpeter (1964) proposed a supermassive black hole (SMBH) as the main central mass instead, which turned out to be the most plausible explanation. The term ‘active galactic nucleus’ was first suggested by Victor A. Ambartsumian in the 1950s (Israelian, 1997). At the Solvey Conference on Physics in Brussels in 1958, he suspected immense explosions to be the cause of the observed energy coming from the galaxy centres, which later turned out wrong, but he rightfully hinted at unknown objects of extremely large mass being involved in the process (Israelian, 1997).

Several different kinds of AGN were discovered in the decades that followed. Among the Seyfert galaxies, two distinct types were found by studying their optical spectra. While all Seyfert galaxies exhibit strong narrow emission lines, only a part of them shows also very broad emission lines (Khachikian & Weedman, 1974). The emission lines, both narrow

¹The NGC naming convention stems from the New General Catalogue (Dreyer, 1888), which is an enlarged and revised version of the catalog provided by Herschel (1864). Because it includes many nebulae that turned out to be galaxies, many of the brighter galaxies have a NGC designation.

²The nomenclature has its origin from the Third Cambridge Catalogue (Edge et al., 1959a), where sources are named after the entry number of the catalogue. Source entries are sorted in ascending order of their right ascension.

³A redshift in a spectrum occurs when a light-emitting source is moving away from the observer. Hubble’s law (Hubble, 1929) describes the connection between the redshift and the distance of extragalactic sources. Hence, the cosmological redshift can be used to estimate extragalactic distances in the Universe.

and broad, are a mixture of so-called allowed and forbidden lines. While the designation of allowed and forbidden lines might be misleading, it is a separation into likely and very unlikely electron transitions occurring in atoms. The broad-line Seyfert galaxies are classified as Seyfert type 1, while those lacking the broad lines are classified as Seyfert type 2. However, intermediate categories, such as Seyfert 1.5, also exist, for which the broad lines gradually weaken, i.e., their equivalent width decreases (e.g., [Osterbrock & Koski, 1976](#), [Osterbrock & Martel, 1993](#)). Furthermore, narrow-line Seyfert 1 galaxies were found, whose spectra showed broad lines that are significantly more narrow than those within Seyfert 1 galaxies ([Osterbrock & Pogge, 1985](#)).

A feature, which is found in $\sim 10\%$ of all quasars ([Kellermann et al., 1989](#), [Ivezić et al., 2002](#)), is a powerful collimated, powerful outflow, called ‘jet’. Interestingly, a jet connected to the source M 87 was observed by Heber D. Curtis, before the *Great Debate* took place. Curtis described his observation as follows: “A curious straight ray lies in a gap in the nebulosity in p.a. 20° , apparently connected with the nucleus by a thin line of matter. The ray is brightest at its inner end, which is $11''$ from the nucleus.” ([Curtis, 1918](#)). [Schmidt \(1963\)](#) also reported the appearance of a jet very close to the source 3C 273 in an optical image. The presence of a jet is typically linked to strong radio emission, though. Hence, a main distinction into groups of radio-loud and radio-quiet AGN can be made. [Kellermann et al. \(1989\)](#) proposed to define a radio-loud source by the ratio of its radio luminosity at 5 GHz to its optical luminosity at 4440 \AA . If the result exceeds a value of 10, an AGN is considered radio-loud. Mapping the radio structure of more than 80 radio-loud AGN, or radio galaxies, revealed that a large amount of sources exhibits a double-sided, or even more complex structure ([MacDonald et al., 1968](#)), indicating that a connection exists between the core and the observed lobes ([Hargrave & Ryle, 1974](#)). By studying the morphology of extended radio emission from AGN, [Fanaroff & Riley \(1974\)](#) discovered a correlation between the positions of the brightest radio spots with the overall radio luminosity of a source. Those sources showing bright, compact radio cores and relatively weak lobes seemed to be less luminous, and are labelled Fanaroff-Riley type I (FR I). Fanaroff-Riley type II (FR II) radio galaxies display very bright lobes, and are more luminous. Typically, FR I sources reveal a two-sided jet, while FR IIs only show one jet feature.

Among the radio-loud quasars, a particular class named flat spectrum radio quasars (FSRQs) was established after [Pauliny-Toth et al. \(1978\)](#) studied a sample of more than 250 radio-loud AGN, and found that roughly 60% of the strong radio sources appear compact and display the flat spectrum previously described for a smaller number of sources by [Kellermann & Pauliny-Toth \(1969\)](#). The ability to create radio maps enabled radio astronomers to resolve the observed radio emission further, which led to the discovery of changes in the brightness distribution. By measuring the changing distance of the weaker spots to the bright core, it appeared as if the component moved at superluminal speed (e.g., [Wittels et al., 1976](#), [Cohen et al., 1977](#), [Seielstad et al., 1979](#)). Furthermore, some of the quasi-stellar radio sources revealed strong and rapid fluctuations (e.g., [Dent, 1965b](#), [Pauliny-Toth & Kellermann, 1966](#), [Allen et al., 1968](#), [Kellermann & Pauliny-Toth, 1968](#)). [Readhead et al. \(1978\)](#) and [Blandford & Königl \(1979\)](#) resolved the conflict regarding the violation of the laws of physics (superluminal motion), and explained the observed variability at the same time by establishing the model of a relativistic, collimated jet, which is seen rather head-on for FSRQ.

Another type of AGN is the so-called BL Lacertae objects (BL Lacs), which were named after the eponymous source BL Lacerta. When first discovered in 1929, the object BL Lacerta was thought to be a very variable star, and received a corresponding designation (Hoffmeister, 1929). In 1968, however, a radio source was found coincident with the position of BL Lacerta, but at that time, the nature of the source was uncertain (Schmitt, 1968). Over the years, many more similar sources were found (e.g., Disney et al., 1974, Stein et al., 1976, Craine et al., 1976, Leacock et al., 1976, Arp et al., 1976), and suspected of being some kind of link between radio galaxies and quasars (e.g., Weiler & Johnston, 1980).

Apart from the emission at radio and optical wavelength, AGN also typically exhibit X-ray emission (e.g., Giacconi et al., 1974, Fabbiano et al., 1992, Tozzi et al., 2006), which is variable (e.g., Lawrence, 1980, Barr & Mushotzky, 1986, McHardy, 1989) and correlated to their optical and radio luminosity, as well as stronger if coming from a radio-loud source (e.g., Zamorani et al., 1981, Worrall et al., 1987, Miller et al., 2011). The X-ray emission of AGN originates both in the region around the SMBH, as well as in the jet.

Some quasar sources exhibit γ -ray emission as well, with 3C 273 being the first discovered at γ -rays (Bignami et al., 1981). In the 1990s, γ -ray emission was detected from a few more quasars (e.g., Dermer & Schlickeiser, 1992), and also BL Lacs (Punch et al., 1992). Many more detections followed with new and more sensitive instruments (see also Sect. 2.1). The γ -ray emission zones, even though not fully resolved yet, lie in the jet.

1.1.2 A unifying model and its limits

Among the different types of AGN, similarities exist between some of those types, which sparked the idea that the AGN phenomenon can be unified. A first attempt was made by Scheuer & Readhead (1979), who tried to unify the radio-loud and radio-quiet quasars. From a study of Seyfert galaxies with X-ray data, Lawrence & Elvis (1982) concluded that the region where broad lines originate, is obscured for Seyfert 2s, because we observe those galaxies from the side. This assumption was further strengthened by Antonucci (1984), who detected broad emission lines in polarised spectra, but not in the total intensity spectra, of the same sources. He proposed a toroidal obscuration structure, which blocks light in general, but reflects polarised light. Barthel (1989) took up the concept of different orientations of the sources as well and suggested that radio-loud quasars are, in principle, FR II galaxies, but seen from a more aligned perspective. In extensive reviews, Antonucci (1993) and Urry & Padovani (1995) unified the various types of AGN. The main concept behind their unification model is a combination of different orientations and intrinsic source power.

Figure 1.1 illustrates this model. The central engine of an AGN is a SMBH, powered by accretion. Material that becomes trapped in the gravitational potential of the SMBH forms an accretion disk to conserve energy and matter (Shakura & Sunyaev, 1973). For a simple thin disk, one can assume that the emission is a mixture of blackbody radiation profiles at different temperatures, as the temperature increases inward. Inside the disk, viscosity is responsible for the outward transport of angular momentum, which results in material falling onto the black hole after it passes the innermost stable orbit. The maximum accretion rate can be estimated by first calculating the Eddington limit, which describes the maximum luminosity of an accreting

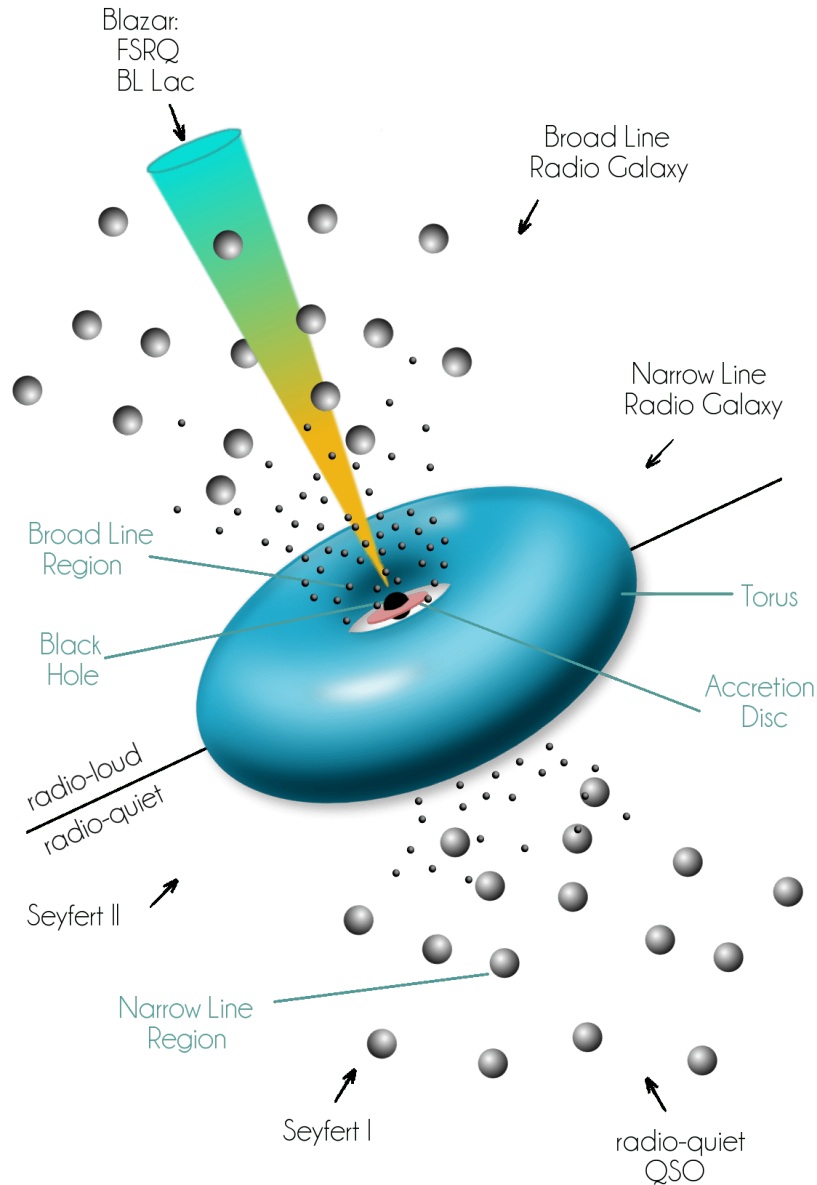


Figure 1.1.: Schematic representation of the unification model (sizes not to scale). Radio-loud AGN are represented above the dividing line. The central black hole is surrounded by an accretion disk, while a dust torus further out is able to block the light for sources seen edge-on. The broad and narrow line region extend further out. According to the model, a relativistic, collimated outflow, or jet, is exhibited by radio-loud AGN. Note that jets are always launched in two opposing directions to fulfil the conservation of angular momentum. This symmetry is not depicted in this illustration. Credit: F. McBride after [Urry & Padovani \(1995\)](#)

body via

$$L_{\text{Edd}} = \frac{4\pi GMm_p c}{\sigma_T} = 1.3 \cdot 10^{38} \frac{M}{M_\odot} \text{ erg s}^{-1}, \quad (1.1)$$

by taking into account the mass of the body, M , the mass of the proton, m_p , the speed of light, c , and the Thomson scattering cross-section, σ_T . The maximum accretion rate, \dot{m}_{max} , can be

determined from L_{Edd} and the efficiency η of the accretion process with

$$\dot{m}_{\text{max}} = \frac{L_{\text{Edd}}}{\eta c}. \quad (1.2)$$

Very few mass compared to the mass of the SMBH is required to keep an AGN active. Assuming an efficiency of $\eta = 0.1$, one to two solar masses of accreted matter per year suffice to generate the observed luminosities (Lasota et al., 1996).

This central region of SMBH and accretion disk is surrounded by the broad line region (BLR). This region exhibits a high density ($n > 10^9 \text{cm}^{-3}$, e.g., Osterbrock, 1989). Because the radiating material is moving around at high velocities (up to 10^4km s^{-1} , e.g., Corbin, 1995), the emission lines, which can be detected in the optical and UV light, are strongly broadened. It is not clear where the material in the BLR originally comes from, but it has been proposed that it in- and outflowing material from the accretion disk or the torus could supply the BLR (Czerny & Hryniewicz, 2011).

Further out and above, a less dense region exists that is responsible for the observed narrow emission lines. The density in this so-called narrow line region (NLR) is low enough to allow forbidden transitions. Its material is highly ionized, and (bi)conically shaped NLRs are also referred to as ionisation cones. The exact origin of the material in the NLR is not clear yet (e.g., Cracco et al., 2011, Congiu et al., 2017).

At a larger distance, a torus made of dust blocks the view to the accretion disk and BLR if the AGN is viewed edge-on. Although illustrated as a consistently thick torus, they have been found to be clumpy (e.g., Krolik & Begelman, 1988, Markowitz et al., 2014, Beuchert et al., 2015). Their formation can be explained by radiative pressure from the accretion disk (Liu & Zhang, 2011), which agrees with a model proposed by Lawrence (1991) according to which the torus originates from expelled shells of gas, while solely the outer edge of it is actually dusty.

Lastly, a double-sided jet is present in radio-loud AGN. Its physics are explained in detail in Sect. 1.2. The majority of the source classes fit within this unification scheme. Objects that are orientated such that we can see the accretion disk and BLR are radio-quiet quasars, Seyfert 1 galaxies, broad line radio galaxies, and blazars, although the emission from the latter is largely dominated by the jet. For the sources that are viewed edge-on, the torus blocks emission from the innermost part of the AGN, and only the NLR and, if present the jet, can be seen. These AGN are Seyfert 2 galaxies, or narrow line radio galaxies. Radio galaxies, independent of the presence of broad lines in their optical spectrum, can either be low or high luminosity sources, i.e., of type FR I or FR II. FSRQ and BL Lacs both fall under the classification of blazars, as their jets point towards us with a very small viewing angle (Urry & Padovani, 1995).

Over the years, however, inconsistencies have been found when applying the unification model to all observed AGN. One example is the possible detection of ‘true’ Seyfert 2 galaxies, i.e., Seyfert galaxies lacking a BLR altogether, which could be very low luminosity AGN (e.g., Tran et al., 2011). A different absorption mechanism than just that provided by the torus is likely as well (e.g., Panessa & Bassani, 2002, Bianchi et al., 2012). Another example are narrow-line Seyfert 1 galaxies, which exhibit less broadened emission lines from the BLR (see Sect. 5.1 for an extensive description of these objects). Furthermore, relativistic jets have been found in AGN that have been classified as radio-quiet or even radio-silent (Lähteenmäki et al., 2018). Padovani himself declared the unified model dead at the conference ‘Active Galactic

Nuclei: what's in a name?', and suggested to classify AGN rather into jetted and non-jetted sources, instead of radio-loud versus radio-quiet (Padovani, 2017).

1.2 Jetted AGN

This thesis covers jetted AGN, and blazars in particular. Hence, I will give an overview of jet physics, AGN variability, and broadband emission from a blazar study's perspective. A very extensive review on relativistic jets was recently given by Blandford et al. (2019), and complemented by Foschini et al. (2021).

1.2.1 Jet formation, structure & emission

Jets are collimated outflows of particles that move at relativistic speed. The process of the particle acceleration is unclear, but it is mainly believed that shock acceleration plays a large role as it is able to produce the observed velocities of jets (Blandford & Königl, 1979).

Two main theories exist that explain how a jet can be launched. The first one has been proposed by Blandford & Znajek (1977) and considers the extraction of angular momentum from the black hole itself. If a black hole is rapidly rotating, that is a so-called *Kerr black hole* described by the Kerr metric (Kerr, 1963), it develops an ergosphere. Inside the ergosphere, particles can interact with one another, which enables the extraction of energy from the black hole (Penrose, 1969). Magnetic field lines are confined within the accretion disk and are subject to the effect of frame-dragging inside the ergosphere of the black hole, which leads to a, potentially helical, twist of the magnetic field lines. Inside the ergosphere, particles can interact with one another, and some of them can escape by being accelerated into the jet by the tangled magnetic field, which enables an energy extraction from the black hole and the production of γ -rays (Penrose, 1969, Williams, 1995). Another theory was presented by Blandford & Payne (1982), who proposed a magneto-centrifugal launching process, during which a magnetically driven wind or outflow of accelerated particles is drawn away perpendicular from the accretion disk. The magnetic field itself is created by the plasma, i.e., charged particles moving around freely and inducing a magnetic field. Very high resolution radio observations might be able to resolve the jet base in the future, and determine if one of these processes is dominant in all or most AGN, or if their occurrence is equally distributed. Furthermore, simulations involving general relativity and magneto-hydro dynamics, and often also radiative transfer and dissipative processes, can reproduce several of the observed jet characteristics (e.g., Meier, 2012, McKinney et al., 2014, Nakamura et al., 2018, Qian et al., 2018). It is still unclear how jets stay so extremely well collimated over distances of several kpc.

The exact particle composition in jets is not known, but it is likely that it contains the plasma from the accretion disk, which is possibly both leptons and hadrons. However, leptonic particles, e.g., electrons and positrons, are much easier to accelerate because of their low mass, which is why they are usually considered as the main contributor to jet emission. In general, the emission of a blazar is largely dominated by the jet as its emission is relativistically boosted towards us. From radio to optical, or up to X-ray emission depending of the type of blazar (see Sect. 1.2.3), the observed radiation of a blazar originates from leptonic synchrotron emission (e.g., Schwinger, 1949). The synchrotron emission is produced due to relativistic particles

being accelerated, e.g., when gyrating in a magnetic field (Ginzburg & Syrovatskii, 1965, Blumenthal & Gould, 1970, Rybicki & Lightman, 1979, Reynolds, 1982), and their equation of motion can be described by

$$\frac{d}{dt}(\gamma m \vec{v}) = \frac{q}{c} \vec{v} \times \vec{B}, \quad (1.3)$$

under consideration of the particle Lorentz factor, γ , the magnetic field, \vec{B} , the speed of light, c , and the mass, charge, and motion of the particle, m , q , and \vec{v} , respectively. The generated power, which is the radiation emitted per particle, is (Rybicki & Lightman, 1979)

$$P = \frac{2q^4 B^2 \gamma^2 v^2}{3m^2 c^5} \sin^2 \alpha, \quad (1.4)$$

including the pitch angle α , which is the angle between the velocity vector and the magnetic field lines. In the rest frame of the particle, the synchrotron emission has a dipole characteristic. In the case of blazar jets, the particles move relativistically towards us, and their emission is Doppler boosted. Leptonic particles, e.g., electrons and positrons, are usually considered as the main contributor to jet emission, because of their much lower rest mass compared to, e.g., protons. Hence, it is much easier to accelerate them, and they also radiate more efficiently, since their radiation scales inverse to the particle mass (see Eq. 1.4).

The energy distribution of the involved leptons in AGN follows a power-law distribution of index p , which results in a power-law spectrum for the overall synchrotron emission that is created by the combination of all individual electron spectra. The spectral index of the synchrotron spectrum is $\alpha = -(p - 1)/2$. At lower energies marking the break frequency of the spectrum, the photons produced in the synchrotron process are being absorbed by the same population of electrons that created them. This mechanism is called synchrotron-self absorption. This part of the spectrum follows a power law with an index of $\alpha = 5/2$. For a detailed derivation of the equation to compute the synchrotron emission, I refer to Gokus (2017, Chapter 2).

The origin of the high energy emission (X-ray to VHE γ -rays) is still of debate. Leptonic emission is produced by the inverse Compton scattering process, i.e., a photon gains energy via an interaction with a relativistically moving electron. Different scenarios exist regarding the origin of the seed photons. One possibility is that the synchrotron photons are up-scattered by the same electrons that emitted them, which is called the synchrotron-self Compton process (SSC; e.g., Ghisellini et al., 1985, Maraschi et al., 1992). Photons could also be provided by external sources, which could be the accretion disk, the broad line region, the torus, or the cosmic microwave background (e.g., Dermer et al., 1992, Sikora et al., 1994, Tavecchio et al., 2000). In these cases, one refers to the inverse Compton process as external Compton (EC).

It is also possible that the high-energy emission has a hadronic origin, even though it is not entirely clear how protons can be accelerated to high enough velocities, as their mass is a factor of >1000 larger compared to electrons. The most likely process involved is shock acceleration (Fermi, 1949). If protons are accelerated in the jet, they are capable of producing γ -ray emission as well as neutrinos (e.g., Mannheim, 1993, Rachen & Mészáros, 1998, Atoyan & Dermer, 2001, Mücke & Protheroe, 2001, Mücke et al., 2003, Kelner & Aharonian, 2008). In the interaction of relativistic protons with low-energy photons, pions can be produced. Depending on their charge, they decay into γ -ray photons, or cascadingly into muons, positrons, and neutrinos, which is called pion photoproduction (Mannheim &

Biermann, 1989, 1992, Mannheim, 1993, Dermer & Schlickeiser, 1993). The ‘smoking gun’ for the presence of protons in the jet would be identifying an AGN as a neutrino source. Kadler et al. (2016) suggested an association of the detection of a 2 PeV neutrino in 2012 with the blazar PKS B1424-418, which went through a major and long-term γ -ray and radio outburst at the same time. The origin of the neutrino was not well constrained, and a large amount of γ -ray blazars was positionally consistent with in the neutrino event. Hence, their association was on a level of 2σ . Recently, the blazar source TXS 0506+056 was spatially coincident with the detection of a high-energy extragalactic neutrino while showing a major γ -flare (Tanaka et al., 2017). Since this neutrino event was track-like, the position of its origin on the sky was fairly well constrained. The significance of this coincidence not being random has been found to be above 3σ (IceCube Collaboration, et al., 2018a). Other teams approached to explained the observed neutrinos by computing the expected neutrino fluence from the radio-brightest blazars within the neutrino error fields (e.g., Krauß et al., 2014, 2015, Kreter et al., 2020b). However, no other AGN or blazar has been clearly identified as a neutrino emitter so far, and some indications exist that the expected correlation with elevated γ -ray emission might not be as essential as previously thought (IceCube Collaboration, et al., 2018b, Krauß et al., 2018, Kiehlmann et al., 2019, Rodrigues et al., 2021).

1.2.2 Variability

AGN exhibit flux variations on different time scales across all kinds of categories. Early on, the variability of some extragalactic objects was detected in the optical band (e.g., Sharov & Efremov, 1963, Sandage, 1964, Goldsmith & Kinman, 1965, Sandage, 1967, Oke et al., 1967, Fitch et al., 1967), among them the bright quasar 3C 273, for which variability was found in the radio band as well (Dent, 1965a). At that time, Rees (1966) already proposed that relativistic effects play a role in the observed radio variability. The first variability signature of AGN at X-ray energies was found for sources like 3C 273 (White & Ricketts, 1979, Bradt et al., 1979), the radio galaxy Centaurus A (Davison et al., 1975), and the Seyfert 1 galaxy NGC 4151 (Ives et al., 1976, Lawrence, 1980), and determined for a larger sample of AGN with data from the Ariel V Sky Survey by Marshall et al. (1981).

Among all sub-categories of AGN, blazars exhibit the strongest flux variations across the electromagnetic spectrum in terms of rapidness and amplitude (e.g., Stein et al., 1976, Wagner & Witzel, 1995, Ulrich et al., 1997). Their variability can be broadly classified into three different time scales (e.g., Singh & Meintjes, 2020): *long-term variability*, which is observed for time ranges covering months to years or decades, *short-term variability*, which describes flux variations happening within a few days up to several weeks, and *micro-variability*, which condenses everything from intra-day variability down to time ranges of a few minutes.

In general, the shortest variability time scales are connected to bright flares, and are typically observed at the highest energies, which can be detected by γ -ray telescopes such as *Fermi*/LAT, H.E.S.S., MAGIC, and VERITAS (see also Sect. 2.1). In particular, the most rapid flux variations observed at γ -ray energies were shorter than ten minutes, and seen during bright flares of PKS 2155–304 (Aharonian et al., 2007), Mrk 501 (Albert et al., 2007), IC 301 (Aleksić et al., 2014), 3C 279 (Ackermann et al., 2016), and CTA 102 (Meyer et al., 2019). This micro-variability seen in blazars is as short as the light crossing time of the black hole, and for some

flaring events even shorter, which indicates that the origin lies either close to the SMBH or in a smaller region further downstream in the jet (e.g., [Vovk & Babić, 2015](#)). However, the exact origin of these flares is still very much debated today.

Current models are challenged to explain the brightness and fast variability in accordance with observed low bulk Lorentz factors, in particular for HBL sources. This ambiguity has been coined the *Doppler crisis* ([Tavecchio, 2006](#)). The measured velocities of the radio jet at parsec-scale are too slow to create the necessary boosting to achieve minute-scale variability at TeV energies, i.e., a bulk Lorentz factor in the range of 50 to 100. In addition, further constraints come from current SED models (see also Sect. 1.2.3), as they can only explain the observed γ -ray emission within weakly magnetised environments, but those lie supposedly only further out in the jet. In order to efficiently produce the amount of detected γ -ray emission, a sufficient amount of photons is needed, which could be supplied by, e.g., the BLR that is located close to the jet base. However, the γ -ray emission can be attenuated by dense optical and UV photon fields ([Jelley, 1966](#)) that originate from the BLR ([Liu & Bai, 2006](#), [Poutanen & Stern, 2010](#)), the jet or the accretion disk ([Dermer et al., 1992](#), [Maraschi et al., 1992](#), [Bednarek, 1993](#)). As no signatures of absorption have been found in the γ -ray spectra of flaring blazars, one usually assumes that the γ -ray emission originates from a certain distance to the BLR (e.g., [Abdo et al., 2010b](#), [Tavecchio et al., 2011](#), [Pacciani et al., 2012](#)).

In the following, I will summarise the most prominent models that have been used so far to explain blazar variability and flares on different variability time scales.

Shock-in-jet model

In order to explain the variability in the optical and radio bands, which are the signatures of synchrotron emission from blazar jets, [Marscher & Gear \(1985\)](#) brought forward a model of electrons traversing recollimation shocks in the jet. Their model was motivated by knots moving downstream the jet that were detected in VLBI images of 3C 273 ([Unwin et al., 1985](#)). In Fig. 1.2a, the schematic structure of the jet from the central SMBH to the NLR is shown. It is assumed that the jet is conical and contains a poloidal magnetic field, and that particles are ejected at the jet base and move downstream at relativistic speed. Fluctuations in the particle flow can create shock waves, where particles gain some energy for each crossing of the shock front, which results in a flare that is first seen at higher energies. X-ray and γ -ray emission due to self-Compton processes are predicted by this model as well. The model by [Marscher & Gear \(1985\)](#) has been refined over the years (e.g., [Daly & Marscher, 1988](#), [Türler et al., 2000](#), [Spada et al., 2001](#), [Nalewajko & Sikora, 2009](#), [Türler, 2011](#), [Nalewajko et al., 2012](#), [Marscher, 2014](#)), and simulations were able to produce the observed properties of (radio-) flaring blazars (e.g., [Komissarov & Falle, 1997](#), [Fromm et al., 2011, 2016](#)). It was also suggested by [Hervet et al. \(2019\)](#) that recurrent flares could be created by the same bunch of particles moving through individual recollimation shocks that are located along the jet, which are observed for several sources.

Spine-sheath model

The spine-sheath model describes a structured jet made of two layers: the fast-moving spine and the slow-moving sheath. This idea was already proposed based on theoretical arguments by

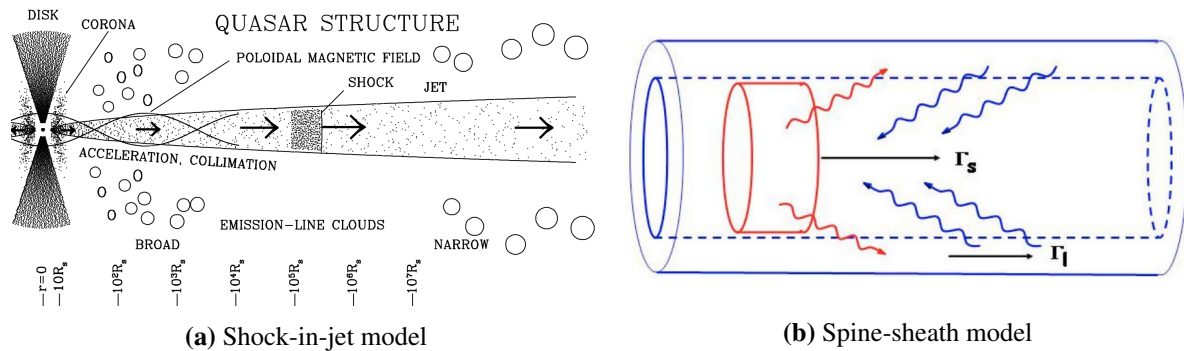


Figure 1.2.: The shock-in-jet model (a) depicts the structures of the entire jet, in which particles move along, and cut across recollimation shocks. The spine-sheath model (b) assumes a jet to be structured into an inner layer, the spine, where particles move very fast, which is encompassed by an outer layer, the sheath. Both layers can interact with one another and irregularly accelerate particles.

Credit: (a): [Marscher \(2005\)](#); (b): [Ghisellini et al. \(2005\)](#)

[Henri & Pelletier \(1991\)](#), and components propagating through the jet at different speeds were suggested to explain observed properties of radio galaxies ([Laing et al., 1983](#), [Komissarov, 1990](#)), or to explain FRI galaxies and BL Lac objects with one theory ([Chiaberge et al., 2000](#)). Motivated by the discovery of limb-brightened jets in VLBI maps (e.g., [Giroletti et al., 2004](#)), [Ghisellini et al. \(2005\)](#) established this model. Variability is supposed to be produced by the interaction and feedback of the two layers, or via irregular particle acceleration (see Fig. 1.2b), which is similar to the shock-in-jet model.

Minijets-in-a-jet model

The discovery of micro-variability, and particularly the flaring behaviour on minute time scales at γ -rays, prompted the development of new, other models, as the established ones could not explain the variability on such short time scales. On top of that, for FSRQ-type blazars, an origin of the γ -ray emission close to the SMBH and within the BLR is unlikely as the large amount of target photons would trigger pair production and would leave signs of γ -ray attenuation. (e.g., [Aleksić et al., 2011](#), [Ackermann et al., 2016](#), [Shukla et al., 2018](#), [Wendel et al., 2021](#)). Over the past years, several models have been suggested, which generally rely on some kind of smaller emission region within the jet that produce an additional particle acceleration, which can cause extremely short flares if the emission of these regions crosses our line of sight. The first one of these models was proposed by [Ghisellini & Tavecchio \(2008\)](#), who explain the fast variability seen in PKS 2155–304 with small regions (‘needles’) moving faster than the ambient jet, and can be observed when moving directly towards us. They suggest that many of these regions exist through the jet, but are differently oriented and might change their direction of motion, which causes random flares. However, the model as such can only account for ‘orphan’ TeV flares, i.e., flares that only occur at VHE γ -rays and are not seen at other wavelengths.

A different approach was chosen by [Giannios et al. \(2009\)](#), who suggested the occurrence of magnetic reconnection in the jet, which can strongly accelerate particle blobs that exhibit a much larger bulk Lorentz factor than the overall jet if moving directly towards our line

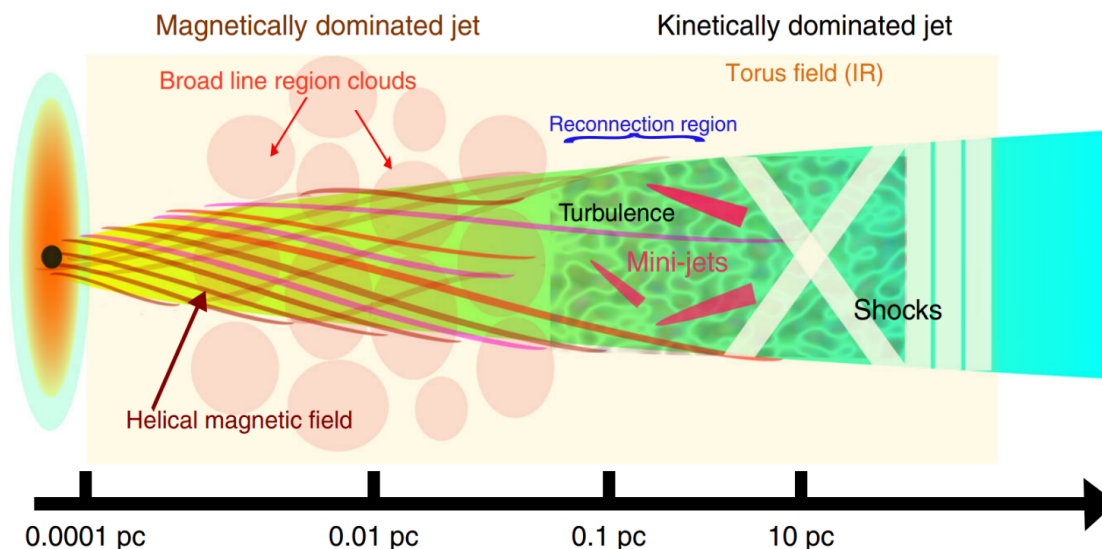


Figure 1.3.: The minijets-in-a-jet model requires turbulent zones of magnetic reconnection that can accelerate plasma blobs that move very fast, and into random directions, within the ambient jet medium. Those form the so-called mini-jets. Credit: [Shukla & Mannheim \(2020\)](#)

sight (see Fig. 1.3). [Narayan & Piran \(2012\)](#) further refined this model and proposed the additional presence of relativistic turbulence, which is created by magneto-hydrodynamic plasma instabilities, and can cause a random motion of these new emission regions. The observed variability time scales during flares correspond to the size of the involved emission region in the co-moving frame.

The general concept of miniflares-in-a-jet is able to produce the statistical properties of γ -ray light curves ([Biteau & Giebels, 2012](#)), and the acceleration due to the process of magnetic reconnection is indeed able to create the observed power-law shape of particle distribution (e.g., [Guo et al., 2014](#), [Sironi & Spitkovsky, 2014](#), [Werner et al., 2016](#), [Li et al., 2018](#)). [Shukla & Mannheim \(2020\)](#) used this model to successfully explain the extremely bright and variable behaviour of 3C 273 in 2018. The spectral properties of the γ -ray emission indicated a co-spatial origin of the major, slowly moving flare envelope and the very fast, minute-scale flares, and the lack of γ -ray absorption places the region just outside of the BLR. Magnetic reconnection also creates specific polarisation signatures, e.g., swings of the polarisation angle. With the recent launch of an X-ray polarisation detector on-board IXPE (see Sect. 2.2.2), it will be possible to test this model for rapid variability for the brightest and very variable HBLs, i.e., Mrk 501 and Mrk 421 ([Zhang et al., 2021](#)).

Jet-Star interaction model

Another model to explain minute-scale variability by blazars involves the interaction of the jet with a crossing star. This idea was first brought forward to explain TeV flares from M 87, a non-blazar AGN ([Barkov et al., 2010](#)), but adapted to explain the rapid variability within blazar jets as well ([Barkov et al., 2012](#)). A jet-star interaction has also been proposed for the radio galaxy Centaurus A, for which VLBI observations revealed a potential obstacle interrupting the jet flow ([Müller et al., 2014](#)). [Barkov et al. \(2012\)](#) describe a scenario, in which a red giant

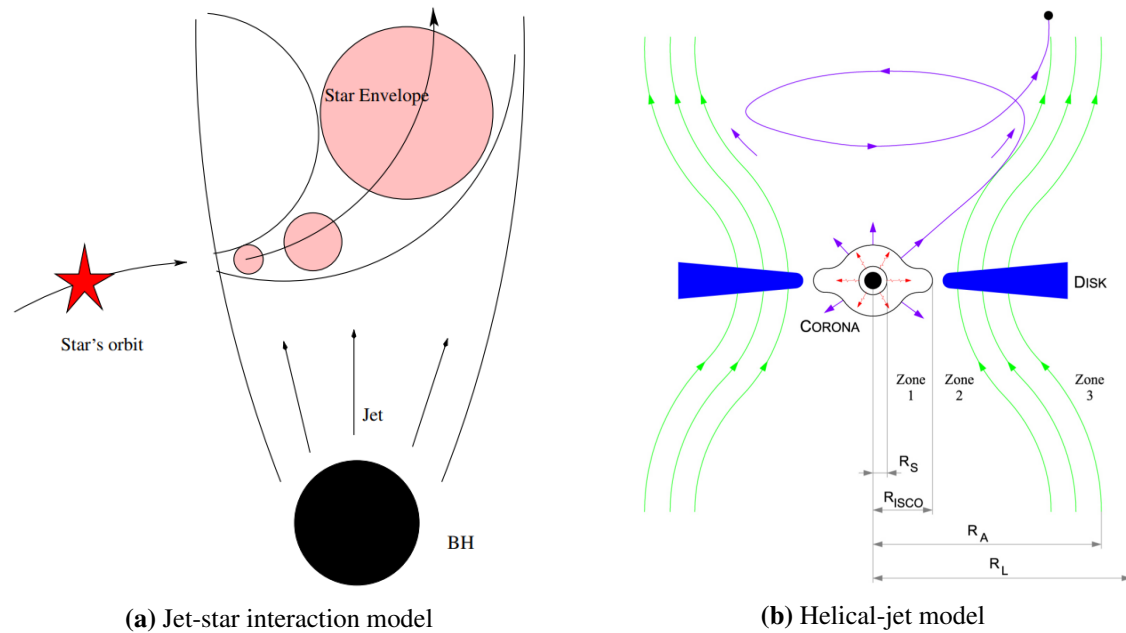


Figure 1.4.: The jet-star-interaction model (a) describes the scenario of a red giant star passing through a powerful blazar jet. The helical-jet model (b) describes how plasma from the accretion disk is dragged away by the magnetic field that builds the base of the jet, whilst taking into account relativistic effects close to the SMBH.

Credit: (a): [Barkov et al. \(2012\)](#); (b): [Mohan & Mangalam \(2015\)](#)

star is in some kind of orbit around the SMBH, and crosses the jet, as illustrated in Fig. 1.4a. The jet can drag along the envelope of the star and even ablate it, which will create several blobs of condensed magnetised plasma that moves with high bulk Lorentz factors and sparks non-thermal leptonic or hadronic processes. In case of very powerful jets, i.e., jets with a luminosity $\geq 10^{46} \text{ erg s}^{-1}$, the bulk Lorentz factors of the blobs can be > 100 , and explain the bright and rapid flares seen at TeV energies for a few sources. It is unclear, however, how likely this scenario is, as it depends on the stellar density in the vicinity of the central part of an AGN. Currently, no measurements exist that can put a constrain on the expected numbers of (red giant) stars. As shown by [Heil & Zacharias \(2020\)](#), a scenario involving a gas cloud would yield similar results.

Disk-jet connection

The process of the jet launch and the connection between the accretion disk and the jet are still not fully understood. The launch of X-ray satellites capable of taking highly resolved light curves, e.g., Exosat, Ginga, and RXTE, sparked a variety of studies of the variability within (black hole) X-ray binaries (e.g., [Hasinger & van der Klis, 1989](#), [Belloni & Hasinger, 1990](#), [Miyamoto et al., 1991, 1992](#), [Nowak et al., 1999](#)). To explain the observed variability, a connection to the accretion disk was proposed (e.g., [Mineshige et al., 1994](#), [Takeuchi et al., 1995](#), [Lyubarskii, 1997](#)). In particular, [Lyubarskii \(1997\)](#) showed that changes in the accretion rate of a black hole can be caused by viscosity within the accretion disk, which results in flicker-noise. This model is consistent with the found linear relation of the flux of a source

with its variability amplitude (Uttley & McHardy, 2001). The discovery of the same relation in X-ray binary systems being powered by a neutron stars instead of a black hole yielded evidence for a fluctuating-accretion scenario (Uttley, 2004). King et al. (2004) proposed a model in which local dynamo processes are able to launch large-scale outflows given the right conditions for a large-scale magnetic field. Fluctuations moving inward to the central black hole can aggregate multiplicatively and produce a flux distribution that follows a log-normal distribution (e.g., Arévalo & Uttley, 2006).

Since the flux distribution of blazars seems to follow a log-normal distribution as well (e.g., Giebels & Degrange, 2009, Shah et al., 2018, Bhatta, 2021), the question was raised whether the variability in blazars can be caused by changes in the accretion rate in a similar way. However, this model can only be applied when the observed X-ray variability time scales are longer than the light-crossing time of the SMBH. A possible way to test for such signatures is to search for a characteristic break within the long-term power spectral density (PSD) of the X-ray emission of a source (e.g., Chatterjee et al., 2018). Such breaks have already been found in the PSDs of X-ray light curves of black-hole X-ray binaries (e.g., Nowak, 2000, Axelsson et al., 2005), and Seyfert galaxies (e.g., Uttley et al., 2002, McHardy et al., 2006).

A tangible suggestion for the connection between accretion disk and jet was made by Mohan & Mangalam (2015). Their ‘helical-jet model’ describes the motion of material from the accretion disk into the jet via a magnetic field that is anchored in the disk (see Fig. 1.4b). To accurately display the processes taking place close to the SMBH, they take into account general relativity. The matter being transported from the disk into the jet can vary in size, and end up randomly distributed in the jet. Furthermore, the helical motion could create quasi-period oscillations, as well as an aperiodic variability in case of many blobs moving independently through the jet.

Stochastic perturbation in particle acceleration

A different approach for understanding blazar variability is describing the observed fluctuations via stochastic perturbations in the particle acceleration. The idea goes back to the ‘shot’ noise model that was used to describe the variability and randomly appearing flickering in X-ray binaries (e.g., Terrell, 1972, Miyamoto & Kitamoto, 1989, Lochner et al., 1991). For the blazar case, Sinha et al. (2018) simulated small, linear Gaussian variations in the process of particle acceleration, and found that those could also reproduce non-Gaussian flux distributions, e.g., log-normal ones, of the observed emission. Similarly, Burd et al. (2021) simulate the long-term γ -ray emission by blazars using Ornstein-Uhlenbeck parameters (Uhlenbeck & Ornstein, 1930), which are based on a description of Brownian noise. Their simulation succeeds in creating light curves, and corresponding PSDs, that are indistinguishable of observed γ -ray light curves as seen with *Fermi*/LAT.

Geometrical changes

The discovery of (large) misalignment in jets (e.g., Pearson & Readhead, 1988, Wehrle et al., 1992, Appl et al., 1996, Cassaro et al., 2002) has sparked the question whether the variability in these jetted sources might be due to geometrical changes in the jet. It was first proposed by Villata & Raiteri (1999) to explain the variable nature of Mrk 501, and then used to model

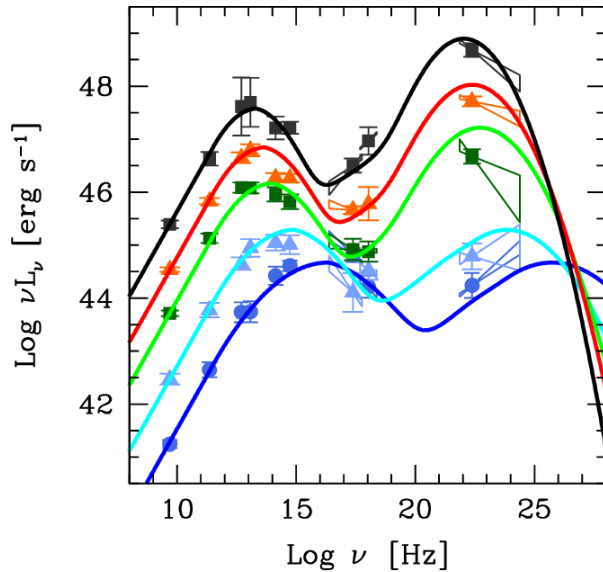


Figure 1.5.: Blazar sequence after [Fossati et al. \(1998\)](#). Several blazar spectra are averaged depending on their peak position. A total of 126 blazars from X-ray and radio-selected samples was taken into account for this plot. A shift of the peak positions of both humps, particularly the low-energy one, is visible for a decreasing average luminosity.

Credit: [Ghisellini et al. \(2017\)](#)

flares observed from sources with an inhomogeneous, curved jet, e.g., in the case of the source CTA 102 ([Raiteri et al., 2017](#)). The benefit of this model is that it is able to explain both fast and long-term variability. The rotation of a twisted jet can change the orientation of several emission regions, which influences the perceived Doppler factor, and can explain fast flares.

1.2.3 Broadband spectral energy distribution

Observational data of one source that are taken at different wavelengths can be combined in a spectral energy distribution (SED). For blazars, this broadband emission is largely dominated by the jet, which is ideal for studying the emission processes within the jet. In general, the non-thermal jet emission follows a power-law distribution, which translates to a constant amount of energy being emitted per frequency decade resulting in a completely flat spectrum in the νF_ν flux spectrum. Hence, the SED is presented in νF_ν space, in units of $\text{erg s}^{-1} \text{cm}^{-2}$. However, the blazar emission is not perfectly power-law distributed, which is why two distinct humps appear in the SED (see also Fig. 1.5). The low-energy hump is attributed to synchrotron emission, while the high-energy hump can be created by leptonic or hadronic, or both emission processes (see Sect. 1.2.1). In addition to the FSRQ and BL Lacertae classification, blazars are also sorted by the peak frequency of the low-energy hump in the νF_ν spectrum ([Padovani & Giommi, 1995](#), [Abdo et al., 2010a](#)). Blazars are characterised as low synchrotron peaked blazars (LSP) if the peak frequency $\nu_{\text{peak}} \lesssim 10^{14} \text{ Hz}$, as intermediate synchrotron peaked blazars (ISP) if $10^{14} \text{ Hz} \lesssim \nu_{\text{peak}} \lesssim 10^{15} \text{ Hz}$, and as high synchrotron peaked blazars (HSP) if $10^{15} \text{ Hz} \lesssim \nu_{\text{peak}}$. For a few blazars, the peak frequency is found at even higher frequencies in the X-ray regime, i.e., $10^{17} \text{ Hz} \lesssim \nu_{\text{peak}}$, and these sources have been dubbed extreme high synchrotron peaked blazars (EHSP; [Costamante et al., 2001](#)). Some of the EHBL sources only show this extreme behaviour only during flaring activities (e.g., [Ahnén et al., 2018](#), [Arbet-Engels et al., 2019](#)). While BL Lacs are distributed over all these categories, FSRQs seem to only be a part of the LSP population. [Fossati et al. \(1998\)](#) introduced the so-called blazar sequence, which describes the behaviour of blazar spectra that are averaged based on their peak position. They found a direct connection between the position of the synchrotron peak and the overall source

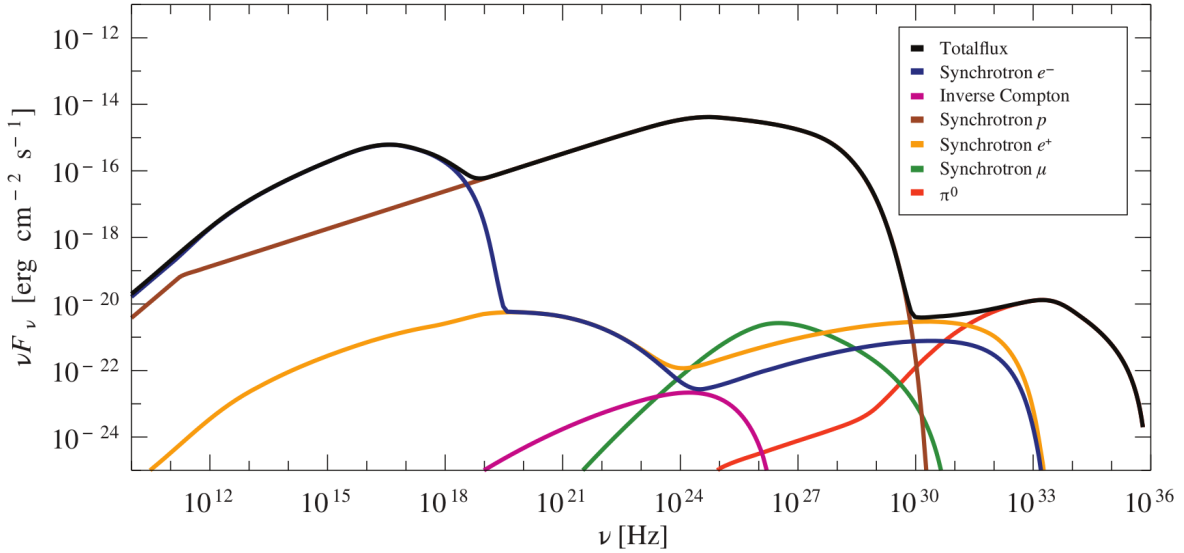


Figure 1.6.: Example SED that is simulated considering both leptonic and hadronic emission processes. The combined flux is displayed in black, the coloured lines represent a different process each (see legend). In this simulation, the high-energy hump is largely dominated by proton synchrotron emission. Credit: [Gokus et al. \(2018\)](#)

power. For less luminous blazars, their ν_{peak} lies at higher frequencies. However, the blazar sequence is heavily debated, and an alternative involving different accretion efficiencies in sources has been proposed to explain the observed anti-correlation of luminosity and peak position ([Meyer et al., 2011](#), [Keenan et al., 2021](#)).

The broadband SED can be modelled with leptonic (e.g., [Ghisellini et al., 1985](#), [Sikora et al., 1994](#), [Celotti et al., 1997](#)), hadronic (e.g., [Mannheim & Biermann, 1989](#), [Dermer & Schlickeiser, 1993](#), [Mannheim, 1993](#), [Petropoulou & Mastichiadis, 2015](#)), or hybrid models, which contain both leptonic and hadronic contributions (e.g., [Weidinger & Spanier, 2015](#), [Gokus et al., 2018](#)). In addition, models can include thermal emission from the accretion disk or the torus if emission from those regions is visible as well. Both hadronic and leptonic models can describe the emission equally well (e.g., [Böttcher et al., 2013](#)). The potential neutrino association with a blazar ([IceCube Collaboration, et al., 2018a](#)) would favour a hybrid or hadronic scenario, though. Hybrid models have the advantage of including both leptons and hadrons. However, the multitude of possible processes is more complex and less constraining (see Fig. 1.6).

For simplicity, it is assumed that the emission originates in one or two zones, although this scenario is highly unlikely (e.g., [Finke et al., 2008](#)). However, to model flaring episodes, a single zone with a one-time particle injection can be used to explain longer-term flaring episodes (e.g., [Eichmann et al., 2012](#)). During rapid spectral changes, the SED ideally contains simultaneous data to perform time-dependent modelling (e.g., [Dimitrakoudis et al., 2012](#), [Richter & Spanier, 2016](#), [Röken et al., 2018](#)), but this is usually not the case. Large efforts are brought forward with multi-wavelength monitoring programmes that can contribute to timely resolve spectral changes in blazars (see also Chapter 3).

1.3 Plan of my thesis

In my thesis I present multi-wavelength studies of AGN that exhibit a major γ -ray flare. The emission and particle acceleration processes in AGN jets are not yet fully understood, and the complexity of the emission needs to be studied with several different instruments that cover a broad range of the electromagnetic spectrum. So far, flares seem to happen randomly, but for some sources more often than for others. Flares can occur in all wavelengths bands, often appearing in several energy regimes at the same time or with a delay of days, or even weeks in the radio band. The trigger for these flares is unknown, but several theories exist. A particular interesting feature is rapid variability on the time scales of only several minutes, which has been observed for several blazars at γ -ray wavelengths. These observations challenge current models. To test those theories and constrain the models, it is crucial to obtain data during the flares, and complement those with observations from before and after a flaring event. In order to acquire these data sets, monitoring programmes have been established, which I introduce in Chapter 3. A range of diverse instruments is involved in AGN multi-wavelength campaigns and I give an overview of radio, optical/UV, X-ray, and γ -ray astronomy in Chapter 2. I focus on instruments measuring high-energy emission, i.e., X-rays and γ -rays, because flares at these energies tend to be the fastest and most powerful.

The first of the two projects presented in this work, is about Mrk 421, which is one of the brightest blazars in the sky. In Chapter 4, I present a multi-wavelength monitoring campaign that is designed to catch the source during a γ -ray flare at TeV energies with the Cherenkov telescope FACT. A flare in June 2019 was successfully detected and followed up by several instruments. I present a variability study of the data. First, I analyse each energy range, from radio up to γ -rays, individually, and then study the behaviour of the low-energy hump in the broadband spectrum of Mrk 421 during the flaring period. Motivated by the detection of extremely short variability time scales in other blazars, which occurred during bright γ -ray flares, I search for signatures of variability on similar time scales in the X-ray data obtained with *XMM-Newton*.

The second project is introduced in Chapter 5 and presents a multi-wavelength study of a γ -ray flare exhibited by the source PKS 2004–447 in October 2019. This source has been classified as a narrow-line Seyfert 1 galaxy, but its radio-loudness and γ -ray emission are untypical features for this classification. In particular, only a handful of NLSy 1s have shown a γ -ray flare, among them PKS 2004–447. I perform a variability analysis of the observational data, which was obtained before, during, and after the flare across the electromagnetic spectrum. The quasi-simultaneous observations of *XMM-Newton* and *NuSTAR* permit a thorough analysis of the X-ray spectrum. Furthermore, broadband SEDs can be constructed, and were modelled with a physical model to determine the possible cause of the γ -ray flare.

In Chapter 6 I summarise and conclude the findings of this work and give an outlook on how to resolve the questions of today in the future.

“The history of astronomy is a history of receding horizons.”

Edwin P. Hubble

Chapter

2

Instruments in Astronomy: Detecting Light across the Broadband Spectrum

The Universe is full of light coming from all kinds of different sources, including active galactic nuclei (AGN, see Chapter 1). To observe light throughout the whole spectrum from radio up to γ -rays, a diverse set of instruments is necessary. As the atmosphere of the Earth is absorbing most of the electromagnetic spectrum (see Fig. 2.1), it is essential to build satellites to observe emission from space. This absorption affects a large part of the infrared emission, very-long wavelength radio emission, and the high-energy part of the spectrum, particularly X-rays and γ -rays. Albeit, very-high energy γ -ray emission can be indirectly observed with Cherenkov telescopes from ground due to its interaction with the atmosphere.

Studying the same object at different wavelengths is called multi-wavelength astronomy, which emerged in only the last few decades, and has allowed astronomers to study sources more thoroughly. Among such sources are AGN, whose different processes and broadband emission I have explained in the previous chapter. To examine their underlying physical processes, and get a full picture, it is essential to combine observations taken both from ground and space .

In this chapter, I give an introduction to the different instruments that have been used to collect observational data for this thesis. First, in Sect. 2.1, I start with a short review of detectors for the most energetic light, γ -rays, and the instruments whose data are used in this thesis. Then, in Sect. 2.2, I continue with a summary of X-ray astronomy, how we detect X-rays, and the instruments that were used in this work. In between these two high-energy sections, I provide an overview of all X-ray and γ -ray observatories (excluding experiments on rockets, space shuttles, and balloons), that have been and are still observing high-energy emission from the Universe, in Fig. 2.6.

I present the optical/UV instruments that contributed data to my work in Sect. 2.3, and complete this chapter with a short introduction to radio astronomy in Sect. 2.4.

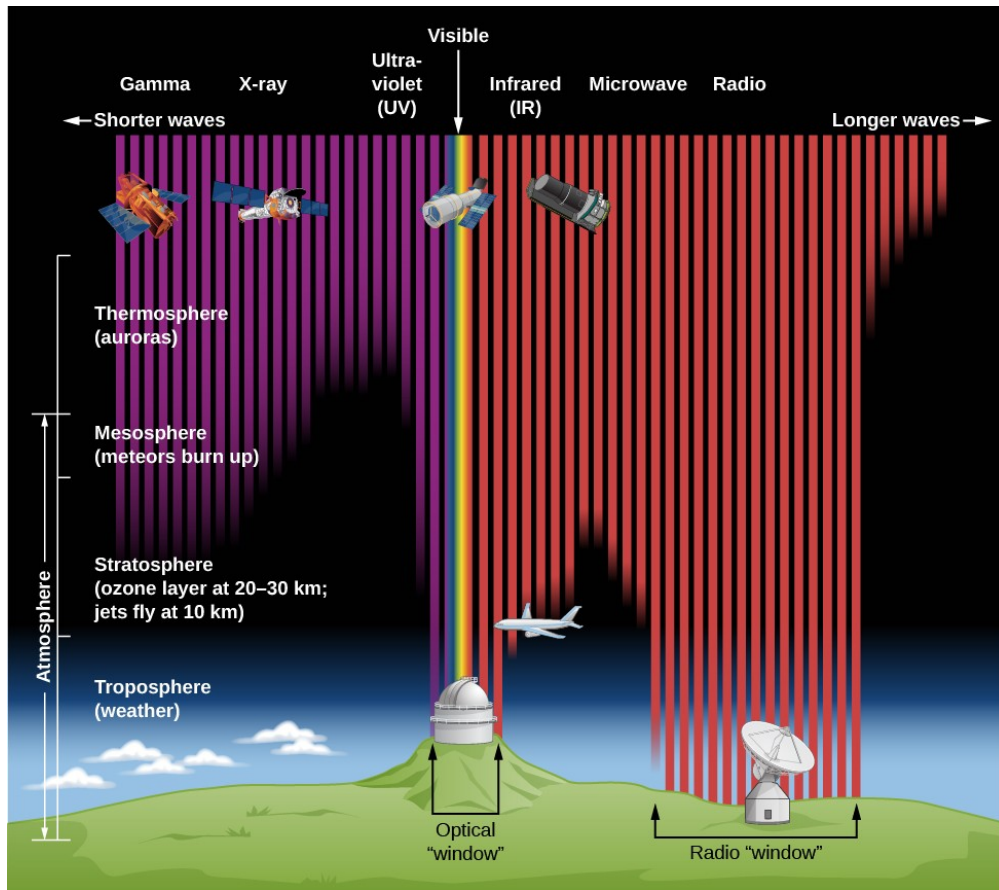


Figure 2.1.: Illustration of the opacity of the Earth’s atmosphere at different wavelengths. At a high altitude from left to right, *Swift*, *Chandra*, *Hubble*, *Spitzer*, are shown as examples for space-based telescopes. On the ground, a typical appearance of large optical and radio observatories is illustrated. Credit: STScI/JHU/NASA

2.1 Gamma-ray astronomy

In this section, I present a short summary of the developments in γ -ray astronomy, and describe two γ -ray telescopes, FACT and *Fermi*/LAT, in greater detail (Sect. 2.1.2 and 2.1.3).

2.1.1 Historical overview

Before γ -ray observations were conducted, it was theorized that γ -ray emission could be produced in space via Compton scattering (Feenberg & Primakoff, 1948), or in the decay of π^0 particles that are created through inelastic nucleon-nucleon collisions in the Galactic disk (Hayakawa, 1952). Morrison (1958) made predictions on the brightness and direction of such γ -ray emission. I have explained some of the different processes producing γ -rays in Sect. 1.2.1, particularly for AGN. The first detection of γ -rays from space was made by the military *Vela* satellites, whose initial mission was monitoring nuclear weapon explosions on Earth. Unintentionally they also discovered γ -ray bursts. The first dedicated missions to explore γ -ray emission in the Universe were the third *Orbiting Solar Observatory* (OSO-3) in 1967, which confirmed galactic γ -ray emission above 50 MeV (Kraushaar et al., 1972), and the

Second Small Astronomy Satellite (SAS-2 [Derdeyn et al., 1972](#)), which identified potentially discrete sources emitting above 10 MeV, such as the Crab nebula, or the Vela super nova remnant. Both were NASA missions. The first European γ -ray instrument was the *Cosmic ray Satellite Option B* (Cos-B; [Bignami et al., 1975](#)), which was launched in 1975. It identified 25 γ -ray sources and produced the first complete map of the Galactic disc at γ -ray energies ([Swanenburg et al., 1981](#)).

In 1991, the *Compton Gamma Ray Observatory* (CGRO; [Kniffen, 1989](#)) started its mission with four onboard instruments, which covered a combined large energy range from 20 keV up to 30 GeV. The *Burst and Transient Source Experiment* (BATSE) searched for γ -ray bursts between 20 keV and 600 keV. The *Oriented Scintillation Spectrometer Experiment* (OSSE), a non-imaging instrument with a sensitivity between 50 keV and 10 MeV, found the first soft γ -ray repeaters. The *Energetic Gamma Ray Experiment Telescope* (EGRET) performed the first γ -ray all-sky survey in the energy range between 20 MeV and 30 GeV and found more than 270 sources emitting γ -rays with an energy higher than 100 MeV ([Hartman et al., 1999](#)). The discovery of γ -ray emission emitted by a large number of blazars was surprising, and hinted at the generation of γ -rays in jets, since blazars were the only type of AGN detected by EGRET ([von Montigny et al., 1995](#)). With the *Imaging Compton Telescope* (COMPTEL; [Schönfelder et al., 1993](#)), the distribution of ^{26}Al could be studied with an all-sky map, and to date COMPTEL still provides the only catalog for sources between 1 MeV and 30 MeV ([Schönfelder et al., 2000](#)). COMPTEL also detected ten blazars and one radio galaxy ([Collmar, 2001](#)).

After CGRO's success, the European Space Agency (ESA) launched the *International Gamma-Ray Astrophysics Laboratory* (*INTEGRAL*; [Winkler et al., 2003](#)) with two on board instruments that are able to detect γ -rays: the spectrometer SPI (20 keV–8 MeV; [Vedrenne et al., 2003](#)), and the imager IBIS (15 keV - 10 MeV; [Ubertini et al., 2003](#)). In addition, there are also two monitor instruments (JEM-X and OMC) on-board to enable simultaneous observations of optical and X-ray emission. *INTEGRAL* was launched in 2002 and was still in operation at the time of writing.

In 2007, the Italian mission *Astro-rivelatore Gamma a Immagini LEggero* (AGILE; [Tavani et al., 2009](#)) joined *INTEGRAL* in space, and has since provided data between 350 keV and 50 GeV by observing with a γ -ray imager and a calorimeter, as well as X-ray data for the energy range of 18-60 keV with a hard X-ray imager. AGILE completed its mission off performing an all-sky scan during its first months, and continued to monitor large fractions of the sky within 24 hours. In addition, it is available for fast follow-up observations of transients. Compared to other γ -ray instruments, the size of AGILE is relatively small, as it is a cube of ~ 60 cm per side.

AGILE was followed into space by the γ -ray satellite *Fermi*, which is continuously monitoring the γ -ray sky between ~ 20 MeV and 1 TeV. The mission and the on board instruments, the *Large Area Telescope* and the *Gamma-ray Burst Monitor*, are described in details in Sect. 2.1.3.

The most recently launched γ -ray observatory is the *Dark Matter Particle Explorer* (DAMPE; [Chang et al., 2017](#)). As the name indicates, its science goal is the search for signatures of Dark Matter. The on-board detector consists of several scintillators, a tracker-converter, and a calorimeter, and is sensitive between 5 GeV and 100 TeV. Since 2015, DAMPE observes elec-

trons and high-energy photons that could be created by the annihilation of Weakly Interacting Massive Particles, which are potential dark matter particles.

To fill the existing gap at MeV energies, a soft γ -ray survey telescope with a sensitivity between 0.2 and 5 MeV is planned to be launched in 2025. The *Compton Spectrometer and Imager* (COSI; [Tomsick et al., 2021](#)) will provide insights on the 511 keV line along the galactic bulge and disk, measure the polarisation at γ -ray energies, and reveal sites of nucleosynthesis in our galaxy. In addition, it will contribute information about the soft γ -ray emission of blazars and assist in finding distant, high-redshift MeV blazars.

Due to low photon statistics and the small detector volumes of space-based instruments, direct observation of γ -rays is possible only up to ~ 1 TeV with current space-based instruments. However, detection of γ -rays with very high energies ($100 \text{ GeV} < E < 100 \text{ TeV}$; from now on referred to as very-high energy/VHE γ -rays) is indeed possible from the ground because of the interaction of γ -rays with nuclei in the atmosphere. The γ -ray photon undergoes pair production, creating an electron-positron pair, which itself emits bremsstrahlung that, in turn, also undergoes pair production, resulting in a cascade, or air shower. Particles created during this shower that are moving faster than the speed of light in some kind of medium, e.g., air or water, emit a short flash of blueish light, called Cherenkov radiation. This kind of radiation has been discovered by [Cherenkov \(1934\)](#) and explained by [Tamm & Frank \(1934\)](#). Cherenkov, Tamm, and Frank received the Nobel prize for their work in 1958. This Cherenkov light emitted by particles in the air shower can be measured with ground-based telescopes. The interaction of γ -rays with the atmosphere starts at ~ 20 km above sea level (a.s.l.), reaches a maximum at roughly 10 km a.s.l., and fades when the particles exceed an energy threshold of 81 MeV. The shape of such a shower is elongated.

However, air showers can also be the result of cosmic rays, i.e., high-energy protons or atomic nuclei, interacting with the atmosphere. Hence, it is necessary to distinguish their signal from the ones caused by VHE γ -rays. The secondary particles of cosmic rays are mainly pions, but also K-mesons or anti-nuclei can be created in the process (see, e.g., [Klapdor-Kleingrothaus & Zuber, 1997](#)). Through decay processes, they can create γ -ray photons, which produce an electromagnetic cascade, but also muons and neutrinos. Hence, showers resulting from cosmic rays have hadronic, leptonic, and electromagnetic components, and they appear broader compared to pure γ -ray induced air showers, due to more transversal momentum.

The technique for γ -ray observations via air showers is called *Imaging Atmospheric Cherenkov Technique* (IACT). The abbreviation IACT is also used for describing the telescopes using this technique, in which case IACT means *Imaging Atmospheric Cherenkov Telescopes*. [Figure 2.2](#) illustrates an air shower resulting from a γ -ray interacting with the atmosphere, and the signal that is seen by an IACT system. Because the air showers usually only last a few nanoseconds, it is required that the detectors have fast electronics to achieve the needed time resolution.

Coincident with the first γ -ray space missions being planned, pathfinding observations of Cherenkov radiation were performed by [Jelley & Porter \(1963\)](#). In 1968, the first ground-based telescope, the *Fred Lawrence Whipple Observatory* (Whipple) measured γ -rays using IACT. The telescope was also formerly known as *Mount Hopkins Observatory*. The telescope, which is located in Arizona, has a diameter of 10 meters, and was in operation until 2009. After its

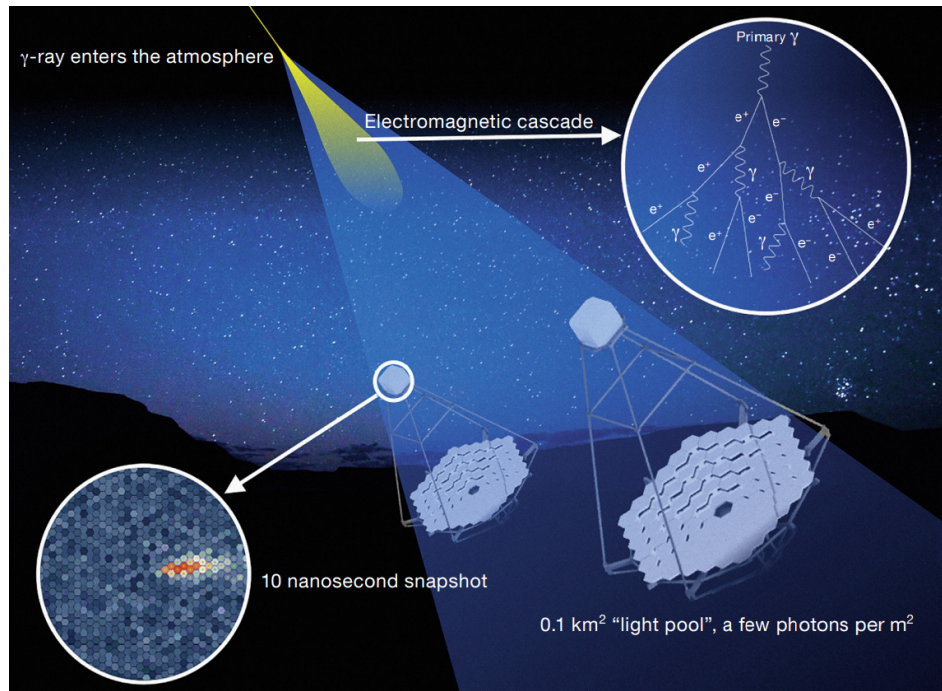


Figure 2.2.: Illustration of an electromagnetic cascade caused by a very-high-energy γ -ray that is interacting with the atmosphere and the corresponding signal in an IACT. Credit: Hofmann (2017)

inauguration, it discovered γ -ray radiation with an energy above 250 GeV via observations, but it took over three years of accumulated data to gain a significance above 3σ (Fazio et al., 1972). In 1989, the discovery of TeV emission from the Crab nebula with the *Whipple* telescope was reported by Weekes et al. (1989). *Whipple* was also the first instrument to detect TeV emission from an extragalactic source, the blazar Mrk 421 (Punch et al., 1992).

The first next-generation IACT was also installed in Arizona at the same site as *Whipple*. The *Very Energetic Radiation Imaging Telescope Array System*¹ (VERITAS; Weekes et al., 2002) has a telescope design similar to *Whipple*, but is a system made of four identical telescopes with a diameter of 12 m. Its first telescope started observing in 2004, while the full array has been operational since September 2007. VERITAS can observe γ -rays between 50 GeV and 50 TeV.

Also in 2004, the *Major Atmospheric Gamma Imaging Cherenkov* telescope² (MAGIC; Aleksić et al., 2012) went into operation on the Canary island La Palma. In the beginning, only one telescope (diameter 17 m) observed the VHE γ -ray sky, but in 2009, a second, identical telescope was added to the site and became part of MAGIC. This IACT system has a sensitivity between 50 GeV and 30 TeV.

On the Southern hemisphere the first Cherenkov telescope was also built in the beginning of the 2000's, in Namibia. The first telescope of the *High Energy Stereoscopic System*³ (H.E.S.S.) started observing in 2002, and two years later, all four telescopes were officially inaugurated. Their diameter is 12 m. In 2012, a fifth, bigger telescope (diameter of 28 m) was placed at the center of the array, which is now also known as H.E.S.S. II. The stereoscopic systems

¹<https://veritas.sao.arizona.edu/>

²<https://magic.mpp.mpg.de/>

³<https://www.mpi-hd.mpg.de/hfm/HESS/>



Figure 2.3.: Photograph of FACT with the Gran Telescopio Canarias in the background. On the right side of the sky, the Milky Way is visible, which is reflected in the segmented mirrors of FACT. Credit: [Miguel Claro](#)

is sensitive in an energy range between 30 GeV up to 100 TeV. In 2011, the *First G-APD Cherenkov telescope* (FACT; [Anderhub et al., 2013](#)) joined MAGIC at their site on La Palma, but observes VHE γ -rays on its own at energies > 300 GeV. FACT is a small-size telescope with a diameter of ~ 3.5 m. The instrument is further introduced in Sect. 2.1.2.

The next step forward in IACT observations is to conduct them with a large array of telescopes. The first instrument operating in this way will be the *Cherenkov Telescope Array*⁴ (CTA; [Cherenkov Telescope Array Consortium, et al., 2019](#)), which will highly impact future research. The sensitivity of CTA is predicted to be more than ten times better than that of current IACT systems. Its array is made of three different classes of telescopes, which are the *Small-Sized Telescopes* (SSTs) with a mirror diameter of 4 m, the *Medium-Sized Telescopes* (MSTs) with a diameter of 12 m, and the *Large-Sized Telescopes* (LSTs) with a diameter of 23 m. In addition, CTA will be installed on both hemispheres, meaning two sites, in order to achieve nearly all-sky coverage for γ -ray observations. The site on the Northern hemisphere will be located on La Palma, where MAGIC and FACT are already operating. On this site, only the MSTs and LSTs will be deployed, which will allow measuring γ -ray emission between 20 GeV and 20 TeV. The site on the Southern hemisphere is located in Chile close to the European Southern Observatory's Paranal Observatory. Currently, no LSTs are planned, but a large array built with SSTs. Because of the SSTs, which are sensitive for the most energetic γ -rays, photons with energies up to 300 TeV will be detectable from the Southern sky.

2.1.2 The First G-APD Cherenkov Telescope

The *First G-APD Cherenkov telescope*⁵ (FACT; [Anderhub et al., 2013](#)) started its operation in autumn 2011 on the Canary Island La Palma. Figure 2.3 presents an image taken of the telescope by night. Its scientific objective is to provide long-term, unbiased VHE γ -ray monitoring for a selected sample of bright blazars. Among these sources are, e.g., Mrk 421, Mrk 501, 1ES 1959+650, and 1ES 2344+51.4. The core sample of five sources is observed daily by FACT within their respective visibility windows. This way, the astronomical community can be alerted reliably in case of a γ -ray flare, and multi-wavelength follow-up observations can be triggered quickly. The outcome includes more than 100 alerts that were sent to either multi-wavelength collaborators or the broad community since March 2014

⁴<https://www.cta-observatory.org/>

⁵<https://fact-project.org/>

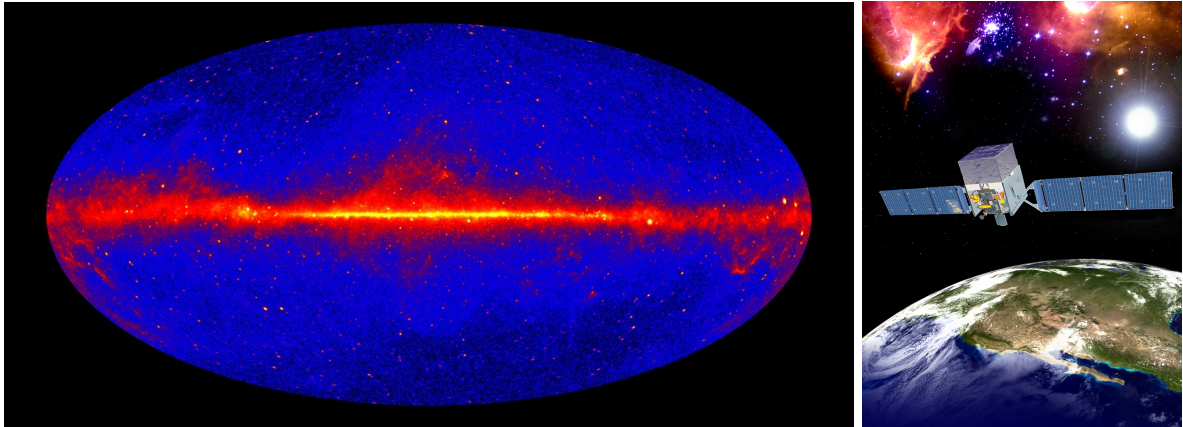


Figure 2.4.: *Left:* All-sky γ -ray map created from data collected between 2008 and 2017 by *Fermi*/LAT. The map shows the average γ -ray emission over a time range of nine years. While the galactic plane is dominated by extended diffuse emission and a few pulsars, the point sources above and below the plane are all bright blazars. *Right:* Artist's impression of *Fermi*/LAT in orbit. Credit: NASA/DOE/*Fermi* LAT Collaboration (*left*), NASA (*right*)

(Dorner et al., 2021), and several papers in which the respective flare and multi-wavelength follow-up observations are studied (e.g., Cologna et al., 2017, MAGIC Collaboration, et al., 2020a). In addition, FACT takes part in planned multi-wavelength campaigns for dedicated studies of particular sources (e.g., Ahnen et al., 2018, MAGIC Collaboration, et al., 2020b), and also follow-up observations in response to multi-messenger alerts (e.g., Satalecka et al., 2021).

In order to minimize gaps in the monitoring program due to moonlit nights, it is necessary to use equipment that can still detect the weak Cherenkov light from air showers against the diffuse night-sky background, which can increase up to four orders of magnitude during full moon. Instead of photomultiplier tubes, which have so far been used for other IACTs, FACT utilizes solid-state Geiger-mode Avalanche Photodiodes (G-APDs). In contrast to photomultiplier tubes, Silicon Photomultipliers (SiPMs) do not degrade when being exposed to bright light, which makes them more favourable for longterm use. For this reason, these detectors will be implemented in the CTA project as well (Aguilar et al., 2016).

2.1.3 The *Fermi* Gamma-ray Space Telescope

The following section summarises the instrument paper by Atwood et al. (2009), in which more details can be found. The *Fermi* satellite was launched on June 11, 2008 by NASA from Cape Canaveral as the *Gamma-ray Large Area Telescope (GLAST)*, and renamed *Fermi Gamma-ray Space Telescope (Fermi)* in honor of Enrico Fermi post-launch. An artist's impression of the satellite in orbit is shown in Fig. 2.4 on the right. At an orbit height of ~ 550 km, the satellite circles the Earth in roughly 96 minutes. On-board there are two instruments, the Large Area Telescope (LAT), which is the main instrument, and the Gamma-ray Burst Monitor (GBM). Both are dedicated to performing continuous monitoring of the high-energy sky. The goals of the *Fermi* mission are developing a better understanding of extreme environments or

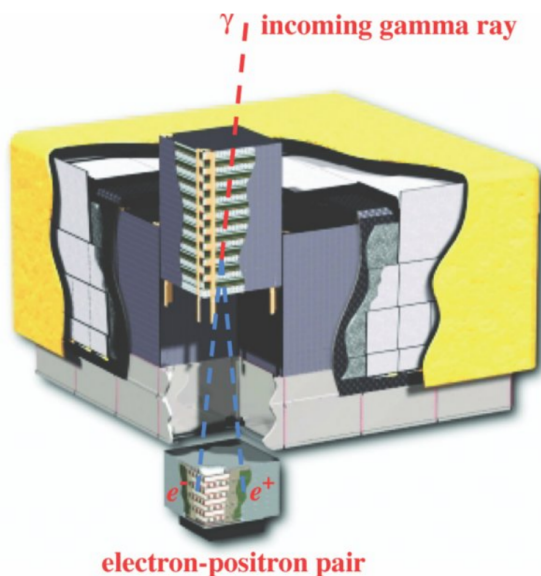


Figure 2.5.: Schematic illustration of the pair-conversion instrument that is the 'heart' of the LAT. The red dashed line depicts a γ -ray photon entering one of the towers and undergoing pair conversion after passing through several detector layers. In the calorimeter, the energy of both the electron and positron is measured to determine the energy of the original photon. Credit: Atwood et al. (2009)

events, e.g., jet acceleration in active galaxies or γ -ray bursts, searching for dark matter and its composition, and studying pulsars, solar flares, and cosmic rays.

The main science goal of GBM is to detect γ -ray bursts and other transient sources. It contains two types of scintillators, and is sensitive between ~ 8 keV and ~ 40 MeV (Meegan et al., 2009).

The LAT is the primary instrument of the *Fermi* mission with an energy sensitivity between 20 MeV and 1 TeV. The underlying detection technique is a pair-conversion telescope that is equipped with an anti-coincidence shielding. The observing mode of LAT follows a continuous all-sky monitoring strategy, which is able to provide a full coverage of the γ -ray sky every two *Fermi* orbits, i.e., ~ 3.2 hours. Since 2008 August 4, *Fermi* has provided the scientific community with continuous γ -ray data⁶, making it an extremely successful instrument for decade-long monitoring of a large amount of galactic and extragalactic γ -ray sources alike. In Fig. 2.4, the all-sky map containing data from nine years of observations is shown on the left.

The LAT consists of 16 identical towers, arranged in a 4×4 array with a total length of 1.6 m each side, and a height of 87.5 cm. A schematic picture of the detector is shown in Fig. 2.5. It is covered by an anti-coincidence shield, the anti-coincidence detector (ACD), that is used for the rejection of charged-particle cosmic rays. It consists of plastic scintillator tiles, which generate a light signal in case of an incoming cosmic ray. The ACD's efficiency is $\sim 99.97\%$. A γ -ray, passing through the ACD undisturbed, enters the precision converter-tracker (red dashed line in Fig. 2.5), which consists of 18 layers of silicon-strip detectors and 16 thin tungsten sheets that are meant to trigger pair production by incoming photons. A γ -ray undergoing pair production creates an electron-positron pair that continues to move through the tracker. This leaves tracks (blue dashed lines in Fig. 2.5), traced by the silicon-strip detectors. After passing through the tracker, the energy of both the electron and the positron is measured in the calorimeter. Because of energy conservation, the combined energy carried by the pair is that of the initial γ -ray photon, and the energy of the original photon can be deduced. The

⁶Except for two safe holds of five and 18 days length in March 2009 and March 2018, respectively, and ten gaps with a length between six and 30 hours maximum since 2008. An updated list can be found at https://fermi.gsfc.nasa.gov/ssc/data/access/lat/lat_data_gaps.html.

combination of the segmentation of the calorimeter, such that the point of entry for each particle can be determined, and the tracks, permits to reconstruct the direction where the initial photon came from. The fourth part of the LAT is the data acquisition module (DAQ), which gathers data from the ACD, the tracker and the calorimeter and performs a first data screening by filtering out unwanted cosmic-ray signals, before the data are downlinked. In addition, it also runs on-board algorithms to scan for γ -ray bursts.

LAT analysis

The LAT data are publicly available immediately after downlinking. The data reduction and analysis requires an installation of the FermiTools⁷, and a python package (`fermipy`; Wood et al., 2017) is available⁸, which provides the user with a large set of functions to create the desired science products, e.g., light curves, or spectra. I will give a concise summary of the LAT analysis, a more detailed description can be found in Müller (2014, Sect. 2.2.2).

For the reduction and analysis of the LAT data, both the raw data, provided via so-called photon files, and continuous, logged information about the instrument status, which is stored in the spacecraft file, are needed⁹. To determine the γ -ray emission for a source of interest, a model that includes all γ -ray sources (point and extended sources) in the vicinity, needs to be compiled. It is usually built from the latest release of the *Fermi*/LAT catalog. The current one is the third data release (DR3; Fermi-LAT collaboration et al., 2022) of the *Fourth Fermi/LAT source catalog* (4FGL; Abdollahi et al., 2020). The 4FGL consists of more than 5000 sources that have been detected in over ten years of continued observation. In addition to those, all-sky models for both the isotropic and the Galactic diffuse γ -ray emission¹⁰ need to be included for the analysis, and are provided by the LAT collaboration as well.

As a first step, the raw data, or events, are selected based on several criteria that one can define. To consider enough sources that are likely contributing to the γ -ray emission around the source of interest, but also to keep the computational time on a reasonable level, one needs to define a region of interest (ROI), which is usually between 10° and 15° . Each event within the ROI can be further filtered based on where photons were converted in the tracker instrument (front, back, or both), their PSF signature, and energy dispersion value. In order to avoid contribution from the Earth's limbs, it is also recommended to apply a zenith angle cut, which is usually set at 90° . Lastly, it is necessary to ensure that only good time intervals (GTI) are considered for the analysis. This information is embedded in the spacecraft file. Excluded time ranges are those, in which collected data might not be valid, namely during spacecraft maneuvers, on-board software updates, and high-background exposures, e.g., when flying through the Southern Atlantic Anomaly (SAA).

After the selection of the events is completed, an exposure map and a livetime cube are calculated. Then, the data can be compared to the input model for the ROI, including γ -ray sources, which can be point sources, e.g., blazars, or extended sources, e.g., features of the Large Magellanic cloud, as well as diffuse emission. Note that the model should include all sources from a slightly larger region than the ROI (typically 5° more) to avoid disregarding

⁷FermiTools github page: <https://github.com/fermi-lat/FermiTools-conda>

⁸fermipy github page: <https://github.com/fermiPy>

⁹Data access is provided at <https://fermi.gsfc.nasa.gov/ssc/data/access/lat/>

¹⁰Background models are available at <https://fermi.gsfc.nasa.gov/ssc/data/access/lat/BackgroundModels.html>

bright sources just outside the ROI. The method with which the best-fit model is determined is based on a Maximum Likelihood analysis (Mattox et al., 1996). For this, a test statistic (TS) is computed for each model component, assuming that the current model is the best description for the underlying data. Mathematically speaking,

$$\text{TS} = 2\Delta \log(\mathcal{L}), \quad (2.1)$$

where \mathcal{L} is the likelihood function representing the difference between two models, one with a point source at the source coordinates, and one without. The TS value can be roughly transferred into significance via $\sigma = \sqrt{\text{TS}}$. To check if every source has been accounted for in the model, one can compute a TS map and validate that no excess emission is left. In case of significant left-over emission, one can add a new object to the model and redo the fitting process. This is not uncommon as some transient sources might not be significantly detected over the whole period of the mission. In addition, it is possible to further refine the source coordinates and corresponding uncertainties in case a localisation analysis is needed.

After a best-fit model has been established, it contains the TS values, i.e., significance of detection, source positions, and spectral parameters, including the slope of the spectrum and the individual source flux. A spectrum with a flexible amount of spectral bins can be computed, which is already corrected for instruments effects, that is, exposures and background.

In addition, a light curve can be computed for the entire time range specified at the beginning of the analysis. This involves dividing the full time range into a specified bin size. Both choosing a fixed bin size, as well as an adaptive bin size is possible. Within each time bin, the analysis starts from the beginning, and searches for a best-fit model in each time frame. The bin size needs to be chosen carefully in order to gain ideally a significant detection for each time bin. This is being taken care of in adaptive binning, however, there the beginning or end of flares can be missed. The majority of blazars can be best studied over a long time range with 14-day or monthly binning, while significant daily detections are possible during flares. For the brightest blazar flares, binning times down to orbital time scales have been possible (Meyer et al., 2019), but only for a very small amount of sources.

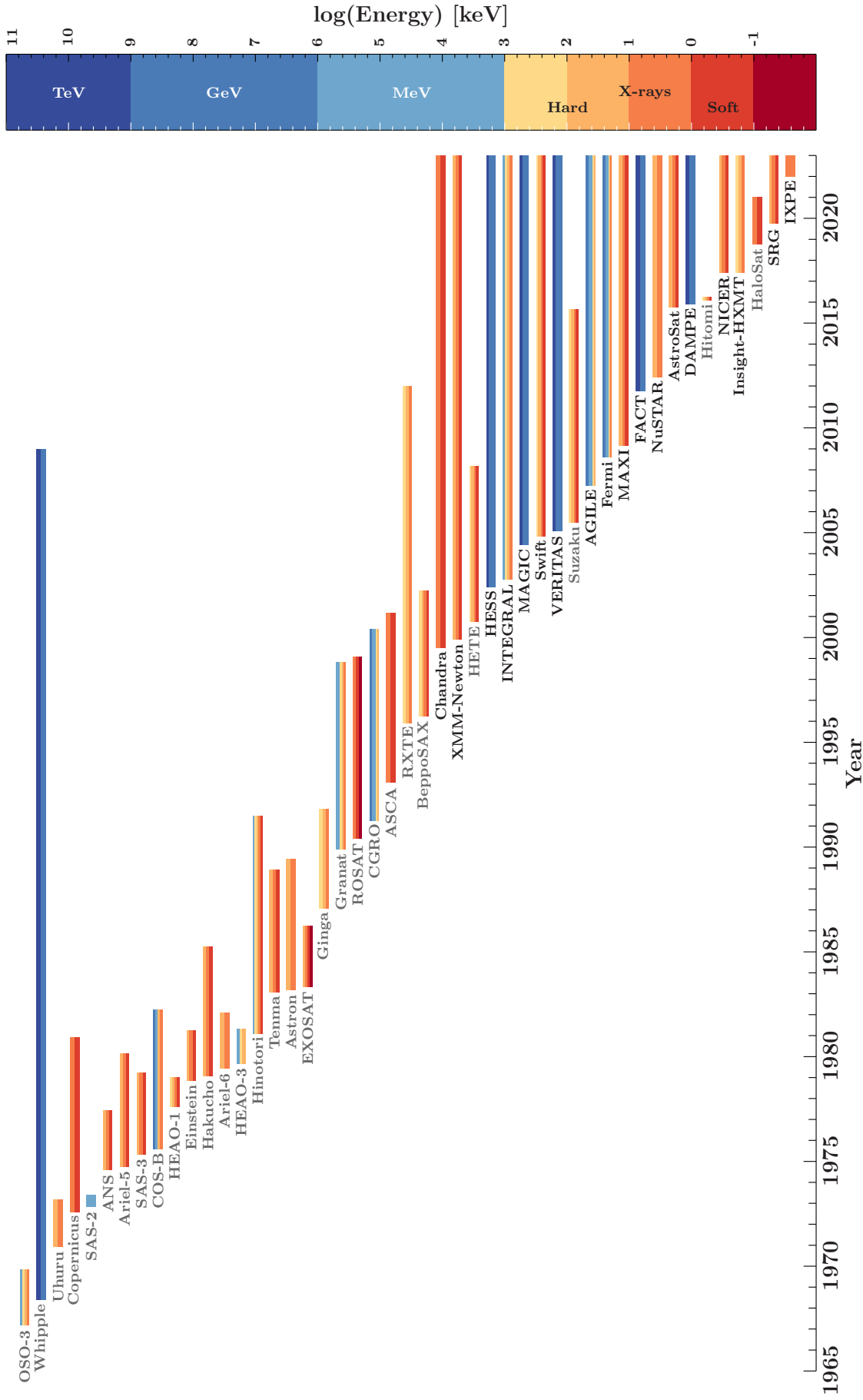


Figure 2.6.: Overview of most of the high-energy (X-ray and γ -ray) missions and telescopes. Failed missions and short-term experiments on rockets, balloons, or space shuttles, are not shown here. The colours indicate the energy range in which on-board instruments can observe the Universe. Currently active missions are plotted in black. This overview is biased towards missions with an ESA or a NASA contribution.

2.2 X-ray astronomy

In this section, I describe the concept of imaging X-ray telescopes, summarise the history of X-ray astronomy, and introduce the X-ray missions whose data I analysed as part of this work. In Section 2.2.1, I begin by explaining the necessary design for focussing X-ray telescopes and how the observational data are stored in charge-coupled devices, before I describe the data extraction for imaging X-ray telescopes. Section 2.2.2 contains a broad overview of most of the past, current, and future X-ray missions, starting with simple X-ray experiments that were sent to space with rockets, to the advanced instruments on X-ray satellites, which we have today. More detailed summaries can be found in, e.g., [Bradt et al. \(1992\)](#) and [Santangelo & Madonia \(2014\)](#). Last, I describe the *XMM-Newton* (Sect. 2.2.3), *Swift* (Sect. 2.2.4), and *NuSTAR* missions (Sect. 2.2.5) in detail.

2.2.1 Design of focusing X-ray telescopes

In this section I give a brief overview of the characteristics that enable imaging observations of X-ray sources, following [Aschenbach \(1985\)](#), [Bradt \(2004\)](#), and [Lutz \(2007\)](#).

Wolter mirror design

The configuration of most current optical telescopes is typically made of two mirrors of parabolic shape, which reflect incoming light to the corresponding focal point. The mirrors are pointed towards the object that is to be observed, such that the light hits them approximately head-on. The size of the primary mirror directly correlates to the overall collecting area. This kind of design, however, does not work for the more energetic X-ray light, as it passes through reflective material when coming from a large angle. This can be explained with Snell's law, which describes the in- and outgoing angles for incoming emission in relation to the refractive index of two involved media (e.g., air and the mirror surface) via (e.g., [Aschenbach, 1985](#))

$$\frac{\sin \alpha_1}{\sin \alpha_2} = \frac{n_2}{n_1} = n. \quad (2.2)$$

The refraction index n depends on the dielectricity constant (ϵ) and the permeability of the material, μ (~ 1 if non-magnetic), as

$$n = \sqrt{\epsilon\mu}, \quad (2.3)$$

and needs to be greater than one in order to allow total reflection ($\alpha_2 = 90^\circ$). Under the assumption of a negligible phase change, the critical angle under which we can obtain total reflection is

$$\theta_c = N_0 \frac{Zr_e}{A2\sqrt{2}\pi} \rho \lambda^2 = 5.6' \sqrt{\frac{\rho}{\text{gcm}^{-3}}} \frac{\lambda}{1\text{mm}} \quad (2.4)$$

with the Avogadro's number, N_0 , the classical electron radius, r_e , the atomic number and weight, Z and A , respectively, and the mass density, ρ . Under the assumption of heavy elements, one can simplify the equation further as is shown in the second term of Eq. 2.4. The critical reflection angle for X-ray light ($\lambda \sim 1$ nm) is therefore $\sim 1^\circ$. However, it is possible to slightly influence and increase this value by choosing different materials for the reflecting

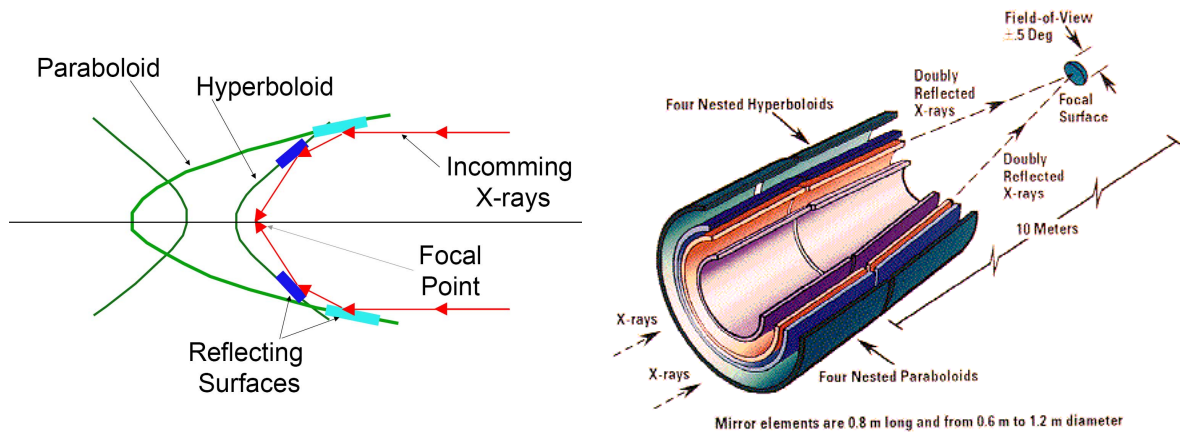


Figure 2.7.: *Left:* Illustration of the mirror configuration and the reflection path for a Wolter Type 1 grazing incidence telescope. *Right:* Visualisation for four nested Wolter Type 1 telescopes. Credit: [NASA Imagine the Universe](#) (*left*), NASA (*right*).

surfaces, because the dielectricity constant depends on the atomic number Z . Typical choices for the mirror material are gold and iridium.

Consequently, focusing X-ray telescopes need to be built such that incoming X-ray photons are reflected at a small angle. This mirror design is called a ‘grazing incidence telescope’. Because the length of X-ray telescopes is limited due to the size of the rockets that transport them into space, it is necessary to decrease the focal length as much as possible. The most commonly used design is the combination of a paraboloid and a hyperboloid, which was invented by Hans Wolter ([Wolter, 1952](#)) in the context of X-ray microscopy. A schematic illustration of his design is shown in Fig. 2.7 (left).

In addition, several of these mirror combinations can be nested inside each other to increase the effective area (see Fig. 2.7, right). A larger area can collect more photons, which enables studies of dim and distant objects within a reasonable amount of exposure time.

Charge-coupled devices

The advance in the field of semiconductors in the second half of the 20th century led to the invention of charge-coupled devices (CCDs; [Boyle & Smith, 1970](#)), and revolutionized how astronomical data could be collected. While originally designed for optical light, CCDs were soon refined to enable X-ray observations as well ([Clarke, 1990, 1994](#)). The main difference for X-ray CCDs is the need for a larger detector volume, as X-ray photons are more energetic and have a larger penetration depth in the detector.

The main component of a CCD is a semiconductor with a depletion zone, realised through a p-n-junction (e.g., [Bradt, 2004](#)). For its creation, the material is contaminated by a very small fraction of foreign atoms, which can greatly increase the conductivity of said material. This process is called doping. By substituting the atoms of the base material with those that have one electron less (p-doping), an electron-hole is left in the valence band. Similarly, one can substitute atoms that have one more electron (n-doping), such that additional electrons become available for charge transfer. Combining a p- and n-doped layer creates a p-n-junction. A depletion zone is established by free electrons from the n-doped layer recombining with

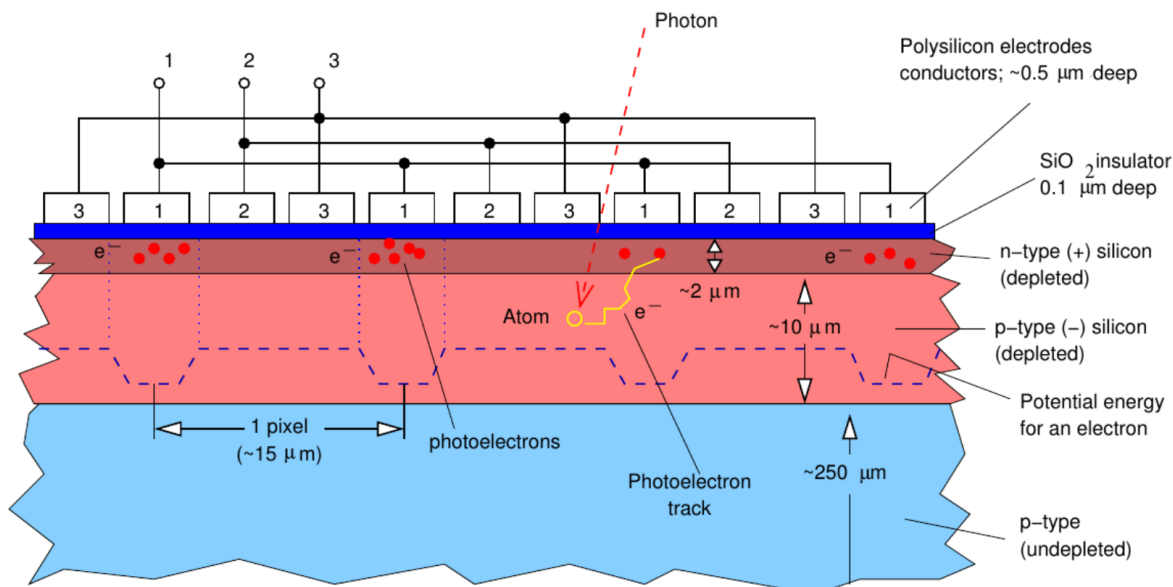


Figure 2.8.: Schematic overview of the layers within a CCD. Credit: Wilms after [Bradt \(2004\)](#).

the free holes in the p-doped layer, and a potential difference builds up until no further charge exchange is possible. This process creates a diode, meaning electric charges can only flow in one direction. Typically, silicon is chosen as the base material for the p-n-junction, with boron atoms substituted to create the p-junction, and phosphorus atoms for the n-junction ([Lutz, 2007](#)). For the CCD, a non-depleted p-doped layer is additionally added underneath.

Photons hitting the p-n-junction are able to excite electrons in the depletion zone, which are then immediately drained from the zone by the electric field, and stored in the potential well of the p-n-junction. The measured current can be used to retrieve the energy of an incident photon. A CCD is made of several hundreds to thousands of such p-n-junctions (i.e., pixels), in a rectangular arrangement. While the columns are separated via physical potential barriers, the pixels in each row are only separated through voltage barriers from one another, which allows a read out of the chip by moving the deposited charge through the rows. In [Fig. 2.8](#), the structure of an X-ray CCD is illustrated.

In order to avoid a spill-over of the potential wells, in which the charges are stored, X-ray CCDs need to be read out continuously. Consequently, it is possible to count individual photons as well as register their energy. For the whole CCD, the duration of one readout cycle last between milliseconds and seconds. However, if more than one photon hits the same pixel within one readout cycle, it is not possible to distinguish those and information is lost. This event is called pile-up, and becomes worse the brighter the observed source is. In order to avoid this problem, instruments like the X-ray detectors on-board *XMM-Newton*, or *Swift*, have different observation modes, for which the size of the illuminated chip can be reduced, which effectively reduces the read out time.

Data analysis and extraction of imaging X-ray telescopes

Comprehension of the X-ray measurement process is necessary in order to correctly interpret and model the data. The measured source count rate n_{ph} in an energy channel c of the detector is described via (e.g., [Arnaud et al., 2011](#), but notation taken from [Wilms, 2020](#))

$$n_{\text{ph}}(c) = \int_0^{\infty} R(c, E) \cdot A(E) \cdot F(E) dE, \quad (2.5)$$

where $R(c, E)$ is the detector response, $A(E)$ is the effective area, and $F(E)$ is the photon flux density. Hence, the photon count rate measured by the detector includes the effective area of the telescope, and the probability of detecting a photon with energy E in said channel, besides the actual photon flux density. As the number of energy channels is not infinite, it is necessary to discretize Eq. 2.5, such that

$$N_{\text{ph}}(c) = \Delta T \sum_{i=0}^{n_{\text{ch}}} A(E_i) \cdot R(c, i) \cdot F(E_i) \Delta E_i. \quad (2.6)$$

As background emission is also included in this overall count rate, an estimate of the source count rate is

$$S_{\text{ph}}(c) = N_{\text{ph}}(c) - B(c), \quad (2.7)$$

including an uncertainty that follows a Poisson distribution. In order to study the original flux from a source, one needs to determine $F(E_i)$. However, inverting Eq. 2.6 is, in general, not possible. To describe the emission coming from a source, one can fit a model that either is an empirical description, or includes physical emission processes. In case the spectrum contains a large amount of photons and the distribution of counts per spectral bin is Gaussian distributed, a χ^2 -minimization approach can be chosen. The goodness-of-fit following χ^2 statistics is computed via ([Gorenstein et al., 1968](#))

$$\chi^2 = \sum_i \frac{(D_i - M_i)^2}{\Delta D_i}, \quad (2.8)$$

which depends on the bins D_i with uncertainty ΔD_i and the model value M_i for each bin. To achieve the necessary Gaussian distribution in the bins, it is required that each bin of the spectrum contains at least 20 counts. It is crucial that an adequate amount of spectral bins exists in order to properly constrain the spectral properties. Hence, for observations with low photons statistics, the binning can result in less than the required 20 counts per bin and those follow a Poisson distribution again. In this case, the goodness-of-fit can be determined with ‘Cash’ statistics ([Cash, 1979](#)), which is defined as

$$C = 2 \sum_i^N (M_i - D_i \log M_i). \quad (2.9)$$

In the following, I give an overview of the principal way of data extraction for imaging X-ray telescopes, as the process is similar for the X-ray instruments used in this work. During an observation, the arrival time and energy of incident photons, also named events, are stored for

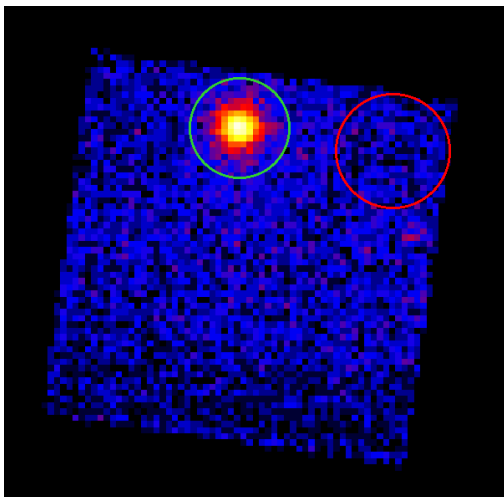


Figure 2.9.: The source PKS 2004–447 observed with the EPIC-pn detector on-board *XMM-Newton* in *Small Window* mode. The green circle (radius = 35'') marks the source region, while the red circle (radius = 40'') describes the region for extraction of a background spectrum.

each observation mode. Unless the observation is done in timing mode, the spatial information of where photons hit the detector in the FOV is kept as well.

In the beginning, events are filtered out based on the information in the spacecraft attitude file, in order to include only time ranges during which all instruments were performing normally. Moreover, the remaining ‘good-time intervals’ (GTIs) should not include background flaring that can heavily influence the gathered data. Hence, strong background emission that can be caused by, e.g., the sun, or the Earth’s radiation belts, is filtered out as well. In addition, data from known ‘bad’ pixels¹¹ are excluded as well.

Similarly, it is checked whether pile-up occurs. Furthermore, analysing the event patterns reveals if a single photon hit just one pixel, or if its charge overflowed to neighbouring pixels. If the readout is not fast enough, the detector is unable to distinguish two or more photons that arrive within one readout cycle. As a result, the spectrum appear harder.

Usually, a first full extraction is done for the entire CCD, which might include other sources depending on the field of view of the chosen observing mode. The next step is to define regions to extract a source, and a background spectrum. This can be done using a software, e.g., *SAOImageDS9*, by inspecting the detector image, and choosing the position, shape (usually circle), and size of the regions (see Fig. 2.9 for an example). The source region should only contain the source of interest, while the background region is supposed to be free of any visible source. If an observation has been performed in *timing* mode, no image has been created, because the pixels have been concatenated into one dimension. Instead of coordinates, one needs to choose a range for the extraction of source and background spectra within the one-dimensional *timing* image.

During the final extraction of the source and background spectra, the redistribution matrix (RMF) and the arcillary response file (ARF) are created. The RMF describes the effects that are created due to excited charge clouds and escape peaks, while the ARF contains details about area-reducing effects of filters, limiting quantum efficiency, and downgrading effects of the mirror shells. Without these, physical interpretation of the data is not possible.

¹¹A bad pixel can be either a ‘dead’ pixel, where the depletion zone is too wide for any electron being able to get excited (= constantly no signal), or a ‘hot’ pixel for which the depletion is so narrow, that electrons are excited even without the need for a photon (= constant signal). Bad pixels can be created, e.g., when a cosmic ray hits the CCD. Sometimes, a dead pixel can affect its entire column, which then becomes a dead column.

2.2.2 Historical overview

The history of X-ray astronomy began slightly before that of gamma-ray astronomy. As the Earth's atmosphere is also opaque in that energy regime, measurements could only be taken after rockets had been developed. A Geiger counter on the V2 rocket was the first instrument to detect X-ray radiation coming from space in the 1940s, which was originating from the sun (Friedman et al., 1951). In 1960, a proposal for an X-ray telescope design was brought forward by Giacconi & Rossi (1960), based on an imaging technique described by Wolter (1952). Because X-rays can only be reflected off a small inclination angle, this design requires an array of parabolic and hyperbolic mirrors in order to create an X-ray image, which has been named after Wolter. In Sect. 2.2.1, the design is explained in detail. Because the specifications for the mirrors, in particular their smoothness, could not be fulfilled in the 60s, the first X-ray detectors were simply Geiger counters or equivalent detectors.

In the early 1960s, X-ray radiation from outside of the solar system was measured and two distinct sources were found to reside in the constellation of Scorpius and Sagittarius, respectively (Giacconi et al., 1962, 1964). In 1964, a balloon observation measured the X-ray spectrum of the Crab nebula from 15 to 60 keV (Clark, 1965). A few more X-ray sources, mainly located in the galactic plane, were discovered by several balloon and rocket flights (e.g., Burbidge et al., 1965, Morrison & Sartori, 1965, Fisher et al., 1966). The series of the US Vela satellites was comprised of four individual satellites, Vela 5A and 5B, which were launched in 1969, and Vela 6A and 6B, which were launched in 1970. Even though the main goal of the satellites was not scientific exploration, they contributed useful data. Vela 5B¹² has proven particularly valuable as it was in operation for ten years, while other spacecrafts were only functional for roughly one year. The satellites could detect both X-ray and gamma-ray emission up to 750 keV, and were one of the first satellites to detect gamma-ray bursts (Klebesadel et al., 1973), and found X-ray bursts that coincided with gamma-ray bursts (Terrell et al., 1982).

The first X-ray instrument on a spacecraft was the X-ray telescope on-board the OSO-3 spacecraft (Hicks et al., 1965), which was mentioned also in the previous chapter as it carried an instrument that measured gamma-rays above 50 MeV for the first time. With the measured X-ray data, it was possible to obtain a spectrum from 7.7 up to 210 keV, and study, e.g., the diffuse cosmic X-ray emission (Schwartz et al., 1970), or the solar spectrum at hard X-rays (Hudson et al., 1969).

The first dedicated X-ray satellite was the *Small Astronomical Satellite 1* (SAS-1; Giacconi et al., 1971), which was launched in 1970 from Kenya. After the successful launch, the satellite was renamed *Uhuru* ('freedom' in the Swahili language) to honor the Kenyan people on their seventh anniversary of independence. *Uhuru* surveyed the sky in an energy range from 2 to 20 keV, and was able to detect 339 X-ray sources, among them X-ray binaries, supernova remnants, Seyfert galaxies, and galaxy clusters (Forman et al., 1978).

After its launch in 1971, the *seventh Orbiting Solar Observatory* (OSO-7)¹³, also performed an X-ray all-sky survey.

¹²<https://heasarc.gsfc.nasa.gov/docs/vela5b/vela5b.html>

¹³<https://heasarc.gsfc.nasa.gov/docs/oso7/oso7.html>

A year later, the *Orbiting Astronomical Observatory 3* (OAO-3 [Sanford, 1974](#)) was launched, which resulted from a collaboration between the United States and the United Kingdom. This spacecraft, which is also known as *Copernicus*, carried an UV telescope, the main instrument, and several X-ray experiments, which were sensitive for emission between 0.5 and 10 keV. With the data, [Davison et al. \(1975\)](#) could detect variability in the radio galaxy Centaurus A, and confirmed its core region to be the source of its X-ray emission.

With the launch of *Ariel V* in 1974, another British-American satellite went to space, which extended the observational energy range in X-rays and enabled a sky survey from 0.3 to 40 keV ([Smith & Courtier, 1976](#)). Due to its mission duration of six years, it was possible to obtain long-term monitoring of bright X-ray sources. The mission team produced two catalogs, which were divided by the Galactic latitude in order to distinguish between possible Galactic and extragalactic sources ([Warwick et al., 1981](#), [McHardy et al., 1981](#)), and also found transient sources ([Kaluzienski, 1977](#)). In addition, iron lines could be detected in the spectra of extragalactic sources ([Mitchell & Culhane, 1977](#)). In the same year, the *Astronomische Nederlandse Satelliet* (ANS; [Brinkman et al., 1974](#)), which was an international project by the United States and the Netherlands, commenced operation and conducted pointed observations in an energy range between 0.1 and 30 keV, and a large part of the UV spectrum. One of the first X-ray bursts, whose origin could be pinpointed to a globular cluster ([Grindlay et al., 1976](#)) was discovered together by ANS and Vela 5B.

For the following mission, which was the *Third Small Astronomy Satellite* (SAS-3; [Mayer, 1975](#)) launched in 1975, three main objectives were set: to study X-ray sources up to energies of 55 keV, to achieve a positional accuracy of up to 15 arcseconds, and to search for novae or flares (e.g., [Lewin et al., 1976](#)). In addition, the soft X-ray background was probed between 0.1 and 0.3 keV ([Marshall & Clark, 1984](#)). With a payload of four X-ray detectors including proportional counters, the usual operation mode of the satellite was a spinning movement, but it could also conduct pointed observations if necessary.

In 1975, another X-ray observatory, the *Eighth Orbiting Solar Observatory* (OSO-8)¹⁴ was launched, which mainly observed the sun, but also detected other X-ray sources up to an energy of 1 MeV. The data from OSO-8 revealed that there is gas in galaxy clusters that emits thermal radiation ([Serlemitsos et al., 1977](#)).

At the end of the 70s, NASA launched the three *High Energy Astronomy Observatories* (HEAOs), which were designed to observe in a broad energy range from X-rays up to MeV gamma-rays. The first one, HEAO-1¹⁵, which was launched in 1977, conducted three sky surveys with four payload instruments in an energy range from 0.2 keV up to 10 MeV and supplied researchers with almost constant monitoring of sources close to the ecliptic poles. While monitoring both AGN and X-ray binaries alike, the instruments detected more, previously unknown X-ray sources ([Wood et al., 1984](#), [Levine et al., 1984](#)). The successor mission, HEAO-2, or more commonly known under its post-launch name *Einstein*, was launched a year later, and carried the first imaging X-ray telescope ([Giacconi et al., 1979](#)). Four different detectors, which were mounted on a rotation wheel behind a Wolter Type 1 grazing incidence telescope, enabled flexibility to change the instrument on flight. These instruments were sensitive in the soft X-ray regime from 0.1 to 4 keV. In addition, a proportional counter, which was

¹⁴https://heasarc.gsfc.nasa.gov/docs/oso8/oso8_about.html

¹⁵<https://heasarc.gsfc.nasa.gov/docs/heao1/heao1.html>

co-aligned with the X-ray telescope, allowed to gather X-ray data up to 20 keV (Gaillardetz et al., 1978). For the first time, NASA offered a Guest Observer program to allow scientists that were not involved with the development of the instrument to apply for data, a practice that has proven very successful regarding the scientific output, and is common nowadays. Due to its imaging capabilities, *Einstein* opened a ‘new window’ for X-ray observations as it could resolve extended or diffuse emission. One of the major discoveries for the research area of AGN was, e.g., the observation of an X-ray jet in M87 and Centaurus A, which aligned with the previously detected radio jets (Feigelson et al., 1981, Schreier et al., 1982). In 1979, the last of these three big missions, HEAO-3, was launched. With three payload instruments onboard, it surveyed the sky in an energy range from 50 keV up to 10 MeV (Mahoney et al., 1980). While coordinated by facilities in the United States, one instrument, the Cosmic Ray Isotope Experiment, was contributed by a collaboration of Danish and French scientists.

In the same year, Japan launched its first X-ray satellite into space, which was developed for locating and observing transient events. The *Corsa-B* satellite was renamed *Hakucho* post-launch, which is the Japanese word for ‘swan’. This name was chosen in recognition of one of the brightest and most interesting sources, Cygnus X-1, which resides in the constellation Cygnus. Its payload, which consisted of three instruments, enabled to study the X-ray sky from 0.1 to 100 keV (Kondo et al., 1981). Due to its design, it was able to detect many X-ray bursts over its mission time of six years (e.g., Koyama et al., 1981, Makishima et al., 1983, Murakami et al., 1983).

Also in 1979, the satellite *Ariel VI*¹⁶, again a british-american collaboration, was sent to space with detectors that were sensitive between 1 and 50 keV. Due to electromagnetic interference that resulted from ground-based radar signals, the pointing of the satellite was impacted such that the scientific output of this mission was highly compromised.

The *Astro-B* satellite¹⁷ was the second mission coordinated by Japan to observe extrasolar X-ray emission. After its launch in 1983, it was renamed *Tenma* (‘Pegasus’ in Japanese). The spacecraft carried both proportional counters and small-sized grazing incidence collectors that were developed at NASA (Tanaka et al., 1984). The data from *Tenma* contributed, e.g., to the discovery and study of the iron line in X-ray binaries, as well as AGN (Makishima, 1986).

A Soviet mission, named *Astron* was launched in the same year as *Tenma*. The main instrument was a UV telescope built by a collaboration between France and the Soviet Union. In addition, the spacecraft carried an X-ray spectrometer, which contained a proportional counter that was sensitive in an energy range from 2 to 25 keV. The target sources were mainly Galactic sources.

Also in 1983, the first X-ray satellite from the European Space Agency, named *EXOSAT*, was launched. On-board were two Wolter Type 1 grazing incidence telescopes that could image the X-ray sky between 0.05 and 2 keV (de Korte et al., 1981). In addition, two proportional counters covered the hard X-ray regime up to 50 keV (Peacock et al., 1981, Turner et al., 1981). A characterising feature of observations with *EXOSAT* was the long, uninterrupted exposure time of up to 90 hours due to an eccentric orbit, which allowed unprecedented time variability studies. Thanks to this, quasi-periodic oscillations (QPOs) were discovered in

¹⁶<https://heasarc.gsfc.nasa.gov/docs/heasarc/missions/ariel6.html>

¹⁷The satellite *Astro-A*, also known as *Hinotori* was launched two years prior, but exclusively studied solar activity at X-ray energies (Enome, 1982).

binary systems (Stella, 1988), and also the X-ray variability for a wide range of AGN could be studied (McHardy, 1988).

In 1987, the third Japanese X-ray satellite, *Astro-C*, or *Ginga* ('galaxy' in Japanese), commenced its mission with three instruments that covered a combined energy range from 1 to 500 keV (Turner et al., 1989, Tsunemi et al., 1989, Murakami et al., 1989). Its data contributed to, e.g., the detection of cyclotron features in several X-ray binaries (e.g., Clark et al., 1990, Makishima et al., 1990, Mihara et al., 1991).

The large mission *GRANAT*, was launched in 1989 by the former Soviet Union. The seven payload instruments were contributed by both the Soviet Union as well as several European countries, namely France, Denmark, and Bulgaria. Among the on-board instruments was a coded-mask X-ray telescope with a sensitivity between 30 keV and 1.3 MeV (SIGMA; Roques et al., 1990), an X-ray proportional counter spectrometer that could detect X-ray emission in an energy range between 3 and 100 keV (ART-S; Siunjaev et al., 1990), and an all-sky monitor for an energy range from 6 to 120 keV (WATCH; Brandt et al., 1990). Combining the sensitivity of all instruments, GRANAT measured high-energy emission between 2 keV and 100 MeV.

In the 70s and 80s, several balloon-borne X-ray experiments were launched as well, and their flights lasted roughly up to a day. Several sources, both of Galactic and extragalactic origin, were successfully observed this way in the hard X-ray regime (Angeloni et al., 1977, Ubertini et al., 1986). The discovery of the Supernova 1987A in the Large Magellanic Cloud (Kunkel et al., 1987), in particular, instigated a few balloon missions to observe its hard X-ray and γ -ray emission, which were launched from Australia (Sood et al., 1988a,b).

A new milestone was reached in 1990 with the *ROentgen SATellite* (ROSAT; Truemper, 1982), which was an international collaborative project between Germany, the United States, and the United Kingdom. Their mission goal was an all-sky survey in soft X-rays (0.1 – 2.5 keV), which was conducted with an imaging telescope, for the first time. The achieved sensitivity was about ~ 1000 times better than what had been obtained with *Uhuru* two decades ago. The resulting X-ray catalogs contain more than 130,000 sources (Voges et al., 1999, Boller et al., 2016). With the resolving capabilities across the entire sky, the morphology of extended X-ray sources could be studied. The X-ray emission detected by ROSAT over the entire sky is shown in Fig. 2.10. In addition to the X-ray instruments, the Wide Field Camera (WFC) with a sensitivity between 62 and 206 eV (EUV) was on-board ROSAT as well, which detected 479 sources (Pye et al., 1995). After the survey was finished, ROSAT performed pointed observations for a broad range of different sources, e.g., supernova remnants, and galaxy clusters. The data delivered by ROSAT also led to the discovery of X-ray emission from comets (Lisse et al., 1996).

In December 1990, the Broad Band X-ray Telescope (BBXRT; Serlemitsos et al., 1984) was a payload on board the space shuttle Columbia, and operated for ~ 10 days, in which it observed 82 sources in 157 separate observations. It was designed to perform imaging observations in a broad energy range from 0.3 and 12 keV for the first time. A similar configuration of an X-ray experiment was flown on-board the Space shuttle Endeavor in 1993. The *Diffuse X-ray Spectrometer* (DXS; Sanders et al., 1992) measured high-resolution spectra of the diffuse X-ray background from 0.15 to 0.28 keV (Sanders et al., 1998).

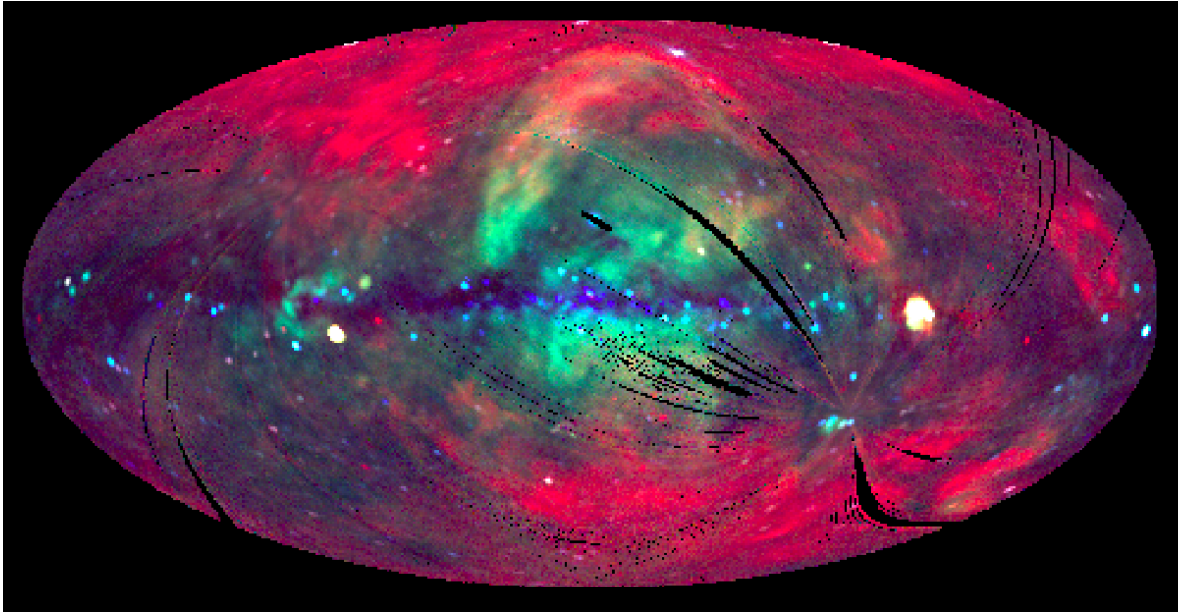


Figure 2.10.: The X-ray view as seen by ROSAT in an energy range from 0.1 to 2 keV in Aitoff projection. The colours indicate the energy of the emission, with red being softer and blue being harder X-ray emission. Credit: MPE & S. L. Snowden

In the same year, the Japanese *Advanced Satellite for Cosmology and Astrophysics* (ASCA; Tanaka et al., 1994), or formerly *Astro-D* was launched. Its payload was developed in an international effort between Japan and the United States. It was the fourth X-ray satellite with Imaging capabilities, and carried four equally-built grazing incidence telescopes with a detector at the focus of each of them. For the first time, Charge-Coupled Device (CCD) cameras were used as detectors, which were part of the two Solid-state Imaging Spectrometer (SIS). A detailed description of CCDs used for X-ray observations is given in Sect. 2.2.1. In addition, ASCA was the first X-ray satellite that was able to combine imaging data for a broad energy range (from 0.4 – 10 keV) with good spectral resolution, and a large effective area. Within its flight duration of seven years, ASCA gathered a lot of enlightening data, e.g., it was now possible to probe the inner region of AGN by studying the gravitationally redshifted emission coming from an accretion disk (e.g., Tanaka et al., 1995).

At the end of 1995, the *Rossi X-ray Timing Explorer* (RXTE; Bradt et al., 1993) was launched to study variability for all kinds of X-ray sources from microsecond to monthly time scales, in an energy range from 2 to 250 keV. With its three on-board instruments, the *Proportional Counter Array* (PCA; Jahoda et al., 1996), the *High Energy X-ray Timing Experiment* (HEXTE; Rothschild et al., 1998), and the *All-Sky Monitor* (ASM; Levine et al., 1996), it detected X-ray afterglows from gamma-ray bursts (see, e.g., Bradt et al., 2001, and references within), and unveiled moving gas clouds around the central region of AGN (Markowitz et al., 2014). RXTE had an exceptionally long mission length of 17 years, which was unprecedented at that time.

In 1996, the Italian-Dutch satellite *BeppoSAX*¹⁸ (Boella et al., 1997) was sent to space. Its instruments provided an extensive view onto the high-energy sky by covering a broad energy range from 0.1 to 300 keV, in better resolution than ever before. While performing pointed observations with the Narrow Field Instruments (NFIs), the two Wide Field Cameras (WFC), which were mounted to face into opposite directions, could simultaneously observe a field of view of $20^\circ \times 20^\circ$ perpendicular to the axis of the NFI. This way, *BeppoSAX* was able to monitor a large amount of sources, including AGN, and search for transients. In particular, the combination of the on-board Gamma-ray Burst Monitor (GRBM) with the two WFC permitted a very good localisation of detected γ -ray bursts (Feroci et al., 1997).

One of the NASA flagships, the X-ray observatory *Chandra*, formerly the *Advanced X-ray Astrophysics Facility* (AXAF; Weisskopf et al., 1996) but renamed to honor the Nobel prize winner Subrahmanyan Chandrasekhar, was launched in 1999, and is still in operation to date. On-board *Chandra* is a single Wolter Type 1 grazing incidence imaging telescope, behind which one of four detectors can be placed into the focal plane. The instruments are sensitive in an energy range from 0.1 to 10 keV. Observations with the High Resolution Camera (HRC; Murray et al., 1997), can achieve a spatial resolution of roughly $0.''5$, which allows to resolve diffuse sub-structure even for weak sources. Gratings available for both soft and hard X-rays can be used with the HRC and the AXAF Charged Coupled Imaging Spectrometer (ACIS; Garmire et al., 2003), respectively. Because of a highly elliptical orbit, *Chandra* can conduct observations with long exposures. By performing several dedicated deep observations, e.g., the *Chandra* Deep Field South (1 Ms exposure; Giacconi et al., 2002), or the *Chandra* Deep Field North Survey (2 Ms exposure; Alexander et al., 2003), a large amount of new, weak X-ray sources have been found.

As one of the cornerstones of the ESA's Horizon 2000 Science Programme, the *X-ray Multi-Mirror Mission* (*XMM-Newton*; Jansen et al., 2001) saw first light in 1999. Just as *Chandra*, *XMM-Newton* is still fully operational. The spacecraft orbits the Earth in an inclined, elliptical orbit every 48 hours, in order to minimize the time per orbit that it has to fly through the radiation belts. The three on-board X-ray telescopes can be operated simultaneously, and are sensitive between 0.1 and 15 keV. *XMM-Newton* has contributed an enormous amount of X-ray observations during its operation in 22 years, including the first detection of a relativistically broadened iron line in an AGN (1H 0707–495; Fabian et al., 2009), and the non-detection of expected cooling flows for low temperatures in three galaxy clusters (Peterson et al., 2001, Kaastra et al., 2001, Tamura et al., 2001), which triggered the development of AGN feedback scenarios. In addition to the X-ray instruments, an optical/UV telescope is mounted on the spacecraft as well. The *Optical Monitor* (OM; Mason et al., 2001) is a 30 cm telescope that can observe sources with eight different filters. In Sect. 2.3.1 I will give a more comprehensive summary of this instrument. More details about the X-ray instruments on-board *XMM-Newton* will be provided in Sect. 2.2.3.

The second *High Energy Transient Explorer*¹⁹ (HETE-2; Ricker et al., 2003) was launched in 2000. The multi-national project, which involved the United States, France, Italy, and Japan, carried three payloads, including the *Soft X-ray Camera* with a sensitivity between 0.5 and

¹⁸The name was chosen to honor the Italian physicist Guiseppe Occhialini. Hence, the name is composed of the physicist's nick name 'Beppo' and the abbreviation of 'Satellite per Astronomia a raggi X'

¹⁹HETE-1 was lost during its launch four years prior due to a failure during the release from the rocket.

14 keV, the *Wide Field X-ray Monitor*, which could detect emission between 2 and 25 keV, and the *French Gamma-ray Telescope* with a large range sensitivity from 6 up to 400 keV. The main goal of HETE-2 was to detect and observe gamma-ray bursts, as well as communicate its detection to the astronomical community for multi-wavelength follow-up observations. The mission was highly successful in its eighth years of operation and revealed the diversity of the GRB population (see, e.g., [Pélangéon et al., 2008](#), and references therein).

Another mission that was mainly built to detect and observe gamma-ray bursts is the *Neil Gehrels Swift Observatory*, which was launched in 2004, and is still operational today ([Gehrels et al., 2004](#)). The spacecraft owes its name to its ability to ‘swiftly’ slew across the sky, as well as the name of its PI, Neil Gehrels, which was added in 2018, after Gehrels died prematurely due to cancer. On-board the spacecraft three telescopes in total observe X-ray, as well as optical/UV emission. The *Burst Alert Telescope* (BAT; [Barthelmy et al., 2005](#)) carries out an all-sky survey in an energy range from 15 to 150 keV, and upon detection of a gamma-ray burst automatically slews to that position on the sky to allow for pointed observations with the other two telescopes. The *X-ray telescope* (XRT; [Burrows et al., 2005](#)) is an imaging telescope, which is sensitive between 0.3 and 10 keV, and can obtain spectra. More details on the XRT is provided in Sect. 2.2.4. The UV/Optical Telescope (UVOT; [Roming et al., 2005](#)) has the same specifications as the OM on-board *XMM-Newton*, and can obtain both images and spectra in six filter bands. A more thorough description of this instrument is given in Sect. 2.3.2. *Swift* has developed from a mission with a single purpose (to observe gamma-ray bursts) to a highly valuable tool for follow-up observations for all kinds of transient and multi-messenger events, e.g., blazar flares (e.g., [D’Ammando et al., 2019](#), [Gokus & Angioni, 2020](#)), or gravitational wave detections (e.g., [Klingler et al., 2019](#), [Page et al., 2020](#), [Keivani et al., 2021](#)). In addition, *Swift* performs monitoring of dedicated sources, e.g., blazars that have been showing high activity at gamma-ray energies ([Stroh & Falcone, 2013](#)).

The Japanese satellite *Astro-E2* was Japan’s fifth X-ray mission. After its successful launch in 2005, it was renamed *Suzaku*, after the mythical ‘vermillion bird’, which is one of four symbols in Chinese constellations. Its payload was comprised of five grazing incidence telescopes to obtain spectra from 0.2 to 12 keV, and a hard X-ray detector to cover an energy range from 10 to 600 keV ([Mitsuda et al., 2007](#)). One of the soft X-ray spectrometers used a micro-calorimeter, the first of its kind to be flown in space. The other spectrometers were equipped with CCD cameras. Observations with *Suzaku* were responsible for the detection of ultra-fast outflows in radio-loud AGN ([Tombesi et al., 2010](#)), the discovery of very Compton thick AGN ([Ueda et al., 2007](#)), and revealed the abundance of essential elements all throughout space ([Simionescu et al., 2015](#)).

The first high-energy experiment for astronomical observations which is operated from the *International Space Station* (ISS) is the *Monitor of All-sky X-ray Image* (MAXI; [Matsuoka et al., 2009](#))²⁰ installed on the Japanese Experiment Module. Since 2009, MAXI surveys the X-ray sky in an energy range from 0.5 to 30 keV, and serves the astronomical community by detecting transient events and monitoring the variability of many sources. Its payload are two different types of slit cameras, the *Gas Slit Camera*, which utilizes proportional gas counters,

²⁰In 1974, the Soviet space station *Salyut 4*, including an onboard X-ray telescope (*Filin*) was launched into space. This was the first X-ray telescope operated long-term on a space station rather than on a satellite ([Berezhnoi et al., 1977](#)).

and the *Solid-state Slit Camera*, which consists of CCDs. MAXI has contributed a large amount of data towards studying X-ray transients that can be used to study their population more generally (e.g., [Corral-Santana et al., 2016](#)), and continues to provide unbiased monitoring for Galactic and extragalactic sources alike ([Grinberg et al., 2013](#), [Gaur et al., 2012](#), respectively).

The *Nuclear Spectroscopic Telescope Array* (*NuSTAR*; [Harrison et al., 2013](#)) was launched in 2012, and is the first mission that is able to image hard X-rays (> 10 keV). Its two co-aligned Wolter Type 1 telescopes observe the sky from 3 to 79 keV. Due to its sensitivity in the hard X-ray regime, *NuSTAR* can detect heavily absorbed AGN, whose soft X-ray emission is nearly completely absorbed by the dust surrounding the central engine (e.g., [Lansbury et al., 2014](#)). Simultaneous observations together with *XMM-Newton* have also proven highly efficient to study the broad X-ray spectrum of, e.g., superluminous X-ray sources (e.g., [Fürst et al., 2016](#)), or, recently, to obtain unbiased measurements of the Hubble constant via X-ray reverberation mapping of AGN ([Ingram et al., 2021](#)). In Sect. 2.2.5, I give a broader overview of the design of *NuSTAR*.

In 2015, India joined the group of nations with active space astronomy programs and launched its first mission, the satellite *AstroSat* ([Rao et al., 2016](#)). The spacecraft carries both X-ray and optical/UV telescopes in order to perform multi-wavelength observations. Two instruments are dedicated to measuring hard X-rays up to 100 keV, while a soft X-ray telescope covers the energy range from 0.3 to 10 keV. In addition, a monitoring instrument scans the sky from 2 to 10 keV. Data from *AstroSat* are used to study the variable behaviour of X-ray binaries (e.g., [Baby et al., 2020](#)) and blazars (e.g., [Bhattacharyya et al., 2020](#), [Singh et al., 2021](#)) alike.

The sixth Japanese mission *Astro-H* was supposed to obtain the best resolved, imaged view into the X-ray sky yet. After its launch in 2016, it was renamed to *Hitomi* to honor this task, as the name means ‘eye’ or ‘pupil’ in Japanese. Contact was lost after only one month in space due to out-of-control spinning of the spacecraft ([Witze, 2016](#)). However, the data of the Perseus cluster, which was taken before the critical failure, were used to map the motion of its hot X-ray emitting gas for the first time (e.g., [Hitomi Collaboration, et al., 2018a,b](#)).

In June 2017, the *Neutron star Interior Composition Explorer* (*NICER*; [Gendreau et al., 2012](#)) joined MAXI on the ISS. Built to explore neutron stars, *NICER* is capable of time-resolved spectrometry in an energy range covering 0.2 to 12 keV. Apart from dedicated observations of known neutron stars, the instrument can also be used for, e.g., monitoring changing-look AGN (e.g., [Ricci et al., 2021](#)), or studying the spectral evolution of X-ray transients (e.g., [Rout et al., 2021](#)).

In 2017, a second X-ray mission was launched into orbit by Chinese institutes: the *Hard X-ray Modulation Telescope* (*HXMT*), which was named *Insight-HXMT* post-launch. With three telescopes, the *Low Energy* (LE; [Chen et al., 2020](#)), *Medium Energy* (ME; [Cao et al., 2020](#)), and *High Energy* (HE; [Liu et al., 2020](#)) X-ray telescopes, *Insight* covers a broad energy range from 1 to 350 keV. Its main science goals are finding new transient sources in the Galactic plane, monitoring variable sources, studying X-ray binaries in order to learn more about the dynamics in extreme environments (i.e., strong magnetic or gravitational fields), and searching for γ -ray bursts. A recent science highlight was its identification of a non-thermal X-ray burst with a fast-radio burst, pointing towards an explosive event from a magnetar as the origin ([Li et al., 2021](#)).

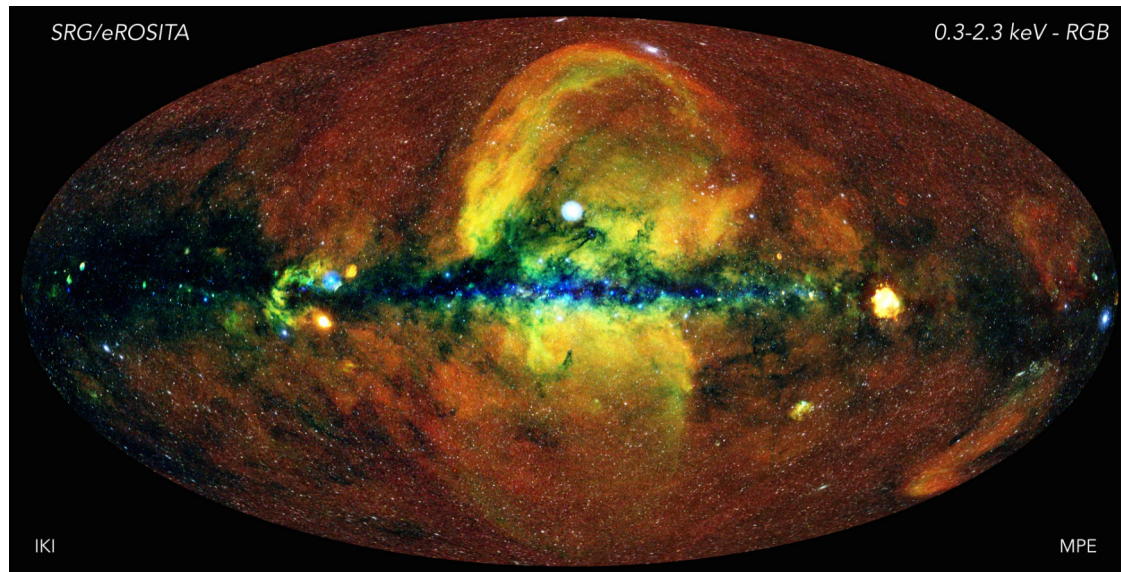


Figure 2.11.: All-sky view of the X-ray sky as seen with SRG/eROSITA in Aitoff projection. While covering an energy band from 0.3 to 2.3 keV, colour-coding reveals the hardness of objects and the diffuse emission (red: 0.3–0.6 keV, green: 0.6–1 keV, blue: 1–2.3 keV). The tiny, star-like white dots are active galaxies. The clearly visible bow-like shape above the Milky is the upper ‘eROSITA bubble’. Credit: Jeremy Sanders, Hermann Brunner and the eSASS team (MPE); Eugene Churazov, Marat Gilfanov (on behalf of IKI)

Nearly twenty years after the last imaging X-ray all-sky survey, which was done by ROSAT, the German-Russian *Spektrum-Röntgen-Gamma* (SRG), or also called *Spectrum-X-Gamma* (SXG), satellite was launched. SRG orbits the second Lagrangian point (L2) and spins around its axis once every four hours. On-board are two telescopes, which, in combination, are sensitive between 0.3 and 30 keV. The *extended ROentgen Survey with an Imaging Telescope Array* (eROSITA; Predehl et al., 2021) is the primary instrument, and consists of seven identical, co-aligned Wolter Type 1 telescopes, which are sensitive for X-rays in an energy range between 0.3 and 8 keV. While moving with the L2 around the sun, eROSITA is able to scan the entire sky within six months. In addition, overlap of regions during the slew allows monitoring of sources every four hours for a period of ~ 24 hours every six months. Sources in the ecliptic polar regions are seen continuously throughout the survey. It is planned that eROSITA conducts eighth all-sky scans over a period of four years, and then switches to a pointed observation mode²¹. The complete survey will be more sensitive by a factor of 25 at soft X-rays compared to ROSAT, and it will also produce the first imaging all-sky view in the hard X-ray regime (2.3 – 8 keV). The X-ray sky, as seen after eROSITA’s first completed scan, is shown in Fig. 2.11. One of the most distinct features found so far are the so-called ‘eROSITA bubbles’, seen as a bow-like shape above and below the Milky Way. They are evidence for a past energetic interaction from the nuclear galactic region with the halo. While probably being of the same origin as the ‘Fermi bubbles’, the cause of their formation is not clear yet (Predehl et al., 2020). The second payload, the *Astronomical Roentgen Telescope* -

²¹This plan is currently delayed. eROSITA was placed into safe mode on February 26, 2022, following the recommendation to freeze co-operation with Russia after their invasion of the Ukraine (<https://www.mpe.mpg.de/7856215/news20220303>)

X-ray Concentrator (ART-XC; Pavlinsky et al., 2018) also contains an array of seven Wolter type 1 telescopes, however with a smaller effective area due to less nested shells than the eROSITA telescopes. It is sensitive in an energy range from 5 to 30 keV.

Within the last few years, the design concept of X-ray experiments has also been adapted to fit into smaller dimensions, similar to the compact setup used in rocket and balloon flights decades ago. Some of these X-ray observatories are attached to space stations (e.g., NICER or MAXI on the ISS), and some are built into micro satellites, or so-called CubeSats. CubeSats are quite small (max. $20 \times 20 \times 30$ cm, but usually smaller) and light-weighted (max. 10 kg), which has the advantage that they don't need their own launch setup, as they can be added onto rockets and be deployed together with other satellites. A successful first example is the *HaloSat* mission, which operated from October 2018 to September 2020. Its goal was a survey of the Milky Way to determine the distribution of hot gas, and constrain both the geometry and the mass of the Galactic halo. With its detectors, it observed a field of view of up to 14 deg, and was sensitive in an energy range from 0.4 to 7 keV (Kaaret et al., 2019). A similarly compact satellite, *Kanazawa-SAT*²³, is also currently in its final stage before the launch²². This Japanese micro satellite is developed at the Kanazawa University, and is designed to search for X-ray transients (Yoshida et al., 2018).

In December 2021, the *Imaging X-ray Polarimetry Explorer* (IXPE; Soffitta et al., 2020) was launched, which is a collaborative project between NASA and the Italian Space Agency. The spacecraft carries three identical telescopes that have both a mirror assembly and a polarisation-sensitive detector. Its expendable boom of 4 m length was expanded in space. IXPE will perform X-ray polarimetry observations of, e.g., supernova remnants, pulsar wind nebulae, and AGN, in an energy range from 2 to 8 keV.

Despite the current richness of available X-ray missions, the golden age of X-ray astronomy is far from over. The planned new design concepts and advanced technology will supply the field of high-energy astrophysics with highly resolved X-ray spectra, and detection limits far below those of current instruments. In the next decades, we will detect many more sources in the early Universe, and study emission and absorption lines with an unprecedented precision.

In 2023, the *X-ray Imaging and Spectroscopy Mission* (XRISM) will be launched. It is designed to recover the scientific potential that was lost when *Hitomi* was destroyed, however, it will only carry instruments for observing the soft X-ray regime. Onboard, there will be a spectrometer using a microcalorimeter to provide extremely resolved X-ray spectra for an energy range between 0.3 and 12 keV, and an imager that is sensitive between 0.4 and 13 keV (XRISM Science Team, 2020).

The next big European flagship will be the *Advanced Telescope for High-Energy Astrophysics* mission²³ (*Athena*; Nandra et al., 2013, Barret et al., 2020), which will be launched in the mid-2030s. *Athena* will be capable of combining high-resolution spectroscopy from 0.2 to 12 keV via the *X-ray Integral Field Unit* (X-IFU; Barret et al., 2018) and wide-field images taken with the *Wide Field Imager* (WFI; Rau et al., 2013, Meidinger et al., 2015). The combination of both instruments on-board *Athena* will provide unprecedented scientific data to study, e.g., the large-scale hot gas structures, or supermassive black holes at a high redshift.

²²Originally, the launch data for *Kanazawa-SAT*³ was in 2019.

²³<https://www.the-athena-x-ray-observatory.eu/>

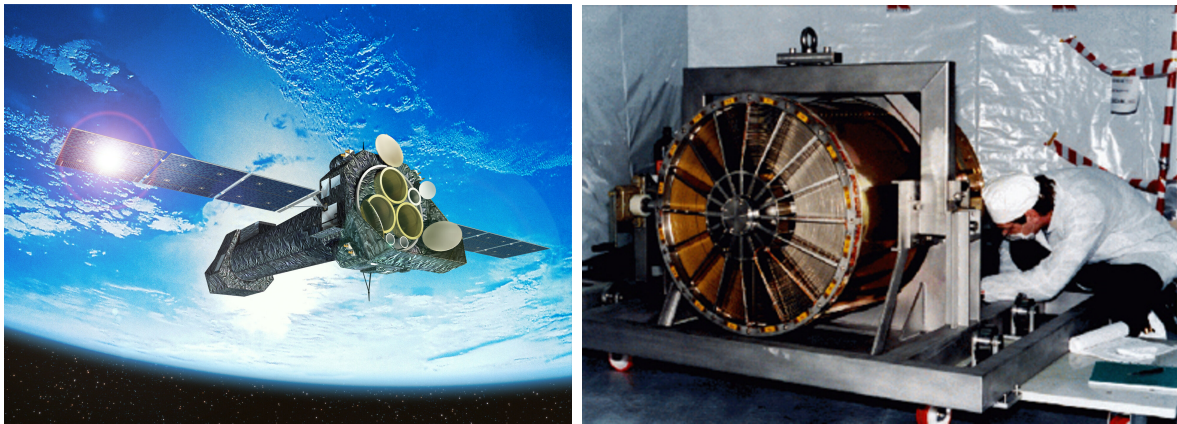


Figure 2.12.: *Left:* Artist's impression of *XMM-Newton* in orbit around the Earth. The opening of all three Wolter Type 1 telescopes is visible, while the interior of the telescope is hidden by the coating. *Right:* One of the three mirror modules, including a human for scale. The module is made of 58 nested mirrors that are coated with gold. Credit: ESA - D. Ducros (*left*), ESA (*right*).

2.2.3 The X-ray Multi-Mirror Mission

Launched as the second cornerstone mission of the Horizon 2000 Science Programme by ESA²⁴ in 1999, the *X-ray Multi-Mirror Mission* (*XMM Jansen et al., 2001*) is an extremely successful X-ray mission that is still in operation today. An artist's impression of the satellite in space, and a photograph of one of the mirror modules during assembly are shown in Fig. 2.12. The work on the design of the spacecraft started already in the 1980s, and was first presented at a workshop in 1985 (*Lumb et al., 2000*). The primary goal has always been to achieve high-resolution spectroscopy by maximising the collecting area, and at that time, the mission design included 19 telescopes, twelve for lower and seven for higher energies. In the end, the spacecraft was equipped with three X-ray telescopes and one optical telescope. Each of the X-ray telescopes is a Wolter type 1 telescope and consists of 58 nested mirrors, which are coated in gold. After its successful launch, Newton's name was added to the name of the spacecraft, to honor him for inventing spectroscopy.

Special CCD cameras were developed for this X-ray mission, which can detect photons in an energy range from 0.1 keV to 15 keV. Two of the so-called 'European Photon Imaging Cameras' (EPICs) are operated with Metal-Oxide-Silicon (MOS) chips (EPIC-MOS; *Turner et al., 2001*), while the third one utilizes a PN-junction array (EPIC-PN; *Strüder et al., 2001*). MOS CCDs work similarly to pn CCD chips, albeit with a slower readout. Both of the EPIC-MOS detectors are made of seven individual, square CCDs with a central one in the focal point and six CCDs surrounding it and following the focal plane curvature in order to improve the focus for the sources that are observed off-axis. The EPIC-pn detector is made of twelve individual, rectangular CCDs that are placed in two rows, and grouped together in four quadrants for a better redundancy. All cameras are able to observe in different operating modes to match the brightness of target sources and avoid pile-up. Both the EPIC-MOS

²⁴The Horizon 2000 programme included four large missions, or cornerstones, which were the combination of the solar observatory SOHO and the Earth observation mission Cluster II (Cluster failed upon launch), *XMM-Newton*, the comet mission *Rosetta*, and the infrared space telescope *Herschel*.

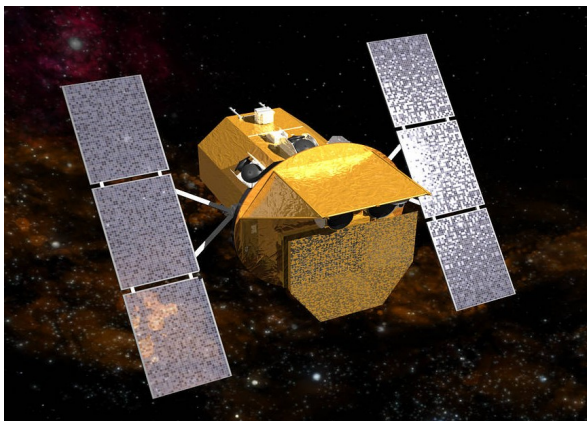


Figure 2.13.: Artist's impression of the *Neil Gehrels Swift* observatory in space. The BAT is the semicircle-like area in the front, while the entries for both the XRT and UVOT are only halfway visible underneath the shielding. Credit: NASA

and the EPIC-pn cameras can operate with all CCDs being read out (*full frame*), which then covers the full field of view (FOV) of the telescope. The EPIC-MOS cameras can only run the standard full-frame imaging mode on the ring of six CCDs, but the central CCD can be operated separately in all other modes. In case the detector is supposed to be only partially exposed, the *large* and *small window* mode are available for both MOS and pn. With MOS, the *large window* mode constrains the read-out detector area to 300×300 pixels on the central CCD, whereas for *small window* mode the area is reduced to 100×100 pixels. The *large window* mode in pn keeps half the area of all twelve CCDs active, while for *small window* mode only the CCD that lies directly at the focal point is read out. Collecting data in the *timing* mode means losing all imaging information. All data from a preselected area on one CCD are reduced into a single row, such that it can be read out at high speed. Moreover, the EPIC-pn camera can also observe in *burst* mode, when the source is too bright for the *timing* mode, albeit the live time, i.e., the time in which data is collected, is only 3%. Hence, most of the incoming photons are not read out and their information is lost.

In addition to different observation modes, physical filters (thin, medium, and thick) are available to limit unwanted interactions of infrared, optical or UV photons with the CCD that can be caused by bright stars in the FOV. These aluminised filters reduce the effective area at lower energies, and thusly prevent an increase of the system noise, changes of the charge transfer efficiency, and an incorrect energy scaling.

The EPIC cameras allow moderate angular (PSF with a full width at maximum of $6''$) and spectral resolution ($E/\Delta E \sim 20 - 50$). A Reflection Grating Spectrometer can be added, which deflects $\sim 50\%$ of incoming light onto the EPIC-MOS detectors. This enables a highly improved spectral resolution at soft X-rays between 0.35 and 2.5 keV.

Lastly, the *XMM-Newton* spacecraft also carries the *EPIC Radiation Monitor* (ERM)²⁵, which is used to gather basic spectral information about the background radiation, and to detect solar flares and radiation belts. This information is valuable for the proper operation of all instruments on-board, as well as for planning future missions.

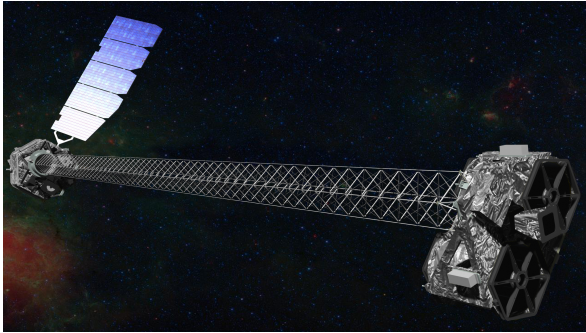


Figure 2.14.: Artist's impression of *NuSTAR* in space. The two optics modules, shown on the right, focus incoming X-rays onto the detectors, which are only connected via a 10-m mast that had been deployed after launch.

Credit: NASA/JPL-Caltech

2.2.4 The Neil Gehrels Swift Observatory

The *Neil Gehrels Swift* Observatory is a multi-wavelength observatory that can simultaneously observe sources in optical, ultraviolet, and both the soft and hard X-ray bands (Gehrels et al., 2004). Figure 2.13 depicts an artistic rendering of the spacecraft in space. *Swift* data are unrestricted for the astronomical community immediately after its procession.

The two X-ray detectors on-board cover an energy range from 0.3 to 150 keV via two instruments: the *X-ray telescope* (XRT; Burrows et al., 2005), and the *Burst Alert Telescope* (BAT; Barthelmy et al., 2005). XRT is a focusing instrument with twelve concentric mirrors that operate in the manner of a Wolter type-1 mirror module. The detector is an EEV CCD-22, consisting of 600×600 pixels. It is the same design used for the EPIC MOS instruments on-board *XMM-Newton* (Holland et al., 1996). Its operational temperature is -100°C to keep the dark current and the sensitivity to irradiation by protons low. The XRT has two readout modes in order to observe both very bright sources, as well as fainter ones. In the *photon counting* (PC) mode, the XRT takes an image of the entire square FOV with a side length of $23.6'$. Above a detector-intrinsic count rate of 1 counts s^{-1} , observations are mainly performed in the *window timing* (WT) mode, which is very similar to the *timing* mode of *XMM-Newton*.

BAT has a very large FOV of 1.4 sr, and is a coded mask instrument. Its main objective is to provide time critical triggers upon gamma-ray bursts. In addition, it also serves as a hard X-ray monitor for X-ray binaries and some of the brighter blazars, since it performs an all-sky survey while waiting for new gamma-ray bursts to detect. BAT can switch between two observational modes: the survey mode, which is the default, and the burst mode. After detection of a gamma-ray burst, BAT switches to the burst mode, computes an initial position with an accuracy of 4 arcmin, and can initiate a slew towards the burst position for further multi-wavelength follow-up observations with *Swift*.

2.2.5 The Nuclear Spectroscopic Telescope Array

Before the launch of the *Nuclear Spectroscopic Telescope Array* (*NuSTAR*; Harrison et al., 2013) in 2012, hard X-ray observations ($> 15 \text{ keV}$) were solely conducted by coded-mask imaging systems (e.g., *Swift*/BAT, *INTEGRAL*). Figure 2.14 shows an artist's impression of the spacecraft in operation.

NuSTAR observes X-rays from 3 to 79 keV with two identical telescopes. Its two mirror modules are made of 133 nested mirrors following the Wolter-I design. While for soft X-ray

²⁵<https://www.cosmos.esa.int/web/xmm-newton/radmon-details>

telescopes a single coating made from high density materials is used, the mirrors on-board *NuSTAR* have a multilayer coating. Such a coating consists of two alternating materials that are stacked on top of each other, typically about 200 pairs. The two different materials need to exhibit a high contrast between their densities. In case of *NuSTAR*, its multilayers are made of a combination of Platinum and Silicon Carbide, and Tungsten and Silicon. This enables the reflection of hard X-rays up to 79 keV.

The two X-ray detectors are similar, and comprised of four rectangular Cadmium-Zinc-Telluride crystals. The detectors and their shielding from background events are called *Focal Plane Modules A* and *B* (FPMA/B), respectively.

NuSTAR was not fully deployed to its final length of 10 m during the launch. The mirrors and the detectors are kept together through a lightweight boom that extended when the spacecraft reached its final orbit.

2.3 Optical astronomy

The very first observations of the night sky date back to the beginning of human civilisations, when stars were used for navigation and calendrical time measurements. Before the windows to other wavelengths were opened in the 20th century, observations were conducted in the optical, and, until the development of the first telescopes in the beginning of the 17th century, only by eye. Since then, the telescope design has evolved from refracting telescopes that were only several centimeters long and pointed to the sky by holding it in hand, to large, mounted mirror telescopes with adaptive optics that are used in ground- and space-based observatories.

The largest telescopes in use today are the *Gran Telescopio Canarias* on the Canary Islands (Alvarez et al., 2000), the *Hobby-Eberly Telescope* in Texas (Savage et al., 2008), the Keck telescopes on Hawaii, and the *Southern African Large Telescope* in South Africa (Buckley et al., 2006), all with effective apertures of more than nine meters. In 2027, the *Extremely Large Telescope* will exceed the size of those by a factor of four. It is currently under construction in the Atacama desert in Chile, and will have a segmented primary mirror with a diameter of 39.3 m.

The most prominent space-based optical telescope is the *Hubble Space telescope*, which has been built by an international collaboration, mainly driven by ESA and NASA. Launched in 1990 and still in operation today, it is one of the greatest success stories in space-based astronomy. Its successor, the *James Webb Space Telescope* (JWST) has just recently been launched and begun observations, and will provide unprecedented data from the optical to the mid-infrared.

As the atmosphere is not a limiting factor for space-based optical instruments, small telescopes (diameter 10–30 cm) can provide sufficient light collectors to measure the flux of weaker sources. Hence, they have been added to a few satellite observatories to allow simultaneous multi-wavelength observations.

2.3.1 The Optical Monitor

XMM-Newton is able to observe optical and ultraviolet emission through its co-aligned *Optical Monitor* (OM; Mason et al., 2001) when performing observations. It has been built by an international collaboration between institutes from the UK, the US, and Belgium. OM is a Ritchey-Chrétien telescope, which is similar to a Cassegrain telescope with the exception that both mirrors are hyperbolic. In the original Cassegrain design, the primary mirror is parabolically shaped, and the secondary mirror is hyperbolic. Its primary mirror diameter is 30 cm, and the telescope body is 2 m long. It has a FOV corresponding to the inner 17' square region of the X-ray FOV. The detector is a CCD, which has been intensified with a micro-channel plate. Directly in front of the CCD, a filter wheel allows observations in three different optical (U, B, V) and ultraviolet (UVW1, UVM2, UVW2) bands, respectively. In addition, a white filter, a magnifier, and a grism for either an optical or ultraviolet spectrum are on the filter wheel. Both the CCD and the filter wheel have a redundant counterpart.

So-called ghost images of ‘smoke rings’ can appear as artifacts in images due to one or more bright sources in the FOV. The reason for this is internal reflection within the detector window. Another artifact can be rays that are caused by off-axis starlight, or general bright

background light. A more detailed description, including images, is given in the *XMM-Newton* User's handbook²⁶.

2.3.2 The UltraViolet and Optical Telescope

The *UltraViolet and Optical Telescope* (UVOT; [Roming et al., 2005](#)) is part of the *Swift* observatory and able to provide data from the ultraviolet to the optical range (170–650 nm). The telescope design is a modified version of a Ritchey-Chrétien telescope with a diameter of 30 cm. The detector CCDs work as photon counting devices with the capability to detect very low signals. Its optics are actually flight spares from OM on-board *XMM-Newton*, as well as the telescope structure, thermal design and the baffle. As the design is very similar to OM, it can exhibit the same artifacts as described for OM.

UVOT is able to observe with eight different filters, which are placed on a wheel that can be rotated during an observation, among them three ultraviolet (UVW1, UVW2, and UVM2) and three optical (U, B, V) filters, as well as the open white filter. Using the white filter, UVOT is able to detect a point source with a magnitude of $m_B = 22.3$ within 1000 s. In addition, low-resolution spectra can be taken with a grism in the UV or optical range. In this work, only photometric data from the six narrow-band filters have been used.

²⁶http://xmm.esac.esa.int/external/xmm_user_support/documentation/uhb_2.1/node77.html

2.4 Radio astronomy

In this section, I give a short introduction on radio astronomy, based on [Burke & Graham-Smith \(2009\)](#).

The foundation for radio astronomy was laid when Karl Jansky unexpectedly discovered radio emission that originated from the center of our Milky Way ([Jansky, 1933](#)). In the 1950s, the first radio surveys of the sky took place (e.g., the first three Cambridge catalogues that found radio sources on the Northern hemisphere; [Ryle et al., 1950](#), [Shakeshaft et al., 1955](#), [Edge et al., 1959b](#)). In the third Cambridge catalogue, quasars were among the newly discovered radio sources. Many sources that were observed as part of this survey are still referred to today with that catalogue nomenclature, e.g., 3C 273 or 3C 279²⁷. Other large surveys on the Northern hemisphere were conducted with the *Very Large Array* (VLA [Becker et al., 1995](#), [Condon et al., 1998](#)). On the Southern hemisphere, a survey done with the Parkes telescope led to a catalog that includes more than 8200 radio sources, and took about 20 years to complete ([Bolton et al., 1979](#)). Sources that are part of this catalog carry the catalogue nomenclature ‘PKS’ in front of the J2000 (FK5) positions²⁸.

Radio observations can be conducted via single antennas, and also via radio interferometers that consist of several antennas. Radio emission is electromagnetic light with a wavelength of ~ 1 mm and larger. It is observed as light waves, unlike for observations in other energy bands, for which individual photons are counted. Radio telescopes consists of a receiving antenna, a receiver, and a recording system. The angular resolution α of a radio telescope can be approximated via the Rayleigh criterion (e.g., [Karttunen et al., 2003](#))

$$\sin(\alpha) \approx 1.22 \frac{\lambda}{d}, \quad (2.10)$$

which depends on the diameter of dish (d), and the wavelength (λ). Higher resolution can be achieved by either increasing the size of the dish, or by observing at smaller wavelengths. Observations in the mm/cm wavelength range are conducted with parabolic reflectors, which are either solid or made of a mesh²⁹. The size of these telescope dishes is limited by their stability and manoeuvrability. The largest fully steerable radio telescope is the *Robert C. Byrd Green Bank Telescope* (GBT; [Prestage et al., 2009](#)) with a size of 110 m \times 100 m. The GBT is located in West Virginia, USA. Closely behind GBT in size is the Effelsberg radio telescope in Germany, which has a diameter of 100 m. This instrument is further introduced in Sect. 2.4.1. Larger radio dishes exist, but are built in valleys, while a moveable receiver is used to observe the desired sources, or regions of the sky. The largest of this kind of telescope is the *Five-hundred-meter Aperture Spherical radio Telescope* (FAST; [Nan et al., 2011](#)), which is located in Guizhou in China. Until the commissioning of FAST, the *Arecibo Telescope*³⁰ in Puerto Rico had the largest radio dish with a diameter of 305 m. In 2020, Arecibo suffered two severe cable breaks, and the National Science Foundation decided to decommission it.

²⁷The ‘3C’ stands for Third Cambridge catalogue, and the digits behind are entry numbers of said catalogue

²⁸The first four digits are the hours and minutes of right ascension, then follows the sign, and degrees and minutes of declination.

²⁹If longer wavelengths (\sim cm) are observed, a mesh with gaps of a few mm will appear solid for the radio light, and has the benefit of being lighter.

³⁰<https://www.naic.edu/ao>



Figure 2.15.: *Left:* Photograph of the 64-meter telescope at Parkes Observatory (Australia), taken in 1969. *Right:* Dipole antennas of the UTR-2 low frequency radio telescope in Ukraine. Credit: CSIRO (*left*), Oleksii Tovpyha (*right*)

Before the controlled demolition could take place, the telescope collapsed on its own at the end of 2020.

The observation of the longest radio wavelengths requires a different type of antenna, ideally dipoles with specific designs (see Fig. 2.15, right). These kind of telescope are often operated in arrays, such as the *Long Wavelength Array* in the desert of New Mexico (Ellingson et al., 2009), the second modification of the *Ukrainian T-shaped Radio telescope* (UTR-2 Braude et al., 1978), or the *LOW-Frequency ARray* (LOFAR; van Haarlem et al., 2013).

The main complications during observations are caused by radio frequency interference, often caused by human-made signals (e.g., Thompson et al., 1991). Hence, the sites for radio observatories are chosen to be in sparsely populated regions, or radio-silent areas, which have been defined within a large perimeter around the telescopes (e.g., Sizemore, 1991, Cohen et al., 2003, Umar et al., 2013, Offringa et al., 2015). Observations at higher radio frequencies are more affected by interference, and more constrained by weather conditions and the water vapor concentration in the atmosphere.

Using a single radio antenna for observations can only resolve the structures of very few sources (e.g., the angular extension of the sun, and the extended emission from the active galaxy Centaurus A), even at mm wavelengths and with larger telescopes. Hence, such single-dish observations are suited to determine the overall flux of a source, which can be used to create a light curve and depict changes in flux. Observations at different frequencies enable measurements of the spectrum of a source.

In order to obtain much better spatial resolution, and thereby create an image of extended radio emission, it is necessary to employ interferometry, i.e., the observing strategy involving two or more telescopes at the same time. For observations with an array of telescopes, the denominator in the Rayleigh criterion (Eq. 2.10) is no longer the diameter of a single dish, but the distance, or baseline, between two telescopes. This so-called very long baseline interferometry (VLBI) technique (Jennison, 1958) achieves an improvement about five orders

of magnitude in resolution compared to single-dish observations. Detailed descriptions on the theory behind VLBI observations are given by, e.g., Müller (2014, Sect. 2.1.2), Beuchert (2017, Sect. 2.1), and Baczko (2019, Sect. 2.4).

An array can consist of many telescopes, which allows to reconstruct images, if the phase and amplitude information of at least three telescopes is known. Choosing longer baselines is immediately transferred to increasing the achievable angular resolution. VLBI networks spanning the globe can construct a telescope that has a virtual dish size of the diameter of the Earth. The utilised telescopes do not necessarily have to have the same size or specifications. Such large networks are, e.g., the *European VLBI Network* (EVN; Paragi et al., 2005, Venturi, 2010), the *Very Long Baseline Array* (VLBA; Napier, 1995), or the *Event Horizon Telescope* (EHT; Event Horizon Telescope Collaboration et al., 2019a, Akiyama et al., 2022a). Smaller arrays, which have been constructed at one site, are, e.g., the *Atacama Large Millimeter/submillimeter Array* (ALMA; Wootten & Thompson, 2009), or the *Australian Telescope Compact Array* (ATCA; Wilson et al., 2011, see also Sect. 2.4.2).

An interferometer measures the coherent wavefront that arrives with a geometrical time delay at each telescope with respect to a reference antenna. As the time delays are very short, very good time resolution is necessary, which is usually achieved with an atomic clock. A correlator obtains the resulting interference pattern, or ‘fringe’. Each telescope pair within the array provides a measurement in the Fourier space (visibility function), and together they determine the Fourier transform of the brightness distribution that is convolved with the reception pattern. This complex function in the spatial frequency domain is called the *Visibility*, $V(u, v)$. The more telescopes are part of the array, the more visibility functions appear in the (u, v) plane, which leads to more steady measurements. In addition, the rotation of the Earth provides more visibility functions as the time delays slightly change during observations, which is called *Earth rotation synthesis* (Ryle & Hewish, 1960, Ryle & Neville, 1962). With the data taken via VLBI observations, images with milliarcsecond resolution can be retrieved. Recently, the efforts of the EHT collaboration were successful in retrieving an image of the shadow of the black hole in M 87 (Event Horizon Telescope Collaboration et al., 2019b), and the shadow of the black hole in the centre of our galaxy, Sagittarius A* (Akiyama et al., 2022b).

Another leap forward in Science is expected for the inauguration of the *Square Kilometre Array* (SKA; Dewdney et al., 2009), which will consist of several thousand radio dishes of 15 m size and up to a million low-frequency antennas. SKA will operate on two sites. The precursors *MeerKAT* (Jonas, 2009) and *Murchison Widefield Array* (Tingay et al., 2013) are located in South Africa and Australia, respectively. SKA will be used to study a variety of phenomena, e.g., star formation in the early Universe, dark energy, and test the predictions of general relativity within the presence of strong gravity fields.

2.4.1 The Radio Telescope Effelsberg: A giant in the Eifel

The radio telescope in Effelsberg³¹, operated by the Max Planck Institute for Radioastronomy, is located in the mountains of the Eifel in Germany (see Fig. 2.16, left), and the second-largest steerable radio telescope with a diameter of 100 m. Inaugurated in 1971, it has now

³¹<https://www.mpifr-bonn.mpg.de/en/effelsberg>



Figure 2.16.: *Left:* The Effelsberg radio telescope and its corresponding operational building. Credit: MPIfR

Right: Five of the six radio antennas of ATCA in a ‘T’-shaped configuration. The tracks of both the East-West and the North spur through which the antennas can be re-arranged are visible as well. Credit: ATNF/CSIRO

been observing sources on the Northern sky for more than 50 years. Among these sources are pulsars, dust clouds, regions of star formation, radio galaxies, and blazars. The usual observation mode with the telescope is single-dish observations, but it is also available for observations within VLBI networks.

The telescope has two receiver cabins, one in the primary focus, and another one in the secondary focus. With the equipment, it is possible to observe radio emission from 1 m to 3.5 mm, or 300 MHz to 90 GHz, in the frequency space.

2.4.2 The Australian Telescope Compact Array

Located close to the town of Narrabri in New South Wales in Australia, the *Australian Telescope Compact Array*³² (ATCA; Wilson et al., 2011) observes radio emission with wavelengths between 20 cm and 3 mm. It is operated by CSIRO since its official opening in 1988³³. The array consists of six identical telescopes that have a diameter of 22 m and can be positioned alongside the East-West track, which is 6 km long in total. In the middle of the East-West track, a perpendicular track allows to place telescopes up to 250 m towards North as well. Figure 2.16 (right), five of the six telescopes are shown in a tight T formation.

³²<https://www.narrabri.atnf.csiro.au/>

³³<https://blog.csiro.au/opening-atca/>

Multiwavelength Monitoring of the Universe: Motivation, Methods and Examples

“If you wish to make an apple pie from scratch, you must first invent the Universe.”

Carl Sagan

The use of instruments that extend the view into the Universe beyond the optical spectral band changed our approach to studying astrophysical sources, and enabled progress in the understanding of our cosmos. The combination of information obtained at different wavelengths is like a jigsaw puzzle. Putting the pieces together can be challenging, but one can gain an advanced insight into the nature of astrophysical sources when this challenge is overcome.

At the same time, variability is a constituting characteristic of a variety of sources, and in some cases, e.g., two merging neutron stars (e.g., [Abbott et al., 2017](#)), bear witness to the most violent events in the universe. In order to detect transient objects, one requires luck for an event to occur within the field of view of a telescope or a survey, e.g., like the discovery of fast radio bursts in archival pulsar survey data ([Lorimer et al., 2007](#)). The study of the variable nature of sources, such as X-ray binaries or blazars, demands continuous observations, which can be achieved with monitoring programmes. Repeated flux measurements over long time ranges creates light curves that can be used to track the activity of an object from days to years, and to reveal existing patterns, such as potential quasi-periodic oscillations (e.g., [Peñil et al., 2020](#)). Similarly, frequent spectral measurements enable us to study changes of physical processes within the components that contribute to the emission of a source. To understand blazars, or more specifically their jets, these kind of periodic observations are necessary throughout the entire electromagnetic spectrum, because their variability is present from the radio up to the γ -ray band (see also Sect. 1.2.2). In Section 3.1 I will explain the different approaches to unbiased monitoring, while focusing on blazar-dedicated monitoring programmes in Sect. 3.2. Section 3.3 will illustrate how multi-wavelength data from monitoring programmes can be used to study blazars in detail.



Figure 3.1.: *Left:* The four cylindrical parabolic reflectors that make up the CHIME radio telescope. Each reflector is 20 m wide and 100 m long. *Right:* The water tanks of HAWC, which are used to detect VHE γ -ray emission.

Credit: Richard Shaw/UBC/CHIME Collaboration (*left*), J. Goodman (*right*)

3.1 Feasibility and limitations of unbiased monitoring

A commonly used approach for unbiased monitoring is to choose a specific part of the sky. This approach has the great advantage that it does not require human-made selection of a target sample and will allow for the detection of new sources or transient events. However, all-sky monitoring programmes have to find a balance between exposure time, field of view, and detector sensitivity, in order to gain the maximum depth and densest monitoring frequency possible. Ground-based observatories are additionally also limited by the part of the sky that is visible from their location on Earth, while telescopes in space are not restricted in that regard, but are much more expensive to construct and operate.

The monitoring strategy can vary depending on the scientific goal behind the observations. One possibility is to choose a certain region in the sky that is mapped in a slow pace, i.e., where regions are observed with a long exposure time to detect even very faint sources and also provide, e.g., high-resolution spectra. Such a monitoring was performed by ESO's *Visible and Infrared Survey Telescope for Astronomy* (VISTA; Emerson et al., 2006) at infrared wavelengths, which resulted in six different kinds of surveys of (parts of) the southern sky that were conducted between 2009 and 2014 (Catelan et al., 2011, Cioni et al., 2011, McCracken et al., 2012, Edge et al., 2013, Jarvis et al., 2013, McMahon et al., 2013).

Fast and dense monitoring programmes using ground-based facilities are, e.g., ASAS-SN¹ (Kochanek et al., 2017), and ZTF² (Bellm et al., 2019). Within ASAS-SN, multiple telescopes around the globe cover the entire night sky in order to discover new supernovae, and other bright transients at optical wavelengths. The network has a sensitivity down to the 18th magnitude, and provides fluxes in the g- and V-band for all sources in the sky that are bright enough. ZTF observes the entire northern night sky every two days by using a telescope at the Palomar Observatory in California, and a camera with an extremely wide-field of view. Photometry data are taken in the g- and r-band, and released bi-monthly to the public.

A different strategy is to monitor the sky with non-aligning telescopes that have a wide field of view, that is telescopes that are pointing at different regions at the sky solely by the

¹All-Sky Automated Survey for SuperNovae

²Zwicky Transient Facility

rotation of the Earth. An example is the radio telescope CHIME³ (Bandura et al., 2014), which is sensitive between 400 and 800 MHz. While its main mission is to map the distribution of hydrogen in the Universe, it also serves as a monitoring instrument for pulsars, and as an efficient discovery instrument for Fast Radio Bursts. An image of the telescope is shown in Fig. 3.1. At the other end of the spectrum, HAWC⁴ (Smith & HAWC Collaboration, 2015) observes γ -rays (100 GeV – 100 TeV) and cosmic rays by utilising 300 water tanks that are placed at 4100 m above sea level in Mexico (see Fig. 3.1, right). HAWC detects particles from air-shower events and, as the detection occurs within water tanks, is insensitive to weather conditions or bright ambient light from the moon, in contrast to IACTs. A very similar concept is used by the Pierre Auger Observatory (Abraham et al., 2004, The Pierre Auger Collaboration, et al., 2016), which also uses water tanks to detect cosmic rays, and, in addition, detectors to observe UV light caused by air-showers in the atmosphere. In contrast to HAWC, the number of water tanks and the area on which they are distributed is much larger. This enables measurements of the most energetic cosmic rays, whose signals are spread over a very large field on the ground.

Space-based observatories are less limited in their monitoring capabilities, but have to be prepared with enormous care as they typically cannot be adjusted or repaired after launch. Successful examples of monitoring observatories or instruments in orbit around the Earth are the *Fermi* satellite, which is described in Sect. 2.1.3, and the *Burst Alert Telescope* (BAT) onboard the Neil Gehrels *Swift* observatory (see also Sect. 2.2.4). The goal of BAT is to detect new transients as well as monitor known, variable sources, within an energy range between 15 and 150 keV (Krimm et al., 2013). *Swift*/BAT, *Fermi*/LAT, and *Fermi*/GBT are able to scan the entire sky roughly within a day, enabling the collection of very dense monitoring information. For several instruments, the second Lagrangian point (L2) is chosen as a position for the satellites to orbit. L2 is one of five balance points where the gravitational force by the Earth and the sun are in equilibrium with the centripetal force of a moving body (Lagrange, 1772), and located 1.5 million kilometers behind the Earth. All Lagrangian points stay at a constant distance to the Earth, and move around the sun at the same speed as the Earth, as a result. Satellites that are put into orbit around L2 (instead of the Earth) avoid regular eclipses of the sky by our planet. For those observatories located at L2, the entire sky is observable over a course of six months. One of these missions is *Gaia* (Gaia Collaboration et al., 2016b), whose goal is a three-dimensional census of the stars in the Milky Way and measuring proper motions of stars with a very high accuracy (Gaia Collaboration et al., 2016a, 2018, 2021), which permits to determine the rotation of our Galaxy in detail. *Gaia* also detects extragalactic sources, and has sent out public alerts regarding transients or flaring behaviour, including photometric information⁵. At X-ray energies, the telescope eROSITA (Predehl et al., 2021) scans the entire sky within six months and can be used for monitoring sources as well. As described in Sect. 2.2.2, it is possible to use the five to six pointings on each sky region within 24 hours to monitor a source on sub-daily scales, in addition to the six-month time period. Interesting transient events are identified by the eROSITA Collaboration members, and

³Canadian Hydrogen Intensity Mapping Experiment

⁴High-Altitude Water Cherenkov Gamma-Ray Observatory

⁵*Gaia* Science alerts are maintained at <http://gsaweb.ast.cam.ac.uk/alerts/home>

communicated to the scientific community, typically with *Astronomer's Telegram* (Rutledge, 1998).

3.2 Monitoring programmes dedicated to blazars

The variable nature of blazars across the entire electromagnetic spectrum makes them favoured targets for monitoring programmes at all frequencies. Monitoring instruments scanning the entire sky are able to deliver data for many sources without introducing a human-made selection. However, their sensitivity and exposure time is often limited, and only enables to detect the brighter population among a source class. Furthermore, all-sky monitoring observatories are rare at radio frequencies, and non-existent at VHE γ -rays. A couple of monitoring programmes have been brought to life⁶, some spanning a decade or more. Each blazar monitoring programme has its own criteria for choosing a sample, however, several were initiated as a multi-wavelength complement to *Fermi*/LAT shortly before, or after its launch in 2008. Hence, one of the selection criteria for many of the blazar monitoring programmes is a detection at γ -rays with LAT. In the following, I will list several major monitoring programmes for blazars that are carried out in different frequency bands, with some of them contributing to the example monitoring campaigns presented in Sect. 3.3.

3.2.1 γ -ray & X-ray monitoring programmes

At the highest energies, that is TeV γ -rays, only 275 sources have been detected so far⁷, among them 84 AGN, which are nearly entirely classified as blazars. As the number of IACTs is very small, with currently three telescopes or telescope arrays residing in the northern hemisphere, and one in the southern hemisphere, the capabilities for monitoring a large amount of sources is limited. The FACT instrument, which has been introduced in detail in Sect. 2.1.2, devotes a large amount of its observing time to monitoring a small sample of bright TeV blazars on a nightly basis, if conditions allow. The sources that have been observed the most, and monitored over more than eight years are Mrk 501, Mrk 421 (see also Chapter 4), 1ES 1959+650, and 1ES 2344+51.4, which are all known for their occasional bright and short γ -ray flares. Other IACTs have also performed monitoring campaigns on specific sources, which are usually the brightest, or most variable blazars. While these monitoring campaigns are in most cases conducted over the course of years as well, these sources are not necessarily visited on a nightly basis in order to monitor a larger amount of sources. Multi-wavelength monitoring and campaigns for the sources are either planned ahead, or organised spontaneously after the occurrence of a bright flare as target-of-opportunity (ToO) observations.

In the X-rays, the *Swift* XRT has been used for monitoring 272 X-ray sources up to now, most of them blazars, but also a few X-ray binaries and Galactic transients. The monitoring programme and the performed data analysis are described by Stroh & Falcone (2013). The original source sample was compiled from the so-called 23 ‘LAT Gamma-ray Sources of Interest’, which are all AGN except for one X-ray binary. The monitoring started at the end of 2004, and still goes on, however, the monitoring density and coverage time ranges are

⁶List of majority of blazar monitoring programmes: <https://www.physics.purdue.edu/MOJAVE/blazarprogramlist.html>

⁷As listed in the TeVCat (<http://tevcad.uchicago.edu/>) in April 2022

different for each individual source. As the main goal of this X-ray monitoring programme is to provide accessible information about targets to help with ToO observations and planning multi-wavelength campaigns, the light curves and hardness ratios are publicly available⁸.

3.2.2 Optical & infrared monitoring programmes

At optical wavelengths, a number of blazar-dedicated monitoring programmes exists, and a recent review was given by [Gazeas \(2019\)](#). Here, I will mention the programmes whose data I used in my work presented in this thesis, or programmes that I deem noteworthy.

The *Tuorla* Blazar monitoring programme ([Takalo et al., 2008](#)) observes a large quantity of blazars, some of them selected based on a detection at TeV energies, or at GeV γ -rays with LAT. This programme takes photometry data in the R-band, and uses various telescopes around the globe, located in Finland, Spain, Chile, the US, and Bulgaria.

Another optical monitoring that chose its sample from variable blazars detected by *Fermi*/LAT is the *Steward* monitoring programme, which is executed by the University of Arizona ([Smith et al., 2009](#)). The three telescopes involved in observing the source sample are located in the Mountain area around Tucson, and observe at a nightly cadence if weather permits. Photometry data in the V- and R-band are collected, as well as spectra between 4000 and 7600 Å, and spectropolarimetric information. The sample consists of 66 blazars, and the data, i.e., light curves, are publicly available⁹.

The *Small & Moderate Aperture Research Telescope System* (SMARTS; [Bonning et al., 2012](#)) monitors *Fermi*/LAT detected sources that show an interesting behaviour with regard to their variability, meaning flares. SMARTS operated from 2008 to 2017, and monitored 105 blazars. SMARTS used two 1 m telescopes located in Chile and only observed sources in the southern sky as a result. Photometry data were taken at optical and infrared wavelengths in the BVRJK bands. The cadence for observations was typically once every three days, however, bright or flaring sources were observed nightly. The data are publicly available¹⁰.

The automatic polarimetric monitoring called *RoboPol* ([Pavlidou et al., 2014](#), [Blinov & Pavlidou, 2019](#)), which has the goal of studying optical polarisation from γ -loud blazars, uses a more unbiased approach to select their target sample. For the RoboPol sample, three criteria were defined for choosing blazars to monitor: the γ -ray flux of a source needs to be above a certain threshold, while the optical magnitude needs to be at least 17.5 mag. Furthermore, a source should not be too close to the Galactic plane. As the telescope used for the RoboPol monitoring is located on Crete, observations are limited to the northern sky. The resulting sample of γ -loud blazars consists of 62 sources. In addition, they compiled a control group sample in order to compare the optical polarisation of γ -loud blazars to γ -quiet, radio-loud AGN. 15 sources are in the control group. In addition to the blazar monitoring programme, RoboPol also monitors Be/X-ray binaries, and maps the magnetic fields in interstellar clouds. Data taken until 2017 are public¹¹.

⁸Available at <https://www.swift.psu.edu/monitoring/>

⁹<http://james.as.arizona.edu/psmith/Fermi/>

¹⁰<http://www.astro.yale.edu/smarts/glast/home.php>

¹¹<https://robopol.physics.uoc.gr/>

A rather unusual monitoring programme in terms of who is carrying it out, is the *Frankfurt Quasar Monitoring*¹². Run privately by Stefan Karge since 1998, an amateur astronomer, the programme has regularly performed photometric measurement for 66 quasars, blazars, and other AGN-types, and has observed ~ 400 AGN. The observations started at the Taunus Observatory in Germany, but are now also conducted remotely with telescopes on Tenerife, in New Mexico, and Australia.

3.2.3 Radio monitoring programmes

Similar to optical wavelengths, a large number of monitoring programmes exists for the broad radio band. Again, I will briefly summarise those that contributed data to projects shown in this thesis.

One of the longest, continuously run monitoring programmes is carried out with the 14m radio telescope at the *Metsähovi* observatory in Finland (Terasranta et al., 1992). The earliest observations of extragalactic sources were done in 1980, resulting in now more than 40 years of AGN monitoring. Up to now, Metsähovi has observed 1206 AGN and microquasars, and provides quick look flux density plots for 271 sources¹³. Observations are performed semi-automatically at 22 and 37 GHz throughout the year, while only the 37 GHz data are visible for the public. The observational cadence varies from source to source, but is typically quite dense for the brighter and more variable AGN.

Another monitoring programme for blazars in the northern sky was conducted by the 40m telescope at the *Owen Valley Radio Observatory* (OVRO). More than 1500 objects were observed twice per week at 15 GHz (Richards et al., 2011) for the duration of the programme, which was run from 2008 to 2020. The main target sources were γ -loud AGN, i.e., mainly blazars detected by *Fermi*/LAT.

The F-GAMMA¹⁴ (Angelakis et al., 2019) programme ran from 2007 to 2015, and conducted multi-frequency observations with a cadence of 1-1.3 months. F-GAMMA collected data at twelve frequencies between 2.6 and 345 GHz with the Effelsberg telescope (see Sect. 2.4.1 in Germany, the IRAM 30m telescope in Spain, and the APEX 12m telescope in Chile. As indicated by the full name of the programme, the sample of monitored blazars was chosen with regard to sources seen with *Fermi*/LAT that were deemed interesting. In total, the sample contained ~ 60 blazars that were regularly monitored, and several sources that were observed as ToOs. F-GAMMA data are publicly available.¹⁵

Recently, the TELAMON¹⁶ programme started its observations of selected TeV-emitting blazars with the Effelsberg telescope (Kadler et al., 2021). With a cadence of two to four weeks, flux density measurements are done at 20 mm, 14 mm, and 7 mm for a sample of more than 30 sources. Additionally, neutrino candidate sources are followed up, and added to the regularly monitored sample in some cases.

In addition to flux density measurements at different radio frequencies, VLBI observations can be used to monitor the structure and individual components of a jet. The images taken

¹²<http://quasar.square7.ch/fqm/fqm-home.html>

¹³As of April 2022, see <http://www.metsahovi.fi/AGN/data/>

¹⁴Fermi-Glast AGN Multi-frequency Monitoring Alliance

¹⁵Available at: <https://www3.mpifr-bonn.mpg.de/div/vlbi/fgamma/fgamma.html>

¹⁶TeV Effelsberg Long-term AGN MONitoring (<http://telamon.astro.uni-wuerzburg.de/>)

over a period of time enable the identification of movements in the jet and the determination of certain physical properties of the jet, such as the jet velocity. VLBI images can also be used to connect the appearance of a new component with, e.g., a flaring event. Hence, VLBI monitoring plays a substantial role in understanding processes within blazar jets.

The MOJAVE¹⁷ programme (Lister et al., 2018) started in 2002 after the *Very Long Baseline Array* (VLBA) 2cm survey was completed (Kellermann et al., 1998). MOJAVE performs VLBI monitoring with the VLBA at 15 GHz for sources observable from the northern hemisphere, with a changing sample size over time. More than 430 blazars have been observed as part of this programme so far, and the monitoring continues for a large fraction of those until today. The flux density and polarisation measurements are provided to the public via their webpage.¹⁸

In 2007, a second monitoring programme that uses the VLBA was started by the blazar group at Boston University (Jorstad & Marscher, 2016), and ran until 2020. The so-called VLBA-BU-BLAZAR programme conducted monthly observations at 43 GHz for > 40 blazars (Jorstad et al., 2017). The original sample of 30 blazars was chosen based on interesting sources found by EGRET. This monitoring programme is now succeeded by a new project, BEAM-ME, which includes VLBA observations at 86 GHz in addition to those at 43 GHz. The target sample consists of γ -ray bright blazars. The data, which include flux density and polarization information, are made public.¹⁹

On the southern hemisphere, the TANAMI²⁰ (Ojha et al., 2010, Müller et al., 2018) project monitors blazars and other AGN using radio antennas distributed over Australia, Africa, South America, New Zealand, and Antarctica. By acquiring very large baselines, it is possible to obtain a resolution at milli-arcseconds, which relates to parsec-scale structures of blazar jets. The monitored sample consists of 135 jetted AGN, most of them being γ -loud. The VLBI observations are performed at source-dependent cadences, and are complemented by flux density measurement with ATCA and the Ceduna 30m dish, which are both located in Australia.

In addition to dedicated programmes, several sources of the interesting-deemed *Fermi*/LAT sources have been or are regularly observed as calibrator sources by the *Submillimetre Array* (SMA; Ho et al., 2004), and the *Atacama Large Millimeter/submillimeter Array* (ALMA; Wootten & Thompson, 2009).

3.3 Performing blazar multi-wavelength monitoring

In this section, I briefly highlight the efforts of multi-wavelength monitoring programmes for two distinct blazars. In addition, Chapter 4 contains a detailed analysis of a multi-wavelength data of the blazar Mrk 421, which were obtained through a monitoring programme led by the γ -ray telescope FACT and the *Swift* satellite.

¹⁷Monitoring Of Jets in Active galactic nuclei with VLBA Experiments

¹⁸Available at: <https://www.physics.purdue.edu/astro/MOJAVE/index.html>

¹⁹Available at: <https://www.bu.edu/blazars/VLBAproject.html>

²⁰Tracking Active Galactic Nuclei with Austral Milliarcsecond Interferometry

3.3.1 PKS 1510–089: a bright and VHE γ -ray emitting FSRQ

Before the detection of flat-spectrum radio quasars (FSRQs) in the VHE regime (< 100 GeV), it was assumed that γ -ray emission is only produced close to the central engine, and that the typically bright broad-line region (BLR) of FSRQs causes the absorption of VHE γ -rays, rendering the detection of VHE emission from FSRQs unlikely. The detection of several exceptions suggests that γ -rays exceeding 100 GeV can be generated further downstream in the jet. The detection of VHE emission from FSRQs has so far always been connected to bright γ -ray flares, and all except one source are not visible during low activity states for current IACTs. As still only a handful of these special FSRQs have been discovered, there are ongoing efforts by all IACTs to follow up reports by the *Fermi*/LAT collaboration, or others using the public LAT data, regarding bright γ -ray flares, spectral hardening of the γ -ray spectrum, or the detection of a γ -ray photon with an energy exceeding ~ 10 GeV (e.g., [Neronov et al., 2010](#), [Pacciani, 2015](#), [Wagner et al., 2021](#)).

Belonging to this group of VHE-emitting FSRQs, and being one of the most variable and γ -ray bright blazars in general, PKS 1510–089 has been a prime target for long-term monitoring programmes since more than a decade. PKS 1510–089 is found at a redshift of $z = 0.361$ ([Jones et al., 2009](#)), and the second FSRQ, for which VHE γ -ray emission (< 100 GeV) was detected ([H. E. S. S. Collaboration et al., 2013](#)). The FSRQ found prior to emit in the VHE regime is 3C 279, another bright and well-studied blazar ([Errando et al., 2008](#)). PKS 1510–089 is so far the only FSRQ for which VHE γ -rays have also been observed during its quiescent state in γ -rays ([MAGIC Collaboration, et al., 2018](#)).

The multi-wavelength light curves of PKS 1510–089 obtained by several monitoring programmes shown in [Fig. 3.2](#). Note that more monitoring programmes than those shown here have or had this source included in regular observations. Numerous flares are visible, with the γ -ray and optical flares showing the largest amplitudes as well as the shortest time scales. In the radio bands, the variable nature of PKS 1510–089 can clearly be seen as well, albeit on longer time scales. One can spot the coincidence of a few flaring events throughout nearly all bands, e.g., the major radio flare responding to the bright γ -ray in 2011, during which, however, no optical and X-ray coverage was possible.

The combination of continuous γ -ray observations and multi-wavelength data taken with a dense cadence enables studying a large part of the emission of PKS 1510–089 with simultaneous data. The Bayesian-block algorithm ([Scargle et al., 2013](#)) is a valuable tool to identify time spans during which a blazar displays a stationary flux in a certain energy band. Applied to long-term light curves, it can be used to statistically study flux variations (e.g., [Krauss, 2016](#), [Wagner et al., 2022](#)), and to select time periods during which multi-wavelength data can be used together for modelling the, supposedly constant, spectral energy distribution (SED) of a source. In [Fig. 3.3](#), the γ -ray light curve, which is also displayed in the top panel of [Fig. 3.2](#), is shown in the upper panel, superimposed by the computed Bayesian blocks in red. The Bayesian blocks have been computed with a prior of `nbp_prior= 3` that controls the tolerance setting for finding change points and correlates with the total number of found blocks. A default value for `nbp_prior` can be derived based on simulations, however, depending on the binning, strong but short variations, which are typical for PKS 1510–089, might be ignored. To illustrate the density and underline the capabilities with the data obtained by monitoring,

3.3. PERFORMING BLAZAR MULTI-WAVELENGTH MONITORING

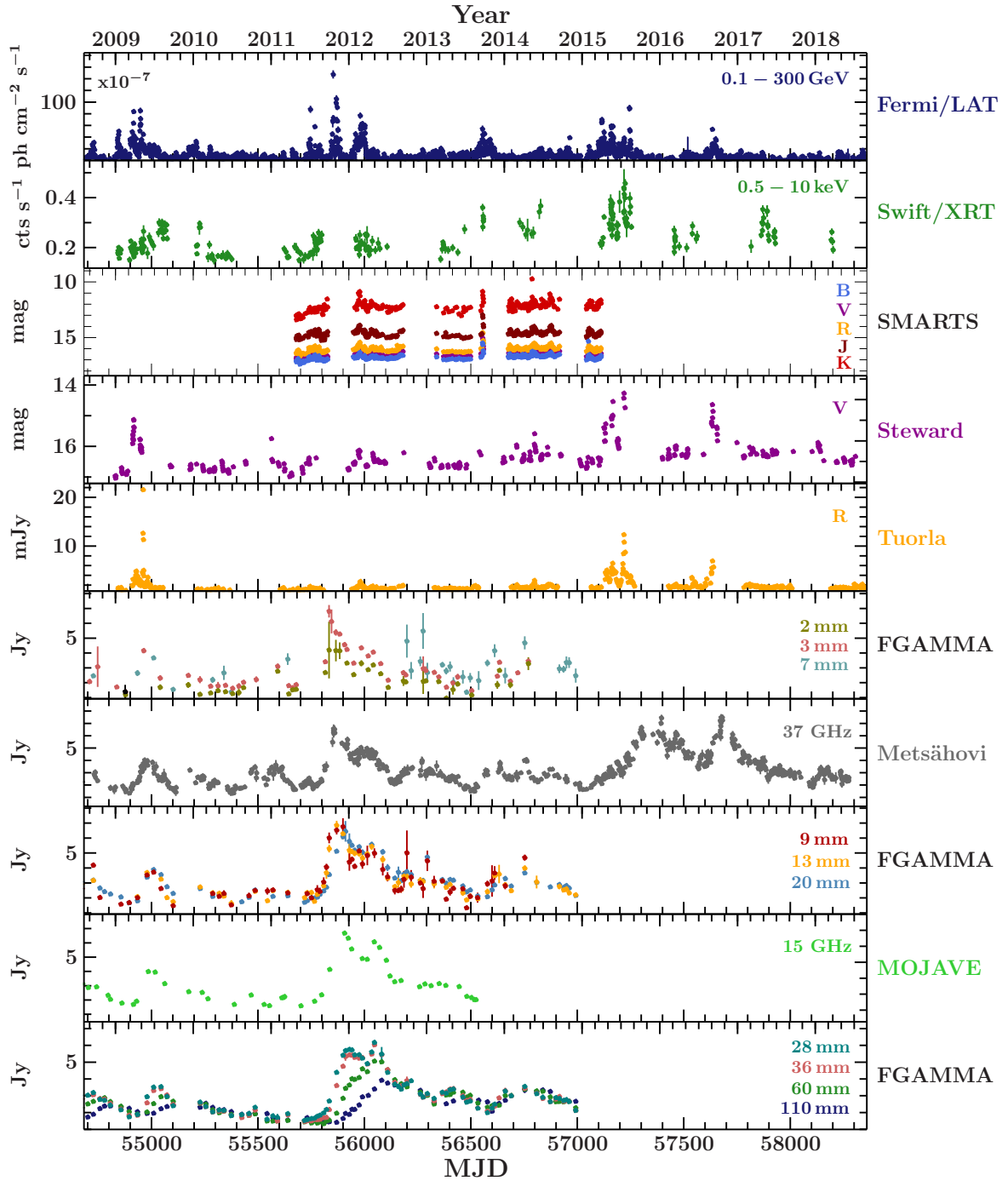


Figure 3.2.: Multi-wavelength light curves of PKS 1510–089 from mid 2008 to the end of 2018, sorted by decreasing energy from top to bottom. The γ -ray light curve is daily binned, the observations at all other energies are individual observations taken at different, partially inconsistent cadences. Data acquisition: *Fermi*/LAT - public data, light curve computed by myself; *Swift*/XRT - public data; SMARTS - public data; Steward - public data; Tuorla - E. Lindfors, priv. comm.; FGAMMA - public data; Metsähovi - provided by courtesy of Aalto University Metsähovi Radio Observatory, Finland; MOJAVE - public data. The links to the public databases are given in the previous sections in the description of each monitoring programme.

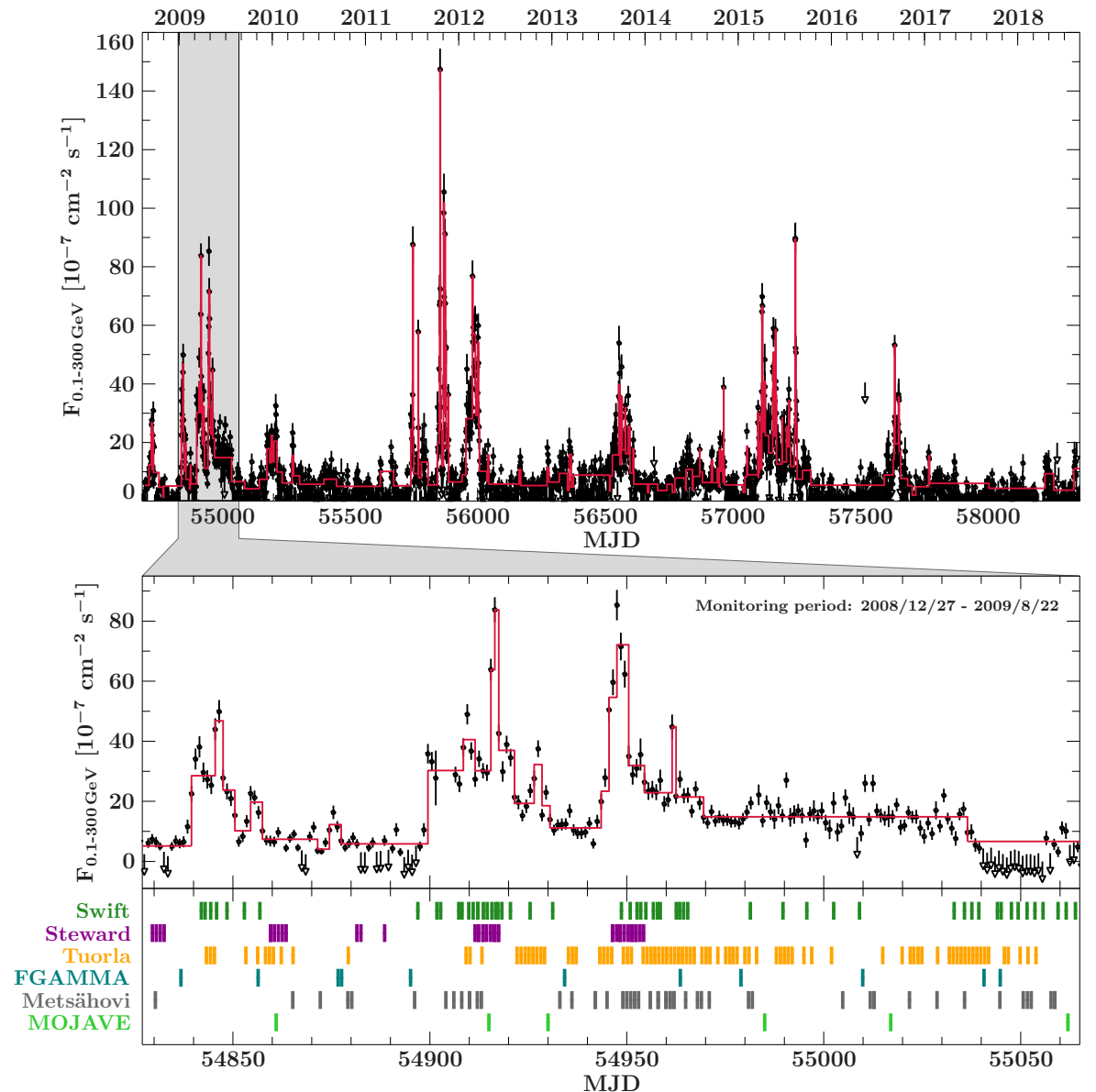


Figure 3.3.: *Upper panel:* Daily-binned γ -ray light curve obtained with *Fermi*/LAT (black), and computed Bayesian blocks (red). *Lower panel – Top:* Zoom into a time range covering ~ 9 months from late 2008 to mid 2009. *Lower panel – Bottom:* Marked times of observations with different radio, optical, and X-ray instruments.

Fig. 3.3 includes a zoom into the active period of PKS 1510–089 in 2009. Several flares can be seen, and are identified with the Bayesian-block algorithm.

For the time range shown here, [Marscher et al. \(2010\)](#) identified eight major γ -ray flaring events, most of them being accompanied by outbursts in the optical regime. In their work, these authors analysed additional VLBI data taken with the VLBA-BU-BLAZAR programme at 43 GHz, and were able to correlate a knot that was propagating downstream the jet, with the strong variability at γ -ray and optical wavelengths, therefore constraining the flares to one single emission region.

The panel below the zoomed-in light curve indicates the times during which an observation was done as part of the respective monitoring programme. The observations with *Swift* and at the Steward Observatory seem to cluster most around the flaring states, while the MOJAVE observations seem to follow a more regular observation schedule. Cross-checking the individual blocks with the available multi-wavelength data during each block reveals a very good coverage that can be used to build stationary, time-resolved SEDs.

The γ -ray flaring period in March 2009 was also observed by the γ -ray satellite AGILE, and these data taken March 9–30 (MJD 54899–54920), were analysed in depth by [D’Ammando et al. \(2011\)](#). The γ -ray spectrum did not reveal drastic spectral changes for this time span, which hints at only one process being responsible for the γ -ray flare. Interestingly, the near-infrared to UV emission increased in brightness at the end of March and revealed a shift of the low-energy peak of the SED. This behaviour could only be discovered due to the density of observations at multiple wavelengths.

3.3.2 TXS 1508+572: a powerful blazar in the early Universe

Among the whole blazar population, sources found at high redshifts ($z > 3$) seem to exhibit the heaviest black holes, some even exceeding a billion solar masses (e.g., [Ghisellini et al., 2010](#), [Belladitta et al., 2022](#)). The circumstances of black holes growing to such extreme masses so soon, in some cases only within several hundred million years after the Big Bang, are not understood yet, which is why ongoing studies and searches for undetected quasars exist. A possible explanation is, e.g., the existence of black hole seeds with more than several hundred solar masses, which were the remnants of the first stars in the Universe (e.g., [Madau & Rees, 2001](#)), or matter collapsing into SMBHs right away (e.g., [Begelman et al., 2006](#)). Furthermore, the first black holes might have been able to accrete matter at a much higher rate than what is observed for SMBHs in the local Universe today (e.g., [Alexander & Natarajan, 2014](#)), in order to explain the discovered *heavyweights*. Additionally, their jets are extremely powerful.

Because of their high redshift, the entire emission from these distant objects is shifted towards lower energies. In case of blazars, this results in the high-energy hump of the SED peaking at MeV γ -rays, an energy range for which we currently do not have a dedicated and sensitive observatory. Because of the position of their high-energy peak, these blazars have been coined *MeV blazars*. Because of a high Compton dominance, MeV blazars are intrinsically bright at γ -ray energies. The increasing attenuation of γ -ray emission due to extragalactic background light, and the peak of the high-energy hump being in the MeV regime, make it difficult to detect high-redshift blazars with current γ -ray observatories. However, detecting unknown high-redshift blazars is also feasible by searching for X-ray emission, which is covering the rising part of the high-energy hump (e.g., [Vito et al., 2018](#)). Future missions, such as *Athena*, will exceed the detection capabilities of current instruments, and open a new window to peak into the early Universe.

The detection of γ -ray emission from high-redshift blazars is difficult with current instruments. Usually, they can only be detected by *Fermi*/LAT or AGILE during longer phases of high activity, or short, very bright flares. On very rare occasions, a flare from a high-redshift

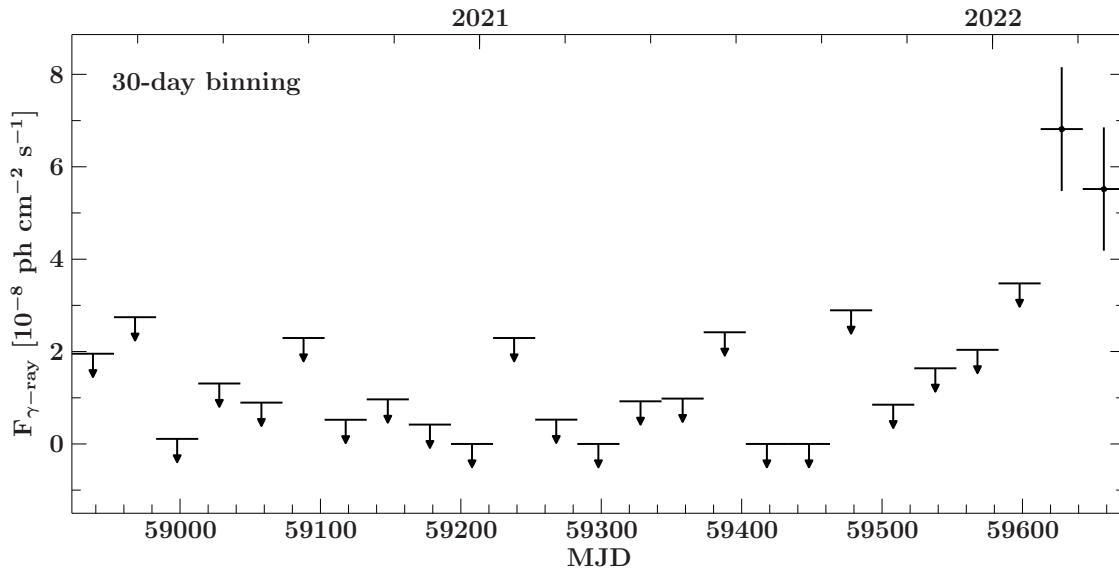


Figure 3.4.: *Fermi*/LAT light curve of TXS 1508+572 with 30-day binning. Upper limits are given for the time periods during which the signal is below a test statistic of 25 ($\sim 5\sigma$).

blazar is detected on daily time scales (Cheung, 2017)²¹. For the compilation of *Fermi*/LAT catalogues, the accumulated data are taken into account, which can result in the detection of new high- z blazars, as well. However, some blazars might only exhibit detectable γ -ray emission on a short time range (e.g., within one or two months), which might not result in a significant detection for the long-term period that is usually considered for the LAT source catalogues.

From August 2008 to April 2019, Kreter et al. (2020a) searched through the data that were obtained by *Fermi*/LAT for γ -ray emission detected on time scales of 30 days. The source sample contained 176 radio and optically detected blazars with a redshift $z \geq 2.5$. We found a γ -ray signal $> 5\sigma$ for four blazars with $z > 3$ that were not reported in previous LAT catalogues (Kreter et al., 2020a).

We used this approach of looking for γ -ray signals on monthly time scales to build a pipeline to look for flaring episodes of high- z blazars in real time, as the previous detections were in the past. We set up a programme to monitor 81 blazars that are listed with $z \geq 3$ in the Roma-BZCAT Multifrequency Catalogue of Blazars²² (Massaro et al., 2009), with the idea of triggering multi-wavelength follow-up observations and gaining a simultaneous data set to study a flaring blazar in the early Universe. So far, two studies of high- z blazars exist that include (quasi-)simultaneous multi-wavelength data: Orienti et al. (2014) modelled the emission from the FSRQ TXS 0536+145 ($z = 2.69$; Sowards-Emmerd et al., 2005), and Liao et al. (2019) studied the blazar CGRaBS J0733+0456 ($z = 3.01$; Healey et al., 2008).

On 2022 February 4, our pipeline reported a detection of the source TXS 1508+572 ($z = 4.31$; Hook et al., 1995), also known as GB 1508+5714 (Gokus et al., 2022). This FSRQ was the first identified radio-loud quasar at a redshift $z > 4$ by Hook et al. (1995), and

²¹Note that there is no official dividing rule that defines when a source is classified as high-redshift. Here, I talk about sources with $z > 3$, albeit, blazars at $z = 1.8$ have also been associated with a high-redshift origin and their flares have been reported as such (e.g., Ciprini, 2009, Orienti & D’Ammand, 2011, Piano et al., 2018)

²²<https://www.ssdsc.asi.it/bzcat/>

detected in the X-rays by the *Einstein Observatory* by Mathur & Elvis (1995) later that year. An observation with *Chandra* revealed extended X-ray emission originating from the jet of the source (Siemiginowska et al., 2003, Yuan et al., 2003). Radio VLBI images confirmed the extended emission (Cheung, 2004). At γ -rays, the source has been reported in the Fourth *Fermi*/LAT source catalog (4FGL; Abdollahi et al., 2020) with the identifier 4FGL J1510.1+5702. More recently, Liao et al. (2020) found mild variability at γ -ray energies, and intraday variability at optical wavelengths in this source, and attempted to model a quasi-simultaneous data set consisting of optical and γ -ray data during an epoch of higher activity displayed by TXS 1508+572 in May/June 2018. However, no X-ray data were considered in the SED. Marcotulli et al. (2020) modelled the SED using data taken at different times and an average γ -ray spectrum. The hard X-ray data obtained with *NuSTAR* revealed an extremely steep rise of the high-energy hump.

The flaring period of TXS 1508+572 in early 2022 provided a unique opportunity to study the outburst of a blazar in the early Universe, and to gain simultaneous data from radio up to γ -rays. The flaring episode lasted over two months (see Fig. 3.4). Immediately after the flare, follow-up observations at radio, optical, and X-ray observations were requested and successfully performed. Furthermore, a monitoring of the radio flux densities was started to search for an expected radio flare in coincidence with the γ -ray flare, and three follow-up VLBI observations will be used to study the jet emission and potential changes in the jet structure at high resolution.

Multi-wavelength study of Mrk 421 during a TeV flare

Twinkle, twinkle quasi-star
Biggest puzzle from afar
How unlike the other ones
Brighter than a billion suns.
Twinkle, twinkle quasi-star
How I wonder what you are.

George Gamow, “*Quasar*” (1964)

Being one of the closest and brightest blazars at VHE γ -rays, the object with the name Markarian 421 (Mrk 421; $\alpha = 11^{\text{h}} 04^{\text{m}} 27.31^{\text{s}}$, $\delta = 38^{\circ} 12' 31.8''$, J2000) is also one of the most well-studied sources. Many observational campaigns have gathered multi-wavelength data spanning decades, which have been used to test our understanding of physical processes in blazars. However, this source is far from being completely understood. In this chapter, I will summarise the work that was carried out and results that were found as part of a multi-wavelength monitoring campaign, which was mainly organised and led by members of the Remeis-Observatory & ECAP (FAU Erlangen–Nürnberg) and the Institute for Astronomy (JMU Würzburg). In Section 4.1, I introduce Mrk 421 and give a concise overview of past studies on this source. Our multi-wavelength monitoring program is described in detail in Sect. 4.2. This work focuses on the TeV flare in June 2019, which is reported in detail in Sect. 4.4. The instruments involved and the method of data extraction is given in Sect. 4.3, while the corresponding multi-wavelength data analysis is explained in Sect. 4.5. Section 4.6 presents the results and interpretation of a detailed timing analysis of the X-ray data obtained with *XMM-Newton*. Final conclusions are given in Sect. 4.7.

4.1 The famous Mrk 421

Mrk 421 belongs to the class of high synchrotron-peaked BL Lac objects (HBLs), i.e., BL Lacs where the peak position of the synchrotron hump ν_{peak} lies beyond 10^{16} Hz. Therefore, the source appears particularly bright at X-rays and TeV γ -rays, as the humps of its spectral energy distribution (SED) peak in these two energy regimes. This blazar has a redshift of $z = 0.031$ (Ulrich et al., 1975), and resides in a very bright elliptical galaxy (Ulrich et al., 1975, Kikuchi & Mikami, 1987). Its central engine is a supermassive black hole with a mass of $1.9 \times 10^8 M_{\odot}$ (Wang et al., 2004). Mrk 421 is the first extragalactic source that has been detected at TeV energies (Punch et al., 1992).

A characteristic of blazars is their variability across the electromagnetic spectrum (see Sect. 1.2.2). Given the proximity of Mrk 421, and the resulting ability to observe the source very well at all wavelengths, the different activity states as well as their transitions have been closely monitored over the past decades. Its shortest variability signatures, which are of sub-hour time scales, have been detected during flaring states at VHE γ -rays (Gaidos et al., 1996, Abeysekara et al., 2020). A large number of multi-wavelength campaigns found a direct correlation between the X-ray and the TeV γ -ray emission during flares (e.g., Macomb et al., 1995, Buckley et al., 1996, Albert et al., 2007, Fossati et al., 2008, Acciari et al., 2011, Cao & Wang, 2013, Bartoli et al., 2016). In a similar manner, a correlation between optical emission and GeV γ -rays has been established in a data set covering the years from 2007 to 2015 (Carnerero et al., 2017). The connection between γ -rays at GeV energies and radio emission remains unclear so far. Only a tentative correlation has been found with a time delay of 40 days at 2.6σ (Max-Moerbeck et al., 2014), as well a correlation with a maximum time delay of 30 days at the 3σ level (Lico et al., 2014). Similar to a trend seen in a few other blazars, Mrk 421 does not show the same behaviour during all of its active phases, or flares. While it is more common that a blazar flare is observed across the full electromagnetic spectrum, a few flares have been visible at TeV γ -rays only (Błażejowski et al., 2005, Fraija et al., 2014). Such events are known as ‘orphan flares’. It is not clear what causes them and which conditions need to be fulfilled in order for one to occur.

As a first unbiased study of Mrk 421, Horan et al. (2009) performed a multi-wavelength campaign to analyse the long-term behaviour, which covered 8 months in 2005–2006. These authors found variability at all wavelengths, but with an increase towards higher energies. A tentative correlation between X-rays and γ -rays was measured during this campaign, but no correlation between other wavebands was apparent.

Another multi-wavelength campaign by Aleksić et al. (2015a) used data from 2009 during a time when Mrk 421 showed ‘typical’ VHE flux levels (~ 0.5 Crab Units/CU¹; Acciari et al., 2014). The observations also revealed variability across all wavelengths, as well as a significant X-ray/ γ -ray correlation with zero time lag during the non-flaring state. The measured power spectral densities (PSDs) could be described by unbroken power laws that showed a red and pink noise behaviour. Based on these data, Aleksić et al. (2015a) used a leptonic model to explain the emission of Mrk 421 during its usual low activity, as the presence of the temporally extended correlation could not have been driven by a single flare, and is, therefore, difficult to explain with a hadronic model.

Baloković et al. (2016) analysed data from a multi-wavelength campaign from January to March 2013, which included *NuSTAR*, and found that the correlation between X-rays and VHE γ -rays persists even at low activity of the source. Their findings included multi-band variability, a low degree of polarisation with significant random variations, and a short electron cooling time in combination with longer variability time scales observed at hard X-rays. Based on these results, they concluded that multiple compact regions are responsible for the observed broadband emission of Mrk 421 in low-activity phases.

Acciari et al. (2021) studied Mrk 421 during its historically low X-ray and γ -ray activity in 2015/2016 with radio, optical/UV, X-ray and γ -ray instruments. Apart from the established correlations and variability patterns, they also made two interesting findings. The first one

¹The VHE emission of the Crab pulsar is used as a standardised flux, the so-called ‘Crab Unit’ (CU).

is an additional spectral component that became visible in the hard X-ray data provided by *Swift*/BAT, which appeared at higher energies and does not fit into the shape of the synchrotron spectrum. The second interesting feature is a fast radio flare at 37 GHz seen with the Metsähovi radio telescope. Since observations around that time suffered from bad weather conditions, it was not possible to see a change in the radio flux.

A multi-wavelength timing analysis was also presented by [Abeysekara et al. \(2017\)](#), for which these authors obtained simultaneous observations with *XMM-Newton* and VERITAS. Their observations were triggered during high VHE γ -ray activity, and led to three data sets containing X-ray and γ -ray data. Creating spectral hysteresis curves, they found that Mrk 421 exhibited the usual ‘harder-when-brighter’ trend during those flares. The computed PSDs from the X-ray light curves, which had a length of ~ 12 – 15 ks, revealed variability on time scales of less than an hour, even changing over the course of ~ 10 minutes during one observation.

Mrk 421 is one of a group of blazars that exhibit unusual behaviour, resulting in the so-called ‘Doppler crisis’. Using VLBA data, [Blasi et al. \(2013\)](#) constrained the viewing angle of Mrk 421 to lie between 2° and 5° . While slightly different jet speeds have been calculated by different authors, all values lie below the highly relativistic regime. [Piner et al. \(1999\)](#) constrained the jet speed to $< 0.3c$ using 15 measurements over 3 years at frequencies between 2.3 GHz and 43 GHz, while in a later work, [Piner et al. \(2010\)](#) found the jet speed to be $0.09c$, when they analysed seven epochs taken over 4 years at 43 GHz. Using 15 GHz monitoring data spanning six years [Kellermann et al. \(2004\)](#) determined an average jet speed of $0.4c$. These speeds are in contrast with the observed short-term variability at very high energies whose production, at least with current models, requires high Doppler factors. A solution to this disagreement has recently been presented by [Hervet et al. \(2019\)](#), in which the knots observed in the radio band might not be the highly accelerated material moving along the jet, but recollimation shocks that accelerate the particles in the jet.

The wealth of data of Mrk 421 summarised above allows us to study and model its broadband SED in detail. So far, leptonic models present more suitable explanations for the observed behaviour (e.g., [Bednarek & Protheroe, 1997](#), [Maraschi et al., 1999](#)), but hadronic models or components cannot entirely be ruled out. Additionally, both one-zone and multi-zone models seem to work well, depending on the data set. [Aleksić et al. \(2015b\)](#) attempted to solve this ambiguity by modelling simultaneous multi-wavelength data sets obtained during 13 days of flaring activity, which provided an average SED for each day, but were not successful. Sometimes, Mrk 421 also exhibits behaviour of extreme HBLs during flares (e.g., [Sahu et al., 2021](#)), i.e., the position of the synchrotron peak shifts to frequencies beyond 10^{17} Hz, which is also not understood.

Currently, the only way to determine hadronic emission with certainty is by the association with one or more neutrino events. To estimate the possibility of observing a neutrino from Mrk 421 with IceCube, [Petropoulou et al. \(2016\)](#) computed the expected high-energy neutrino flux of a 13-day flaring period observed in 2010. While these authors found hints of a correlation between γ -ray emission and PeV neutrinos, they concluded that one flare is not enough to provide a significant signal, because the inferred high-energy neutrino rate needs to be convolved with IceCube’s current observational abilities. Only by accumulating data from similar flares over several years, might it be possible to retrieve the smoking gun evidence for the presence of hadronic components in the jet of Mrk 421 ([Petropoulou et al., 2016](#)).

4.2 Multi-wavelength monitoring program

In this section, which is partly taken verbatim from [Gokus et al. \(2021a\)](#), I will give a concise overview of the multi-wavelength monitoring program for three HBLs.

In order to fully comprehend the emission of blazars, as well as their very variable nature, it would be desirable to obtain long-term uninterrupted data sets that cover the full electromagnetic spectrum. As this is not feasible logistically, we have set up a program to combine a long-term snapshot monitoring of selected blazars with deep Target-of-Opportunity (ToO) quasi-simultaneous multi-wavelength observations during characteristic flaring states. In this program, we make use of the Cherenkov telescope FACT (see Sect. 2.1.2) and the X-ray satellite *Swift* (see Sect. 2.2.4) to monitor the flux of three HBLs, namely Mrk 421, Mrk 501, and 1ES 1959+650, at TeV, with nightly cadence, X-ray and optical/UV energies, with a cadence of four to five days ([Gokus et al., 2021a](#)).

The monitoring data are complemented by ToO observations during a γ -ray flare that is observed with FACT. To gain high-resolution spectral and timing information in the soft X-ray band, as well as a spectrum covering the hard X-ray band, *XMM-Newton* and *INTEGRAL* are triggered, respectively. In addition, *Swift* is triggered to conduct daily snapshot observations outside of the regular monitoring schedule. The trigger is determined by a source-dependent flux threshold at TeV γ -rays. When a flux higher than this threshold is observed by FACT (as determined by the quick-look analysis), a request for a ToO observation is sent to the other observatories. Observations are ideally performed as soon as possible, which is possible within 24 hours for *Swift* and *XMM-Newton*, and within a few days for *INTEGRAL*. In the beginning of our monitoring program, a trigger threshold of 3 CU was chosen, which was estimated to represent an exceptionally bright flare. The choice of this value was affected by the previous activity of Mrk 421. However, over the years, the activity of Mrk 421 decreased slightly, and we decided to reassess and reduce the trigger threshold to 2 CU in 2018.

However, the ability of joint observations with such a large amount of instruments is constrained logistically by the different visibility periods of some of the instruments. The TeV monitoring is affected by moon-lit nights and the visibility of the sources during the night, which creates gaps in their otherwise continuous light curves. The visibility for *INTEGRAL*, *XMM-Newton*, and *Swift* is also constrained by the position of target sources with respect to the sun. In addition, the elliptical orbits by *XMM-Newton* and *INTEGRAL* allow long, uninterrupted exposures, but constrain the visibility further. The visibility of the three target sources is shortest for the *XMM-Newton* spacecraft. Therefore, *Swift* monitors the source intermittently during the periods when they are not visible to FACT or *INTEGRAL*². The reason for this is a practical one: the *Swift* pointings are part of the proposal to the *INTEGRAL* team, and the combination of both instruments covers the full X-ray range. This strategy allows more opportunities and flexibility to obtain broadband data during a flare, as they can happen at any time³.

²To express it in numbers: the average visibility is ~ 32 weeks for 1ES1959+650, ~ 32 weeks for Mrk 501, but split into two time ranges, and ~ 18 weeks for Mrk 421, also split into two periods.

³Fun fact: Biased by our visibility constraints, Mrk 421 seems to favour christian holidays: FACT observed flares on Christmas 2017 ([Biland & FACT Collaboration, 2017](#)), Easter 2019 ([Biland & FACT Collaboration, 2019](#)), and Pentecost 2019 ([Gokus et al., 2021a](#), and Sect. 4.4).

The combined observations of these instruments enable a rapid detection of a flare at high energies, and make deep observations possible during and after the flare. The monitoring gives detailed information on the behaviour of a source before it begins exhibiting high activity. Since the instruments of our monitoring program cover most of the broadband spectrum, it is possible to create several SEDs to depict the spectral changes with simultaneous data. The program has been run since 2012, and a more detailed description, as well as first results from a moderately bright flare of Mrk 421, are presented by [Kreikenbohm \(2019\)](#).

4.3 Multi-wavelength observations & data processing

In this section I describe the methods of data extraction for the instruments involved in the multi-wavelength campaign, including FACT (Sect. 4.3.1), *Fermi*/LAT (Sect. 4.3.2), *INTEGRAL* (Sect. 4.3.3), *XMM-Newton* (Sect. 4.3.4), *Swift* (Sect. 4.3.5), and the Effelsberg radio telescope (Sect. 4.3.6).

4.3.1 FACT

Due to its nightly observations of Mrk 421, FACT is able to provide densely sampled flux information at TeV energies for the times in which the source is visible from La Palma. In this thesis, I use a preliminary light curve, which covers the first half of 2019 from January 2 – June 27. The light curve extraction was performed and provided by the FACT team.

4.3.2 *Fermi*/LAT

The γ -ray data (Pass 8) from the LAT on-board *Fermi* were analysed using the `ScienceTools 1.2.23`, `fermipy version 0.20.0`, and instrument response functions `P8R3_SOURCE_V2`. I extracted all events (photons) with an energy between 100 MeV and 300 GeV in a region of interest (ROI) with a diameter of 10° around the position of Mrk 421. I require the events to be suitable for an analysis and therefore include only those which fulfill `DATA_QUAL > 0` and `LAT_CONFIG == 1`. I further selected only events from the LAT event class = 128 and event type = 3. In order to exclude γ -ray signals that are produced via Earth-limb effects, I only consider events that reach the LAT with a zenith angle $\leq 90^\circ$. To fully describe the ROI, I include all sources from the 4FGL within a circle of 15° in diameter around the source position of Mrk 421, as well as using the Galactic diffusion model `gll_iem_v07` and the isotropic diffusion emission model `iso_P8R3_SOURCE_V2_v1` to model the diffuse γ -ray background. The data are modelled via a Maximum Likelihood analysis following [Mattox et al. \(1996\)](#). As described previously in Sect. 2.1.3, the significance of each γ -ray signal is determined with the test statistic, which is defined as $TS = 2\Delta\log(\mathcal{L})$. To translate the TS values into a significance of σ , the relation $\sigma = \sqrt{TS}$ is a good approximation. The likelihood \mathcal{L} expresses the difference between two models: one with and one without the source included in the model at certain coordinates. After a first initial fit, I exclude all sources from the model that show a TS value of lower than 1. For the remaining sources in our model, I keep the following parameters free for the likelihood fit: both the normalisation and the spectral parameters

for Mrk 421 as well as for sources within 3° of Mrk 421, and the normalisation for sources within 5° of the center of the ROI and all sources that have a very strong signal (exceeding a significance of $TS = 500$ or $\sigma = 22$). I also leave the diffusion models free to vary. The time range that is taken into account in this work is from 2019 January 1 (MJD 58484) to 2019 June 27 (MJD 58661) inclusive. After finding our best-fit model, I compute light curves with 3-day and daily binning, which are shown in Fig. 4.3 and 4.5, respectively. During the computation of each light curve bin, I only keep the source parameters of Mrk 421 free, as well as the normalisation for sources within 3° and those with a significance $TS > 500$. In the case that the detection significance of Mrk 421 is below a value of $TS = 4$ or 2σ , the corresponding 2σ upper limit is shown in the light curve.

4.3.3 INTEGRAL

We obtained hard X-ray band information from 15 keV to 10 MeV with the ISGRI detector of the IBIS instrument on-board *INTEGRAL*. Our triggered observation began on 2019 June 11 at 11:10 UTC, and ended on June 13 at 11:04 UTC, and provided a total of 160 ks exposure time. We create a light curve with ~ 55 min binning, and three spectra for the time ranges June 11 11:10 – June 12 00:34 UTC, June 12 00:37–14:51 UTC, and June 12 14:53 – June 13 11:04 UTC. The *INTEGRAL* light curve and spectra were provided by Ingo Kreykenbohm and Philipp Thalhammer (both Remeis-Observatory & ECAP, FAU Erlangen-Nürnberg).

4.3.4 XMM-Newton

Our triggered *XMM-Newton* observation (ObsID: 0845000901) started on 2019 June 10 at 18:54 UTC, and ended on June 11 at 20:27 UTC, providing us nominally with 92 ks of exposure time. This observation provided highly resolved timing and spectral information during the brightest flare of Mrk 421 that *XMM-Newton* has observed to date. While a high X-ray flux had been expected during this follow-up observation of a γ -ray flare, *XMM-Newton* registered a large increase in brightness during the observation, which made it necessary to switch from *Timing* to *Burst* mode. Because the observation initially started in *Burst* mode as well, two gaps exist in the light curve with a length of 3.4 ks and 3 ks, respectively.

I reduced the data with the *XMM-Newton* Science Analysis System (SAS; version 18.0.0) by following the standard methods and making use of the XMM data pipeline maintained at the Remeis-observatory. The two data sets in *Burst* mode and the data set in *Timing* mode had to be extracted separately. For the source region, I chose the columns as $20 \leq RAWX \leq 60$ for the *Burst* mode, and $20 \leq RAWX \leq 56$ for the *Timing* mode. Because there was pile-up present in the *Timing* mode data, the five inner columns on the chip ($RAWX = 36-40$) were excluded. The background regions were chosen at $2 \leq RAWX \leq 10$ for the *Burst* mode, and $2 \leq RAWX \leq 13$ for the *Timing* mode. For the data taken in *Burst* mode, an additional cut was used to only consider events that fulfilled $RAWY \leq 140$, in order to avoid pile-up that can occur during the readout (Kirsch et al., 2006). I extracted light curves with 100 s-binning for each of the light curve ‘chunks’ in the full energy band (0.3–10 keV, see Fig. 4.1) and several sub bands (0.3–2 keV and 2–10 keV; 0.3–1 keV, 1–4 keV, and 4–10 keV). Furthermore, I split the full observation into spectra with corresponding exposure time of 2 ks in order to derive

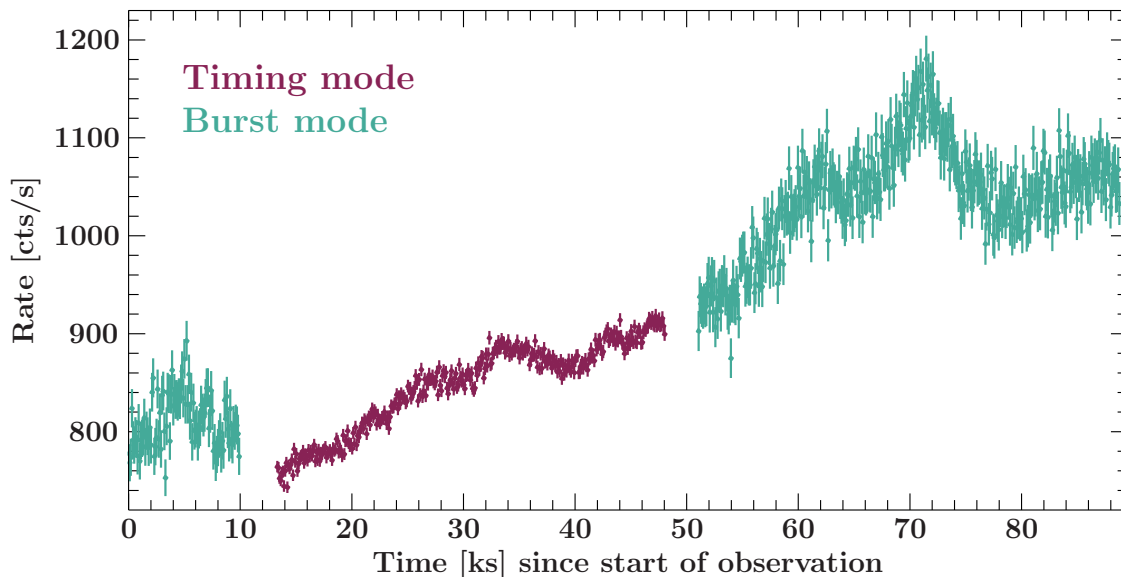


Figure 4.1.: *XMM-Newton* light curve with 100s-binning of the triggered Mrk 421 observation, adapted from Gokus et al. (2021a). The light curve shows the count rates in the energy range 0.3–10 keV. The parts of the light curve that have been observed in either *Timing* or *Burst* mode are indicated in blue and red, respectively.

time resolved spectral information over the duration of the observation. I model all spectra with an absorbed power law using `tbabs` (Wilms et al., 2000), and keep the absorption fixed to the Galactic absorption of $1.3 \times 10^{20} \text{ cm}^{-2}$ (HI4PI Collaboration, et al., 2016). For the spectral modelling, I use the cross-sections and abundances from Verner et al. (1996), and Wilms et al. (2000), respectively. The results of the X-ray spectral fits, which are used for the hysteresis curve, are listed in Table A.1 in the Appendix. An alternative model that has also been found to describe the X-ray spectrum of Mrk 421 well, is an absorbed log-parabolic model (e.g., Sinha et al., 2015, Kreikenbohm, 2019). However, the energy band studied here is too narrow to reliably constrain the curvature, and I chose the simpler power-law model to avoid a strong correlation between the photon index and the spectral curvature of the parabola.

4.3.5 *Swift*: XRT & UVOT

In this work, I include all observations that *Swift* performed between 2019 January 1 and June 27, which totals 71 pointings. While each of the pointings yields an X-ray spectrum, a large fraction of these observations contain simultaneous UV observations in one or more of the UVW1, UVW2, or UVM2 band-passes. All *Swift* data were processed using the standard methods in the software package `HEASoft` (version 6.29). Data from the XRT were filtered, calibrated, and cleaned using the `xrtpipeline` with standard filter criteria and the calibration database (Version 20200724). Mrk 421 was observed in the WT mode of the XRT due to its high X-ray flux. In order to determine the X-ray flux, I model the spectrum of each observation with an absorbed power law, and keep the absorption value fixed to the Galactic value of $1.3 \times 10^{20} \text{ cm}^{-2}$ (HI4PI Collaboration, et al., 2016), in the same manner as for the

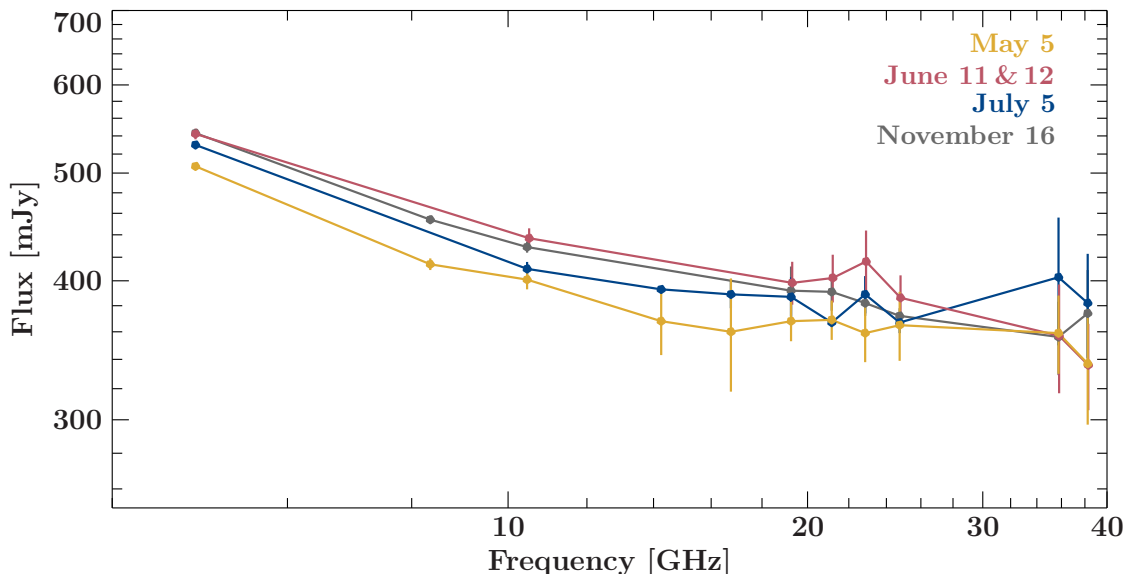


Figure 4.2.: Radio spectra of Mrk 421, obtained before, during, and after its multi-wavelength flare in June 2019. Credit: [Gokus et al. \(2021a\)](#)

XMM-Newton spectra. The fit results are given in Table A.2 in the Appendix, and the fluxes are included in the light curves in Fig. 4.3 and 4.5.

UVOT data were used to obtain photometry information for all pointings with an observation in at least one of the three UV band-passes. The central wavelengths of the UVW1, UVW2, and UVM2 bands are 260 nm, 193 nm, and 220 nm, respectively. I use the standard routines `uvotimage` and `uvotpha` to extract source counts within a $8''$ circular region at the position of Mrk 421, and background counts in an annulus with inner and outer radius of $10''$ and $35''$, respectively. In total, we could obtain UV fluxes in at least one UV band (mainly UVW1) for 51 pointings. All fluxes were dereddened and corrected for Galactic extinction with the $E(B - V)$ relation, following [Fitzpatrick \(1999\)](#), and converted from magnitudes into fluxes via unfolding within the *Interactive Spectral Interpretation System* (ISIS; [Houck & Denicola, 2000](#)).

4.3.6 Effelsberg

We observed Mrk 421 with the 100 m-dish radio telescope in Effelsberg in several observing sessions in May, June, July and November 2019. Using the second receiver of the telescope, the source was observed at a broad range of frequencies in the cm waveband via several cross scans in azimuth and elevation direction, including correcting for pointing offsets. To determine the fluxes, we averaged over individual subscans, corrected for the opacity of the atmosphere and gain-elevation effects, and calibrated the measured fluxes by using 3C 286, and NGC 7027 as calibrator sources. A detailed description of the data extraction can be found in [Heßdörfer \(2021, Sect. 3.3\)](#). The resulting fluxes for each observation and in each frequency band are listed in Table 4.1.

The radio spectra before, during, and after the multi-wavelength flare of Mrk 421 are shown in Fig. 4.2. Apart from a slight flattening of the spectrum taken on 2019 July 5, which was

Table 4.1.: Radio fluxes for Mrk 421 during 4 epochs observed with the Effelsberg radio telescope in 2019. Only statistical errors are given.

Frequency [GHz]	May 5	Jun 11/12	Jul 5	Nov16
	Flux [mJy]			
4.85	507 ± 3	542 ± 6	530 ± 1	543 ± 1
8.35	414 ± 5	-	-	454 ± 4
10.45	401 ± 8	437 ± 9	410 ± 6	429 ± 5
14.25	368 ± 25	-	393 ± 1	-
16.75	360 ± 42	-	389 ± 11	-
19.25	368 ± 15	398 ± 17	387 ± 16	392 ± 20
21.15	369 ± 15	402 ± 20	367 ± 3	391 ± 15
22.85	359 ± 21	416 ± 28	389 ± 15	382 ± 10
24.75	365 ± 26	386 ± 18	367 ± 8	372 ± 6
35.75	359 ± 29	357 ± 40	403 ± 53	356 ± 27
38.25	337 ± 40	336 ± 30	382 ± 41	374 ± 35

one month after the flare, there are no significant changes within the radio spectra. While the observations on 2019 June 11/12 seem to exhibit the highest flux across all frequencies, the change with respect to the other observations is small. Similar variations have been observed for Mrk 421, e.g., in the TELAMON programme (Kadler et al., 2021). As no change is visible in the observation five months after the γ -ray and X-ray flare, we conclude that the event did not trigger a major change within the parsec-scale radio jet.

4.4 Outburst in June 2019

As expected due to its variability, Mrk 421 showed several flares over the years of our monitoring program. However, follow-up observations were not feasible during a lot of these opportunities, due to a lack of visibility with either *INTEGRAL*, *XMM-Newton*, or both. In the beginning of 2019, Mrk 421 showed a prolonged phase of high activity at TeV energies, during which the flux increased above 3 CU on several nights (Biland & FACT Collaboration, 2019, Garcia-Gonzalez & Martinez, 2019). This flaring period is visible in the long-term light curve in Fig. 4.3 from MJD 58570 – 58590. We succeeded in triggering a denser follow-up with *Swift*, and the data we obtained with XRT revealed coincident high activity in X-rays, while the emission observed with UVOT in the UV bands exhibited a longer-term increase with a delay of several days after the high γ -ray activity. Unfortunately, there was no visibility available with *XMM-Newton*. In addition, *INTEGRAL* was not available for a ToO observation as it was taking part in the search for a counterpart to a gravitational wave event during that time.

About two months after that active phase, FACT registered another spike at TeV energies in June. On June 9, Mrk 421 exhibited a flux exceeding 2 CU at VHE γ -rays, upon which we sent ToO triggers to *INTEGRAL*, *XMM-Newton*, and *Swift* at 22:30 UTC (Gokus et al., 2021a). In addition, we asked for follow-up observations of the source with the Effelsberg

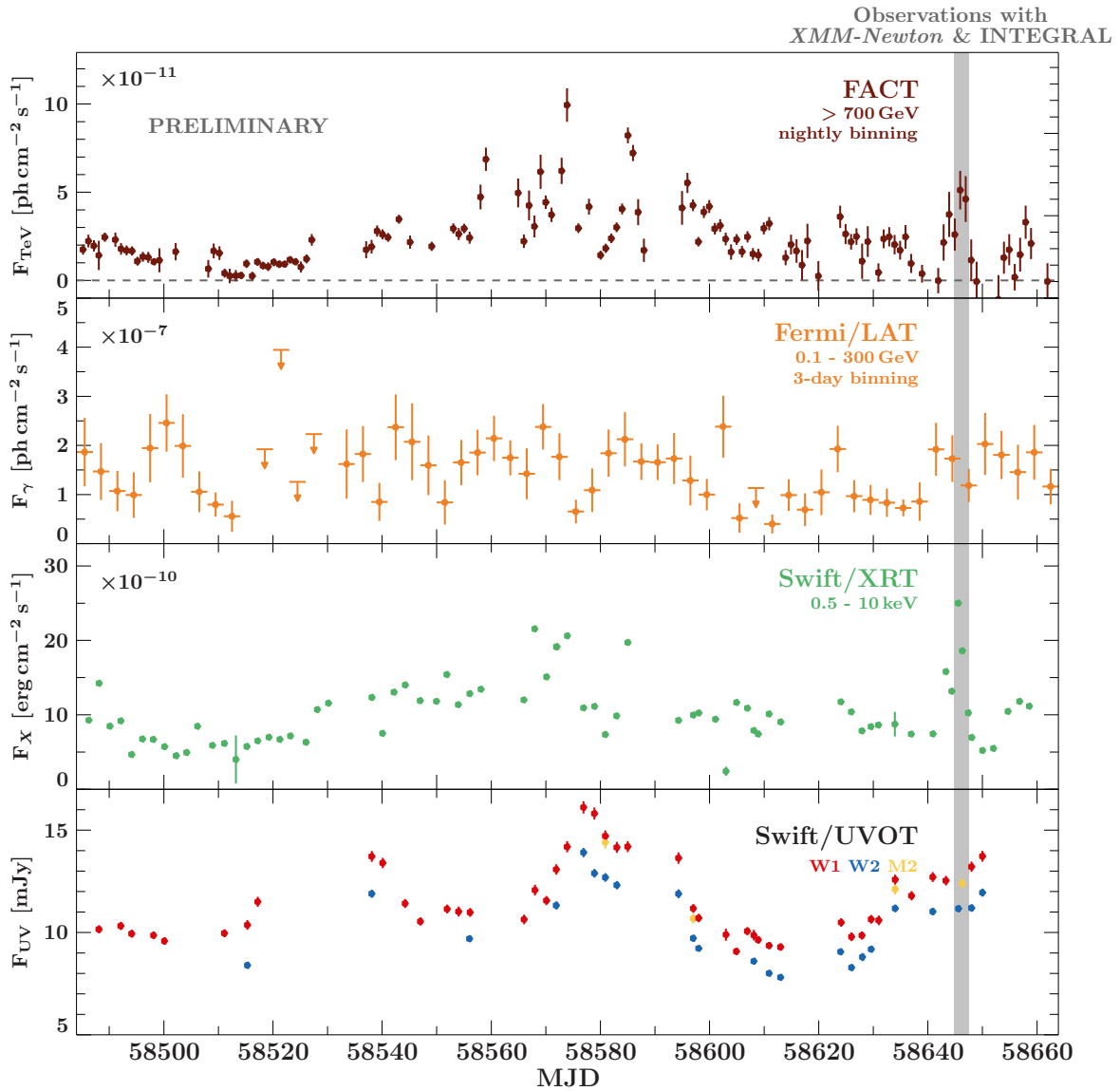


Figure 4.3.: Light curves of Mrk 421, showing the time range from 2019 January 1 to 2019 June 29 in multiple energy bands. The time range of simultaneous observations with *XMM-Newton* and *INTEGRAL* as follow-up of the flare in June is shaded in grey.

radio telescope, in order to assess the current radio flux as well. An overview of the multi-wavelength observations following the flare is shown in Fig. 4.4. In this schematic illustration the different reaction times for the satellites become apparent. Both the *Swift* and the *XMM-Newton* spacecraft began observing Mrk 421 within 24 hours. *INTEGRAL* was able to start its observation within 48 hours. During that time of year, the visibility of Mrk 421 was already quite low for FACT, and the observation time with FACT before the flare was 40 min in the regular scheduling. After the flare was detected, the observation time of Mrk 421 was extended to its maximum possible length in order to be able to construct γ -ray spectra (~ 2.3 hours).

Figure 4.5 shows the zoomed-in version of the multi-wavelength light curve with additional data from the ToO observation with *XMM-Newton* and *INTEGRAL*. During the follow-up observations, the VHE γ -ray flux again increased substantially two days after the trigger

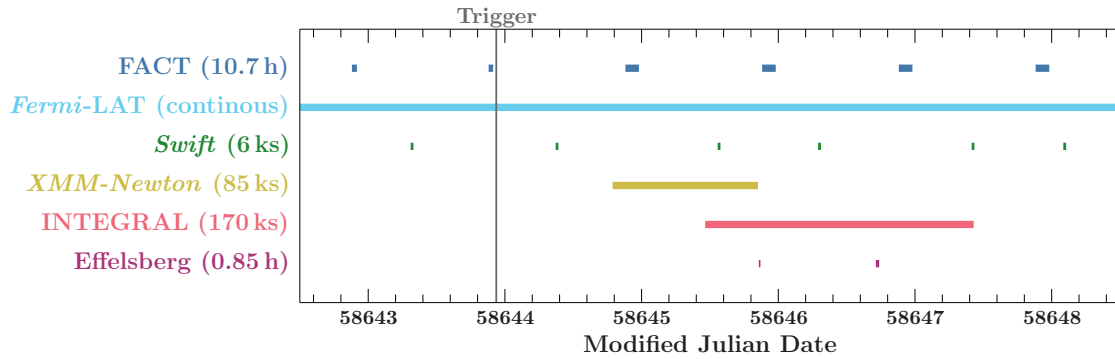


Figure 4.4.: Time-resolved overview of all follow-up observations related to the flare of Mrk 421 in June 2019. The time range in this sketch is from June 8 until June 14. The trigger time is shown with the vertical grey line. All observations are shown in true relation to their observation and exposure times. The accumulated exposure/observation times on the left only account for the time range depicted in this plot. Credit: [Gokus et al. \(2021a\)](#)

to an even higher flux, which accompanied a significant increase in the X-ray band. The *XMM-Newton* observation coincided with this fast flux increase in the X-rays and filled the gap between two *Swift* snapshots. The *INTEGRAL* observation started during the *XMM-Newton* observation around the time when Mrk 421 reached its maximum X-ray flux. The binning of the light curve equals the time ranges of each ‘Science Window’ (~ 55 min), which are individual pointings of *INTEGRAL* while it performs a dithering around the source coordinates. Bins with a detection significance of Mrk 421 below 5σ are shown as upper limits. While the source is significantly detected in the science windows obtained at the beginning, the detection significance decreases over time. In the second half of the light curve, individual bins lie above the 5σ , which could hint at variability on time scales of roughly one hour. However, because *INTEGRAL* dithers around the target coordinates, the distance between those and the pointing coordinates changes for each bin. A comparison of the angular separation between the source and pointing coordinates reveals that the last significant bin in the light curve coincides with *INTEGRAL* pointing close to the coordinates of Mrk 421. However, no similar overlapping of a high detection significance with a small off-axis angle is found for the other bins in the second half of the light curve. Hence, it is possible that short-time variability in the hard X-ray band was present during the flare. The *Swift*/XRT observations indicate that the X-ray flux decreased slowly over the following three to four days. However, these observations are just snapshots, which are not able to reveal possible variability that may have occurred between each pointing. Another short flaring period in the X-rays cannot be ruled out. In contrast, the γ -rays observed with *Fermi*/LAT show no prominent increase, or decrease, over this time period. At UV energies, a long-term increase started about one month prior to the high activity event (see Fig. 4.3). Afterwards, the flux in the W1 band increased further, while the W2 emission decreased, indicating a spectral change in the UV band.

4.5 Multi-wavelength analysis

Given the extensive multi-wavelength data set, I performed an analysis with regard to the variability of Mrk 421 (Sect. 4.5.1), and studied how the low-energy hump of the broadband

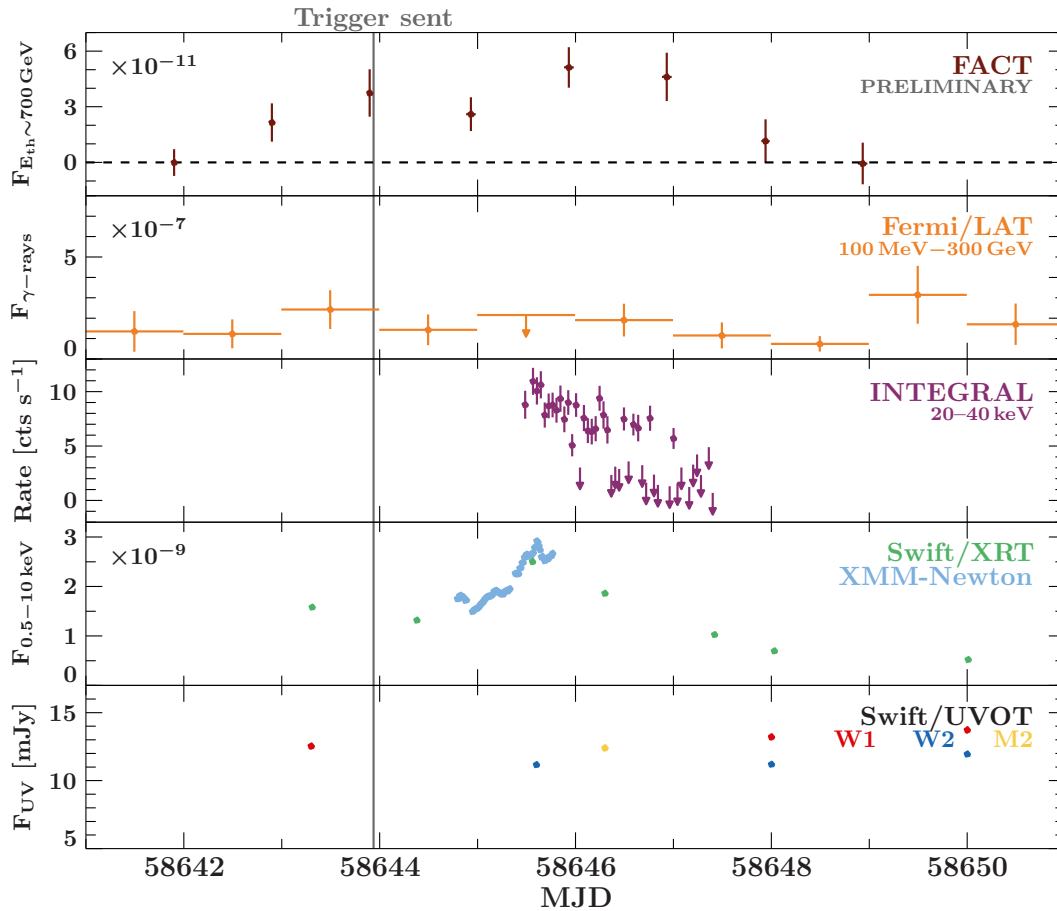


Figure 4.5.: Multi-wavelength light curves zoomed into the flaring time range in June 2019. The FACT and *Swift* flux values are plotted within one bin per pointed observation. The *Fermi*/LAT light curve is shown with a daily binning. The *INTEGRAL* light curve contains bins of ~ 55 minutes, with upper limits for bins with $< 5\sigma$. The binning of the *XMM-Newton* observation is 1 ks.

SED evolved during the flaring activity (Sect. 4.5.2). Due to the long observation with *XMM-Newton*, I was also able to conduct a high-resolution X-ray timing analysis (Sect. 4.6).

4.5.1 Variability analysis

The X-ray and TeV flux of Mrk 421 can change quite dramatically on short time scales (< 1 day), as can be seen in the light curves in Fig. 4.3. Changes in the UV band are clearly visible as well, but they seem happen on longer time scales. The MeV–GeV γ -ray flux does not seem to follow any long-term trend, but it might appear this way due to the relatively short time of half a year in this work. Light curves including longer time ranges also show long-term variability in the GeV γ -ray band (see, e.g., Kreikenbohm, 2019). To quantify and compare the variability in each energy band, I use the fractional variability amplitude F_{var} (Vaughan et al., 2003), which is defined as

$$F_{\text{var}} = \sqrt{\frac{S^2 - \sigma_{\text{err}}^2}{\bar{x}^2}}. \quad (4.1)$$

The numerator is the definition of the so-called ‘excess variance’ (Nandra et al., 1997, Edelson et al., 2002), which can be determined by subtracting the contribution of expected measurement uncertainties $\overline{\sigma_{\text{err}}^2}$ from the general variance S^2 . The denominator is the mean of all flux values in the light curve, and is used to normalise the variability amplitude to represent it percentage-wise. The uncertainty of the fractional variability amplitude is given by

$$\text{err}(F_{\text{var}}) = \sqrt{\left(\sqrt{\frac{1}{2N}} \frac{\overline{\sigma_{\text{err}}^2}}{\bar{x}^2 F_{\text{var}}}\right)^2 + \left(\sqrt{\frac{\overline{\sigma_{\text{err}}^2}}{N}} \frac{1}{\bar{x}}\right)^2}, \quad (4.2)$$

where N is the number of the measurements that are taken into account when computing F_{var} . It should be noted that the binning of a light curve has an influence on this quantity. The FACT light curve has continuous, nightly observations except for the times around full moon, but can be considered nearly complete for the six months investigated in this work. For the data obtained with instruments on-board *Swift* the binning depends on the monitoring cadence, which varies between daily and weekly observations. Hence, the variability could be underestimated. For the LAT data, I can choose the binning due to the constant monitoring with the *Fermi* satellite. In this work, I have chosen a three-day binning, as this yields a good amount of light curve bins with a significant detection ($\text{TS} > 25$, or $> 5\sigma$), while maximising the time resolution. I compute the fractional variability amplitude for both a daily-binned and the three-day binned LAT light curve to determine whether a significant difference exists. I find that $F_{\text{var}} = 0.19 \pm 0.05$ for the three-day binning (also listed in Table 4.2), and $F_{\text{var}} = 0.16 \pm 0.05$ for the daily binning. Since both values agree within their uncertainties, I continue with the analysis of the three-day binned light curve.

All resulting F_{var} values are listed in Table 4.2, and plotted in Fig. 4.6 for a direct comparison of all energy bands covered in this study.

It is clear that the variability appears to be strongest at TeV γ -rays, followed by a moderately high value in the X-ray band as captured by *Swift*, while the GeV γ -rays and the UV flux seems to exhibit a moderate to low variability. These findings are similar to previous studies. Ahnen et al. (2016) studied the multi-wavelength data from 2007 to 2009, and found a F_{var} slightly below 0.7 for the TeV energy range, and $F_{\text{var}} \sim 0.5$ for the soft X-ray regime. In a study of the multi-wavelength data of Mrk 421 during historically low activity from 2015–2016, Acciari et al. (2021) determined $F_{\text{var}} \sim 0.68$ at VHE γ -rays with the FACT data, and $F_{\text{var}} \sim 0.42$ and 0.68 for the X-rays in the 0.3–2 keV and 2–10 keV band, respectively. F_{var} of the GeV γ -ray band was ~ 0.25 , while the UV band yielded ~ 0.2 . Kreikenbohm (2019) studied multi-wavelength light curves that covered the time from December 2015 until May 2017. She found slightly elevated fractional variability amplitudes across the analysed wavebands compared to the values presented here. For the TeV energy range, she determined a very high fractional variability amplitude of ~ 0.98 . The full X-ray band (0.5–10 keV) exhibited $F_{\text{var}} \sim 0.6$, while a strong energy dependence was also found, with $F_{\text{var}} \sim 0.5$ for the 0.5–2 keV band, and $F_{\text{var}} \sim 0.75$ for the 2–10 keV band. At GeV γ -rays, $F_{\text{var}} \sim 0.28$, while for the UV W1 band she found $F_{\text{var}} \sim 0.55$, which is significantly higher than what is found in this work.

F_{var} is heavily biased by the chosen time range and binning, as can be seen by comparing F_{var} for *Swift* and *XMM-Newton*. The *Swift* data cover 6 months and are able to reveal large amplitude changes that can happen within a few days. The *XMM-Newton* light curve covers

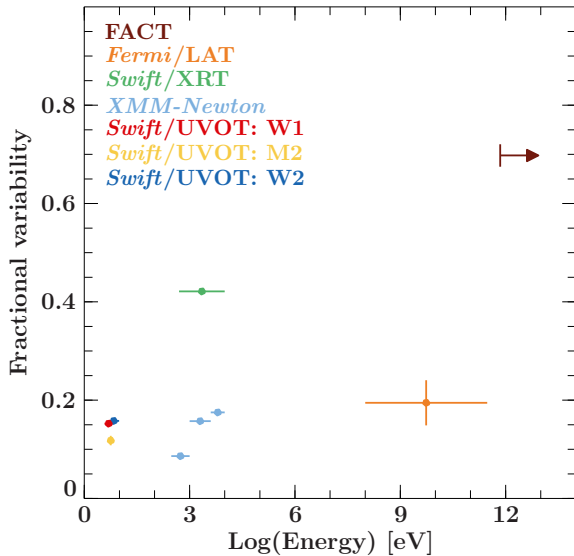


Figure 4.6.: Fractional variability in different energy bands. The data from FACT, *Fermi*, and *Swift* cover the first half of 2019, while the *XMM-Newton* data only applies to the ToO observation during the flaring state in June 2019. Because FACT detects γ -rays above a certain threshold (700 GeV) without a strict limitation towards higher energies, the F_{var} value is shown as a rightward-pointing arrow. Note that the uncertainties of the F_{var} results in the UV and X-ray range are too small to be visible in this plot.

~ 90 ks, and has a binning of 100 s. It can reveal short time variability during a fixed amount of time, in this case during a γ -ray flare. However, the overall flux changes during the flare are not as extreme as in the long-term light curve, which is why F_{var} seems to appear much lower for the *XMM-Newton* light curve. With the *XMM-Newton* light curve split into three energy bands, the energy dependence of the variability is quite significant, and is further investigated in Sect. 4.6. Comparing our results to those of [Abeysekara et al. \(2017\)](#), who obtained three observations with *XMM-Newton* in a multi-wavelength campaign with VERITAS, this significant energy dependence appears in two out of three of their observations, too. However, the fractional variability amplitude for each observation and in each bands does not exceed 0.08, which is significantly smaller than the values for F_{var} obtained with our observation. One reason for this difference could be that the length of each of their *XMM-Newton* observations was between 13 and 15 ks, while our observation is six times longer. Another distinction between these observations is that I am analysing a light curve that was obtained during a very bright X-ray flare. The count rate in the *XMM-Newton* light curve (see Fig. 4.1) reaches 1200 counts s^{-1} , while the count rates in the *XMM-Newton* light curves by [Abeysekara et al. \(2017\)](#) vary between 260 and 460 counts s^{-1} .

4.5.2 Low-energy SED evolution

The densely sampled multi-wavelength light curves allow a dedicated study of the evolution of a blazar SED during a flare. As the γ -ray spectra for the VHE regime had not yet been available at the time of writing, I concentrate on the low-energy hump of the SED of Mrk 421. In order to construct the low-energy part of the SED, I combine the *Swift*/XRT and UVOT data, and *INTEGRAL* data when available, to cover the hard X-ray band. The model used for fitting the data using χ^2 -statistics is the empirical model *logpar*,

$$F(E) = K \cdot \left(\frac{E}{E_{\text{pivot}}} \right)^{-(\alpha + \beta \log(E/E_{\text{pivot}}))}, \quad (4.3)$$

which describes a logarithmic parabola with photon index α at E_{pivot} , curvature β , and a normalisation factor K . As an empirical model *logpar* does not include any physical parameters,

Table 4.2.: Fractional variability amplitudes (F_{var}) for the UV, X-ray, and γ -ray bands. For a comparison, they are plotted together in Fig 4.6. Remarks: $^\dagger F_{\text{var}}$ of *XMM-Newton* is determined for the duration of the *XMM-Newton* observation, and therefore not directly comparable to F_{var} determined for the other light curves.

Instrument	Energy range	Fractional variability
FACT	> 700 GeV	0.698 ± 0.023
<i>Fermi</i> /LAT	0.1 - 300 GeV	0.19 ± 0.05
<i>Swift</i> /XRT	0.5 - 10 keV	0.421 ± 0.003
<i>XMM-Newton</i> [†]	0.3 - 1 keV	0.086 ± 0.001
	1 - 4 keV	0.157 ± 0.001
	4 - 10 keV	0.175 ± 0.003
	0.3 - 10 keV	0.119 ± 0.001
<i>Swift</i> /UVOT	3.7 eV (W1)	0.152 ± 0.003
	4.5 eV (M2)	0.12 ± 0.01
	4.9 eV (W2)	0.158 ± 0.003

Table 4.3.: Results of fitting the multi-wavelength data of Mrk 421 in each time span with a logpar model. The corresponding plots are shown in Fig. 4.7

Date	MJD	α	β	ν_{peak} [10^{17} Hz]	$\nu F(\nu)_{\text{peak}}$ [10^{-10} erg cm^{-2} s^{-1}]	Fit statistic $\chi^2/\text{d.o.f.}$	
S1	2019-6-02	58636.9	2.01 ± 0.02	0.09 ± 0.01	1.98 ± 0.47	2.61 ± 0.04	359.76/27
S2	2019-6-06	58640.9	2.10 ± 0.02	0.12 ± 0.01	0.94 ± 0.15	2.96 ± 0.06	75.46/31
S3	2019-6-09	58643.3	1.86 ± 0.01	0.07 ± 0.01	24.59 ± 4.73	5.70 ± 0.15	677.96/58
S4	2019-6-10	58644.4	1.97 ± 0.01	0.10 ± 0.01	3.47 ± 0.49	4.50 ± 0.05	124.73/49
S5	2019-6-11	58645.6	1.8748 ± 0.0016	$0.0623_{-0.0022}^{+0.0023}$	24.5 ± 0.8	6.09 ± 0.02	1466.32/538
S6	2019-6-12	58646.3	1.91 ± 0.01	0.11 ± 0.00	6.21 ± 0.47	5.72 ± 0.06	1051.91/71
S7	2019-6-13	58647.4	2.04 ± 0.01	0.11 ± 0.01	1.66 ± 0.17	3.61 ± 0.04	296.13/45
S8	2019-6-14	58648.0	2.15 ± 0.02	0.14 ± 0.01	0.70 ± 0.12	3.08 ± 0.09	30.74/21
S9	2019-6-16	58650.0	2.22 ± 0.02	0.15 ± 0.01	0.42 ± 0.07	2.61 ± 0.10	33.43/23

but it has been shown to describe the data reasonably well, and can be used to estimate the properties of the synchrotron peak (e.g., [Massaro et al., 2004](#), [Krauß et al., 2016](#)). After obtaining the best-fit model parameters, it is straightforward to determine the position, i.e., frequency, at the peak of the hump via

$$\nu_{\text{peak}} = \frac{E_{\text{peak}}}{h} = \frac{E_{\text{pivot}}}{h} 10^{(2-\alpha)/2\beta}, \quad (4.4)$$

with h being the Planck constant, and the flux at the peak of the hump at $\nu = \nu_{\text{peak}}$ via

$$\nu F(\nu)_{\text{peak}} = 1.60 \cdot 10^{-9} \cdot K E_{\text{pivot}}^2 10^{(2-\alpha)^2/4\beta} \text{ erg cm}^{-2} \text{ s}^{-1}. \quad (4.5)$$

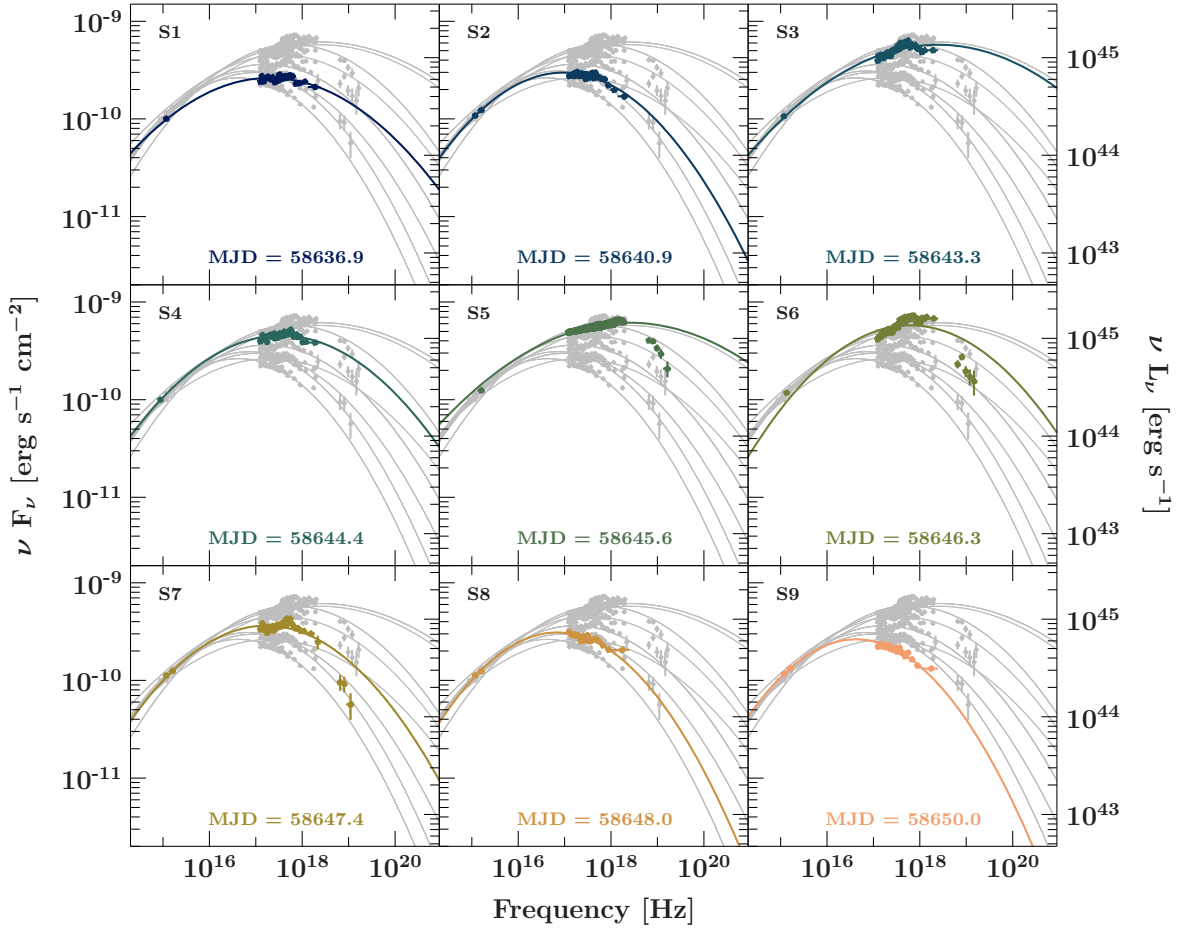


Figure 4.7.: Evolution of the low-energy hump of the SED of Mrk 421 during the flare in June 2019, covering the time range from MJD 58636.9-58650. At MJD 58645.6, the *XMM-Newton* EPIC/pn spectrum taken in Timing mode was used, since the *Swift*/XRT spectrum exhibited ‘wiggly’ features, which are also present in the two spectra before and after that observation, and which might be due to pile-up.

The time-dependent low-energy parts of the SED have been constructed around available X-ray and UV data, and cover simultaneous data snippets, starting at a pre-flare state on MJD 58636.9. These SEDs are shown in Fig. 4.7. The best-fit results and the derived properties of the synchrotron hump are listed for each constructed SED in Table 4.3. The maximum peak flux of the synchrotron hump is reached at MJD 58645.6. Before, a steady increase of the peak flux is seen. In addition, the peak positions shift to higher energies by about one order of magnitude comparing S4 to S5. A shift is also suggested in S3, however, this is not well constrained since hard X-ray data were not available for that time. After the flare reached its maximum, ν_{peak} slowly declines again over the following days. The shift beyond 10^{18} Hz validates that Mrk 421 behaves like an extreme HBL object. This type of behaviour has already been observed during high activity in 2010 (Sahu et al., 2021). Furthermore, this study clearly shows the importance of instruments that can observe the hard X-ray regime, as otherwise the shape of the synchrotron peak cannot be constrained.

The soft X-ray flux exhibits a large change in the probed time range, and I take a deeper look into the spectral properties by constructing a hysteresis curve, which depicts the slope of

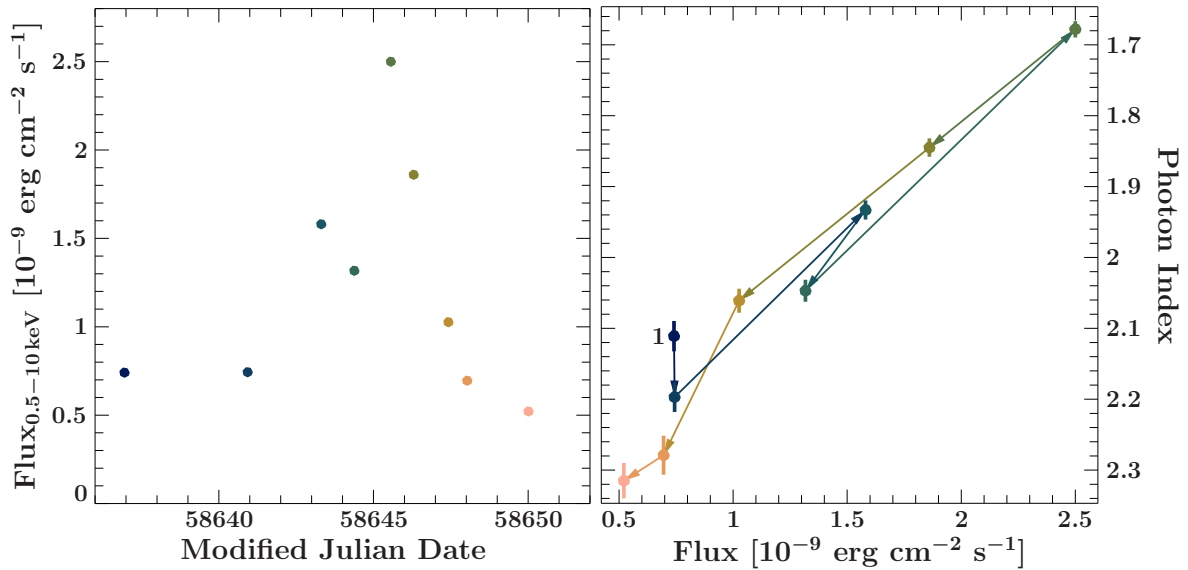


Figure 4.8.: *Left:* *Swift*/XRT light curve of Mrk 421 containing nine observations in the time range MJD 58636.9 - 58650. *Right:* Hysteresis curve built from the same observations as depicted in the light curve on the left. In addition to the colour coding, arrows connect the data points in temporal order. The values are part of the larger sample of *Swift* observations that were fitted with an absorbed power law, and the best fit values are listed in Table A.2. Note that the flux uncertainties are too small to be visible in the plots.

the spectrum in relation to the measured flux for a time series of observations. The hysteresis curve built from the nine observations with *Swift*/XRT, around which the SEDs have been constructed, is shown in Fig. 4.8 (right). The prominent feature of this hysteresis curve is the clear harder-when-brighter trend, which has been commonly observed for Mrk 421 (e.g., Abeysekara et al., 2017, Acciari et al., 2021), as well as other HBLs in the X-rays (Zhang et al., 2006, Bhatta et al., 2018). Furthermore, if the spectral hardness is different during the rise and the decay of the flare, a loop or spectral hysteresis can be found. In Fig. 4.8, the flux is higher in the positive x -axis direction, while the slope of the spectrum is harder in the positive y -axis direction. This way, the orientation of the hysteresis curve can give some indication about the competition between acceleration and cooling timescales. The loop is very elongated, but describes an anti-clockwise orientation, which indicates a ‘hard lag’. Relating this to the acceleration and cooling mechanisms, this means that particles in the jet get accelerated faster than they can cool, and the flare propagates (Kirk et al., 1998). However, the timescales probed by the *Swift*/XRT data are much longer than the actual duration of the flare, and it is likely that behaviour on intra-day time scales is missed. In the next section, Sect. 4.6, I will present a detailed study of the *XMM-Newton* data that were taken during the flare of Mrk 421 in June 2019, which is able to probe these short time scales.

4.6 X-ray timing analysis

So far, I presented a variability study of Mrk 421 based on short-exposure observations, which permitted us to track the long-term behaviour of the flux in all wavelengths. To gain insight into possible short-time variability within the jet, snapshot observations are only marginally

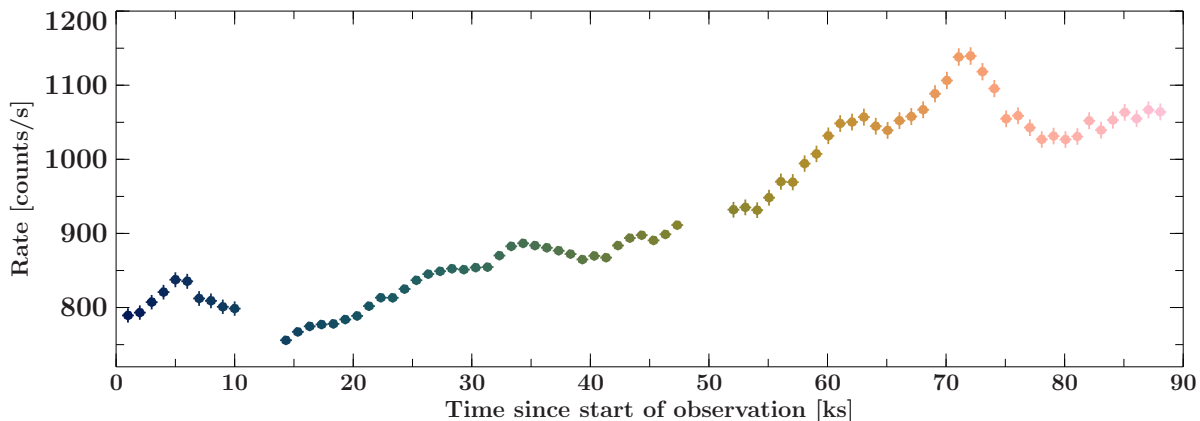


Figure 4.9.: Same as Fig. 4.1, but with 1 ks binning. Each data point matches the bins of the hardness-intensity diagram in Fig. 4.10 in color in order to track the hardness evolution throughout the *XMM-Newton* observation.

valuable, e.g., the *Swift*/XRT observations are only 1 ks in duration. Observations at TeV energies tend to be several hours under ideal conditions, but these vary throughout the year due to visibility, weather, and the full-moon periods during which observations have been suspended. The observation of Mrk 421 by *XMM-Newton* aimed to study its X-ray emission in depth during a high-energy flare, and in this section, I explore these data with several methods to search for the pattern of spectral variability and the shortest time scales.

4.6.1 Spectral variability

As shown previously, the spectral characteristics in the X-ray emission from Mrk 421 varied significantly over the course of less than two weeks. With the *XMM-Newton* observation, which covered 90 ks (25 hrs) nearly continuously, I am able to reveal spectral changes on hour-to-minute time scales. In order to significantly determine spectral properties, I extracted the *XMM-Newton* light curves in 1 ks binning (instead of the default 100 s binning, which is used in the search for the shortest time scales in Sect. 4.6.2). I define three energy bands that I compare with one another. For the low-energy band I choose the range from 0.3–1 keV, for the medium-energy band the range from 1–4 keV, and for the high-energy band the range from 4–10 keV. The full-energy light curve of the *XMM-Newton* observation with a binning of 1 ks is shown in Fig. 4.9, which includes a colour-coding that is also used in the subsequent plots in order to distinguish the individual parts of the light curve.

A model-independent way of investigating the spectral changes over time is employing a hardness-intensity diagram (HID). The intensity is given by the count rate, while the hardness states a ratio of counts in the low-energy band versus counts in the high-energy band, and is defined (e.g., Park et al., 2006) via

$$\text{Hardness} = \frac{H - S}{H + S}, \quad (4.6)$$

where H is the number of counts in the higher energy (harder) band, and S being the number of counts in the lower energy (softer) band. The ‘Hardness’ can range from -1 , i.e., the softer band has a staggering amount of photons, to $+1$, i.e., significantly more photons are found in

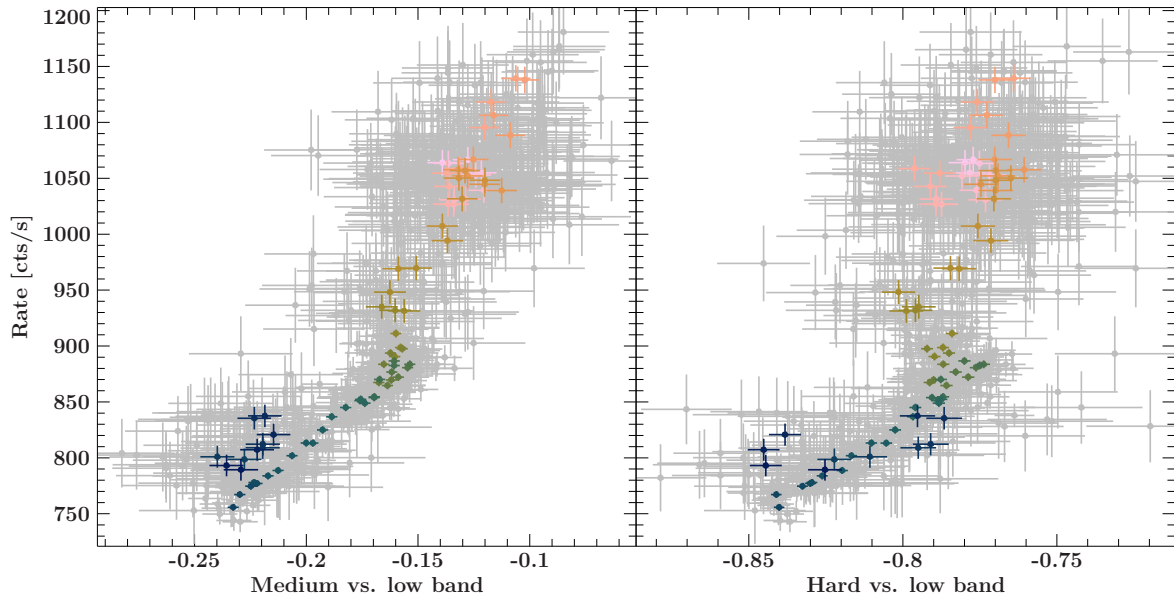


Figure 4.10.: Hardness intensity diagrams illustrating the change of the spectral hardness in the X-ray spectrum during the observation with *XMM-Newton*. The grey data points in the background are the values obtained from the 100 s binned light curve, and shown as a reference for the scattering on shorter time scales. The colour-coded data points are obtained from the 1 ks binned light curve, and can constrain the evolution of the HID much better. *Left:* HID for the medium- (1–4 keV) vs. low-energy (0.3–1 keV) band. *Right:* HID for the hard- (4–10 keV) vs. low-energy band.

the hard band. Naturally, more photons are detected at lower energies, but changing emission processes or absorption can affect this order. Even though this quantity does not rely on any physical assumptions, it is biased towards the chosen energy ranges that are compared to one another. The uncertainty on the hardness is computed via Gaussian error propagation.

In Fig. 4.10, HIDs are shown for the medium- versus low-energy band on the left, and the hard- versus low-energy band on the right. The colour-coding is the same as for the 1 ks-binned light curve in Fig. 4.9 to enable identifications of the respective sections within the light curve. Both HIDs show that the number of counts in the 0.3–1 keV band exceed those in the medium and hard band, but this is not surprising. With a typical photon index of 2 during quiet states, the X-ray emission from Mrk 421 is rather soft, similar to that of all HBL sources. In both HIDs, the trend of the hardening spectrum during the increase of the X-ray emission is evident, and marginally more prominent for the medium vs. low band. Additionally, the behaviour in the medium- and low-energy bands looks more correlated as the corresponding HID exhibits a clearly linear trend. In contrast, the hardness of the hard vs. low band seems to be more independent from the luminosity of the source. For the first ~ 10 ks (dark blue data points), during which the count rate is varying between 832 and 883 counts s^{-1} and not changing as much as in the other sections of the light curve, the hardness is spread out and varies quite a lot, indicating fast spectral variability in the hard band. In the second part of the light curve, during which the flux constantly rises, the harder-when-brighter trend is visible as well, although between 40 and 50 ks the spectrum becomes slightly softer again. The third part of the light curve shows a further increase of the count rate initially, during which the spectrum becomes a little bit harder again, however the hardness stays at the same level when

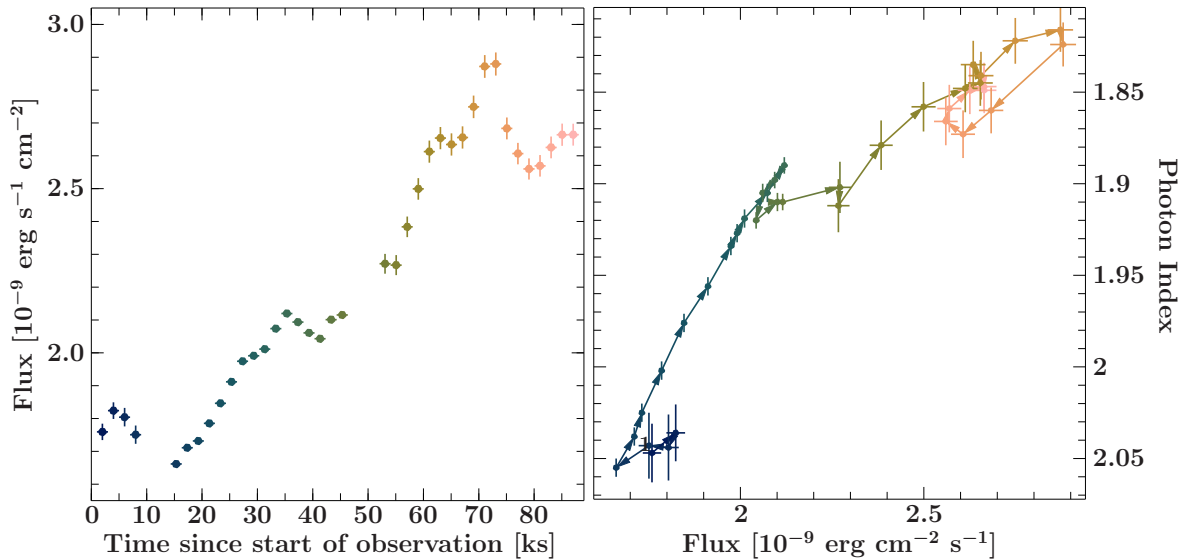


Figure 4.11.: *Left:* XMM-Newton light curve of Mrk 421 with the flux determined from modelling the data with an absorbed power law. *Right:* Hysteresis curve built from the 2 ks binned light curve. In addition to the colour coding, arrows connect the data points in temporal order.

the count rate exceeds $\sim 1100 \text{ counts s}^{-1}$. Interestingly, when the count rate returns to a level of $\sim 1100 \text{ counts s}^{-1}$ after the peak of the flux, the hardness decreases. This is not seen for the HID in the medium- vs. low-energy band, where the hardness seems to follow the same trend during either a rising or decaying count rate.

The time-resolved spectral changes can also be visualised with a hysteresis curve, similar to the hysteresis built for the *Swift*/XRT spectra shown in the previous section. With the XMM-Newton data, it is possible to probe the continuous X-ray emission for 25 hrs and resolve the processes in the jet better. For the hysteresis curve, I extracted spectra with an exposure time of 2 ks, which are able to verify sub-hour changes, while at the same time providing adequately constrained flux and photon index values. The fit results are listed in Table A.1. The resulting hysteresis curve with an accompanying light curve is shown in Fig. 4.11. For most of the observing time, the X-ray flux of Mrk 421 is increasing, hence the movement from the lower left corner to the upper right corner in the hysteresis plot. In addition to the increasing flux, the spectrum becomes significantly harder, as already seen in the HID. The hardening takes place within less than 1 day, with the continuous increase being roughly 65 ks long.

Because of the chosen binning, the first part of the light curve contains only four bins. In the hysteresis curve, these bins make a slight clockwise rotation. For the second part of the light curve, no hysteresis can be seen, as the flux steadily increases most of the time, and the photon index decreases and increases by the same amount as the flux changes for the small, intermediate peak seen at ~ 35 ks. In the third and last section of the light curve, the flux peaks at ~ 70 ks, before it visibly drops. For this behaviour, a clear clockwise rotation can be observed. This behaviour indicates that the cooling time scale dominates the underlying physical processes, as the high-energy particles cool efficiently and the acceleration reaches the low-energy photons later, i.e., showing a ‘soft lag’ (e.g., Kirk et al., 1998). The ‘soft lag’-behaviour is a common occurrence in the X-ray emission of HBL-type blazars (e.g., Falcone

et al., 2004, Wang et al., 2018), and has also been found for optical emission (Agarwal et al., 2021). For Mrk 421 both clockwise and anti-clockwise rotating hysteresis curves have been found during different observing times (e.g., Rivasio et al., 2004, Cui, 2004, Abeysekara et al., 2017). The circumstance that the X-ray flux and spectral shape can change in various way, not necessarily connected to one another, indicates that we might see different kind of flares, or different stages within flaring events. This behaviour still appears random to us. The observing times often only cover a relatively short period of time compared to the length of an activity phase. As long as dense, continuous monitoring with an instrument like *XMM-Newton* is not feasible, it is necessary to make do with data that covers only a segment.

Power spectral density

A powerful tool to study and classify the variability of a source is the computation of the power spectral density (PSD; for a detailed description and review see, e.g., van der Klis, 1989, Nowak et al., 1999, Pottschmidt, 2002), which is the multiplication of the discrete Fourier transform X_j with its complex conjugate, that is

$$P_j = X_j \cdot X_j^*. \quad (4.7)$$

The discrete Fourier transform of a time series with m evenly spaced time bins x_h is defined as

$$X_j = \sum_{h=0}^{m-1} x_h \exp^{2\pi i j h / m}, \quad (4.8)$$

where h is the designated number of the time bin in the series, and $i = \sqrt{-1}$. Depending on the length of the light curve (T) and the size of the time bins (Δt), a certain frequency range can be used for a variability study. The minimum frequency is $f_{\min} = 1/T$, while the maximum frequency, which is called the Nyquist frequency, is $f_{\max} = 1/(2\Delta t)$.

Each measured light curve contains noise, which is primarily counting (Poisson) noise in the case of X-ray light curves. Therefore, the discrete Fourier transform of a light curve is composed of a signal as well as a noise signal, i.e., $X_j = S_j + N_j$. As a result, the PSD for a light curve also contains noise, which needs to be considered for the interpretation of the variability of a source.

The values of a single PSD contain statistical uncertainties that are about as large as the PSD values themselves, which results in very noisy, scattered PSDs. However, it is possible to average PSDs and scale down the uncertainties by a factor that is proportional to the square root of the number of PSDs taken into account for the averaging. One method of averaging PSDs is to rebin the frequencies and their values to a grid with larger bin widths. Another option is to segment the light curve and compute a PSD for each segment, which can then be used together to create the averaged PSD. This procedure, however, decreases the frequency range, as the minimum frequency depends on the length of a segment. Generally, both of these methods are used in combination.

In addition, different normalisations N for a PSD can be introduced. If it is necessary to take the background into account, i.e., if the source count rate is low to moderate, one can use the ‘Miyamoto’ normalisation (Miyamoto et al., 1992)

$$N_{\text{Miyamoto}} = \frac{2}{T R R_{\text{sig}}}, \quad (4.9)$$

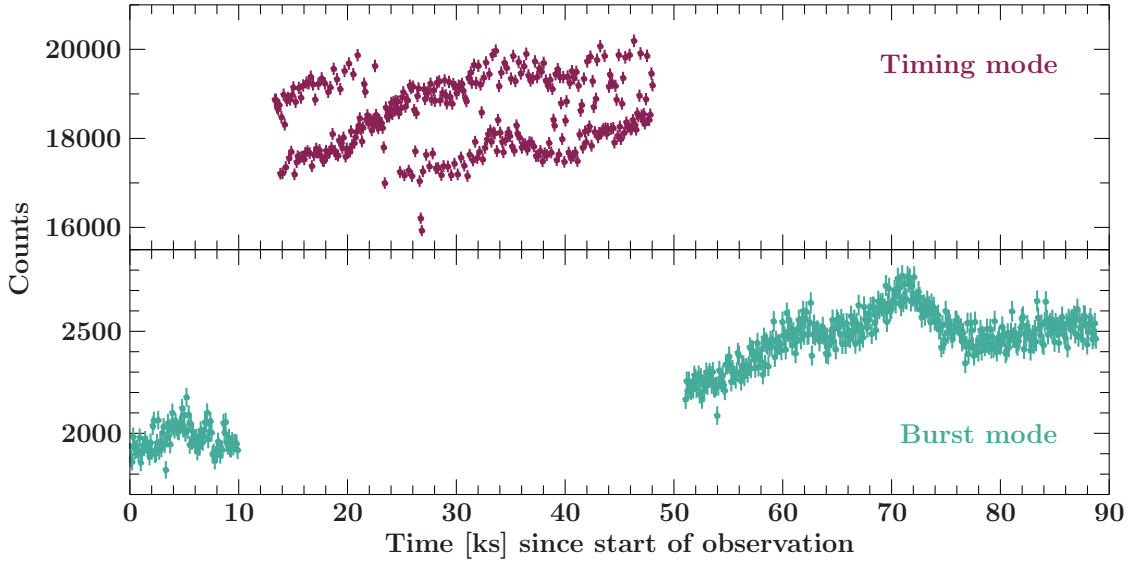


Figure 4.12.: *XMM-Newton* light curve (0.3–10 keV) with 100s-binning of the Mrk 421 observation, shown in the raw ‘count space’. The parts of the light curve that have been observed in either *Timing* or *Burst* mode are indicated in blue and red, respectively, and are split into the upper and lower panel as the measured counts are a factor of ~ 10 higher for the *Timing* mode

which takes into account the light curve length (T), the average rate (R), and the average signal rate (R_{sig}), which is determined by removing the background rate from the overall rate. The ‘Leahy’ normalisation (Leahy et al., 1983) is defined as

$$N_{\text{Leahy}} = \frac{2}{TR}, \quad (4.10)$$

such that Poisson noise has a power of 2. This normalisation can be used to determine the shortest time scales above Poisson noise by finding the frequency at which the PSD reaches the Leahy normalised power of 2. Given that Mrk 421 showed very high count rates exceeding $1000 \text{ counts s}^{-1}$, it is unlikely that any background events significantly influenced the light curve. Hence, I use the Leahy normalisation to easily determine the highest frequencies up to which the source exhibits intrinsic variability.

I compute PSDs on the 100s-binned light curve for a broad energy range from 0.3 to 10 keV, as well as PSDs for the three energy bands: 0.3–1 keV, 1–4 keV, and 4–10 keV. The light curves used for the PSDs were taken from the original, uncorrected count light curve (see Fig. 4.12), i.e., not the light curve shown in Fig. 4.1. As is visible from from Fig. 4.12, the light curve bins of the *Timing mode* part of the light curve first exhibit periodic spikes and then drops. While the reason for this is not entirely clear, I suspect that the fractional exposure frequently dropped to a very low level. This is confirmed by a filtering process, which I apply before the PSD computation to remove sections of the light curve, where the fractional exposure per bin was not above 95%. I use the `foucalc` algorithm (Pottschmidt, 2002, Grinberg et al., 2014), which is part of the `ISISscripts`⁴. I use the original, uncorrected count light curves, and consider only bins in the light curve that have a fractional exposure > 0.95 , and fall within the GTIs of the observation. After the filtering, I convert the counts to count rates. Furthermore,

⁴Provided by ECAP/Remeis observatory and MIT (<http://www.sternwarte.uni-erlangen.de/isis/>)

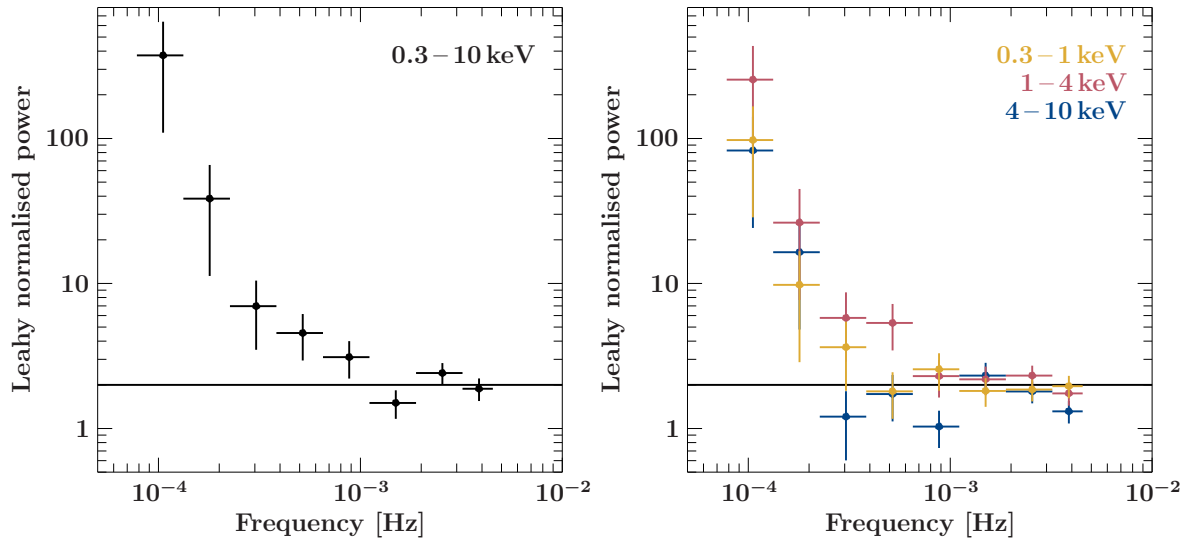


Figure 4.13.: *Left:* PSD of the light curve in the full energy range from 0.3 to 10 keV. *Right:* PSDs for the light curve in each of the energy ranges. In both plots, the horizontal line at the Leahy normalised power value of 2 indicates the power level of the underlying Poisson noise.

I split the lightcurve into two segments with a length of 12800 s, and apply a logarithmic rebinning of the frequency of $\Delta f/f = 0.7$.

The resulting PSDs are shown in Fig. 4.13. I determine the shortest source intrinsic variability as described above. The horizontal line marks the Leahy normalised power of 2. Here, I define that the PSD reaches the Poisson noise level at the centre of a bin (incl. error) for the first one of the PSD bins that flatten towards higher frequencies. For the full energy range, the PSD crosses the noise level at $\sim 10^{-3}$ Hz, which corresponds to time scales of 1000 s, or 16 minutes. The PSDs of the light curves in each energy band seem to display a slightly longer-term variability. The shortest variability frequency is $\sim 5 \times 10^{-4}$ Hz ($= 2000$ s ≈ 33 min) for the low energy band, $\sim 8.5 \times 10^{-4}$ Hz (≈ 1180 s ≈ 20 min) for the medium energy band, and $\sim 3 \times 10^{-4}$ Hz (≈ 3340 s ≈ 56 min) for the high energy band. In general, the PSDs reveal sub-hour variability within the jet of Mrk 421 during its flaring activity in June 2019, which matches the larger scale up-and-downs visible in the light curve.

4.6.2 Searching for the shortest variability time scales

So far, the grand-scale variability during the *XMM-Newton* observation has been presented. However, the instruments on-board *XMM-Newton* are able to resolve much smaller time scales. Using different methods, I have searched for the shortest time scales on which variability is present in Mrk 421.

Modelling long-term fluctuations with Savitzky-Golay Polynomial

As a first step, I want to look at the data without the long-term variations that are present in the light curves. In order to get rid of those, I use a method which was originally designed to determine the amplitude and width of emission lines within noisy spectra. Before presenting the results, I will give a concise overview of this method following Sect. 14.9 in *Numerical*

Recipes by Press et al. (2007). The first to develop this low-pass filter to smooth noisy data were Savitzky & Golay (1964), hence these filters are often referred to as *Savitzky-Golay* smoothing filters. Other names for these are *least-squares* (Hamming, 1983), or *Digital smoothing polynomial* (DISPO; Ziegler, 1981) filters. The idea behind the method is to somehow determine the underlying signal, which is polluted by, e.g., white noise, without transferring the data to the Fourier domain and back. In general, the data are assumed to consist of equally spaced values. The Savitzky-Golay smoothing filter is a more advanced version of *moving window averaging*. The most simple procedure to smooth data is to take the average value of surrounding data points for each data point g_i , meaning

$$g_i = \sum_{n=-n_L}^{n_R} c_n f_{i+n} = \frac{1}{n_L + n_R + 1} \sum_{n=-n_L}^{n_R} f_{i+n}, \quad (4.11)$$

where c_n is a filter coefficient that becomes the constant factor before the sum, n_L is the number of data points that lie ‘to the left’ of data point i , and n_R is the number of data points ‘to the right’ of said data point. This smoothing function remains unbiased as long as the underlying function is simply a constant value, or follows a strictly linear trend. As soon as it is more complicated, i.e., involving local minima or maxima, a bias is introduced. This becomes apparent for the case of, e.g., spectral lines, for which the moving window averaging reduces the height of the lines, but increases their width, and as a result the physical properties of those emission lines can no longer be retrieved. However, the total area underneath emission lines is preserved. Now, for Savitzky-Golay filtering, the filter coefficients c_n are set to preserve the non-linear features in the smoothed data. The idea is similar to approaching each data point by fitting a polynomial of higher order to a defined amount of neighbouring data points, instead of just averaging them.

While the Savitzky-Golay filtering is typically used to smooth data and discard noise, I use it to detrend the data and determine the slowly varying underlying features of the light curve to subtract them and study the short-term fluctuations in order to determine whether intrinsic variations can be found on top of the expected Poisson noise. In Figure 4.14, the *XMM-Newton* light curves from our observation of Mrk 421 are shown for three energy bands, including the smoothed light curves as obtained with the Savitzky-Golay filter method. I exclude the section of the light curve that was taken in *Timing* mode. The most noteworthy feature in the three light curves displaying different energy bands is the significantly stronger fluctuations in the first part of the light curve in the high-energy band. Both sections of the light curve that were taken in *Burst* mode were individually smoothed. For the second section of the light curves, the parameters for the smoothing algorithm were $n_L = n_R = 100$, and the polynomial order was set to six. Since the length of the first part is only $\sim 1/3$ of the length of the second part, the parameters for this part were $n_L = n_R = 50$ and a polynomial order of three was used. These parameters were chosen to filter out the visible longer-term variations down to ~ 5 ks.

In order to look at variations on short timescales, I divide the original light curve by the smoothed curves that represent the long term average. The resulting, normalised light curves are displayed in Fig. 4.15. In general, the high-energy band is the most variable, which can also be seen by illustrating the variations in a histogram (see Fig. 4.17, left) and the short-term fluctuations in the first part of the light curves continue to be the most prominent feature. To all normalised, energy-resolved light curves, I apply the Bayesian block algorithm (Scargle

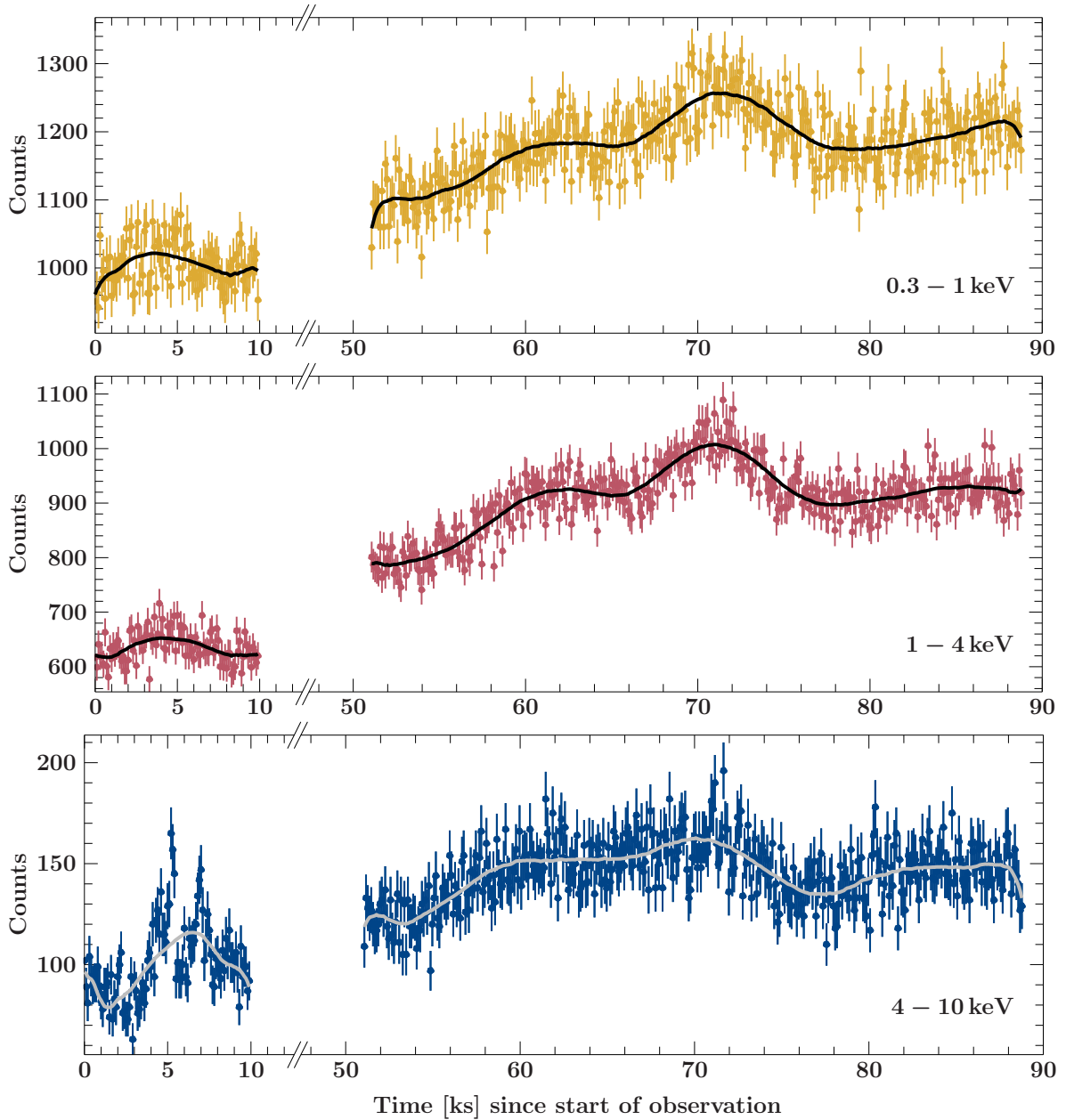


Figure 4.14.: *XMM-Newton* light curve of Mrk 421 split in three energy bands: 0.3-1 keV (yellow, upper panel), 1-4 keV (red, middle panel), and 4-10 keV (blue, lower panel). To distinguish the long-term fluctuations from minute-scale variability, smoothed light curves have been computed with the Savitzky-Golay filtering method, and are depicted by the solid line curves plotted on top of the data points.

et al., 2013), which is an algorithm identifying change points in data series and can be used to find flares in light curves. The algorithm only finds change points in the first section of the high-energy band light curve (see Fig. 4.16), which have a false positive rate of 5% each. The width of the block showing an enhanced amount of normalised counts is 1.2 ks. However, even shorter fluctuations are visible, which I want to investigate.

I therefore just concentrate on the first 10 ks of the *XMM-Newton* observation of Mrk 421, and determine whether these fluctuations lie above the expected level of Poisson noise. As a

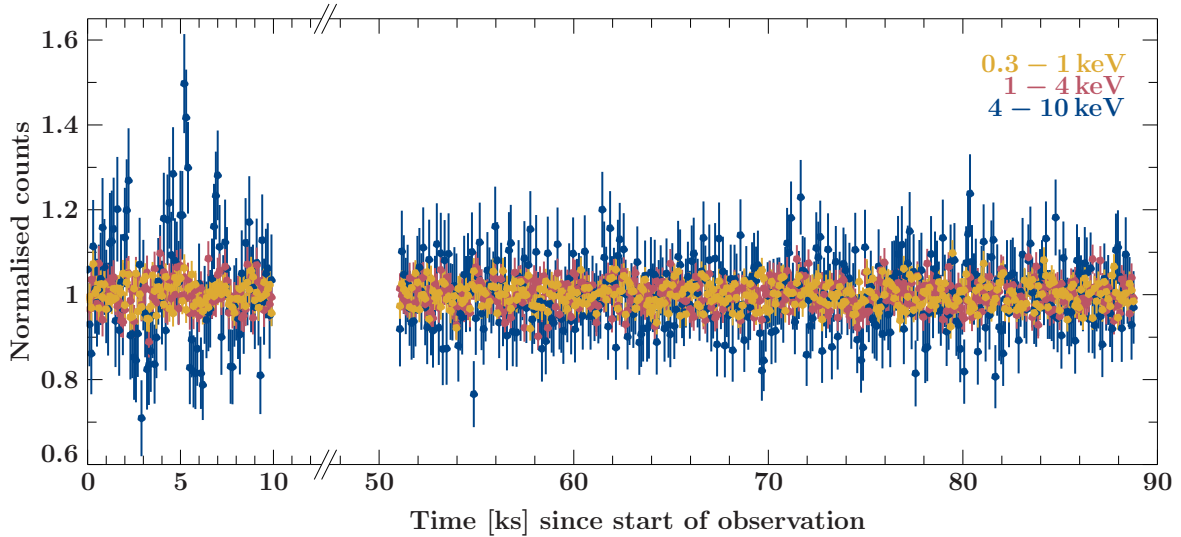


Figure 4.15.: The light curves from Fig. 4.14 after normalisation with the smoothed light curves determined by the Savitzky-Golay smoothing method.

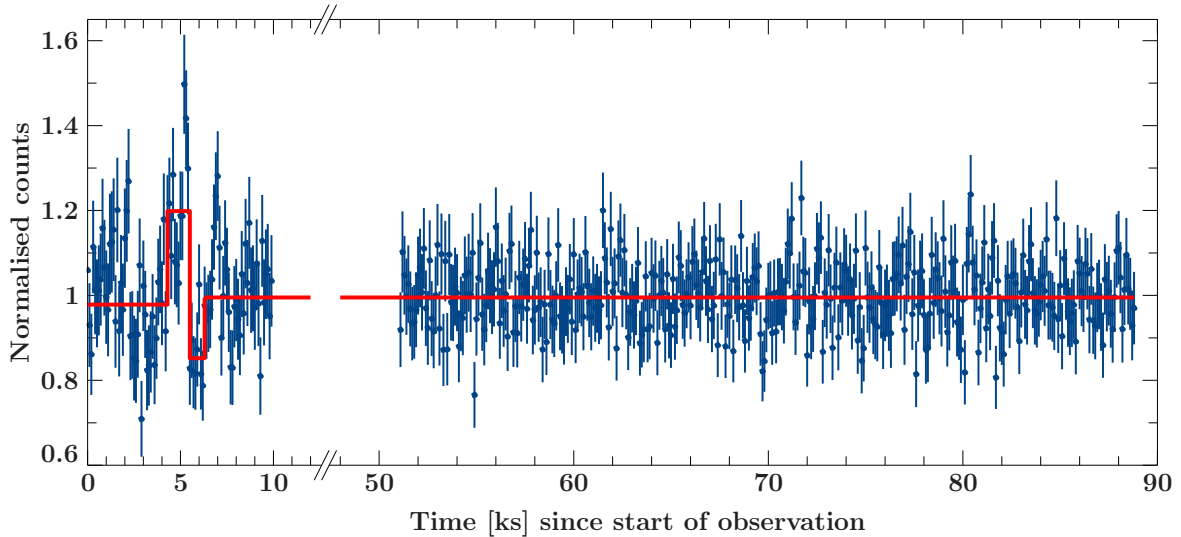


Figure 4.16.: High-energy (4–10 keV) light curve after normalisation with the smoothed light curves determined by the Savitzky-Golay smoothing method and with the applied Bayesian block algorithm (solid red line).

testing approach, I simulate 10^5 light curves with the same underlying smoothed light curve that contain random Poisson-distributed noise. Note that for the simulations, I use the full light curve, not just the first 10 ks. For each point in the light curve, the simulated values are sorted. The large number of simulated data points results in a normal distribution. Therefore, the 2σ and 3σ deviations are defined such that they lie outside of 95.45% and 99.73% of the simulated values, i.e., two and three times the standard deviation respectively (similar to [Benlloch et al., 2001](#)). The first part of the light curve in the high-energy band, including lines marking the 2σ and 3σ threshold for excess outside of Poisson noise for an individual data point, is shown in Fig. 4.17 in the right plot. Two ‘features’ stand out: Two data points ($t = 5.2$ ks) show a clear excess above 3σ , and are followed by another adjacent data point at the 3σ threshold.

Table 4.4.: Bins of the two mini-flares that lie above the 2σ line in Fig. 4.17 (right). For each bin, I list their position (t) and normalised count value (NC value) in the light curve, as well as their individual deviation σ from the expected normalised count value of 1.

	Excess 1			Excess 2	
t [ks]	5.2	5.3	5.4	6.9	6.9
NC value	1.50 ± 0.12	1.42 ± 0.11	1.30 ± 0.11	1.23 ± 0.10	1.28 ± 0.11
Deviation [σ]	5.3 ± 1.3	4.5 ± 1.2	3.2 ± 1.2	2.5 ± 1.1	3.0 ± 1.1

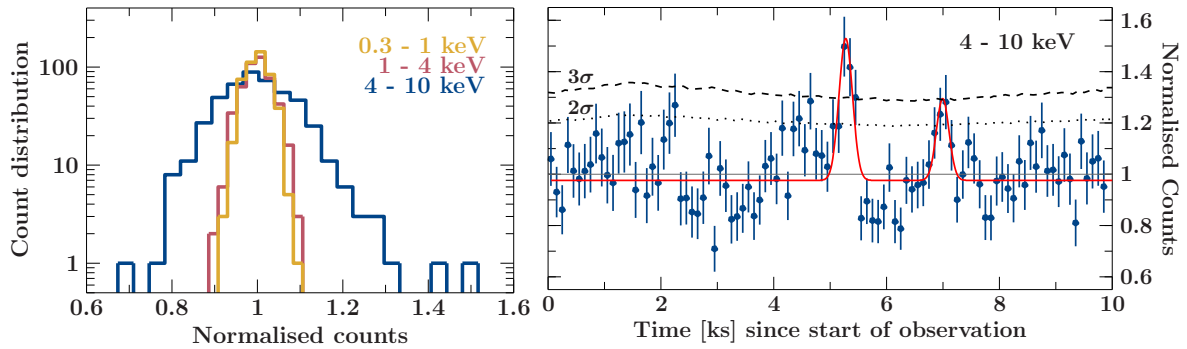


Figure 4.17.: *Left:* Histogram of the rate distribution for the normalised light curves (see Fig. 4.15) in each energy band. *Right:* The first part of the normalised light curve in the high-energy band, including significance lines that mark the expected scattering of data points due to Poisson noise for 2σ (dotted) and 3σ (dashed). The red line is the best-fit model of two gaussian lines plus a constant, which was used to determine the time scales of these variations.

Furthermore, a smooth increase and decrease is visible at 7 ks, which appears as if the data points are correlated. However, the highest bin only reaches the 3σ threshold. The data points above the 2σ line that are part of these features are listed in Table 4.4, including their exact deviation from the average normalised counts. While random scattering up to those thresholds can be expected to some extent (see, e.g., the data point at $t = 4.5$ ks), I estimate the possibility of the clustered, adjacent excesses further.

Following a similar approach as before, I use the simulated light curves and count the number of occurrences of three adjoining data points resembling the feature at ~ 5 ks, i.e., with two data points above 4σ and one above 3σ , in all possible chronological order. Furthermore, I count all data point clustering similar to the feature at ~ 7 ks, that is, one data point above 2σ , and one above 3σ , again in both possible ways of chronological order. In 10^5 simulated light curves, I find 2678 patterns of adjacent data points equal to the excess at 7 ks, which yields a probability of $\sim 2.7\%$ that the excess appeared randomly. For the excess at ~ 5.2 ks, which includes more significant deviations, no similar constellation of adjacent data points was found. Hence, I can only give an upper limit of 0.001% for the excess being of random origin. I conclude that these fluctuations do not originate from Poisson noise, and suggest that they might be ‘mini-flares’ at the highest X-ray energies on top of the general flaring state.

To estimate the time scales, I fit the first part of the light curve with a constant and two Gaussian profiles (see Fig. 4.17, right), centered on the excesses at $t \sim 5.2$ ks and $t \sim 7$ ks, and compute the full width at half maximum (FWHM) from the resulting σ of each Gaussian line.

Table 4.5.: Best-fit results retrieved by using the model Constant+Gauss+Gauss on the first 10 ks of the high-energy band light curve of Mrk 421. The fit statistic is $\chi^2/\text{d.o.f.} = 125.71/92 = 1.37$.

	Center [ks]	Sigma [ks]	Area	Time scale [s]
Gaussian 1	5.22 ± 0.06	0.12 ± 0.05	$1.2^{+0.6}_{-0.4}$	280^{+103}_{-105}
Gaussian 2	$6.94^{+0.07}_{-0.09}$	$0.11^{+0.09}_{-0.07}$	$0.67^{+2.44}_{-0.27}$	263^{+193}_{-156}
Constant	0.976 ± 0.018			

The FWHM is defined as

$$\text{FWHM} = 2 \sqrt{2 \log 2} \sigma, \quad (4.12)$$

and I use it as an estimate of the time scales during which the X-ray flux of Mrk 421 changed rapidly. Uncertainties are derived from simple error propagation. The best-fit results and subsequent time scales are listed in Table 4.5. Even though the resulting time scales contain relatively large uncertainties, I find that they can be pinned down to be something roughly between 3.5 to 6.5 minutes. Such time scales are unprecedented for blazar variability at X-ray energies.

Flux variability time scale

Another mathematical approach to search for short-time variability is computing the flux variability time scale, also known as *e*-folding time. [Burbidge et al. \(1974\)](#) defined an estimate of the flux normalised (or weighed) variability time scale via

$$\tau_{\text{var}} = \left| \frac{\Delta t}{\Delta \ln F} \right| = \left| \frac{t_1 - t_2}{\ln(F_1/F_2)} \right|, \quad (4.13)$$

with Δt being the time interval between two selected flux measurements, F_1 and F_2 . The uncertainty can be estimated by using the standard error propagation (see also [Bhatta et al., 2018](#)), which yields

$$\Delta \tau_{\text{var}} \simeq \sqrt{\frac{F_1^2 \Delta F_2^2 + F_2^2 \Delta F_1^2}{F_1^2 F_2^2 (\ln[F_1/F_2])^4}} \Delta t. \quad (4.14)$$

Here, I use the light curve displaying the rates that are corrected for fractional exposure, etc., in order to take the data obtained in *Timing* mode into consideration as well.

I compute τ_{var} for all combinations of two data points, but for each of the three parts of the light curve individually. From the computed τ_{var} , I select the smallest value that fulfils the condition of $|F_1 - F_2| > \Delta F_1 + \Delta F_2$, which ensures that the variation lies outside of the flux uncertainties. I calculate τ_{var} for both a 100s-binned and a 400s-binned light curve to gain insight into how strongly the binning correlates with the found variability. The resulting τ_{var} values are listed in Table 4.6, while the values obtained with 100s- and 400s-binning are plotted in Fig. 4.18. In general, the variability time scale is larger by a factor of two, or more, for the data obtained in Timing mode compared to the Burst mode.

The variability time scale found for the first 10 ks of the high-energy band light curve is similar to the fluctuations found in the previous section. Furthermore, the τ_{var} values found for

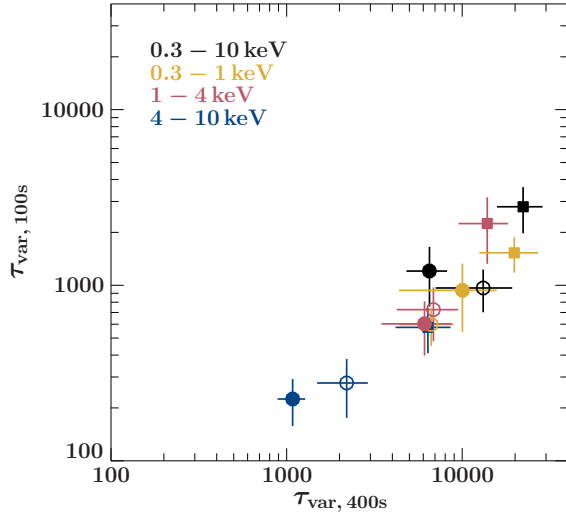


Figure 4.18.: Correlation of τ_{var} determined for a different binning of the three light curves sections. While the different colours indicate the different energy bands, the square symbols mark τ_{var} in the Timing mode section, while the filled and empty circular symbols mark τ_{var} in the first and second Burst mode section, respectively.

Table 4.6.: Shortest variability time scale τ_{var} , separately computed for the three parts of the *XMM-Newton* light curve.

100s binning			
Energy band	τ_{var} [s]		
	0 – 10 ks <i>Burst mode</i>	13 – 48 ks <i>Timing mode</i>	51 – 89 ks <i>Burst mode</i>
0.3-10 keV	1205 ± 450	2798 ± 822	964 ± 263
0.3-2 keV	1071 ± 422	2232 ± 611	824 ± 224
2-10 keV	408 ± 153	1155 ± 355	402 ± 123
0.3-1 keV	935 ± 393	1530 ± 350	598 ± 147
1-4 keV	603 ± 206	2245 ± 921	726 ± 246
4-10 keV	225 ± 67	576 ± 166	278 ± 102
400s binning			
0.3-10 keV	6506 ± 1695	22230 ± 6452	13168 ± 6103
0.3-2 keV	8114 ± 3065	21361 ± 6909	11200 ± 5162
2-10 keV	2584 ± 687	9570 ± 3073	3819 ± 1304
0.3-1 keV	10034 ± 5668	19799 ± 7269	6660 ± 2259
1-4 keV	6095 ± 2631	13884 ± 4369	6857 ± 2620
4-10 keV	1082 ± 193	6376 ± 2206	2196 ± 705

the 400s-binned light curves are significantly larger than their smaller binned counterparts. However, a larger binning averages over variations on smaller time scales, and the shortest time scales found in the 100-binned light curve seem to lie below 400s.

4.6.3 Physical interpretation of the variability

In order to interpret our results of the variability analysis, I first convert the time scales into the appropriate jet frame, and then derive properties of the emission region. An important

quantity for the frame conversion is the Doppler factor δ , which is defined as

$$\delta = \frac{\sqrt{1 - \beta^2}}{1 - \beta \cos(\theta)}, \quad (4.15)$$

and depends on the viewing angle (θ) and the jet speed ($\beta = v/c$). I can transfer observed time scales (t_{obs}) into the intrinsic jet scales by considering δ and the redshift z via

$$t_{\text{jet}} = \frac{\delta}{(1 + z)} t_{\text{obs}}. \quad (4.16)$$

From the time scale, I can estimate an upper limit of the size of the emission region with

$$d_r = c \cdot t_{\text{jet}}. \quad (4.17)$$

Furthermore, I assume a conical shape for the jet, which has been found to be true for most HBL and Quasars up to several kpc (Pushkarev et al., 2017). If the jet has an opening angle α , and I assume that the emission region covers the full width of the jet, I can compute the distance to the jet base by

$$d_{\text{jb}} = \frac{d_r}{2 \tan(\alpha/2)}. \quad (4.18)$$

For the calculations, I use $M_{\text{BH}} = 1.9 \times 10^8 M_{\odot}$ (Wang et al., 2004), and $z = 0.031$ (Ulrich et al., 1975). The Doppler factor of blazars is generally determined by SED modelling, and ranges between 20 and 40 during high activity states of Mrk 421 (Donnarumma et al., 2009, Kapanadze et al., 2016, Banerjee et al., 2019, Zheng et al., 2021). Hence, I assume $\delta = 30$. The intrinsic opening angle of blazar jets can range between 0.1° and 9.4° , but the median is 1.2° for LAT detected sources (Pushkarev et al., 2017), which I choose for Mrk 421⁵. I compute t_{jet} , d_r , and d_{jb} for three derived t_{obs} (see Sect. 4.6.2), which are the shortest variability time scales for the full and the highest energy band, and the time scale of the larger ‘mini-flare’ modelled by a Gaussian. The results are listed in Table 4.7.

Our findings are that the emission region responsible for the rapid variability would be located relatively close to the central engine and well within the broad line region (BLR)⁶, if the rapid variability is taken as a proxy for the total size of the emission region. Even though several BL Lac objects have been found to be missing a BLR (e.g., Plotkin et al., 2012), optical spectra of Mrk 421 revealed weak $L\alpha$ emission, which can be interpreted to have originated in a BLR (Stocke et al., 2011). Given that the X-ray flare occurred coincidentally with a TeV γ -ray flare, it is unlikely that the emission originated close to the jet base, as BLR photons would be able to attenuate any γ -ray emission by triggering pair production.

Hence, a better approach is to consider the short time variability being additional fluctuations on top of a more slowly varying envelope that represents the full emission region. The *XMM-Newton* observation covers a time span of ~ 90 ks, which is slightly longer than a day. The overall flare in the X-ray band is visible in the X-ray light curve (see Fig. 4.1), and shows a steady increase that starts at 13 ks, and peaks at 70 ks, before it declines again. Using a crude estimate that this time scale of ~ 60 ks is the slower-moving envelope and represents the entire

⁵Pushkarev et al. (2017) reported no significant difference for opening angles of FSRQs and BL Lacs.

⁶The broad line region extends in a distance from 0.01 to 1 pc to the SMBH (Cox, 2002), which is roughly $500 - 5 \times 10^4 R_g$ for Mrk 421.

Table 4.7.: Transferred time scales in the jet frame (t_{jet}), size of the emission region (d_r), and distance of the emission region to the jet base (d_{jb}) under the assumption that the region covers the full width of the jet.

	Energy band [keV]	t_{obs} [s]	t_{jet}		d_r [R_s]	d_{jb} [R_s]
			[s]	[min]		
Variability	0.3 – 10	964 ± 263	28050 ± 7653	468 ± 128	14.9 ± 4.1	711 ± 194
time scale	4 – 10	225 ± 67	6547 ± 1950	109 ± 32	3.5 ± 1.0	166 ± 49
Gaussian fit	4 – 10	280 ± 104	8147 ± 3026	136 ± 50	4.3 ± 1.6	207 ± 77

Notes. For convenience, I used the mean error for the t_{obs} value derived by the Gaussian fit.

emission region, I would determine that the emission region, if filling the full width of the jet again, is located outside of the BLR.

In this case, the observed rapid variations are better explained by models such as the ‘minijets-in-jet’, ‘spine-sheath’, or ‘star-in-jet’ scenario (see also Sect. 1.2.2). However, these were developed to explain rapid γ -ray emission, and might not necessarily produce rapid fluctuations in the X-rays as well. If γ -ray data existed that had been taken simultaneously to the first 10 ks of the *XMM-Newton* observation, we would be able to determine if the rapid X-ray and γ -ray variability have the same origin. Unfortunately, this is not the case.

4.7 Outlook

Our long prepared and executed monitoring programme of Mrk 421 has fulfilled its goal of obtaining very good multi-wavelength coverage during a major TeV flare. The γ -ray flare in June 2019 was accompanied by a flare at X-ray energies, which I could study in detail due to our triggered and very long *XMM-Newton* observation. The brightness of the X-ray flare exceeded that of all previous observations of Mrk 421 done with *XMM-Newton*. The X-ray data taken with *XMM-Newton* revealed a strong spectral hardening within ~ 65 ks, which, together with an *INTEGRAL* observation providing additional constraints, indicates that the synchrotron peak shifted to higher energies during the flare. The radio emission does not seem to be largely affected by the flaring event in June. In a search for very short time scales, I find two ‘mini-flares’ the 4–10 keV energy band within the first 10 ks of the *XMM-Newton* observation, which appears on top of the generally increasing and varying X-ray emission. The observed time scales are shorter than 5 min, and transfer to emission region sizes of ~ 4 Schwarzschild radii (under the assumption of $\delta = 30$) in the jet frame.

Even though Mrk 421 has been extensively studied in this work as well as in the past, many questions remain, particularly regarding its jet emission. The extremely short time X-ray variability found in the observation with *XMM-Newton* is on the same order of magnitude as the rapid γ -ray variability found in some other blazars, and suggests the possibility that the variability is caused by the same mechanism. The recent launch of the *Imaging X-ray Polarimetry Explorer* (IXPE; Soffitta et al., 2020) will shed some light on this matter as it might be able to detect polarisation angle swings during X-ray flares, which could be pointers to magnetic reconnection processes.

AGN outside the unification scheme - What is the nature of PKS 2004–447?

“It was like a bunch of lizards watching the World Cup. Politely put, they weren’t sure what they were looking at.”

James S. A. Corey, *Caliban’s War*

Among the meticulously sorted classes of AGN, there are several source types that have been found to contradict their belonging to a certain AGN class in the last couple of years. A prominent example are γ -loud narrow-line Seyfert 1 (NLSy 1) galaxies, which were found by *Fermi*/LAT. In this chapter, I will present a multi-wavelength analysis of one of these peculiar sources, PKS 2004–447, during a γ -ray outburst in October 2019, which has been published in [Gokus et al. \(2021b\)](#). Hence, large parts are taken in verbatim from this publication and the text uses ‘we’, where appropriate. In Sect. 5.2 I will introduce what has been known so far about PKS 2004–447. In Sect. 5.3, the multi-wavelength analysis, including a variability study, the X-ray spectrum analysis, and the SED modelling, is presented. A discussion of our findings is given in Sect. 5.4, and a summarising conclusion is drawn in Sect. 5.5.

5.1 Narrow-line Seyfert 1 galaxies

Typically classified as radio-quiet sources, Seyfert 1 objects reside in the centers of spiral galaxies and their optical spectra exhibit both broad and narrow lines (see Chap. 1). For some of the those sources, however, the broad lines are unusually narrow, with FWHM ($H\beta$) $\leq 2000 \text{ km s}^{-1}$ ([Osterbrock & Pogge, 1985](#)). In addition, these emission lines are proportionally strong in comparison to the narrow, forbidden [O III] $\lambda 5007\text{\AA}$ line. The flux ratio between both lines is $[\text{O III}]/H\beta \leq 3$. Other features of their spectra are the prominent optical Fe II emission line complex, which anti-correlates with the strength of the [O III] emission line, and a soft excess below 2 keV in their X-ray spectrum ([Grupe, 2004](#)).

The narrow lines originating in the broad-line region (BLR) can indicate smaller central black hole masses compared to typical Seyfert 1 galaxies, while accreting close to the Eddington limit (e.g., [Grupe, 2004](#), [Grupe et al., 2010](#), [Xu et al., 2012](#)). NLSy 1s could therefore present young or re-activated Seyfert galaxies and mark the first step in AGN evolution ([Mathur, 2000](#), [Järvelä et al., 2017](#)). Alternatively, it is possible to explain the appearance of

narrow instead of broad lines from the BLR with a particularly small inclination angle to the observer. However, [Järvelä et al. \(2017\)](#) have shown that the average large-scale environment density of NLSy 1s significantly differs from that observed in broad-line Seyfert 1 galaxies, meaning that this difference cannot be solved by unification via the orientation angle.

Interestingly, a small sample of the known NLSy 1 objects ($< 7\%$) exhibits radio-loudness (e.g. [Komossa et al., 2006](#), [Rakshit et al., 2017](#), [Chen et al., 2018](#), [Singh & Chand, 2018](#)). [Komossa et al. \(2006\)](#) found that, in general, SMBH masses of radio-loud NLSy 1s were significantly below those of the radio-loud AGN population, while exhibiting high Eddington ratios of L/L_{Edd} . In addition, 70% of the radio-loud NLSy 1 sources in their sample were compact radio sources as they were unresolved by the FIRST survey¹, and have steep spectra, which is similar to compact steep-spectrum (CSS) sources².

There are still ongoing debates regarding two main properties of radio-loud NLSy 1s, namely the masses of their black holes, and in which host galaxies they reside. The most common method to derive the SMBH mass is to use the full width at half maximum (FWHM) of prominent emission lines in optical spectra (e.g., [Vestergaard & Peterson, 2006](#), [Shen et al., 2011](#)). This method, though, has been criticized for being biased towards projection effects. For example, a disk-shaped BLR in combination with a very small viewing angle, meaning observing the source pole-on, could explain the narrowness of the lines of the BLR, while leading to an underestimation of the SMBH masses of NLSy 1s ([Collin & Kawaguchi, 2004](#), [Jarvis & McLure, 2006](#), [Decarli et al., 2008](#)). Several other methods, for example spectropolarimetry ([Baldi et al., 2016](#)), reverberation mapping ([Wang et al., 2016](#)), or a determination via the break frequency of a PSD (e.g., [Pan et al., 2018](#), using an X-ray light curve), have also been applied to measure the mass of central engines in radio-loud NLSy 1s. Currently, a comparison of the different methods has not been applied to a large sample yet. The use of seven different techniques for the source 1H 0323+342 yielded largely scattered results ($M_{\text{BH}} = 10^6\text{--}10^8 M_{\odot}$), but the majority of results showed a tendency towards a small black hole mass estimate (see Table 2 in [Komossa, 2018](#)). Still, the investigation regarding their masses is ongoing, and individual observations that yield different results make it difficult to converge to a conclusion.

The debate regarding their host galaxies is equally unresolved, as only a few radio-loud NLSy 1s have been systematically observed in order to determine the nature of their host galaxy. This topic, however, is particularly relevant to better understand what might trigger the jet production, especially if NLSy 1s are young AGN. A recent study by [Olguín-Iglesias et al. \(2020\)](#) of 29 radio-loud NLSy 1s suggests that a large fraction of those reside in disk galaxies. About half of these show no indication that they are involved in a merger. However, they exhibit bars, which could feed the central engine via gas-inflow. Such bars have also been found in the hosts of radio-quiet NLSy 1s and serve as an explanation how nuclear activity can be triggered through secular processes. This is in contrast to what has been found for other radio-loud AGN, e.g., quasars and blazars, which are hosted in elliptical galaxies ([Dunlop et al., 2003](#), [Olguín-Iglesias et al., 2016](#)). Some radio-loud NLSy 1s appear to be in a merging

¹FIRST stands for Faint Images of the Radio Sky at Twenty-Centimeters and is a survey conducted at ~ 1400 MHz with the NRAO Very Large Array (VLA; <http://sundog.stsci.edu/>).

²Powerful radio sources with a size between 1 and 20 kpc, and showing a convex radio spectrum peaking below 500 MHz (see, e.g., recent review by [O’Dea & Saikia, 2021](#))

process (Paliya et al., 2018, Berton et al., 2019, Paliya et al., 2020, Salomé et al., 2021). As the majority of radio-loud NLSy 1s is found at redshifts $z > 0.2$, it is currently not possible to study resolved images of the host galaxies for a large sample of sources with the SDSS³. Deep, pointed observations of individual sources with sensitive instruments, like the Hubble Space Telescope, are needed to make progress at the moment, until a more sensitive survey is in place and can shed more light on the nature of the host galaxies of radio-loud NLSy 1s.

Among the radio-loud NLSy1s, a few have been detected by the *Fermi*/LAT, which is observing the γ -ray sky (see Sect. 2.1.3). The second data release of the Fourth *Fermi*/LAT source catalog (4FGL; Abdollahi et al., 2020) lists nine γ -ray emitting NLSy 1 (γ -NLSy 1) galaxies, while other studies have announced a few more identifications (e.g., Romano et al., 2018, Ciprini & *Fermi*-LAT Collaboration, 2018, Paliya et al., 2018). Including those, up to 20 γ -NLSy 1s are known. Their γ -ray emission serves as evidence for the presence of a relativistic jet, which is a typical characteristic of blazars. The powerful relativistic jets of blazars are linked to SMBH masses exceeding $10^8 M_{\odot}$ (e.g., Chiaberge & Marconi, 2011, Sikora et al., 2007), so the rather small SMBH masses of γ -NLSy 1s, if confirmed, challenges the understanding of how jets are formed. The determination of the SMBH masses and hosts of γ -NLSy 1s is equally unclear as those of radio-loud NLSy 1s. For two of the γ -NLSy 1s their hosts have been identified with elliptical galaxies (FBQS J1644+2619 and PKS 1502+036, D’Ammando et al., 2017, 2018, respectively), but for the rest, the optical images suggest either disk-like galaxies, or they lack the resolution to allow a solid conclusion.

γ -NLSy 1s exhibit several similarities to blazar, one of which is γ -ray variability that can even result in γ -ray flares, which are typical for blazars. Up to now, five γ -NLSy 1s have shown at least one flare. These sources are 1H 0323+342 (Paliya et al., 2014), SBS 0846+513 (D’Ammando et al., 2012), PMN J0948+0022 (Foschini et al., 2011, D’Ammando et al., 2015), which has been observed in outburst twice, PKS 1502+036 (Paliya & Stalin, 2016, D’Ammando et al., 2016), and PKS 2004–447 (Gokus et al., 2021b), which is presented in this work.

5.2 The γ - and radio-loud NLSy1 galaxy PKS 2004–447

PKS 2004–447 was among the first γ -NLSy 1s detected by *Fermi*/LAT, which constituted a new class of γ -ray emitting AGN next to blazars and radio galaxies (Abdo et al., 2009). Located on the Southern Hemisphere with a redshift of $z = 0.24$ (Drinkwater et al., 1997), it was classified as a NLSy 1 candidate by Oshlack et al. (2001) based on the width and strength of its $H\beta$ emission lines. Still, the classification of PKS 2004–447 as a NLSy 1 galaxy has been under dispute, because the source is an outlier in several regards. While Sulentic et al. (2003) proposed a type 2 AGN classification for this source after examining the strength of optical [Fe II] emission lines in radio-loud AGN, and finding a lack thereof in the spectra of PKS 2004–447, Berton et al. (2021), analysing high-quality spectral data, confirmed that the optical spectrum of PKS 2004–447 includes all characteristics of a NLSy 1 source. Another proposition was that PKS 2004–447 could be a narrow-line radio galaxy (Komossa et al., 2006). While the classification remains an issue, the newest study of the source during a

³The Sloan Digital Sky Survey is an optical survey covering a large fraction of the sky (<https://www.sdss.org/>).

γ -ray outburst suggests that PKS 2004–447 could also belong to the blazar class (Gokus et al., 2021b).

PKS 2004–447 stands out in the sample of radio-loud NLSy 1s due to its remarkably high radio brightness. Oshlack et al. (2001) reported $R = 1700 - 6300$, Gallo et al. (2006), using simultaneous optical and radio emission measurements, found $R = 3800$. Previous analyses of the radio spectrum of PKS 2004–447 revealed the CSS character of the source (Oshlack et al., 2001, Gallo et al., 2006). A recent study by Schulz et al. (2016) confirms former findings and determined a turnover in the radio spectrum below 2 GHz, while their VLBI images taken with TANAMI at 8.4 GHz revealed a one-sided jet with some extended emission.

While a soft excess in their X-ray spectra is a common feature among NLSy 1s, only a tentative hint has been found by Gallo et al. (2006), and could not be confirmed in an extensive analysis, including all available X-ray data up to 2014 (Kreikenbohm et al., 2016). In regards to similarities with other CSS sources, Kreikenbohm et al. (2016) found that both the X-ray photon index and the unabsorbed luminosity (0.5–10 keV band) of PKS 2004–447 fall in the range of usual attributes of low-powered CSS sources. The featureless X-ray spectrum of the source can be well described with an absorbed power law and indicates that the main contribution of X-ray emission is made by the jet.

PKS 2004–447 is one of the sources for which the mass estimate has been under debate for several years. Using the virial method and calculating the mass of the SMBH based on the width of the $H\beta$ emission line in the spectrum, Oshlack et al. (2001) reported a mass of $M_{BH} \sim 5 \cdot 10^6 M_{\odot}$. However, comparing the continuum luminosity at 5100Å of their spectrum with that by Drinkwater et al. (1997) as well as recent measurements by Berton et al. (2019), it turns out that the spectrum normalisation by Oshlack et al. (2001) was underestimated. Taking this into account, and using the values of the $H\beta$ line dispersion and luminosity reported by Foschini et al. (2015), the black hole mass of PKS 2004–447 should be $7 \cdot 10^7 M_{\odot}$. This value has recently been confirmed by Berton et al. (2021) using also the virial method, but with new high-resolution data. They obtained a value of $M_{BH} \sim (1.5 \pm 0.2) \times 10^7 M_{\odot}$. Baldi et al. (2016), determining the black hole mass via spectropolarimetry, however, reports $M_{BH} = 6 \cdot 10^8 M_{\odot}$ for PKS 2004–447, which is one order of magnitude above the value derived from the dispersion line measurement. As mentioned above, this topic is still under debate for several radio-loud NLSy 1s, as different methods can yield quite different results.

The host of PKS 2004–447 was found to be a barred galaxy with two spiral arms, while also exhibiting a pseudo-bulge (Kotilainen et al., 2016).

In a study by Paliya et al. (2013), the properties of PKS 2004–447 were compared with the FSRQ 3C 454.3, and the BL Lac Mrk 421. Overall, the SED of PKS 2004–447 resembles more that of typical FSRQs, while for several characteristics, like the Compton dominance, the X-ray and γ -ray spectral index, and the γ -ray luminosity, the γ -NLSy 1 lies in between the values of the typical FSRQ and BL Lac. Including three other γ -NLSy 1s in the comparison confirmed the similarities towards FSRQs, even though the γ -ray luminosities of all γ -NLSy 1s differed from each other.

5.3 Multiwavelength analysis of its first γ -ray flare

Up until October 2019, PKS 2004–447 had shown moderate long-term variability in the γ -ray regime. On 2019 October 25, however, the source exhibited a strong γ -ray flux increase on a short time scale, similar to what is usually only seen in blazars. Compared to the 10-year average flux level, its flux rose by a factor of 55 (Gokus, 2019). PKS 2004–447 is the fifth γ -NLSy 1 source to show such a γ -ray flare, showing how small the sample of flaring γ -NLSy 1s actually is.

In order to take full advantage of this opportunity and study the source and its multi-wavelength behaviour in detail, we obtained several follow-up observations in different energy bands, namely with *NuSTAR*, *XMM-Newton*, *Swift*, and the Australia Compact Telescope Array (ATCA).

In Sect. 5.3.1, I will describe the data analysis of the observations at different wavelengths. Section 5.3.2, Sect. 5.3.3, and Sect. 5.3.4 cover the variability analysis at different energies, the X-ray spectral analysis, and the SED modelling, respectively. A detailed discussion of our findings is given in Sect. 5.4, including a comparison of the flaring state SED of PKS 2004–447 with that of the few other γ -ray flaring NLSy 1 galaxies.

5.3.1 Observations and data reduction

This section has been taken for most parts in verbatim from Gokus et al. (2021b).

Fermi/LAT observations

The reduction of the *Fermi*/LAT data follows the standard data reduction process⁴ and uses the `Science Tools v11r04p00`. We extract those events suitable for an analysis⁵ with energies in the range from 100 MeV to 300 GeV in a region of interest (ROI) of 15° centred at the 4FGL position of PKS 2004–447. We ignore all events with zenith angles $\geq 90^\circ$, in order to exclude γ -rays originating from Earth-limb effects. We use the post-launch instrument response function `P8R3_SOURCE_V2`, `gll_iem_v07` as the Galactic diffuse model and `iso_P8R3_SOURCE_V2_v1` to model the isotropic diffusion emission⁶. We use a maximum likelihood analysis to optimise our model parameters and determine the significance of the modelled γ -ray signal via the test statistic $TS = 2\Delta \log \mathcal{L}$, where \mathcal{L} is the likelihood function that represents the difference between models with and without a point source at the source coordinates (Mattox et al., 1996). Our model includes all 4FGL sources within a field of 20° in diameter, centred on PKS 2004–447. Following the 4FGL, we model the spectrum of PKS 2004–447 with a logarithmic parabola and discuss the significance of the spectral curvature during the time of the flare in Section 5.3.2. For all sources within 3° that have $TS \geq 10$, as well as for the isotropic and Galactic diffuse components, we leave the normalisation free to vary but keep the spectral parameters as reported in the 4FGL. For the sources not fulfilling these requirements, the normalisation is set to their respective 4FGL value as well.

⁴<https://fermi.gsfc.nasa.gov/ssc/data/analysis/documentation/>

⁵We use SOURCE class events and set the following flags: `(DATA_QUAL>0)&&(LAT_CONFIG==1)`

⁶The background models are available at <https://fermi.gsfc.nasa.gov/ssc/data/access/lat/BackgroundModels.html>

Data used for compiling the low-state SED are centred in time on *Swift* and *XMM-Newton* observations performed in 2012 March and May, respectively (see [Kreikenbohm et al., 2016](#)). They cover 24 months from 2011 May 1 through 2013 May 1.

We compute a daily-binned light curve from 2019 September 26 to 2019 November 19, shown in Fig. 5.1, and keep the parameters of all sources in the ROI fixed to the values derived by the analysis over this time range. For a deeper investigation of the γ -ray variability in the source around the time of the γ -ray flare, we go to smaller time binnings (12 h, 6 h, and 3 h). We generate these light curves similarly to the daily-binned light curve, but over a slightly shorter time range, from 2019 October 10 to 2019 November 14. Uncertainties for all *Fermi*/LAT light curves are shown at the 1σ level.

Neil Gehrels Swift Observatory observations

Following our detection of the flare of PKS 2004–447 on 2019 October 25 ([Gokus, 2019](#)), we triggered a target of opportunity observation with the *Swift* satellite (see also Sect. 2.2.4), which was performed on 2019 October 27 ([D’Ammando et al., 2019](#)). Further follow-up observations were performed on 2019 October 28 and 30 and 2019 November 4, 6, 9, and 13, in photon counting mode. In order to clean the data and create calibrated event files we used the standard filtering methods and `xrtpipeline`, as distributed in the HEASOFT (v6.26) package. The spectrum of the source was accumulated from a circular region with a radius of $35''$. The background region was defined by an annulus with an inner radius of $50''$ and an outer radius of $150''$ at the same coordinates as the source region.

To derive the source fluxes and describe the spectral shape, we use the Interactive Spectral Interpretation System (ISIS, Version 1.6.2-40, [Houck & Denicola, 2000](#)). Throughout this chapter, we describe the absorption in the interstellar medium using `vern` cross sections ([Verner et al., 1996](#)) and `wilm` abundances ([Wilms et al., 2000](#)). We use C-statistics ([Cash, 1979](#)) and estimate all uncertainties at 68% confidence (1σ). The source spectra are binned after the algorithm described by [Kaastra & Bleeker \(2016\)](#) in order to ensure optimal binning. We adopt an absorbed power law (`tbabs*powerlaw`) to model each spectrum. The Galactic H I column density, $N_{\text{H,Gal}} = 2.97 \times 10^{20} \text{ cm}^{-2}$, is taken from the H I 4π survey (HI4PI; [HI4PI Collaboration, et al., 2016](#)), modelled with `tbabs` ([Wilms et al., 2000](#)), and kept fixed during the fit. The observations confirm a high state of the X-ray flux compared to previous X-ray data (an overview of all X-ray observations between 2004 and 2012 is given by [Kreikenbohm et al., 2016](#)). The results are listed in Table 5.1, including those from the *XMM-Newton* and *NuSTAR* data analysed in this work. For the X-ray light curve we analyse each *Swift*/XRT observation individually. In order to build SEDs we stack all *Swift* observations that fall into the time interval considered.

Simultaneously to the XRT, the Ultraviolet/Optical Telescope (UVOT) on board *Swift* was observing the source, and we use this instrument to derive optical and ultraviolet fluxes. The data are reduced using the standard procedures with a source region of $5''$ and a background annulus with an inner radius of $7''$ and an outer radius of $21''$. The optical-UV fluxes shown here are dereddened via the $E(B - V)$ correction using the Fitzpatrick parametrisation ([Fitzpatrick, 1999](#)). The magnitude values are converted to flux units using the unfolding procedure implemented in ISIS, which is a model-independent approach described by [Nowak et al. \(2005\)](#). The optical-UV light curve is shown in Fig. 5.1.

XMM-Newton observations

In addition to the *Swift* monitoring, we performed an *XMM-Newton* ToO observation on 2019 October 31 with an exposure time of 11 ks (ObsID: 0853980701). Archival data taken during the low state of the source were obtained from an observation in 2012 May, which has been discussed in detail by Kreikenbohm et al. (2016). The observations by *XMM-Newton* (see details on this instrument in Sect. 2.2.3) were performed with both the EPIC-PN and the EPIC-MOS CCD arrays. Simultaneously to the X-ray observation, the optical-UV emission was observed with OM.

The observation with the EPIC was performed in the Small Window Mode with a thin filter. We use standard methods of the *XMM-Newton* Science Analysis System (SAS, Version 18.0) to process the observation data files, and to create calibrated event lists and images. We extract the source spectrum and a light curve for an energy range from 0.5 keV to 10 keV from a circular region of 35'' radius around the source. The background is taken from a circle with a radius of 60''. For both the source and the background spectra we extract the single and double event patterns for the EPIC-pn detector and all events for the EPIC-MOS detectors. Pile-up during the observation is negligible. We fit the spectra of the EPIC-MOS and EPIC-pn detectors simultaneously with an absorbed power law, while using the optimal binning approach. The result is listed in Table 5.1 together with the results from the analysis of *Swift*/XRT and *NuSTAR* observations. The X-ray flux of PKS 2004–447 seen by *XMM-Newton* shortly after the flare is also part of the X-ray light curve in Fig. 5.1.

The OM observed the source in the *v*, *b*, *u*, *w1*, and *m2* filters in imaging mode with an exposure time of 1200 s, 1200 s, 1200 s, 1780 s, and 2200 s, respectively. The data were processed using the SAS task `omichain` and `omsource`. For the count rate to flux conversion we used the conversion factors given in the SAS watchout dedicated page⁷. The optical/UV fluxes were dereddened via $E(B - V)$ correction, using the same approach as for *Swift*, and are included in the light curve shown in Fig. 5.1.

NuSTAR observations

We performed a ToO observation with *NuSTAR* (see Sect. 2.2.5) with an exposure of 30 ks on 2019 November 1 (ObsID: 90501649002). We use standard methods of the software package NUSTARDAS (Version v1.8.0) distributed in HEASOFT and the calibration database (CALDB) version 20190812 to reduce and extract the data for both Focal Plane Modules A and B (FPMA, FPMB). We use `nuproducts` to create spectra and response files. We choose a circular region with 50'' radius for the source region, and a circle with 120'' radius in a source-free region as the background region. We use the same binning method as we used for the *Swift*/XRT and *XMM-Newton* spectra and fit the spectra from FPMA and FPMB simultaneously with an absorbed power law from 3 to 79 keV. The result is given in Table 5.2. In order to compare the flux directly with the other X-ray observations in the light curve in Fig. 5.1, we extrapolate the flux down to 0.5 keV and list this value for the flux in Table 5.1. Initial modelling of the data shows a slight indication for a spectral hardening at higher energies that is, however, also compatible with residuals caused by slight variations of the background at the $\sim 10\%$ level. In our final fits we therefore vary the normalisation of the background by introducing a multiplicative constant that accounts for this variation.

⁷<https://www.cosmos.esa.int/web/xmm-newton/sas-watchout-uvflux>.

Table 5.1.: Results from the analysis of the individual X-ray observations by *Swift*/XRT (S), *XMM-Newton*/MOS+pn (X) and *NuSTAR*/FPMA+B (N). We report unabsorbed fluxes in units of 10^{-12} erg cm $^{-2}$ s $^{-1}$. The photon index (Γ) reported for *NuSTAR* is the index for the full *NuSTAR* energy range from 3 to 79 keV and the flux is extrapolated down to 0.5 keV. This table is taken from Gokus et al. (2021b).

ObsDate	Instrument	ObsID	Exposure [ks]	$\Gamma_{0.5-10 \text{ keV}}$	Flux $_{0.5-10 \text{ keV}}$	C-stat./dof
2019-10-02	S	00081881003	1.2	1.3 ± 0.4	$1.2^{+0.5}_{-0.3}$	55.72/45
2019-10-05	S	00081881004	0.9	1.4 ± 0.4	$1.1^{+0.5}_{-0.3}$	27.30/45
2019-10-09	S	00081881005	2.0	1.02 ± 0.21	1.9 ± 0.4	40.03/45
2019-10-27	S	00032492020	2.9	1.62 ± 0.18	$1.59^{+0.25}_{-0.22}$	59.59/46
2019-10-28	S	00032492021	2.0	1.14 ± 0.21	$2.0^{+0.4}_{-0.3}$	46.34/45
2019-10-30	S	00032492022	1.6	$0.69^{+0.29}_{-0.30}$	$3.5^{+1.1}_{-0.9}$	61.51/45
2019-10-31	X	0853980701	11.2	1.424 ± 0.024	2.06 ± 0.05	97.23/80
2019-11-01	N	90501649002	30.1	1.31 ± 0.05	1.10 ± 0.04	357.54/331
2019-11-04	S	00032492024	3.6	1.31 ± 0.15	$1.90^{+0.29}_{-0.25}$	61.64/46
2019-11-06	S	00032492025	0.7	$1.79^{+0.26}_{-0.25}$	$2.8^{+0.7}_{-0.6}$	33.31/45
2019-11-09	S	00032492026	3.4	1.97 ± 0.23	$0.88^{+0.17}_{-0.14}$	38.50/45
2019-11-13	S	00032492027	2.5	1.27 ± 0.19	$1.9^{+0.4}_{-0.3}$	50.87/45

ATCA observations

For our study, we used ATCA (see Sect. 2.4.2) monitoring data between 5.5 GHz and 40 GHz, which were collected for the pre-flare and the flaring states⁸. The data consist of snapshot observations of PKS 2004–447 covering a duration of several minutes, and were calibrated against the ATCA primary flux calibrator PKS 1934–638. Data reduction is carried out in the standard manner with the MIRIAD software package⁹.

5.3.2 Variability

This section has been taken in verbatim from Gokus et al. (2021b).

Figure 5.1 shows the light curves for PKS 2004–447 based on the daily-binned γ -ray emission, and individual X-ray observations by *Swift*/XRT and *XMM-Newton*/EPIC, and optical-UV observations by *Swift*/UVOT and *XMM-Newton*/OM. The γ -ray flux started to rise on 2019 October 23 (MJD 58779). It reached a daily-averaged maximum of $(1.2 \pm 0.2) \times 10^{-6}$ ph cm $^{-2}$ s $^{-1}$, which was maintained over about two days. After that, the flux decreased within two days, returning to the same flux level as before the flare. In the 3 h binned γ -ray light curves, on 2019 October 26 (MJD 58782.6), we find a maximum flux of $(2.7 \pm 0.6) \times 10^{-6}$ ph cm $^{-2}$ s $^{-1}$. This is the highest γ -ray flux ever measured for PKS 2004–447. Using the spectral index of $\Gamma_{0.1-300\text{GeV}} = 2.42 \pm 0.09$ measured during the flare, we derive an isotropic γ -ray luminosity of $(2.9 \pm 0.8) \times 10^{47}$ erg s $^{-1}$. The light curves binned on different timescales are shown in Fig. 5.4. For all analyses that follow, we do not include any time bins

⁸Supplementary data from the C 007 ATCA calibrator programme were used.

⁹<http://www.atnf.csiro.au/computing/software/miriad/>

5.3. MULTIWAVELENGTH ANALYSIS OF ITS FIRST γ -RAY FLARE

Table 5.2.: Summary of the analysis of each individual energy range for each SED. The optical-UV fluxes are in units of 10^{-12} erg cm $^{-2}$ s $^{-1}$. For the X-rays, we report the unabsorbed flux. This table adapted from Gokus et al. (2021b).

		Gamma-ray				
Activity state	Time bin (MJD)	$\Gamma_{0.1-300 \text{ GeV}}$	$F_{0.1-300 \text{ GeV}}$ [10^{-8} ph cm $^{-2}$ s $^{-1}$]	TS		
Low	55682–56413	2.39±0.13	1.2±0.3	50.4		
Pre-flare	58754–58770	2.62±0.22	16±4	38.8		
Flare	58781–58784	2.42±0.09	130.0±11.6	472		
Post-flare	58787–58789	2.22±0.17	43±9	97		
		Soft X-ray				
Activity state	Exposure (ksec)	$\Gamma_{0.5-10 \text{ keV}}$	Flux $_{0.5-10 \text{ keV}}$ [10^{-12} erg cm $^{-2}$ s $^{-1}$]	Statistics C-stat./dof		
Low (<i>XMM</i>)	31.76	1.682 ± 0.029	0.451 ± 0.013	80.36/76		
Pre (<i>Swift</i>)	4.05	1.14 ± 0.16	1.53 $^{+0.25}_{-0.22}$	55.06/45		
Flare (<i>Swift</i>)	2.90	1.62 ± 0.18	1.59 $^{+0.25}_{-0.22}$	59.59/46		
Post (<i>XMM</i>)	7.77	1.424 ± 0.024	2.06 ± 0.05	97.23/80		
		Hard X-ray				
Activity state	Exposure (ksec)	$\Gamma_{3-79 \text{ keV}}$	Flux $_{3-79 \text{ keV}}$ [10^{-12} erg cm $^{-2}$ s $^{-1}$]	Background norm	Statistics C-stat./dof	
Post-flare (<i>NuSTAR</i>)	30.07	1.31 ± 0.05	6.3 $^{+0.5}_{-0.4}$	0.89 ± 0.12 (A) 1.07 $^{+0.14}_{-0.13}$ (B)	357.54/331	
		Optical-UV				
Activity state	V	B	U	UVW1	UVM2	UVW2
Low	0.72 ± 0.05	0.50 ± 0.03	0.34 ± 0.02	0.18 ± 0.01	0.12 ± 0.01	0.12 ± 0.01
Pre	0.55 ± 0.24	0.55 ± 0.14	0.44 ± 0.09	0.23 ± 0.05	0.11 ± 0.04	0.12 ± 0.04
Flare	3.12 ± 0.24	2.99 ± 0.14	2.05 ± 0.10	0.92 ± 0.06	0.73 ± 0.20	0.44 ± 0.03
Post	2.8 ± 0.3	1.90 ± 0.18	1.32 ± 0.14	0.65 ± 0.11	0.31 ± 0.07	0.27 ± 0.05

with TS < 4, but, for visual purposes, we plot these data points as upper limits in Fig. 5.1 and Fig. 5.4. The *Fermi*/LAT upper limits state the maximum possible flux at a 2σ level for a very low or zero detection significance, and are strongly correlated with the exposure time, i.e., the amount of data taken into account for the analysis.

At X-ray energies (0.5–10 keV), the maximum flux was measured on 2019 October 30 (MJD 58786), with $3.3^{+1.1}_{-0.9} \times 10^{-12}$ erg cm $^{-2}$ s $^{-1}$ and a power law index of 0.8 ± 0.3 . The short exposure time of this observation results in poor constraints on the spectral parameters. The optical emission in the V, B, and U bands shows strong variations. The maximum flux occurred on 2019 October 27 (MJD 58783), which coincides with the γ -ray flare.

To quantify the variability, we first apply a χ^2 test against the null hypothesis that the emission from PKS 2004–447 is constant in each energy band. In the γ -ray band, we find a null-hypothesis probability of $p < 0.006$ for each of the light curves, regardless of their time binning, thus confirming variability. With a p -value < 0.00001, the X-ray light curve shown in Fig. 5.1 exhibits significant variability as well. On shorter timescales, however, significant variability is neither detected in the *XMM-Newton* ($p = 0.06$) nor the *NuSTAR* ($p \sim 1$) data. In the optical-UV band, strong variability ($p < 0.03$) at a level of up to a factor of five compared

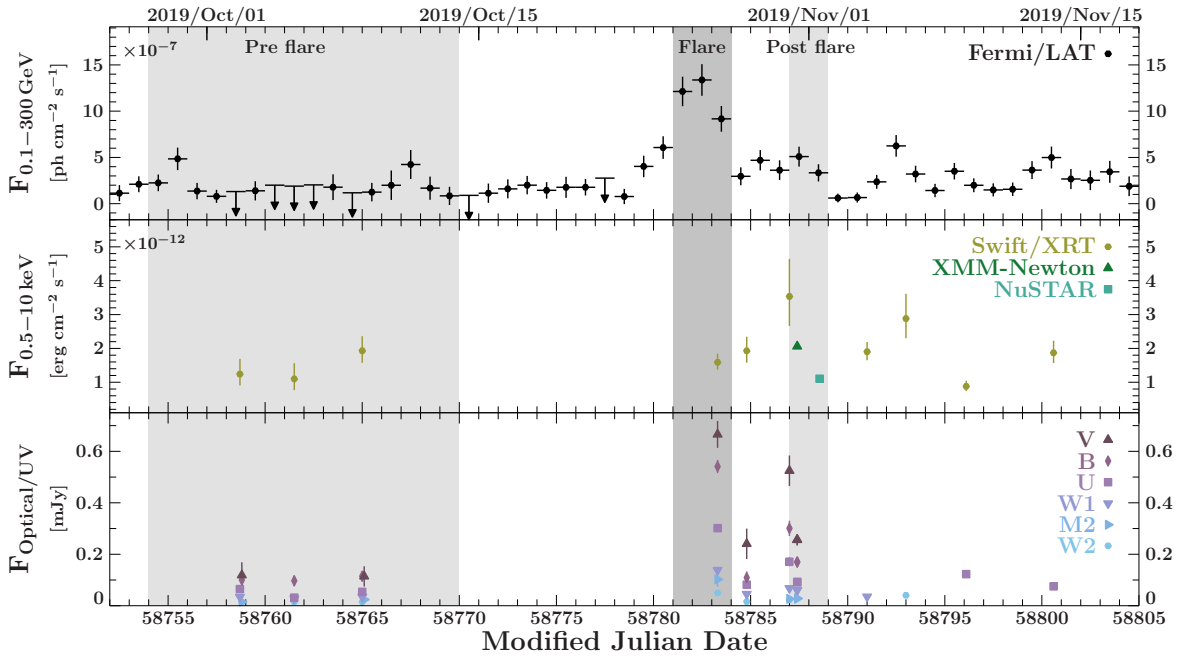


Figure 5.1.: Light curves in the γ -ray (top), X-ray (middle), and UV/optical (bottom) regimes from 2019 September 27 until 2019 November 19. The *Fermi*/LAT light curve shows the daily binned flux of the bins with $\text{TS} \geq 1$. LAT light curve bins with $\text{TS} < 1$ are represented as 2σ upper limit arrows. All errors represent the 1σ uncertainties. For *NuSTAR*, the flux is interpolated down to 0.5 keV. The dark-grey shadowed region marks the time range that is used for the flare SED, while the pre- and post-flare time ranges are shown in light grey.

Credit: Gokus et al., *A&A*, 649, A77, 2021, reproduced with permission © ESO

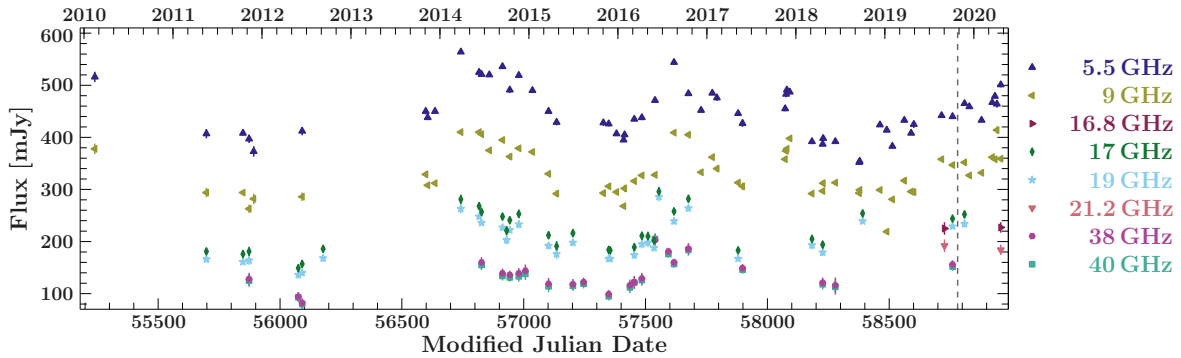


Figure 5.2.: ATCA light curves taken from 2010–2020 in the $\lambda 4$ -cm (5.5 GHz, 9 GHz), $\lambda 15$ -mm (16.8 GHz, 17 GHz, 19 GHz, and 21.2 GHz) and $\lambda 7$ -mm band (38 GHz, 40 GHz). The time of the flare is marked by a dashed grey line.

Credit: Gokus et al., *A&A*, 649, A77, 2021, reproduced with permission © ESO

to the flux before the flare is observed with the maximum roughly coinciding with the γ -ray flare.

Variability is also seen in the ATCA radio light curves (see Fig. 5.2). This is in agreement with earlier work by Schulz et al. (2016), who discussed the radio variability of PKS 2004–447 based on TANAMI/ATCA observations between 2010 and 2014 and found moderate variability. Given that only two observations are located in the time range in which we analysed the γ -

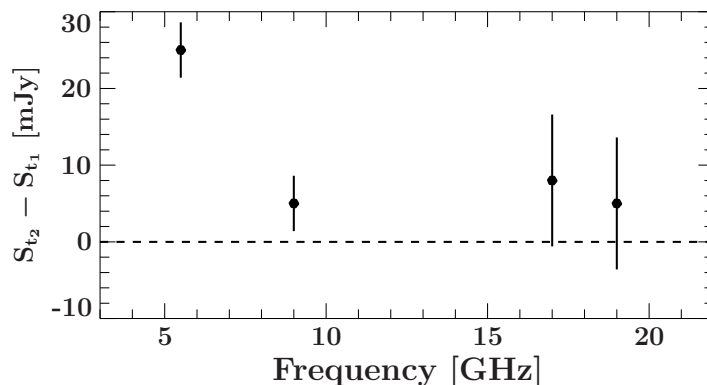


Figure 5.3.: Difference spectrum derived from the radio observations 21 days before (t_1) and 28 days after (t_2) the flare. The dashed line marks the zero change of the flux.

Credit: Gokus et al., *A&A*, 649, A77, 2021, reproduced with permission © ESO

and X-ray variability, we do not conduct the chi-squared test on these. Following the ATCA calibrator database documentation¹⁰, we have flagged several epochs that were plotted in Schulz et al. (2016). We show an updated version of the PKS 2004–447 radio light curve, including data up to early 2020. These data are presented in Table A.4 in the Appendix. The uncertainties reported are statistical only and do not include any systematic errors, which in general are known to be smaller than 5% in the centimetre bands (Tingay et al., 2003).

The radio emission of PKS 2004–447 from 2018 through early 2020 can be described with an overall rising trend in all radio bands. In the months prior to the γ -ray flare (marked by the dashed grey line in Fig. 5.2), PKS 2004–447 showed a relatively constant flux-density level of about 440 mJy at 5.5 GHz and 350 mJy at 9 GHz. Full broadband radio spectra of PKS 2004–447 were taken on 2019 October 4 and 2019 November 22, namely about 21 days before and 28 days after the 2019 October 25 γ -ray flare. Figure 5.3 shows a difference spectrum, which illustrates the difference between the spectra derived during each of these two epochs. While the higher frequencies show only a mild increase in radio emission after the flare, the 5.5 GHz emission rose by ~ 25 mJy ($\sim 6\%$). It is not possible to determine whether this increase is related to the γ -ray flare. For other AGNs, delays of a few months have been reported between γ -ray flares and subsequent radio flux density increases (e.g. Fuhrmann et al., 2014, Ramakrishnan et al., 2015).

To look further into the flare behaviour in γ -rays, the Bayesian-block algorithm is applied (Scargle et al., 2013, Wagner et al., 2022).¹¹ According to Meyer et al. (2019), a flare can be described as a group of blocks, which is determined by applying the HOP¹² algorithm. In this algorithm, each Bayesian block that surpasses a certain baseline is assigned to belong to its highest adjacent block. For this work, we chose the mean flux of each light curve to represent the baseline flux, as illustrated in yellow in Fig. 5.4. The total duration of the flare can then be defined as the time range between the beginning of the first block and the end of the last block

¹⁰https://www.narrabri.atnf.csiro.au/calibrators/calibrator_database_documentation.html

¹¹See also the repository by S. Wagner, which contains the analysis of flares in γ -ray light curves, including the Bayesian Block and HOP algorithm: <https://github.com/swagner-astro/lightcurves>

¹²The name HOP is not an acronym, but taken from the verb ‘to hop’ to each data element’s highest neighbour (Eisenstein & Hut, 1998).

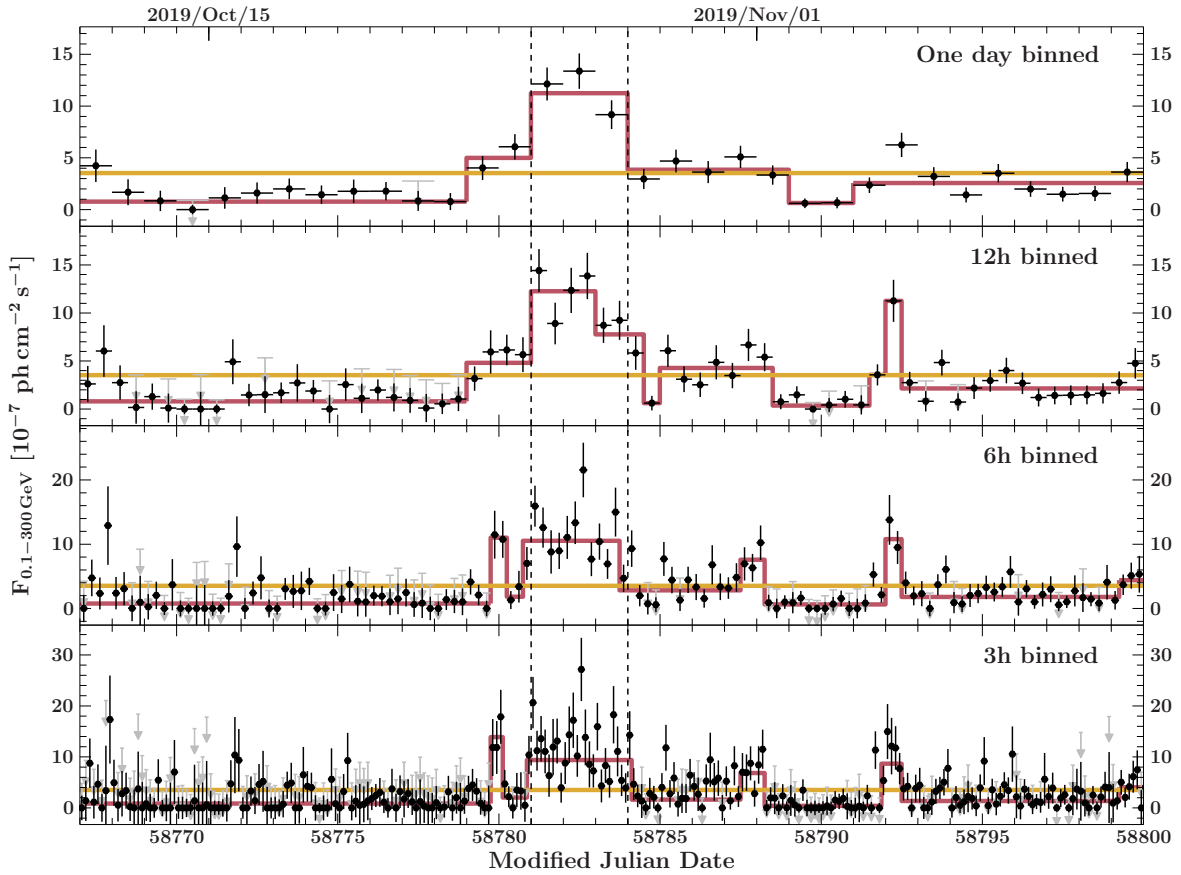


Figure 5.4.: Gamma-ray light curves of PKS 2004–447 during the 2019 GeV flare for the different time binnings of the LAT data. Time bins with $TS < 1$ have an estimated error that was derived using their 1σ upper limit value. For those bins we show the 2σ upper limits in grey to visually show how many bins would have been rejected from the analysis otherwise. The Bayesian blocks are shown in red, while the baseline (average flux during the time range from 2019 October 10 to 2019 November 14) is shown in yellow. The dashed lines mark the time range chosen to construct the broadband SED of the flaring state.

Credit: Gokus et al., *A&A*, 649, A77, 2021, reproduced with permission © ESO

above the baseline, while the peak is assumed to be located at the centre of the maximum block. This time range is defined as a HOP group¹³, for which we measure the rise time τ_{rise} from the beginning of the HOP-group to the peak, and the decay time τ_{decay} from the peak to the end of the HOP-group. We conservatively estimate the error on the edge of each Bayesian block to be as big as the binning of each respective light curve (e.g., $\pm 1\text{d}$ in daily binning). To apply this method to the *Fermi* light curves of PKS 2004–447, we calculate the Bayesian blocks as described by Scargle et al. (2013), and set the parameter $\text{ncp_prior} = 2$.

A source is not necessarily detected significantly in each light curve bin, hence upper limits on the flux are usually reported (see e.g., the *Fermi*/LAT light curve in Fig. 5.1) in order to give an indication about the trend of the flux of a source. In a standard LAT light-curve analysis, it is not straightforward to deal with data bins that have a low test statistic. Moreover, the

¹³Meyer et al. (2019) added an additional criterion requiring that the maximum block is at least five times above the average flux in order to single out only the brightest flares, which we drop in our analysis.

Table 5.3.: Flare lengths in days for the different binnings of the *Fermi* light curves. The times τ_{rise} and τ_{decay} are derived via the HOP algorithm applied on the Bayesian block analysis. A is the asymmetry as defined in Eq. 5.1. This table is taken from Gokus et al. (2021b).

	τ_{rise} [d]	τ_{decay} [d]	A
Daily	3.5 ± 1	6.5 ± 1	-0.30 ± 0.15
12 h	3.0 ± 0.5	2.5 ± 0.5	0.09 ± 0.13
6 h	1.5 ± 0.25	1.5 ± 0.25	0.00 ± 0.12
3 h	1.625 ± 0.125	1.625 ± 0.125	0.00 ± 0.05

number of such low-significance flux bins typically increases for a finer binning. Specifically, this is problematic for the Bayesian-block point algorithm which assumes that the flux in each bin follows Gaussian statistics. For a low source significance this assumption is not valid. A common approach is to ignore the upper limits altogether, since upper limits cannot be inserted as such in the Bayesian-block algorithm, and therefore waive the information contained in data points with low significance, thus biasing the analysis results. To avoid this, we take all data into account and calculate best-possible flux values also in the case of low-significance data bins following the standard analysis procedure.

For light-curve bins that have a low significance, a problem that occurs in the determination of the fluxes and their corresponding uncertainties with the Likelihood calculation is that the Likelihood fit does not converge and this can then yield unreasonably small values for the flux uncertainties. This can have a strong influence on the Bayesian-block algorithm. Hence, to avoid this issue, rather than relying on the Likelihood to provide the uncertainties on the flux values, we calculate the 1-sigma upper limits for the flux in the low-flux bins and use the difference between these upper-limit values and the flux returned by the Likelihood as a conservative proxy for the magnitude of the flux uncertainties. This way, our light curve does not exhibit gaps and the Bayesian-block algorithm can be applied to a continuous dataset.

The results from the Bayesian-block algorithm are shown in red in Fig. 5.4. Following Meyer et al. (2019) we define the flare asymmetry via

$$A = \frac{\tau_{\text{rise}} - \tau_{\text{decay}}}{\tau_{\text{rise}} + \tau_{\text{decay}}}. \quad (5.1)$$

Uncertainties are obtained using Gaussian error propagation. The results are shown in Table 5.3.

The asymmetry values depend on the binning size chosen for the light curve. For the daily-binned light curve, the procedure yields an asymmetry value $A < 0$, indicating a faster rise than decay of the flare. The 12-hour binned light curve resolves more structure and a local dip at MJD 58785 followed by an increased flux level separated from the flare. Due to this the resulting Bayesian blocks indicate a slightly faster decay than rise ($A > 0$). The 6- and 3-hour binning, in turn, resolve this to consist of a very short and a longer symmetric flare. We focus on the latter, which lies within the time range chosen to construct the SED of the flaring state as indicated with dashed lines in Fig. 5.4. The properties of this flare and the corresponding higher binnings are reported in Table 5.3, but it is important to note that the 6- and 3-hour flares only represent a fraction of the daily and 12-hour one. Furthermore, the 6- and 3-hour binned flares consist of one block only which, by definition, results in $A = 0$.

Thus, the perceived flare symmetry is most likely due to the analysis procedure and limited sensitivity rather than actual symmetry of the flux behaviour and the true flare shape remains unknown. Interestingly, nine days after the main flare a second, shorter flare is identified by the Bayesian-block algorithm in all light curves but the daily-binned one. This demonstrates that the γ -ray variability of the source takes place on sub-day scales. What appears to be one flare in daily binning is shown to consist of three independent flares in 6- and 3-hour binning. Unfortunately, the sensitivity of the instrument is not high enough to fully resolve this structure. In general, care has to be taken in the interpretation of Bayesian flare-duration studies by considering and testing different bin sizes.

To quantify this sub-dayscale variability, we scan all *Fermi* light curves for significant jumps in flux between adjacent data points and calculate the minimum doubling and halving times. The most significant flux difference ($\sim 2.88\sigma$) between adjacent data points is found in the 6-hour binned light curve at MJD 58792.0, during the second, shorter flare. We compute a flux-doubling timescale of $\tau_d = 2.2 \pm 0.8$ hours, assuming an exponential rise (Zhang et al., 1999).

We search for the presence of spectral curvature in the γ -ray spectrum of the brightest state during the flare (MJD 58781–58784) and obtain the curvature via

$$\text{TS}_{\text{curve}} = 2(\log\mathcal{L}(\text{logparabola}) - \log\mathcal{L}(\text{powerlaw})) \quad (5.2)$$

from Nolan et al. (2012). Our analysis yields $\text{TS}_{\text{curve}} = 11.66$, providing tentative evidence for the presence of curvature in the γ -ray spectrum. Although the photon index of 2.42 ± 0.09 measured during the flare is marginally harder than the average photon index of 2.60 ± 0.05 reported in 4FGL (Abdollahi et al., 2020), the difference is not large enough to claim that spectral hardening has taken place during the flare. PKS 2004–447 is significantly detected up to an energy of 3 GeV during the flare. The slight curvature of the spectrum and the increasing flux threshold for detection are responsible for the non-detection at higher energies. Attenuation of the γ -ray emission seen by *Fermi*/LAT due to pair production with the extragalactic background light (EBL) is negligible at these energies for the redshift ($z = 0.24$) of PKS 2004–447.

5.3.3 X-ray analysis

This section has been taken in verbatim from Gokus et al. (2021b).

As already mentioned, a feature often seen in X-ray spectra of NLSy 1 galaxies is a soft excess below 2 keV (Vaughan et al., 1999, Grupe, 2004). Previously, Gallo et al. (2006) found an indication of a soft excess in PKS 2004–447 in *XMM-Newton* data from 2004, while the source was in a higher state. However, Orienti et al. (2015) and Kreikenbohm et al. (2016) did not find an excess for PKS 2004–447 during its low state in 2012, and Kreikenbohm et al. (2016) could not confirm the excess in the data from 2004.

Given that the source showed its brightest X-ray flux compared to previous observations during the γ -ray flare reported here, we search for an excess below 2 keV in the *XMM-Newton* spectrum. We apply a simple, unbroken power law model with Galactic H I absorption. Similar to the analysis of the individual X-ray spectra, we use C-statistics (Cash, 1979) and estimate all uncertainties at 1σ confidence. All spectra are binned following the optimal binning procedure

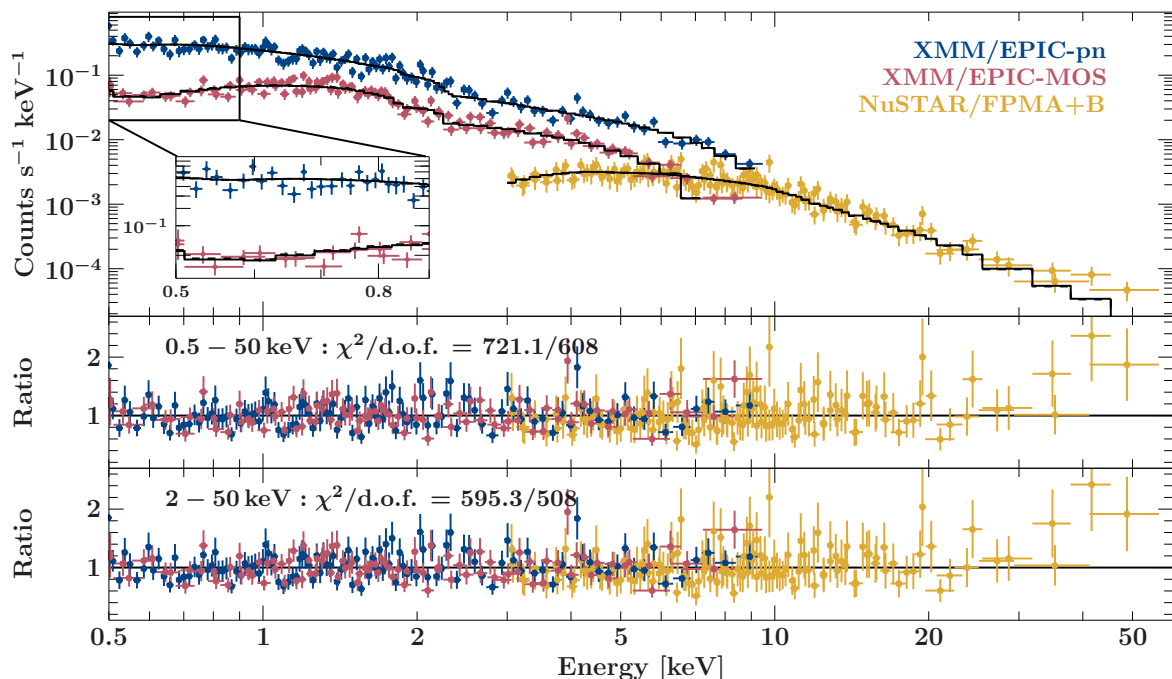


Figure 5.5.: *XMM-Newton* and *NuSTAR* spectra with the best-fit results of an absorbed power-law model. For plotting purposes only the spectra are binned to a S/N of 5 and 3 for *XMM-Newton* and *NuSTAR*, respectively. Bins from the *NuSTAR* spectrum are only shown up to 50 keV, because at energies above this, no significant bin for the given S/N value is found. *Upper panel:* EPIC pn (blue), MOS (red) and FPMA/FPMB (yellow) data together with the best fits for the full (0.5–80 keV) energy range (solid line) as well as the hard (2–80 keV) energy range (dashed line). The zoom window shows small deviations between the fits of the full and the hard energy range. *Middle panel:* Data-to-model ratio for the best fit to the full energy range. *Lower panel:* Data-to-model ratio for the best-fit to the hard energy range with extrapolating the model down to 0.5 keV.

Credit: Gokus et al., *A&A*, 649, A77, 2021, reproduced with permission © ESO

of [Kaastra & Bleeker \(2016\)](#). Modelling both the spectra obtained with *XMM-Newton* and *NuSTAR* individually between 3 and 10 keV with a power law yields compatible values for the power-law indices for both instruments ($\Gamma_{3-10\text{keV}} = 1.33 \pm 0.09$ for *XMM-Newton* vs. 1.37 ± 0.10 for *NuSTAR*). Although the observations are separated by one day, this result justifies the use of the spectra from both instruments for a combined analysis.

First, we fitted the data in the full energy range from 0.5 keV to 79 keV with a fixed N_{H} , which yields a good fit with $\chi^2_{\text{red}} = 1.18$ (721.1/608) and a best-fit power-law index of $\Gamma = 1.45 \pm 0.02$. Freeing the N_{H} parameter, we find an upper limit of ≤ 0.75 times the Galactic value for the absorption, meaning there is no evidence for significant intrinsic absorption in PKS 2004–447. Therefore, we kept this parameter fixed at the Galactic value in the further analysis.

To search for a soft excess, we fitted the spectra again, but only for the 2 – 79 keV band, and extrapolated the best fit down to 0.5 keV. We show the EPIC-pn and EPIC-MOS spectra in Fig. 5.5, where the fits to the full and the hard energy range are shown as a solid and a dashed line, respectively. For plotting purposes, the *XMM-Newton* spectra are binned with a signal-to-noise (S/N) ratio of 5 per energy bin, and the *NuSTAR* spectra with a S/N ratio of 3. The

fit results in a $\chi_{\text{red}}^2 = 1.17$ (595.3/508), and a photon index of $\Gamma = 1.45_{-0.02}^{+0.01}$. This power-law index agrees with that obtained from modelling the full fitted energy range. Describing the data with a broken power law also yields no evidence for a soft excess. We therefore conclude that there is no evidence for a soft excess in the X-ray spectrum of PKS 2004–447 during the 2019 October outburst as the fits are indistinguishable.

The presence of an iron $K\alpha$ line at 6.4 keV is also a common feature in NLSy 1 galaxies. Among the small γ -NLSy 1 sample, however, only 1H 0323+342 shows an indication for an Iron-line feature. For our data, adding an unresolved Gaussian line at 6.4 keV does not improve the fit statistics. We determine an upper limit for the equivalent width of $EW_{6.4\text{keV}} \leq 73$ eV at the 90% confidence level. This limit is slightly less constraining than what has been reported for this source in previous analyses (Gallo et al., 2006, Orienti et al., 2015, Kreikenbohm et al., 2016).

The photon index derived from the *XMM-Newton* observation is harder compared to the values derived from the low state analysed by Orienti et al. (2015) and Kreikenbohm et al. (2016), This fits into the ‘harder-when-brighter’ behaviour of blazars, more precisely BL Lacs (e.g. Giommi et al., 1990, Wang et al., 2018). During an *XMM-Newton* observation in 2004, and also at the end of 2013 during a monitoring campaign with *Swift*, PKS 2004–447 was in a bright state as well. However, a spectral hardening was not observed at these times (Gallo et al., 2006, Kreikenbohm et al., 2016), which suggests that different processes might be responsible for the X-ray variability that is present on monthly and yearly timescales.

5.3.4 SED modelling

The analysis of available broadband data is done by modelling the SED of PKS 2004–447 during different activity states. Archival data from 2012 revealed a low activity state of the source, and we use *Swift* and *XMM-Newton* observations taken in March and May of 2012, respectively, to obtain optical-UV and X-ray data. A *Fermi*/LAT spectrum was computed for a time range of 24 months from 2011 May 1 to 2013 May 1 in order to obtain enough statistics of the, at that time, weak γ -ray radiation and construct a spectrum. For the activity period in 2019, *Swift* observations are available for ca. one month, which allowed us to build three SEDs during different states: one covers a pre-flare state (MJD 58754–58770), another one the γ -ray flare (MJD 58781–58784), and the last one the time shortly after the flare (MJD 58787–58789).

A model to sufficiently describe the broadband emission is a simple one-zone synchrotron inverse Compton model (e.g., Sikora et al., 2009, Ghisellini & Tavecchio, 2009, Dermer & Menon, 2009), for which a spherical emission region with radius R_{blob} is assumed to travel along the jet with a bulk Lorentz factor Γ_b . The semi-opening angle of the jet is considered to be 0.1 radian, while the emission region covers the complete cross-section. A small viewing angle of 2° was assumed, similar to those selected for modelling the emission of beamed AGN (e.g., Ghisellini & Tavecchio, 2015). Interestingly, VLBA observations at 1.5 GHz have revealed a possible counter-jet (Schulz et al., 2016), which is in contradiction to a small viewing angle. Considering a correspondingly larger viewing angle would, however, results in an extreme reduction of the Doppler boosting (e.g., Dermer, 1995), but for which a large value is necessary to explain the large-amplitude γ -ray flare. One of the possibilities to resolve this

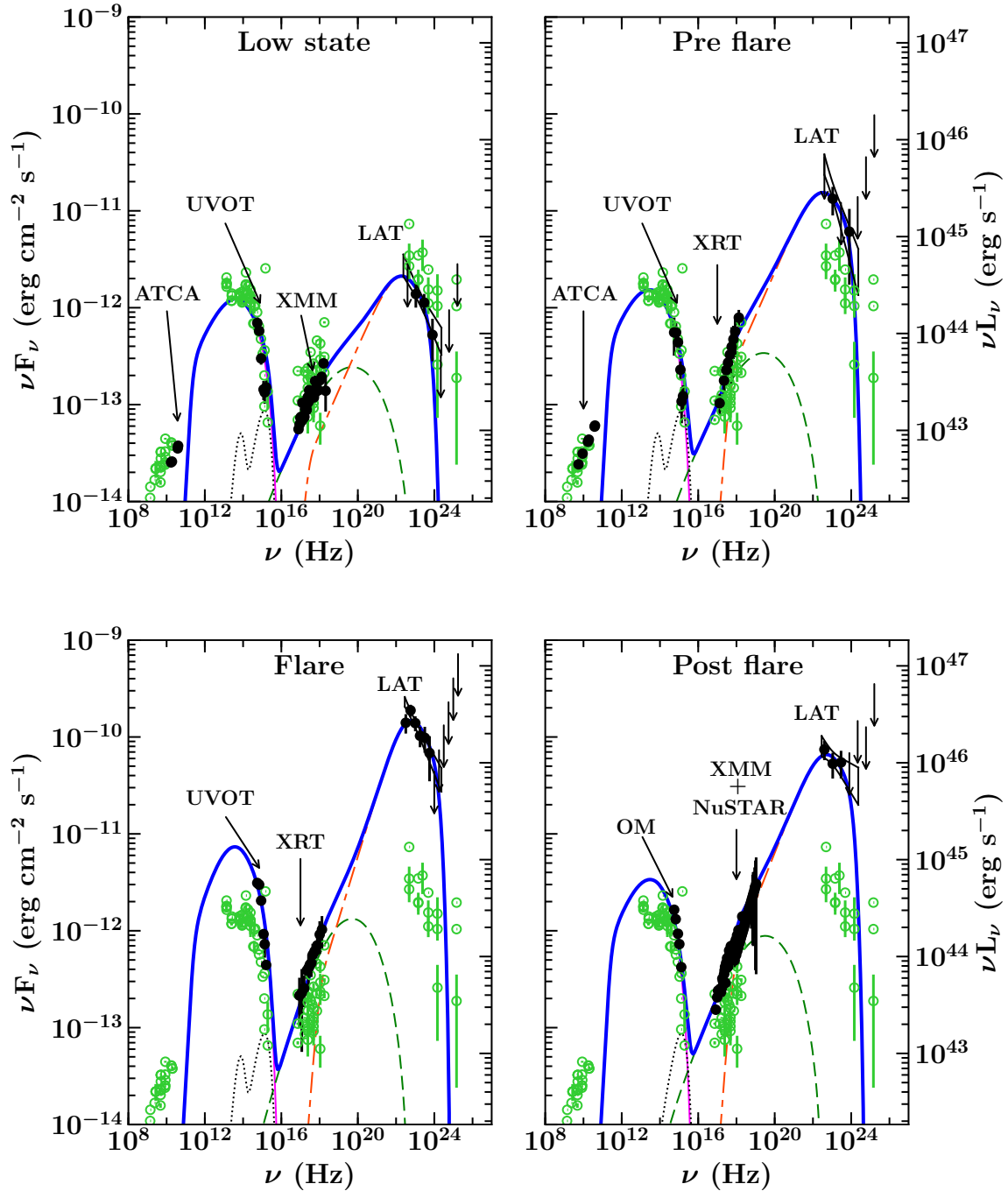


Figure 5.6.: Spectral energy distribution of PKS 2004–447 modelled with a simple leptonic emission model during different activity states. Open green circles refer to archival measurements taken from the SSDC SED builder (<https://tools.ssdc.asi.it/>), filled black circles represent the data analysed by us. Thin solid pink line: synchrotron emission; dashed green: SSC; dash-dash-dot orange: EC; dotted black line: thermal emission from accretion disk and dusty torus; thick solid blue line sum of all radiative components. The time ranges for each activity state are MJD 55682–56413 (low), MJD 58754–58770 (pre-flare), MJD 58781–58784 (flare), MJD 58787–58789 (post-flare).

Credit: Gokus et al., *A&A*, 649, A77, 2021, reproduced with permission © ESO

Table 5.4.: Summary of the model parameters of the multi-epoch SEDs of PKS 2004–447 (see Fig. 5.6). This table is taken from Gokus et al. (2021b).

Parameter	Symbol	Low	Pre-flare	Flare	Post-flare
Particle spectral index before break energy	s_1	2.1	2.1	1.7	2.0
Particle spectral index after break energy	s_2	4.0	4.0	4.0	4.0
Min. Lorentz factor of particle distribution	γ'_{\min}	4	4	4	4
Break Lorentz factor of particle distribution	γ'_b	1300	1100	900	1100
Max. Lorentz factor of particle distribution	γ'_{\max}	6000	5500	5000	5000
Particle energy density, in erg cm^{-3}	U'_e	0.18	0.22	0.10	0.22
Magnetic field, in Gauss	B	0.4	0.3	0.3	0.3
Bulk Lorentz factor	Γ_b	11	20	26	24
Dissipation distance, in 10^{-2} parsec	R_{dist}	2.01	2.01	2.01	2.01
Size of the emission region, in 10^{15} cm	R_{blob}	6.2	6.2	6.2	5.17
Compton dominance	CD	2	10	18	20
Jet power in electrons, in erg s^{-1} , log scale	P_e	44.2	44.8	44.7	45.0
Jet power in magnetic field, in erg s^{-1} , log scale	P_B	42.7	43.0	43.2	43.0
Radiative jet power, in erg s^{-1} , log scale	P_r	43.7	44.9	45.2	45.2
Jet power in protons, in erg s^{-1} , log scale	P_p	46.2	46.8	46.3	46.9

Notes. The central black hole mass and the accretion disk luminosity are taken as $7 \times 10^7 M_\odot$ and $2 \times 10^{43} \text{ erg s}^{-1}$, respectively, and we assume the characteristic temperature of the IR-torus to be 1100 K. A viewing angle of 2° is adopted. For the given accretion disk luminosity, the size of the BLR and dusty torus are $4.6 \times 10^{-3} \text{ pc}$ and $3.4 \times 10^{-2} \text{ pc}$, respectively. We note that the jet powers are computed by assuming a two-sided jet.

discrepancy was suggested by Berton et al. (2021), which is a change of the jet inclination over time. This has already been found for one source, which seemed to have transformed from a radio galaxy into a blazar (Hernández-García et al., 2017).

Since our model is a leptonic one, we only consider electrons for the observed emission. In our emission region, we assume a uniform and tangled magnetic field. This region is filled with a relativistic population of electrons, which emits both synchrotron and inverse Compton radiation. The energy distribution is described by a smooth broken power law between a minimum (γ_{\min}) and maximum (γ_{\max}) energy as

$$Q(\gamma) = Q_0 \frac{\gamma_b^{-s_1}}{(\gamma/\gamma_b)^{s_1} + (\gamma/\gamma_b)^{s_2}} \quad (5.3)$$

where γ_b denotes the break Lorentz factor and the spectral indices above and below γ_b are given as s_1 and s_2 . Q_0 is a normalisation constant. Regarding the inverse Compton emission, we consider various sources of seed photons in our model. Seed photons can originate from the original synchrotron emission by the electron population, for which the high-energy emission is then created via synchrotron self Compton (SSC; e.g., Finke et al., 2008, van den Berg et al., 2019). Another possibility is seed photons coming from thermal emission, which can stem from the accretion disk, X-ray corona, broad line region, and the dusty torus. Such a process is called external Compton (EC; e.g., Sikora et al., 1994, Błażejowski et al., 2000). To adopt

the comoving-frame radiative energy densities of all AGN components contributing to the EC flux, we followed the instructions of [Ghisellini & Tavecchio \(2009\)](#). We computed the jet powers assuming a two-sided jet, which includes an equal number density of electrons and protons, where the latter are considered to participate solely in carrying the momentum of the jet and are otherwise cold, meaning not radiating.

The four SEDs displaying different activity states of PKS 2004–447 are shown in Fig. 5.6 and the model parameters for each SED are given in Table 5.4.

5.4 Discussion of analysis results

In the following section, I discuss the results of the variability analysis (Sect. 5.4.1) and the SED modelling (Sect. 5.4.2). In addition, I compare the flaring state of PKS 2004–447 with those of other γ -NLSy 1s (Sect. 5.4.3).

5.4.1 Variability

This section is taken in verbatim from [Gokus et al. \(2021b\)](#).

The detection of a γ -ray flare from PKS 2004–447 provides more observational evidence supporting the blazar-like behaviour of γ -NLSy 1 galaxies (see also e.g. [Baldi et al., 2016](#)). In general, γ -ray variability is an indicator for the presence of a closely aligned, relativistic jet. For blazars variability on timescales as short as minutes is commonly observed at TeV energies (e.g. [Rieger & Volpe, 2010](#), [Aleksić et al., 2011](#)), but such short timescales have only been observed in few sources at GeV energies (e.g. [Meyer et al., 2019](#)).

It has been proposed that γ -NLSy 1s represent the start of the life of an AGN, when the central black hole mass is still below $10^8 M_\odot$ and the source appears not as bright as a full-grown FSRQ ([Mathur, 2000](#), [Foschini, 2017](#), [Paliya, 2019](#)). Nevertheless, the detection of blazar-like short-term variability in γ -NLSy 1 galaxies, which has been seen previously in 1H 0323+342 (flux doubling timescales of ~ 3 h; [Paliya et al., 2014](#)) and PKS 1502+036 (variability on 12 h timescales; [D’Ammando et al., 2016](#)), suggests that the physical mechanisms operating in the relativistic jet of γ -NLSy 1s are similar to those working in blazar jets resulting in fast γ -ray variability (e.g. [Shukla & Mannheim, 2020](#)). For PKS 2004–447, we find indications for sub-daily variability with flux doubling times as short as 2.2 hours at a 2.8σ level.

We note that if we consider only GeV flares with fluxes above 10^{-6} ph cm $^{-2}$ s $^{-1}$, the few observed flares by γ -NLSy 1 galaxies lasted roughly 1–4 days. The brightest blazar flares at γ -ray energies have a tendency to last longer, and for some sources occur more often. However, a strong bias exists towards the most luminous and extreme detections due to the different sensitivities and observing constraints of space-based and ground-based γ -ray telescopes: While the large field of view and observing strategy of *Fermi*/LAT offers unbiased all-sky observations of many blazars in the GeV energy regime, its relatively small collection area renders it less sensitive to weak flares. In the TeV energy range Cherenkov telescopes have large collection areas giving them good sensitivity to short time variability, but with their relatively small fields of view and low duty cycles, their observations are limited to a smaller sub-sample of targeted observations on blazars. Even though observing programmes often include scheduled observations on a selection of blazars during the parts of the year that they

are visible from the ground, many blazar observations are triggered and therefore take place during a particularly active period. This leads to an under-reporting of short, less luminous blazar flares, which could in turn belong to a class of less luminous blazars that might be missing in the AGN evolution scenario.

5.4.2 SED parameters

We started the SED modelling processes with the low activity broadband spectrum in order to determine a set of parameters representing the usual state. We then continued to model and explain the SED during the active phase in October/November 2019 by only changing a minimum of the input parameter, in order to obtain knowledge about the principal factors that caused the γ -ray flare.

Using the values of the dispersion (1869 km s^{-1}) and luminosity of the $H\beta$ emission line computed by Foschini et al. (2015), which was determined from the optical spectrum published by Drinkwater et al. (1997), we determined a black hole mass of $M_{\text{BH}} = 7 \times 10^7 M_{\odot}$, which is within most predictions regarding the SMBH mass of PKS 2004–447 (see Section 5.2). On deriving a luminosity of the accretion disk, we find that our optical-UV data during the low activity state do not agree with the reported value of $L_{\text{disk}} = 4.8 \times 10^{44} \text{ ergs}^{-1}$ (Foschini, 2017). An accretion disk with such a luminosity would leave a trace in the form of a big blue bump at optical-UV frequencies. None of the broadband SEDs in Fig. 5.6 exhibit such a feature, not even in the data of the low state, when the synchrotron emission was significantly weaker than during the flaring activity in 2019. We thereby constrain the accretion disk luminosity to $2 \times 10^{43} \text{ ergs}^{-1}$. With those derived quantities (M_{BH} and L_{disk}) we determine an accretion rate of $\sim 0.4\%$ of the Eddington rate. A value lower than 1% of the Eddington rate is usually exhibited in systems with radiatively efficient accretion (e.g., Ghisellini et al., 2017), which could put PKS 2004–447 in the small group of AGN for which a radiatively efficient accretion is occurring despite a low level of accretion activity.

We start with the interpretation of the results for the low activity SED. The decrease of the low-energy bump is covered by the optical-UV data obtained with *Swift*/UVOT. Since the data describes a steeply falling shape, it is possible to constrain some of the parameters that describe the electron distribution, namely the high-energy spectral index (s_2), the break (γ_b), and the maximum energy (γ_{max}). The low-energy spectral index (s_1) can be constrained via the shape of the X-ray spectrum. Because radio emission from a compact region is synchrotron self-absorbed, and our model does not include additional large-scale emission regions, the archival and ATCA radio data are not described by our model. The high-energy hump during the low activity state is explained by a combination of a SSC process in the X-ray energy range and an EC process including seed photons from the dusty torus, which explains the γ -ray emission. The combination of the amount of SSC together with the constrained synchrotron emission allows us to assume the size of the emission region as well as the strength of the involved magnetic field (given in Table 5.4). According to our assumptions, the location of the emission region is consequently outside the BLR, but still inside the dusty torus.

The determined SED parameters for the low activity state of PKS 2004–447 are comparable to those derived in previous studies on this source (Paliya et al., 2013, Orienti et al., 2015). One of the minor differences is a larger bulk Lorentz factor that was used for modelling the

respective SEDs by [Oriente et al. \(2015\)](#). However, they did not use the same data set presented in this study, nor the same underlying assumptions regarding the leptonic model. Furthermore, [Oriente et al. \(2015\)](#) model the X-ray range of the SED with an EC process involving seed photons from the torus during a low activity state.

The SED representing the pre-flare phase (see upper right panel in Fig. 5.6) reveals that the optical-UV emission is at a similar level compared to the low-activity state. The X-ray spectrum has hardened and both the X-ray and γ -ray emission, which are connected to SSC and EC processes, have slightly increased. Because the synchrotron emission has not changed, we explain this increase in SSC and EC emission with a decrease of the magnetic field strength, which demands more electrons in order to produce the same amount of synchrotron radiation, and leads to a higher flux produced by inverse Compton processes (e.g., [Dermer & Menon, 2009](#)). In general, we observe an increase in Compton dominance, meaning the ratio of synchrotron to inverse Compton peak luminosities (e.g., [Finke, 2013](#)), in comparison to the low activity state. This significant increase can be explained by an enhanced Doppler boosting that is caused by a now larger bulk Lorentz factor.

During the flare, both the synchrotron and the inverse Compton peak of the SED have increased, with the most dramatic change seen at γ -ray energies. The γ -ray spectrum has shifted about two orders of magnitude to a higher flux compared to the low activity state. We interpret the enhanced synchrotron emission with an injection of fresh, energetic electrons into the emission region, which can also describe the increase of SSC radiation that is seen in the X-ray energy band. However, to explain the extreme variations at γ -ray energies, we need to consider an even stronger boosting for the EC radiation in addition to the regular beaming due to relativistic motion of material in the jet towards the observer. To obtain fitting conditions, we assume that the external photon field is additionally boosted by the motion of the emission region with respect to it ([Dermer, 1995](#)). The radiation pattern of the EC emission becomes anisotropic, even in the comoving frame, and therefore it becomes more sensitive to Doppler boosting itself. As a result, the Doppler boost increases. The bulk Lorentz factor, which we need to model the SED during the flaring state, is indeed reasonably larger compared to those of the two SEDs before that.

After the flare, the overall emission slightly decreases, but the SED shape still reveals a stronger Compton dominance compared to the pre-flare state. The γ -ray emission remaining bright indicates a still large Doppler boosting. A separate analysis of the X-ray spectra of *XMM-Newton* and *NuSTAR*, respectively, reveals a slight spectral hardening at higher energies (see Table 5.2), even under consideration of background influence. As mentioned before, this is an indication of SSC processes being the dominant part at energies below 10 keV. Hence, *NuSTAR* with its sensitivity up to 80 keV plays a crucial role in determining these slight distinctions and helps to untangle the different overlay of physical mechanisms in the broadband data.

From the SED model and the change in parameters for each activity state we can deduce the jet powers involved (see all values in Table 5.4). Comparing the jet powers for each of the four SEDs, an interesting pattern can be seen. In the pre-flare state particularly the radiative power, P_r , but also the kinetic power of the particles, P_p and P_e , have increased up to a magnitude larger compared to the low activity state. While P_r increases even further during the flare, the kinetic powers of the particles decreases again. In the post-flare state, P_p and P_e have a similar

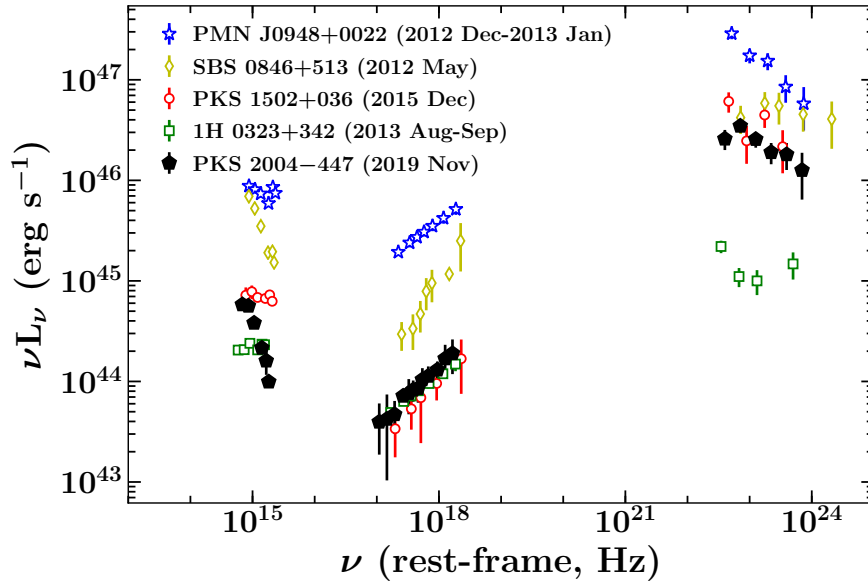


Figure 5.7.: Comparison of the rest-frame SEDs of γ -ray flaring NLSy 1 galaxies during their GeV flaring epochs. The epochs of the flares are given in their labels. The data taken for this comparison for all sources except PKS 2004–447 were analysed by Paliya & Stalin (2016) and D’Ammando et al. (2013).

Credit: Gokus et al., A&A, 649, A77, 2021, reproduced with permission © ESO

or even slightly higher energy output compared to the pre-flare state. We interpret this outcome of our modelling as a sign for an efficient conversion of P_p and P_e into radiation during the flare. Radiatively efficient jets during γ -ray flares have already been found among sources of the blazar class (e.g., Tanaka et al., 2011, Saito et al., 2013, Paliya et al., 2015). Furthermore, the radiative power that we observe during the flare exceeds the total available accretion power. This, and the circumstance of this γ -ray flare being the first from PKS 2004–447 within 10 years of all-sky monitoring by *Fermi*/LAT, makes this a rather exceptional event that is likely rare and short-lived (e.g., Tavecchio et al., 2010).

5.4.3 Comparison with other SEDs

The following section is taken in verbatim from Gokus et al. (2021b).

Since the sample of flaring γ -NLSy 1 galaxies is so small, not much is known about their typical flaring behaviour nor about their possible differences. We compare the flaring state broadband SED of PKS 2004–447 with four γ -NLSy 1 galaxies that have shown a GeV flare in the past. The data for 1H 0323+342, PMN J0948+0022, and PKS 1502+036 are taken from Paliya & Stalin (2016). Although the brightest flare of SBS 0846+513, which happened in 2011, is not covered by multi-wavelength data, this source showed high γ -ray activity in May 2012 as well. During that time, the γ -ray emission was slightly below the flare of 2011, but X-ray and optical-UV data are available. We take data of SBS 0846+513 from D’Ammando et al. (2013). All SEDs obtained from data throughout their respective flares are plotted in Fig. 5.7. The parameters discussed in this comparison are also listed in Table 5.5.

Table 5.5.: Comparison of chosen SED model parameters of the flaring γ -NLSy 1 galaxies. Paper abbreviations: G-2021: [Gokus et al. \(2021b\)](#); P-2014: [Paliya et al. \(2014\)](#); P&S-2016: [Paliya & Stalin \(2016\)](#); D'A-2013: [D'Ammando et al. \(2013\)](#); D'A-2015: [D'Ammando et al. \(2015\)](#). This table is taken from [Gokus et al. \(2021b\)](#).

	PKS 2004–447	1H 0323+342	PKS 1502+036	SBS 0846+513	PMN J0948+0022
Reference	G-2021	P-2014	P&S-2016	D'A-2013	D'A-2015
Redshift z	0.24	0.061	0.409	0.5835	0.584
Optical/UV:					
L_{disk} [erg s ⁻¹]	2×10^{43}	1×10^{45}	6×10^{44}	4.4×10^{43}	5.7×10^{45}
Origin of emission	Synchrotron	Accretion disk	Synchrotron + accretion disk	Synchrotron	Synchrotron + accretion disk
X-ray:					
Index	1.38 ± 0.29	1.55 ± 0.08	1.33 ± 0.56	1.6 ± 0.3	1.55 ± 0.11
Dominance	SSC	EC	EC	EC	EC
γ-ray:					
$\Gamma_{0.1-300\text{GeV}}$	2.42 ± 0.09	2.47 ± 0.11	2.57 ± 0.16	2.13 ± 0.05	2.65 ± 0.11
L_{γ} [erg s ⁻¹]	2.9×10^{47}	4.7×10^{46}	1.2×10^{48}	$5 \times 10^{47} - 10^{48}$	1.5×10^{48}
Γ_b	26	7	25	40	30
Process	EC/Torus	EC/BLR	EC/Torus	EC/Torus	EC/Torus

The shape of the optical-UV emission from PKS 2004–447 is similar to that of SBS 0846+513, but differs from the other three sources: Although the level of luminosity is different for 1H 0323+342, PMN J0948+0022, and PKS 1502+036, their observed optical-UV spectra could all be explained with a combination of the synchrotron and accretion disk emission ([Paliya et al., 2014](#)). For 1H 0323+342, the optical-UV emission remains disk dominated even during the GeV flare. Such thermal emission, however, is not observed in PKS 2004–447 (see also Fig. 5.6). Taken together with SED modelling, this indicates that emission from the accretion disk is negligible compared to the synchrotron emission.

In the X-rays, the luminosity of PKS 2004–447 is similar to that of PKS 1502+036 and 1H 0323+342. Within the soft X-rays, models predict a transition from SSC to EC emission. During flaring states, the EC can become dominant over SSC, as it is the case for 1H 0323+342, PMN J0948+0022 and PKS 1502+036. The EC component of PKS 2004–447, however, starts at higher energies compared to the other γ -NLSy 1 galaxies; therefore most of its soft X-ray emission originates from SSC. The spectral shapes of γ -NLSy 1 galaxies behave similarly by showing a harder spectral index during a flare compared to low states. All sources, including PKS 2004–447, show photon indices between 1.3 and 1.6.

In the γ -rays, PKS 2004–447 reaches about the same luminosity as PKS 1502+036, and is about one order of magnitude more luminous than 1H 0323+342 (see Fig. 5.7). SBS 0846+513 showed a slightly higher luminosity, while PMN J0948+0022 presents the highest luminosity ever observed for a γ -ray flare of a NLSy 1 galaxy, exceeding the luminosity of PKS 2004–447 by a factor of ten. The γ -ray photon indices during the flaring state are ~ 2.5 , with the exception of SBS 0846+513, which shows a significantly harder spectrum. Both PKS 2004–447 and

PKS 1502+036 exhibit a similar luminosity and bulk Lorentz factor (PKS 1502+036 has $\Gamma = 25$; Paliya & Stalin, 2016). The mass of their central black holes is similar as well. However, the accretion disk luminosity of the latter is a factor of ~ 30 larger indicating a higher accretion rate in Eddington units. Since the sizes of the BLR and the torus adjust to the luminosity of the accretion disk, they are likely ten times larger as well for PKS 1502+036. For PKS 2004–447, in order to be able to produce a similar γ -ray luminosity, a higher particle density is required.

The γ -ray emission of PKS 2004–447 is explained by the EC process with seed photons provided by the dusty torus, as already reported for SBS 0846+513, PMN J0948+0022, and PKS 1502+036 during flaring episodes (D’Ammando et al., 2013, 2015, 2016). As is observed for PKS 2004–447, a high Compton dominance has also been seen in these sources at the peak of the activity, confirming that the EC emission is the main mechanism for producing γ -rays, similar to several FSRQs. This result confirms the similarities between γ -NLSy 1s and FSRQs. In contrast to PKS 2004–447, for which an increase in the bulk Lorentz factor is the driver of the change in the SED for different activity states, comparing low and flaring activity states, the SEDs of SBS 0846+513, PMN J0948+0022, and PKS 1502+036 can be described satisfactorily by changing the electron distribution parameters as well as the magnetic field. In the same way, a significant shift of the synchrotron peak has been observed during the flaring states of SBS 0846+513 and PMN J0948+0022, while it was not observed for PKS 2004–447.

5.5 Conclusions from our multi-wavelength analysis

The detection of γ -ray flares from NLSy 1 galaxies shows us that labelling sources based on few characteristic features does not necessarily paint the full picture. While the different classes in the AGN unification scheme can provide some kind of order among the vast amount of sources, over the decades we have found new, peculiar sources that seem to contradict certain parts of the interpretation that we relied on, so far.

The case of γ -ray emitting NLSy 1 galaxies is one of the odd cases, which makes it necessary to develop a new perspective on AGN evolution. Multi-wavelength studies of these jetted AGN, like the one presented here, indicate that they seem to belong to the blazar-class, albeit with a lower-than typical SMBH mass and possibly in barred or spiral galaxies. Our findings contradict earlier assumptions that jets can only be launched by the most massive SMBHs that typically reside in elliptical galaxies.

The compactness of the radio emission of several γ -NLSy 1s further indicates a rather young age of these AGN, and poses the question whether they are currently in the phase of transforming from a non-jetted to a jetted AGN. Due to their small inclination angle, their light from the radio up to γ -rays is largely unobscured, which can make it easier for us to spot an AGN in its early phase of launching a jet, compared to side-viewed AGN. The inner part of AGN viewed from the side is usually heavily obscured by the dusty torus and the host galaxy. A jet might only be observable when it has reached a certain expansion, which could prevent observations of the earliest stage of jet launching for such sources.

The number of known γ -NLSy 1s is very small compared to the overall number of AGN, and given their unusual properties, dedicated MWL studies on each of these sources is necessary to gain more insights. It is also promising to search for a γ -ray signal among the known

radio-loud NLSy 1, which are outliers from the usual NLSy 1 class themselves. As stated in the beginning of this chapter, the radio emission of the majority of the radio-loud NLSy 1s seems to be similar to that of CSS sources, and might be young jetted systems.

To advance our current knowledge, investigations to sufficiently constrain the mass of their central SMBHs and to determine the nature of their host galaxies are crucial. Additionally, in case radio-loud and γ -NLSy 1s are AGN in the immediate process of launching large, powerful jets, X-ray observations to probe their innermost region could help to shed light on the jet launching process. However, the X-ray emission is very likely contaminated, or even dominated, by the emission from the jet. Sources with a rather low radio-loudness value might be better candidates for dedicated X-ray studies than those with a strong radio signal. Also, observations with the newly-launched mission IXPE can determine the fraction of synchrotron emission from the jet within the X-ray emission, and could help disentangle the emission from the jet and the innermost AGN region, when accompanied by an observation with a high-resolution X-ray spectrometer.

It's been a long road
Getting from there to here
It's been a long time
But my time is finally near

Theme song of *Star Trek: Enterprise*

Chapter

6

Conclusion and Outlook

Active galactic nuclei are the most luminous persistent objects in the Universe, and powered by accretion onto a supermassive black hole. AGN come in different forms and sizes, and can display various characteristics based on the viewing angle, and their intrinsic power. They can be detected across the whole electromagnetic spectrum, and typically show variable emission at all wavelengths. In order to study AGN emission processes and fully understand the nature of these sources, multi-wavelength observations are required. Blazars belong to the group of jetted AGN, and exhibit relativistic outflows called jets that point towards us. This configuration leads to Doppler-boosted emission, which is the reason for the brightness and extremely variable nature of blazars. A high-amplitude increase in luminosity can occur on time scales of weeks to hours, and has been labelled blazar flare. Several models exist to explain the observed variability, from long-term to extremely rapid flux variations, but the processes and particles responsible for the high energy emission have not been fully constrained yet (Böttcher et al., 2013). A puzzling item has been the discovery of extremely rapid variations of γ -ray emission on time scales of a few minutes, which would translate to emission regions with a size of only a few Schwarzschild radii or below. Various models have been used to explain this intriguing behaviour, including, e.g., an interaction of a star with the jet (Barkov et al., 2012), mini-jets (e.g., Ghisellini & Tavecchio, 2008, Giannios et al., 2009, Shukla & Mannheim, 2020), or a layered structure of the jet (Chiaberge et al., 2000, Ghisellini et al., 2005).

The first project presented in this thesis is a multi-wavelength campaign for Mrk 421, which is one of the brightest blazars. In order to retrieve timely information about its flaring behaviour, Mrk 421 was monitored with nightly observations in the VHE γ -ray regime by FACT, and weekly snapshots by *Swift* to obtain optical, UV, and X-ray fluxes. In June 2019, the blazar showed a bright γ -ray flare, which was followed up with target-of-opportunity observations in the X-rays with *XMM-Newton*, *INTEGRAL*, and additional *Swift* pointings. Additional radio data were acquired with the Effelsberg 100m radio telescope. In Chapter 4, I presented an analysis of the variability at different wavelengths, and an analysis of the changes in the synchrotron hump of the double-humped blazar SED. Modelling the optical to hard X-ray data with a simple logparabola model revealed a shift of the synchrotron peak towards

higher energies. The hardening of the X-ray spectrum was also revealed in the *XMM-Newton* data and constrained to a duration of ~ 18 hours. As part of a timing analysis to find potentially shorter time scales, I found two rapid ‘mini-flares’ in the 4–10 keV energy band on top of the more slowly varying X-ray emission. The observed corresponding time scales are shorter than five minutes, which corresponds to \sim two hours in the jet frame, or a light-travelling distance of about four Schwarzschild radii of the SMBH of Mrk 421. An interpretation that these time scales represent the entire emission region is unlikely, which raises the question of how this rapid variability is created. So far, models have addressed the rapid variability of blazar jets observed in the (VHE) γ -ray regime, and several different suggestions have been brought forward. Unfortunately, FACT was not able to observe Mrk 421 in the exact time range of the detected rapid X-ray variability of Mrk 421, which would have given a better constraint on existing models. A possible mechanism being involved could be magnetic reconnection. The detection of a (time-dependent) polarisation signal in the X-rays with the newly launched IXPE mission could help to disentangle the structure of the magnetic field during a flaring event in a blazar, but would only be possible in case of a very bright flare (Zhang et al., 2021).

The second project of my dissertation concerns a γ -ray flaring event of a narrow-line Seyfert 1 galaxy (Chap. 5). NLSy 1 galaxies are classified based on properties in their optical spectrum, and typically non-jetted AGN, but a few objects exist that exhibit a relativistic jet. Among those, a few (~ 20) have been detected in the γ -ray regime by *Fermi*/LAT. PKS 2004–447 belongs to that class of γ -loud NLSy 1s, and showed a bright γ -ray flare in October 2019, which was similar in brightness to typical blazar flares. Multiwavelength data in the radio (ATCA), optical/UV (*Swift*/UVOT), and X-ray (*Swift*, *XMM-Newton*, and *NuSTAR*) were obtained and the broadband spectral energy distribution of the source was modelled during different activity states. The overall emission and flaring behaviour appeared to be very similar to that of blazars, and FSRQs in particular. Furthermore, I analysed the combined *XMM-Newton* and *NuSTAR* spectra, which yielded an X-ray spectrum from 0.3 to 80 keV. I detected no distinct features of NLSy 1s, such as a soft excess or an iron line, but it is likely that the X-ray emission is largely dominated by the jet rather than the accretion disk and its surroundings. A multi-wavelength variability analysis revealed variability on longer time scales from the radio up to the X-ray, and short-time variability on scales of hours in the γ -rays.

My results are similar to those of studies of other γ -ray flaring NLSy 1s regarding the blazar-like behaviour. Generally, these sources are especially interesting as they seem to be able to launch blazar-like jets, but are not showing the same properties that were deemed necessary to produce powerful jets. Above all, their central SMBH seems to be less massive than those powering blazars (e.g., Komossa, 2018). A few radio-loud NLSy 1 seem to be merging with another galaxy (e.g., Paliya et al., 2018, Berton et al., 2019), which could possibly trigger AGN activity capable of jet formation, but most optical images of radio-loud NLSy 1s are not resolved enough to yield clear clues. In addition, the majority appears to be in disk galaxies, and, if not through merging, they might have obtained an active nucleus through gas-inflow via their galaxy bars (Olguín-Iglesias et al., 2020). It is a possibility that jetted NLSy 1 galaxies are young AGN and can become powerful blazars over time. Among those, PKS 2004–447 seems to be more of an outlier, as it does not exhibit many of the characteristics typically seen in NLSy 1s. Its radio emission is matching that of compact steep spectrum sources, which are

thought of as young radio sources with the jet only extending up to 20 kpc, which would also be a hint for a rather young age regarding its activity.

In my thesis, I touched upon two of the main topics in current AGN research. The first one concerns the jets and, in particular, their particle acceleration mechanisms. The individual contributions from leptons and hadrons in the high-energy emission of blazars is not known, while the extreme brightness and variability at VHE γ -rays challenges current models. The Cherenkov Telescope Array will push forward our knowledge about AGN as it is expected to at least double the amount of known VHE-emitting AGN, and will be sensitive enough to retrieve high-resolution light curves to study the rapid variability at γ -ray energies (Sol et al., 2013). The second subject I address is AGN evolution, and also certain inconsistencies within the AGN classification scheme. The radio dichotomy, in particular, might be misleading, as strong radio emission and variability has been found for sources deemed radio-quiet or radio-silent (Lähteenmäki et al., 2018). Foschini et al. (2021) took a deep look at about half of the known γ -ray sources, and found that classifications and also redshift information need to be updated, but about a third of their analysed sources still remains unclassified. Both findings might have a large impact on how we view AGN in the future. The *eROSITA* telescope will detect up to three million AGN in its full four-year X-ray all-sky survey (Kolodzig et al., 2013), and provide data for a large scale population study. In terms of understanding more about AGN evolution, it will also be necessary to study the earliest AGN in our Universe, which appear extremely weak due to their immense distance. Several very bright specimen have already been detected, but these discoveries are biased towards the most extreme sources. While the γ -ray emission is severely attenuated with increasing redshift, future X-ray missions, such as *Athena* (Nandra et al., 2013), are currently under design with the aim to detect high-redshift galaxies beyond $z > 6$. *Athena*'s very sensitive instruments are crucial to detect a larger population of high-redshift AGN to obtain a more complete source sample.

Bibliography

- Abbott B.P., Abbott R., Abbott T.D., et al., 2017, *ApJL* 848, L12
- Abdo A.A., Ackermann M., Agudo I., et al., 2010a, *ApJ* 716, 30
- Abdo A.A., Ackermann M., Ajello M., et al., 2010b, *Nature* 463, 919
- Abdo A.A., Ackermann M., Ajello M., et al., 2009, *ApJL* 707, L142
- Abdollahi S., Acero F., Ackermann M., et al., 2020, *ApJS* 247, 33
- Abeysekera A.U., Archambault S., Archer A., et al., 2017, *ApJ* 834, 2
- Abeysekera A.U., Benbow W., Bird R., et al., 2020, *ApJ* 890, 97
- Abraham J., Aglietta M., Aguirre I.C., et al., 2004, *NIMPA* 523, 50
- Acciari V.A., Aliu E., Arlen T., et al., 2011, *ApJ* 738, 25
- Acciari V.A., Ansoldi S., Antonelli L.A., et al., 2021, *MNRAS* 504, 1427
- Acciari V.A., Arlen T., Aune T., et al., 2014, *APh* 54, 1
- Ackermann M., Anantua R., Asano K., et al., 2016, *ApJL* 824, L20
- Agarwal A., Mihov B., Andruchow I., et al., 2021, *A&A* 645, A137
- Aguilar J.A., Bilnik W., Borkowski J., et al., 2016, *NIMPA* 830, 219
- Aharonian F., Akhperjanian A.G., Bazer-Bachi A.R., et al., 2007, *ApJL* 664, L71
- Ahnen M.L., Ansoldi S., Antonelli L.A., et al., 2016, *A&A* 593, A91
- Ahnen M.L., Ansoldi S., Antonelli L.A., et al., 2018, *A&A* 620, A181
- Akiyama K., Alberdi A., Alef W., et al., 2022a, *ApJL* 930, L13
- Akiyama K., Alberdi A., Alef W., et al., 2022b, *ApJL* 930, L12
- Albert J., Aliu E., Anderhub H., et al., 2007, *ApJ* 663, 125
- Aleksić J., Alvarez E.A., Antonelli L.A., et al., 2012, *APh* 35, 435
- Aleksić J., Ansoldi S., Antonelli L.A., et al., 2015a, *A&A* 576, A126
- Aleksić J., Ansoldi S., Antonelli L.A., et al., 2015b, *A&A* 578, A22
- Aleksić J., Ansoldi S., Antonelli L.A., et al., 2014, *Science* 346, 1080
- Aleksić J., Antonelli L.A., Antoranz P., et al., 2011, *ApJL* 730, L8
- Alexander D.M., Bauer F.E., Brandt W.N., et al., 2003, *AJ* 126, 539
- Alexander T., Natarajan P., 2014, *Science* 345, 1330
- Allen R.J., Barrett A.H., Crowther P.P., 1968, *ApJ* 151, 43
- Alvarez P., Rodriguez-Espinosa J.M., Kabana F.R., 2000, In: Sebring T.A., Andersen T. (eds.) *Telescope Structures, Enclosures, Controls, Assembly/Integration/Validation, and Commissioning*, SPIE (Bellingham, WA, USA), Proc. SPIE 4004, p.26
- Anderhub H., Backes M., Biland A., et al., 2013, *JInstr* 8, P06008
- Angelakis E., Fuhrmann L., Myserlis I., et al., 2019, *A&A* 626, A60
- Angeloni L., Auriemma G., Belli B.M., et al., 1977, *Mem. Soc. Astron. It.* 48, 780
- Antonucci R., 1993, *ARA&A* 31, 473
- Antonucci R.R.J., 1984, *ApJ* 278, 499
- Antonucci R.R.J., Ulvestad J.S., 1985, *ApJ* 294, 158
- Appl S., Sol H., Vicente L., 1996, *A&A* 310, 419
- Arbet-Engels A., Manganaro M., Dorner D., et al., 2019, In: Desiati P., Gaisser T., Karle A. (eds.) *36th International Cosmic Ray Conference, PoS(ICRC2019)* 620
- Arévalo P., Uttley P., 2006, *MNRAS* 367, 801

- Arnaud K., Smith R., Siemiginowska A., 2011, Handbook of X-ray Astronomy, Cambridge Univ. Press, UK
- Arp H., Sulentic J.W., Willis A.G., de Ruiter H.R., 1976, ApJL 207, L13
- Aschenbach B., 1985, RPPh 48, 579
- Atoyán A., Dermer C.D., 2001, PRL 87, 221102
- Atwood W.B., Abdo A.A., Ackermann M., et al., 2009, ApJ 697, 1071
- Axelsson M., Borgonovo L., Larsson S., 2005, A&A 438, 999
- Baade W., Minkowski R., 1954, ApJ 119, 206
- Babichenko S.I., Burgin M.S., Vojnakov S.M., et al., 1990, KosIs 28, 587
- Baby B.E., Agrawal V.K., Ramadevi M.C., et al., 2020, MNRAS 497, 1197
- Baczko A.K., 2019, Ph.D. thesis, University of Würzburg, Germany
- Baldi R.D., Capetti A., Robinson A., et al., 2016, MNRAS 458, L69
- Baloković M., Paneque D., Madejski G., et al., 2016, ApJ 819, 156
- Bandura K., Addison G.E., Amiri M., et al., 2014, In: Stepp L.M., Gilmozzi R., Hall H.J. (eds.) Ground-based and Airborne Telescopes V, SPIE (Bellingham, WA, USA), Proc. SPIE 9145, p.738
- Banerjee B., Joshi M., Majumdar P., et al., 2019, MNRAS 487, 845
- Barkov M.V., Aharonian F.A., Bogovalov S.V., et al., 2012, ApJ 749, 119
- Barkov M.V., Aharonian F.A., Bosch-Ramon V., 2010, ApJ 724, 1517
- Barr P., Mushotzky R.F., 1986, Nature 320, 421
- Barret D., Decourchelle A., Fabian A., et al., 2020, AN 341, 224
- Barret D., Lam Trong T., den Herder J.W., et al., 2018, In: den Herder J.W.A., Nikzad S., Nakazawa K. (eds.) Space Telescopes and Instrumentation 2018: Ultraviolet to Gamma Ray, SPIE (Bellingham, WA, USA), Proc. SPIE 10699, p.324
- Barthel P.D., 1989, ApJ 336, 606
- Barthelmy S.D., Barbier L.M., Cummings J.R., et al., 2005, Space Sci. Rev. 120, 143
- Bartoli B., Bernardini P., Bi X.J., et al., 2016, ApJS 222, 6
- Becker R.H., White R.L., Helfand D.J., 1995, ApJ 450, 559
- Bednarek W., 1993, A&A 278, 307
- Bednarek W., Protheroe R.J., 1997, MNRAS 292, 646
- Begelman M.C., Volonteri M., Rees M.J., 2006, MNRAS 370, 289
- Belladitta S., Caccianiga A., Diana A., et al., 2022, A&A 660, A74
- Bellm E.C., Kulkarni S.R., Graham M.J., et al., 2019, PASP 131, 018002
- Belloni T., Hasinger G., 1990, A&A 227, L33
- Benlloch S., Wilms J., Edelson R., et al., 2001, ApJL 562, L121
- Berezhnoi V.I., Grechko G.M., Gubarev A.A., et al., 1977, In: Rycroft M.J. (ed.) Space Research XVII, Pergamon Press (Oxford, UK, and Elmsford, NY, USA), p.757
- Berton M., Congiu E., Ciroi S., et al., 2019, AJ 157, 48
- Berton M., Peluso G., Marziani P., et al., 2021, A&A 654, A125
- Beuchert T., 2017, Ph.D. thesis, Friedrich Alexander University, Erlangen-Nürnberg, Germany
- Beuchert T., Markowitz A.G., Krauß F., et al., 2015, A&A 584, A82
- Bhatta G., 2021, ApJ 923, 7
- Bhatta G., Mohorian M., Bilinsky I., 2018, A&A 619, A93
- Bhattacharyya S., Ghosh R., Chatterjee R., Das N., 2020, ApJ 897, 25
- Bianchi S., Panessa F., Barcons X., et al., 2012, MNRAS 426, 3225
- Bignami G.F., Bennett K., Buccheri R., et al., 1981, A&A 93, 71
- Bignami G.F., Boella G., Burger J.J., et al., 1975, Space Sci. Instr. 1, 245
- Biland A., FACT Collaboration 2017, ATel 11086
- Biland A., FACT Collaboration 2019, ATel 12680
- Biteau J., Giebels B., 2012, A&A 548, A123
- Blandford R., Meier D., Readhead A., 2019, ARA&A 57, 467
- Blandford R.D., Königl A., 1979, ApJ 232, 34
- Blandford R.D., Payne D.G., 1982, MNRAS 199, 883
- Blandford R.D., Znajek R.L., 1977, MNRAS 179, 433

- Blasi M.G., Lico R., Giroletti M., et al., 2013, *A&A* 559, A75
- Błażejowski M., Blaylock G., Bond I.H., et al., 2005, *ApJ* 630, 130
- Błażejowski M., Sikora M., Moderski R., Madejski G.M., 2000, *ApJ* 545, 107
- Blinov D., Pavlidou V., 2019, *Galaxies* 7, 46
- Blumenthal G.R., Gould R.J., 1970, *RMP* 42, 237
- Boella G., Butler R.C., Perola G.C., et al., 1997, *A&AS* 122, 299
- Boller T., Freyberg M.J., Trümper J., et al., 2016, *A&A* 588, A103
- Bolton J.G., Savage A., Wright A.E., 1979, *AuJPA* 46, 1
- Bonning E., Urry C.M., Bailyn C., et al., 2012, *ApJ* 756, 13
- Böttcher M., Reimer A., Sweeney K., Prakash A., 2013, *ApJ* 768, 54
- Boyle W.S., Smith G.E., 1970, *BSTJ* 49, 587
- Bradt H., 2004, *Astronomy Methods: A Physical Approach to Astronomical Observations*, Cambridge Univ. Press, UK
- Bradt H., Levine A.M., Marshall F.E., et al., 2001, In: Costa E., Frontera F., Hjorth J. (eds.) *Gamma-ray Bursts in the Afterglow Era*, Springer Berlin, Heidelberg, Proc. Internat. Workshop, p. 26
- Bradt H.V., Doxsey R.E., Johnston M.D., et al., 1979, *ApJL* 230, L5
- Bradt H.V., Rothschild R.E., Swank J.H., 1993, *A&AS* 97, 355
- Bradt H.V.D., Ohashi T., Pounds K.A., 1992, *ARA&A* 30, 391
- Brandt S., Lund N., Rao A.R., 1990, *AdSpR* 10, 239
- Braude S.I., Megn A.V., Riabov B.P., et al., 1978, *Ap&SS* 54, 3
- Brinkman A.C., Heise J., de Jager C., 1974, *PhiTR* 34, 43
- Buckley D.A.H., Swart G.P., Meiring J.G., 2006, In: Stepp L.M. (ed.) *Ground-based and Airborne Telescopes*, SPIE (Bellingham, WA, USA), Proc. SPIE 6267, p.333
- Buckley J.H., Akerlof C.W., Biller S., et al., 1996, *ApJL* 472, L9
- Burbidge G.R., Gould R.J., Tucker W.H., 1965, *PRL* 14, 289
- Burbidge G.R., Jones T.W., O'Dell S.L., 1974, *ApJ* 193, 43
- Burd P.R., Kohlhepp L., Wagner S.M., et al., 2021, *A&A* 645, A62
- Burke B.F., Graham-Smith F., 2009, *An Introduction to Radio Astronomy*, Cambridge Univ. Press, UK
- Burrows D.N., Hill J.E., Nousek J.A., et al., 2005, *Space Sci. Rev.* 120, 165
- Cao G., Wang J., 2013, *PASJ* 65, 109
- Cao X., Jiang W., Meng B., et al., 2020, *SCPMA* 63, 249504
- Carnerero M.I., Raiteri C.M., Villata M., et al., 2017, *MNRAS* 472, 3789
- Cash W., 1979, *ApJ* 228, 939
- Cassaro P., Stanghellini C., Dallacasa D., et al., 2002, *A&A* 381, 378
- Catelan M., Minniti D., Lucas P.W., et al., 2011, In: McWilliam A. (ed.) *RR Lyrae Stars, Metal-Poor Stars, and the Galaxy*, Pasadena, CA, USA, Carnegie Obs. Astrophys. Ser. 5, p. 145
- Celotti A., Padovani P., Ghisellini G., 1997, *MNRAS* 286, 415
- Chang J., Ambrosi G., An Q., et al., 2017, *APh* 95, 6
- Chatterjee R., Roychowdhury A., Chandra S., Sinha A., 2018, *ApJL* 859, L21
- Chen S., Berton M., La Mura G., et al., 2018, *A&A* 615, A167
- Chen Y., Cui W., Li W., et al., 2020, *SCPMA* 63, 249505
- Cherenkov P.A., 1934, *Doklady Akad. Nauk SSSR* 2, 451
- Cherenkov Telescope Array Consortium, Acharya B.S., Agudo I., et al., 2019, *Science with the Cherenkov Telescope Array*, World Scientific, Singapore
- Cheung C.C., 2004, *ApJL* 600, L23
- Cheung C.C., 2017, *ATel* 10356
- Chiaberge M., Celotti A., Capetti A., Ghisellini G., 2000, *A&A* 358, 104
- Chiaberge M., Marconi A., 2011, *MNRAS* 416, 917
- Christie I.M., Petropoulou M., Sironi L., Giannios D., 2020, *MNRAS* 492, 549
- Cioni M.R.L., Clementini G., Girardi L., et al., 2011, *A&A* 527, A116

- Ciprini S., 2009, ATel 2136
- Ciprini S., *Fermi-LAT Collaboration* 2018, In: Berton M., Antón S., Foschini L., Ilic D., Kharb P., Kollatschny W., Lähteenmäki A., Peterson B., Popovic L., Rafanelli P., Sani E. (eds.) *Revisiting Narrow-Line Seyfert 1 Galaxies and their Place in the Universe*, PoS(NLS1-2018) 020
- Clark G.W., 1965, *Phys. Rev. Lett.* 14, 91
- Clark G.W., Woo J.W., Nagase F., et al., 1990, *ApJ* 353, 274
- Clarke R., 1990, *NIMPA* 291, 117
- Clarke R., 1994, *NIMPA* 347, 529
- Cohen J., Delgado G., Hardy E., et al., 2003, In: Schwarz H.E. (ed.) *Light Pollution: The Global View*, Springer, Dordrecht (NL), *Astrophysics and Space Science Library* 284, p. 225
- Cohen M.H., Kellermann K.I., Shaffer D.B., et al., 1977, *Nature* 268, 405
- Collin S., Kawaguchi T., 2004, *A&A* 426, 797
- Collmar W., 2001, In: Aharonian F.A., Völk H.J. (eds.) *High Energy Gamma-Ray Astronomy: International Symposium*, AIP Publishing (Melville, NY, USA), *AIP Conf. Proc.* 558, p.656
- Cologna G., Chakraborty N., Jacholkowska A., et al., 2017, In: 6th International Symposium on High Energy Gamma-Ray Astronomy, AIP Publishing (Melville, NY, USA), *AIP Conf. Proc.* 1792, p. 050019
- Condon J.J., Cotton W.D., Greisen E.W., et al., 1998, *AJ* 115, 1693
- Congiu E., Contini M., Ciroi S., et al., 2017, *FrASS* 4, 27
- Conselice C.J., Wilkinson A., Duncan K., Mortlock A., 2016, *ApJ* 830, 83
- Corbin M.R., 1995, *ApJ* 447, 496
- Corral-Santana J.M., Casares J., Muñoz-Darias T., et al., 2016, *A&A* 587, A61
- Costamante L., Ghisellini G., Giommi P., et al., 2001, *A&A* 371, 512
- Cox A.N., 2002, *Allen's astrophysical quantities*, Springer, New York, USA, 4th edition
- Cracco V., Ciroi S., di Mille F., et al., 2011, *MNRAS* 418, 2630
- Craine E.R., Strittmatter P.A., Tapia S., et al., 1976, 17, 123
- Crameri F., 2018, *Scientific Colour Maps*, Zenodo
- Crameri F., Shephard G.E., Heron P.J., 2020, *Nat. Commun.* 11, 5444
- Cui W., 2004, *ApJ* 605, 662
- Curtis H.D., 1918, *Publ. of Lick Obs.* 13, 9
- Czerny B., Hryniewicz K., 2011, *A&A* 525, L8
- Daly R.A., Marscher A.P., 1988, *ApJ* 334, 539
- D'Ammando F., Acosta-Pulido J.A., Capetti A., et al., 2018, *MNRAS* 478, L66
- D'Ammando F., Acosta-Pulido J.A., Capetti A., et al., 2017, *MNRAS* 469, L11
- D'Ammando F., Gokus A., Kadler M., Ojha R., 2019, ATel 13233
- D'Ammando F., Orienti M., Finke J., et al., 2016, *MNRAS* 463, 4469
- D'Ammando F., Orienti M., Finke J., et al., 2013, *MNRAS* 436, 191
- D'Ammando F., Orienti M., Finke J., et al., 2012, *MNRAS* 426, 317
- D'Ammando F., Orienti M., Finke J., et al., 2015, *MNRAS* 446, 2456
- D'Ammando F., Raiteri C.M., Villata M., et al., 2011, *A&A* 529, A145
- Davison P.J.N., Culhane J.L., Mitchell R.J., Fabian A.C., 1975, *ApJL* 196, L23
- de Korte P.A.J., Bleeker J.A.M., den Boggende A.J.F., et al., 1981, *SSR* 30, 495
- de Vaucouleurs G., 1959, In: Flüge S. (ed.) *Encyclopedia of Physics: Astrophysics IV: Stellar Systems*, Springer Berlin, Heidelberg
- Decarli R., Dotti M., Fontana M., Haardt F., 2008, *MNRAS* 386, L15
- den Herder J.W., Brinkman A.C., Kahn S.M., et al., 2001, *A&A* 365, L7
- Dent W.A., 1965a, *Science* 148, 1458
- Dent W.A., 1965b, *AJ* 70, 672
- Derdeyn S.M., Ehrmann C.H., Fichtel C.E., et al., 1972, *NuclIM* 98, 557
- Dermer C.D., 1995, *ApJL* 446, L63
- Dermer C.D., Menon G., 2009, *High Energy Radiation from Black Holes: Gamma Rays, Cosmic Rays, and Neutrinos*, Princeton Univ. Press, Princeton, NJ, USA
- Dermer C.D., Schlickeiser R., 1992, *Science* 257, 1642
- Dermer C.D., Schlickeiser R., 1993, *ApJ* 416, 458
- Dermer C.D., Schlickeiser R., Mastichiadis A., 1992, *A&A* 256, L27

- Dewdney P.E., Hall P.J., Schilizzi R.T., Lazio T.J.L.W., 2009, *IEEE Proc.* 97, 1482
- Dimitrakoudis S., Mastichiadis A., Protheroe R.J., Reimer A., 2012, *A&A* 546, A120
- Disney M.J., Peterson B.A., Rodgers A.W., 1974, *ApJL* 194, L79
- Donnarumma I., Vittorini V., Vercellone S., et al., 2009, *ApJL* 691, L13
- Dorner D., Arbet-Engels A., Baack D., et al., 2021, In: Keilhauer B., Kappes A. (eds.) 37th International Cosmic Ray Conference, PoS(ICRC2021) 851
- Dotson A., Georganopoulos M., Meyer E.T., McCann K., 2015, *ApJ* 809, 164
- Dreyer J.L.E., 1888, *Mem. R. Astron. Soc.* 49, 1
- Drinkwater M.J., Webster R.L., Francis P.J., et al., 1997, *MNRAS* 284, 85
- Dunlop J.S., McLure R.J., Kukula M.J., et al., 2003, *MNRAS* 340, 1095
- Edelson R., Turner T.J., Pounds K., et al., 2002, *ApJ* 568, 610
- Edge A., Sutherland W., Kuijken K., et al., 2013, *The Messenger* 154, 32
- Edge D.O., Shakeshaft J.R., McAdam W.B., et al., 1959a, *Mem. R. Astron. Soc.* 68, 37
- Edge D.O., Shakeshaft J.R., McAdam W.B., et al., 1959b, *Mem. R. Astron. Soc.* 68, 37
- Eichmann B., Schlickeiser R., Rhode W., 2012, *ApJ* 744, 153
- Eisenstein D.J., Hut P., 1998, *ApJ* 498, 137
- Ellingson S.W., Clarke T.E., Cohen A., et al., 2009, *IEEE Proc.* 97, 1421
- Emerson J., McPherson A., Sutherland W., 2006, *The Messenger* 126, 41
- Enome S., 1982, *AdSpR* 2, 201
- Errando M., Bock R., Kranich D., et al., 2008, In: Aharonian F.A., Hofmann W., Rieger F. (eds.) 4th International Meeting on High Energy Gamma-Ray Astronomy, AIP Publishing (Melville, NY, USA), AIP Conf. Proc. 1085, p.423
- Event Horizon Telescope Collaboration Akiyama K., Alberdi A., et al., 2019a, *ApJL* 875, L2
- Event Horizon Telescope Collaboration Akiyama K., Alberdi A., et al., 2019b, *ApJL* 875, L1
- Fabbiano G., Kim D.W., Trinchieri G., 1992, *ApJS* 80, 531
- Fabian A.C., Rees M.J., 1979, In: Baity W.A., Peterson L.E. (eds.) X-ray Astronomy; Proc. of the Symposium, Pergamon Press (Oxford, UK), p.381
- Fabian A.C., Zoghbi A., Ross R.R., et al., 2009, *Nature* 459, 540
- Falcone A.D., Cui W., Finley J.P., 2004, *ApJ* 601, 165
- Fanaroff B.L., Riley J.M., 1974, *MNRAS* 167, 31P
- Fath E.A., 1909, *PASP* 21, 138
- Fazio G.G., Helmken H.F., O'Mongain E., Weekes T.C., 1972, *ApJL* 175, L117
- Feenberg E., Primakoff H., 1948, *Phys. Rev.* 73, 449
- Feigelson E.D., Schreier E.J., Delvaille J.P., et al., 1981, *ApJ* 251, 31
- Fermi E., 1949, *Phys. Rev.* 75, 1169
- Fermi-LAT collaboration: Abdollahi S., et al., 2022, *ApJS*, in press (arXiv:2201.11184)
- Feroci M., Frontera F., Costa E., et al., 1997, In: Siegmund O.H., Gummin M.A. (eds.) EUV, X-Ray, and Gamma-Ray Instrumentation for Astronomy VIII, SPIE (Bellingham, WA, USA), Proc. SPIE 3114, p.186
- Fichtel C., Greisen K., Kniffen D., 1975, *Phys. Today* 28, 42
- Finke J.D., 2013, *ApJ* 763, 134
- Finke J.D., Dermer C.D., Böttcher M., 2008, *ApJ* 686, 181
- Fisher P.C., Johnson H.M., Jordan W.C., et al., 1966, *ApJ* 143, 203
- Fitch W.S., Pacholczyk A.G., Weymann R.J., 1967, *ApJL* 150, L67
- Fitzpatrick E.L., 1999, *PASP* 111, 63
- Forman W., Jones C., Cominsky L., et al., 1978, *ApJS* 38, 357
- Foschini L., 2017, *FrASS* 4, 6
- Foschini L., 2022, *FrASS* 8, 234
- Foschini L., Berton M., Caccianiga A., et al., 2015, *A&A* 575, A13
- Foschini L., Ghisellini G., Kovalev Y.Y., et al., 2011, *MNRAS* 413, 1671
- Foschini L., Lister M.L., Antón S., et al., 2021, *Universe* 7, 372
- Fossati G., Buckley J.H., Bond I.H., et al., 2008, *ApJ* 677, 906

- Fossati G., Maraschi L., Celotti A., et al., 1998, *MNRAS* 299, 433
- Fraija N., Cabrera J.I., Benítez E., Hiriart D., 2014, In: Caraveo P., D’Avanzo P., Gehrels N., Tagliaferrri G. (eds.) *Swift: 10 Years of Discovery*, PoS(SWIFT 10) 152
- Friedman H., Lichtman S.W., Byram E.T., 1951, *Phys. Rev.* 83, 1025
- Fromm C.M., Perucho M., Mimica P., Ros E., 2016, *A&A* 588, A101
- Fromm C.M., Perucho M., Ros E., et al., 2011, *A&A* 531, A95
- Fuhrmann L., Larsson S., Chiang J., et al., 2014, *MNRAS* 441, 1899
- Fürst F., Walton D.J., Harrison F.A., et al., 2016, *ApJL* 831, L14
- Gaia Collaboration Brown A.G.A., Vallenari A., et al., 2018, *A&A* 616, A1
- Gaia Collaboration Brown A.G.A., Vallenari A., et al., 2021, *A&A* 649, A1
- Gaia Collaboration Brown A.G.A., Vallenari A., et al., 2016a, *A&A* 595, A2
- Gaia Collaboration Prusti T., de Bruijne J.H.J., et al., 2016b, *A&A* 595, A1
- Gaidos J.A., Akerlof C.W., Biller S., et al., 1996, *Nature* 383, 319
- Gaillardetz R., Bjorkholm P., Mastronardi R., et al., 1978, *ITNS* 25, 437
- Gallo L.C., Edwards P.G., Ferrero E., et al., 2006, *MNRAS* 370, 245
- Garcia-Gonzalez J.A., Martinez I., 2019, *ATel* 12683
- Garmire G.P., Bautz M.W., Ford P.G., et al., 2003, In: Truemper J.E., Tananbaum H.D. (eds.) *X-Ray and Gamma-Ray Telescopes and Instruments for Astronomy*, SPIE (Bellingham, WA, USA), Proc. SPIE 4851, p.28
- Gaur H., Gupta A.C., Wiita P.J., 2012, *AJ* 143, 23
- Gazeas K., 2019, *Galaxies* 7, 58
- Gehrels N., Chincarini G., Giommi P., et al., 2004, *ApJ* 611, 1005
- Gendreau K.C., Arzoumanian Z., Okajima T., 2012, In: Takahashi T., Murray S.S., den Herder J.W.A. (eds.) *Space Telescopes and Instrumentation 2012: Ultraviolet to Gamma Ray*, SPIE (Bellingham, WA, USA), Proc. SPIE 8443, p.322
- Ghisellini G., Della Ceca R., Volonteri M., et al., 2010, *MNRAS* 405, 387
- Ghisellini G., Madau P., 1996, *MNRAS* 280, 67
- Ghisellini G., Maraschi L., Treves A., 1985, *A&A* 146, 204
- Ghisellini G., Righi C., Costamante L., Tavecchio F., 2017, *MNRAS* 469, 255
- Ghisellini G., Tavecchio F., 2008, *MNRAS* 386, L28
- Ghisellini G., Tavecchio F., 2009, *MNRAS* 397, 985
- Ghisellini G., Tavecchio F., 2015, *MNRAS* 448, 1060
- Ghisellini G., Tavecchio F., Chiaberge M., 2005, *A&A* 432, 401
- Giacconi R., Branduardi G., Briel U., et al., 1979, *ApJ* 230, 540
- Giacconi R., Gursky H., Paolini F.R., Rossi B.B., 1962, *PRL* 9, 439
- Giacconi R., Gursky H., Waters J.R., 1964, *Nature* 204, 981
- Giacconi R., Kellogg E., Gorenstein P., et al., 1971, *ApJL* 165, L27
- Giacconi R., Murray S., Gursky H., et al., 1974, *ApJS* 27, 37
- Giacconi R., Rossi B., 1960, *JGR* 65, 773
- Giacconi R., Zirm A., Wang J., et al., 2002, *ApJS* 139, 369
- Giannios D., Uzdensky D.A., Begelman M.C., 2009, *MNRAS* 395, L29
- Giebels B., Degrange B., 2009, *A&A* 503, 797
- Ginzburg V.L., Syrovatskii S.I., 1965, *ARA&A* 3, 297
- Giommi P., Barr P., Garilli B., et al., 1990, *ApJ* 356, 432
- Giroletti M., Giovannini G., Feretti L., et al., 2004, *ApJ* 600, 127
- Gokus A., 2017, Master’s thesis, FAU Erlangen-Nürnberg, Germany
- Gokus A., 2019, *ATel* 13229
- Gokus A., Angioni R., 2020, *ATel* 13774
- Gokus A., Kreikenbohm A., Leiter K., et al., 2021a, In: Keilhauer B., Kappes A. (eds.) *37th International Cosmic Ray Conference*, PoS(ICRC2021) 869
- Gokus A., Kreter M., Kadler M., et al., 2022, *ATel* 15202

- Gokus A., Paliya V.S., Wagner S.M., et al., 2021b, *A&A* 649, A77
- Gokus A., Richter S., Spanier F., et al., 2018, *AN* 339, 331
- Goldsmith D.W., Kinman T.D., 1965, *ApJ* 142, 1693
- Gorenstein P., Gursky H., Garmire G., 1968, *ApJ* 153, 885
- Grinberg V., Hell N., Pottschmidt K., et al., 2013, *A&A* 554, A88
- Grinberg V., Pottschmidt K., Böck M., et al., 2014, *A&A* 565, A1
- Grindlay J., Gursky H., Schnopper H., et al., 1976, *ApJL* 205, L127
- Grupe D., 2004, *AJ* 127, 1799
- Grupe D., Komossa S., Leighly K.M., Page K.L., 2010, *ApJS* 187, 64
- Guo F., Li H., Daughton W., Liu Y.H., 2014, *PRL* 113, 155005
- H. E. S. S. Collaboration Abramowski A., Acero F., et al., 2013, *A&A* 554, A107
- Hamming R.W., 1983, *Digital filters*, Prentice-Hall, USA, 2nd edition
- Hargrave P.J., Ryle M., 1974, *MNRAS* 166, 305
- Harris G.L.H., Rejkuba M., Harris W.E., 2010, *Proc. Astron. Soc. Aust.* 27, 457
- Harrison F.A., Craig W.W., Christensen F.E., et al., 2013, *ApJ* 770, 103
- Hartman R.C., Bertsch D.L., Bloom S.D., et al., 1999, *ApJS* 123, 79
- Hasinger G., van der Klis M., 1989, *A&A* 225, 79
- Hayakawa S., 1952, *PThPh* 8, 571
- Hazard C., Mackey M.B., Shimmins A.J., 1963, *Nature* 197, 1037
- Healey S.E., Romani R.W., Cotter G., et al., 2008, *ApJS* 175, 97
- Heil J., Zacharias M., 2020, *A&A* 641, A114
- Henri G., Pelletier G., 1991, *ApJL* 383, L7
- Hernández-García L., Panessa F., Giroletti M., et al., 2017, *A&A* 603, A131
- Herschel J.F.W., 1864, *RSPT* 154, 1
- Hervet O., Williams D.A., Falcone A.D., Kaur A., 2019, *ApJ* 877, 26
- Heßdörfer J., 2021, Bachelor's thesis, University Würzburg, Germany
- HI4PI Collaboration, Ben Bekhti N., Flöer L., et al., 2016, *A&A* 594, A116
- Hicks D.B., Ried L., Peterson L.E., 1965, *ITNS* 12, 54
- Hitomi Collaboration, Aharonian F., Akamatsu H., et al., 2018a, *PASJ* 70, 9
- Hitomi Collaboration, Aharonian F., Akamatsu H., et al., 2018b, *PASJ* 70, 11
- Ho P.T.P., Moran J.M., Lo K.Y., 2004, *ApJL* 616, L1
- Hoffmeister C., 1929, *AN* 236, 233
- Hofmann W., 2017, *The Messenger* 168, 21
- Holland A.D., Turner M.J., Abbey A.F., Pool P.J., 1996, In: Siegmund O.H., Gummin M.A. (eds.) *EUV, X-Ray, and Gamma-Ray Instrumentation for Astronomy VII*, SPIE (Bellingham, WA, USA), *Proc. SPIE* 2808, p.414
- Hook I.M., McMahon R.G., Patnaik A.R., et al., 1995, *MNRAS* 273, L63
- Horan D., Acciari V.A., Bradbury S.M., et al., 2009, *ApJ* 695, 596
- Hoskin M.A., 1976, *JHA* 7, 169
- Houck J.C., Denicola L.A., 2000, In: Manset N., Veillet C., Crabtree D. (eds.) *Astronomical Data Analysis Software and Systems IX*, *Astron. Soc. Pacific* (San Francisco, CA, USA), *ASP Conf. Ser.* 216, p. 591
- Hoyle F., Fowler W.A., 1963, *MNRAS* 125, 169
- Hubble E., 1929, *PNAS* 15, 168
- Hubble E.P., 1926, *ApJ* 64, 321
- Hudson H.S., Peterson L.E., Schwartz D.A., 1969, *ApJ* 157, 389
- IceCube Collaboration, Aartsen M.G., Ackermann M., et al., 2018a, *Science* 361, eaat1378
- IceCube Collaboration, Aartsen M.G., Ackermann M., et al., 2018b, *Science* 361, 147
- Ingram A., Mastroserio G., van der Klis M., et al., 2021, *MNRAS*
- Israelian G., 1997, *BAAS* 29, 1466
- Ives J.C., Sanford P.W., Penston M.V., 1976, *ApJL* 207, L159
- Ivezić Ž., Menou K., Knapp G.R., et al., 2002, *AJ* 124, 2364
- Jahoda K., Swank J.H., Giles A.B., et al., 1996, In: Siegmund O.H., Gummin M.A. (eds.) *EUV, X-Ray, and Gamma-Ray Instrumentation for Astronomy VII*, SPIE (Bellingham, WA, USA), *Proc. SPIE* 2808, p.59

- Jansen F., Lumb D., Altieri B., et al., 2001, *A&A* 365, L1
- Jansky K.G., 1933, *Nature* 132, 66
- Järvelä E., Lähteenmäki A., Lietzen H., et al., 2017, *A&A* 606, A9
- Jarvis M.J., Bonfield D.G., Bruce V.A., et al., 2013, *MNRAS* 428, 1281
- Jarvis M.J., McLure R.J., 2006, *MNRAS* 369, 182
- Jelley J.V., 1966, *Nature* 211, 472
- Jelley J.V., Porter N.A., 1963, *QJRAS* 4, 275
- Jennison R.C., 1958, *MNRAS* 118, 276
- Jennison R.C., Das Gupta M.K., 1953, *Nature* 172, 996
- Johnston S., Taylor R., Bailes M., et al., 2008, *ExA* 22, 151
- Jonas J.L., 2009, *IEEE Proc.* 97, 1522
- Jones D.H., Read M.A., Saunders W., et al., 2009, *MNRAS* 399, 683
- Jorstad S., Marscher A., 2016, *Galaxies* 4, 47
- Jorstad S.G., Marscher A.P., Morozova D.A., et al., 2017, *ApJ* 846, 98
- Joye W.A., Mandel E., 2003, In: Payne H.E., Jedrzejewski R.I., Hook R.N. (eds.) *Astronomical Data Analysis Software and Systems XII*, Astron. Soc. Pacific (San Francisco, CA, USA), ASP Conference Series 295, p. 489
- Kaaret P., Zajczyk A., LaRocca D.M., et al., 2019, *ApJ* 884, 162
- Kaastra J.S., Bleeker J.A.M., 2016, *A&A* 587, A151
- Kaastra J.S., Ferrigno C., Tamura T., et al., 2001, *A&A* 365, L99
- Kadler M., Bach U., Berge D., et al., 2021, In: Keilhauer B., Kappes A. (eds.) *37th International Cosmic Ray Conference*, PoS(ICRC2021) 974
- Kadler M., Krauß F., Mannheim K., et al., 2016, *Nat. Ph.* 12, 807
- Kaluźniński L.J., 1977, Ph.D. thesis, University of Maryland, USA
- Kapanadze B., Dorner D., Vercellone S., et al., 2016, *ApJ* 831, 102
- Karttunen H., Kroeger P., Oja H., et al., 2003, *Fundamental astronomy*, Springer Verlag Berlin Heidelberg New York, 3rd edition
- Keenan M., Meyer E.T., Georganopoulos M., et al., 2021, *MNRAS* 505, 4726
- Keivani A., Kennea J.A., Evans P.A., et al., 2021, *ApJ* 909, 126
- Kellermann K.I., Lister M.L., Homan D.C., et al., 2004, *ApJ* 609, 539
- Kellermann K.I., Pauliny-Toth I.I.K., 1968, *ARA&A* 6, 417
- Kellermann K.I., Pauliny-Toth I.I.K., 1969, *ApJL* 155, L71
- Kellermann K.I., Sramek R., Schmidt M., et al., 1989, *AJ* 98, 1195
- Kellermann K.I., Vermeulen R.C., Zensus J.A., Cohen M.H., 1998, *AJ* 115, 1295
- Kelner S.R., Aharonian F.A., 2008, *Phys. Rev. D* 78, 034013
- Kerr R.P., 1963, *PRL* 11, 237
- Khachikian E.Y., Weedman D.W., 1974, *ApJ* 192, 581
- Kiehlmann S., Hovatta T., Kadler M., et al., 2019, *ATel* 12996
- Kikuchi S., Mikami Y., 1987, *PASJ* 39, 237
- King A.R., Pringle J.E., West R.G., Livio M., 2004, *MNRAS* 348, 111
- Kirk J.G., Rieger F.M., Mastichiadis A., 1998, *A&A* 333, 452
- Kirsch M.G.F., Schönherr G., Kendziorra E., et al., 2006, *A&A* 453, 173
- Klapdor-Kleingrothaus H.V., Zuber K., 1997, *Particle astrophysics*, CRC Press, Boca Raton, Florida, USA
- Klebesadel R.W., Strong I.B., Olson R.A., 1973, *ApJL* 182, L85
- Klingler N.J., Kennea J.A., Evans P.A., et al., 2019, *ApJS* 245, 15
- Kniffen D.A., 1989, *NYASA* 571, 482
- Kochanek C.S., Shappee B.J., Stanek K.Z., et al., 2017, *PASP* 129, 104502
- Kolodzig A., Gilfanov M., Sunyaev R., et al., 2013, *A&A* 558, A89
- Komissarov S.S., 1990, *SvAL* 16, 284
- Komissarov S.S., Falle S.A.E.G., 1997, *MNRAS* 288, 833
- Komossa S., 2018, In: Berton M., Antón S., Foschini L., Ilic D., Kharb P., Kollatschny W., Lähteenmäki A., Peterson B., Popovic L., Rafanelli P., Sani E. (eds.) *Revisiting Narrow-Line Seyfert 1 Galaxies and their Place in the Universe*, PoS(NLS1-2018) 015

- Komossa S., Voges W., Xu D., et al., 2006, *AJ* 132, 531
- Kondo I., Inoue H., Koyama K., et al., 1981, *Space Sci. Instr.* 5, 211
- Königl A., 1981, *ApJ* 243, 700
- Kotilainen J.K., León-Tavares J., Olguín-Iglesias A., et al., 2016, *ApJ* 832, 157
- Koyama K., Inoue H., Makishima K., et al., 1981, *ApJL* 247, L27
- Kraushaar W.L., Clark G.W., Garmire G.P., et al., 1972, *ApJ* 177, 341
- Krauss F., 2016, Ph.D. thesis, Friedrich Alexander University, Erlangen-Nürnberg, Germany
- Krauß F., Deoskar K., Baxter C., et al., 2018, *A&A* 620, A174
- Krauß F., Kadler M., Mannheim K., et al., 2014, *A&A* 566, L7
- Krauß F., Wang B., Baxter C., et al., 2015, In: Fukazawa Y., Tanaka Y., Itoh R. (eds.) 5th International Fermi Symposium, Nagoya, Japan, arXiv:1502.02147
- Krauß F., Wilms J., Kadler M., et al., 2016, *A&A* 591, A130
- Kreikenbohm A., 2019, Ph.D. thesis, ITAP, University Würzburg, Germany
- Kreikenbohm A., Schulz R., Kadler M., et al., 2016, *A&A* 585, A91
- Kreter M., Gokus A., Krauss F., et al., 2020a, *ApJ* 903, 128
- Kreter M., Kadler M., Krauß F., et al., 2020b, *ApJ* 902, 133
- Krimm H.A., Holland S.T., Corbet R.H.D., et al., 2013, *ApJS* 209, 14
- Krolik J.H., Begelman M.C., 1988, *ApJ* 329, 702
- Kunkel W., Madore B., Shelton I., et al., 1987, 4316, 1
- Lagrange J.L., 1772, *Prix de l'académie royale des Sciences de paris* 9, 292
- Lähteenmäki A., Järvelä E., Ramakrishnan V., et al., 2018, *A&A* 614, L1
- Laing R.A., Riley J.M., Longair M.S., 1983, *MNRAS* 204, 151
- Lansbury G.B., Alexander D.M., Del Moro A., et al., 2014, *ApJ* 785, 17
- Lasota J.P., Abramowicz M.A., Chen X., et al., 1996, *ApJ* 462, 142
- Lawrence A., 1980, *MNRAS* 192, 83
- Lawrence A., 1991, *MNRAS* 252, 586
- Lawrence A., Elvis M., 1982, *ApJ* 256, 410
- Leacock R.J., Smith A.G., Edwards P.L., et al., 1976, *ApJL* 206, L87
- Leahy D.A., Darbro W., Elsner R.F., et al., 1983, *ApJ* 266, 160
- Leavitt H.S., Pickering E.C., 1912, *Harvard College Obs. Circ.* 173, 1
- Levine A.M., Bradt H., Cui W., et al., 1996, *ApJL* 469, L33
- Levine A.M., Lang F.L., Lewin W.H.G., et al., 1984, *ApJS* 54, 581
- Lewin W.H.G., Hoffman J.A., Doty J., et al., 1976, *MNRAS* 177, 83P
- Li C.K., Lin L., Xiong S.L., et al., 2021, *Nat. Astron.* 5, 378
- Li X., Guo F., Li H., Li S., 2018, *ApJ* 866, 4
- Liao N.H., Dou L.M., Jiang N., et al., 2019, *ApJL* 879, L9
- Liao N.H., Li S., Sheng Z.F., Fan Y.Z., 2020, *ApJL* 898, L56
- Lico R., Giroletti M., Orienti M., et al., 2014, *A&A* 571, A54
- Lisse C.M., Dennerl K., Englhauser J., et al., 1996, *Science* 274, 205
- Lister M.L., Aller M.F., Aller H.D., et al., 2018, *ApJS* 234, 12
- Liu C., Zhang Y., Li X., et al., 2020, *SCPMA* 63, 249503
- Liu H.T., Bai J.M., 2006, *ApJ* 653, 1089
- Liu Y., Zhang S.N., 2011, *ApJL* 728, L44
- Lochner J.C., Swank J.H., Szymkowiak A.E., 1991, *ApJ* 376, 295
- Lorimer D.R., Bailes M., McLaughlin M.A., et al., 2007, *Science* 318, 777
- Lumb D., Gondoin P., Erd C., et al., 2000, *ESA bulletin* 104, 20
- Lutz G., 2007, *Semiconductor Radiation Detectors*, Springer-Verlag Berlin Heidelberg, 2nd edition
- Lyubarskii Y.E., 1997, *MNRAS* 292, 679
- MacDonald G.H., Kenderdine S., Neville A.C., 1968, *MNRAS* 138, 259
- Macomb D.J., Akerlof C.W., Aller H.D., et al., 1995, *ApJL* 449, L99
- Madau P., Rees M.J., 2001, *ApJL* 551, L27

- MAGIC Collaboration, Acciari V.A., Ansoldi S., et al., 2018, *A&A* 619, A159
- MAGIC Collaboration, Acciari V.A., Ansoldi S., et al., 2020a, *MNRAS* 496, 3912
- MAGIC Collaboration, Acciari V.A., Ansoldi S., et al., 2020b, *A&A* 637, A86
- Mahoney W.A., Ling J.C., Jacobson A.S., Tapphorn R.M., 1980, *NuclIM* 178, 363
- Makishima K., 1986, In: Mason K.O., Watson M.G., White N.E. (eds.) *The Physics of Accretion onto Compact Objects*, Springer Verlag Berlin Heidelberg New York, Lecture Notes in Physics 266, p. 249
- Makishima K., Mihara T., Ishida M., et al., 1990, *ApJL* 365, L59
- Makishima K., Mitsuda K., Inoue H., et al., 1983, *ApJ* 267, 310
- Mannheim K., 1993, *A&A* 269, 67
- Mannheim K., Biermann P.L., 1989, *A&A* 221, 211
- Mannheim K., Biermann P.L., 1992, *A&A* 253, L21
- Maraschi L., Fossati G., Tavecchio F., et al., 1999, *ApJ* 526, L81
- Maraschi L., Ghisellini G., Celotti A., 1992, *ApJL* 397, L5
- Marcotulli L., Paliya V., Ajello M., et al., 2020, *ApJ* 889, 164
- Markowitz A.G., Krumpe M., Nikutta R., 2014, *MNRAS* 439, 1403
- Marscher A.P., 2005, *Mem. Soc. Astron. It.* 76, 168
- Marscher A.P., 2014, *ApJ* 780, 87
- Marscher A.P., Gear W.K., 1985, *ApJ* 298, 114
- Marscher A.P., Jorstad S.G., Larionov V.M., et al., 2010, *ApJL* 710, L126
- Marshall F.J., Clark G.W., 1984, *ApJ* 287, 633
- Marshall N., Warwick R.S., Pounds K.A., 1981, *MNRAS* 194, 987
- Mason K.O., Breeveld A., Much R., et al., 2001, *A&A* 365, L36
- Massaro E., Giommi P., Leto C., et al., 2009, *A&A* 495, 691
- Massaro E., Perri M., Giommi P., Nesci R., 2004, *A&A* 413, 489
- Mathur S., 2000, *MNRAS* 314, L17
- Mathur S., Elvis M., 1995, *AJ* 110, 1551
- Matsuoka M., Kawasaki K., Ueno S., et al., 2009, *PASJ* 61, 999
- Mattox J.R., Bertsch D.L., Chiang J., et al., 1996, *ApJ* 461, 396
- Max-Moerbeck W., Hovatta T., Richards J.L., et al., 2014, *MNRAS* 445, 428
- Mayer W.F., 1975, *JHATD* 14, 14
- McCracken H.J., Milvang-Jensen B., Dunlop J., et al., 2012, *A&A* 544, A156
- McHardy I., 1988, *Mem. Soc. Astron. It.* 59, 239
- McHardy I.M., 1989, In: Hunt J., Battrick B. (eds.) *The 23rd ESLAB Symposium on Two Topics in X Ray Astronomy. Volume 2: AGN and the X Ray Background*, ESA SP 296, p.1111
- McHardy I.M., Koerding E., Knigge C., et al., 2006, *Nature* 444, 730
- McHardy I.M., Lawrence A., Pye J.P., Pounds K.A., 1981, *MNRAS* 197, 893
- McKinney J.C., Tchekhovskoy A., Sadowski A., Narayan R., 2014, *MNRAS* 441, 3177
- McMahon R.G., Banerji M., Gonzalez E., et al., 2013, *The Messenger* 154, 35
- Meegan C., Lichti G., Bhat P.N., et al., 2009, *ApJ* 702, 791
- Meidinger N., Eder J., Fürmetz M., et al., 2015, In: Siegmund O.H. (ed.) *UV, X-Ray, and Gamma-Ray Space Instrumentation for Astronomy XIX*, SPIE (Bellingham, WA, USA), Proc. SPIE 9601, p.72
- Meier D.L., 2012, *Black Hole Astrophysics: The Engine Paradigm*, Springer Berlin, Heidelberg
- Meyer E.T., Fossati G., Georganopoulos M., Lister M.L., 2011, *ApJ* 740, 98
- Meyer M., Scargle J.D., Blandford R.D., 2019, *ApJ* 877, 39
- Mihara T., Makishima K., Kamijo S., et al., 1991, *ApJL* 379, L61
- Miller B.P., Brandt W.N., Schneider D.P., et al., 2011, *ApJ* 726, 20
- Mills B.Y., 1952, *AuSRA* 5, 456
- Mineshige S., Ouchi N.B., Nishimori H., 1994, *PASJ* 46, 97
- Mitchell R.J., Culhane J.L., 1977, *MNRAS* 178, 75P
- Mitsuda K., Bautz M., Inoue H., et al., 2007, *PASJ* 59, S1

- Miyamoto S., Kimura K., Kitamoto S., et al., 1991, *ApJ* 383, 784
- Miyamoto S., Kitamoto S., 1989, *Nature* 342, 773
- Miyamoto S., Kitamoto S., Iga S., et al., 1992, *ApJL* 391, L21
- Mohan P., Mangalam A., 2015, *ApJ* 805, 91
- Morrison P., 1958, *NCim* 7, 858
- Morrison P., Sartori L., 1965, *PRL* 14, 771
- Mücke A., Protheroe R.J., 2001, *APh* 15, 121
- Mücke A., Protheroe R.J., Engel R., et al., 2003, *APh* 18, 593
- Mukherjee S., Mitra K., Chatterjee R., 2019, *MNRAS* 486, 1672
- Müller C., 2014, Ph.D. thesis, University of Würzburg, Germany
- Müller C., Kadler M., Ojha R., et al., 2014, *A&A* 569, A115
- Müller C., Kadler M., Ojha R., et al., 2018, *A&A* 610, A1
- Murakami T., Fujii M., Hayashida K., et al., 1989, *PASJ* 41, 405
- Murakami T., Inoue H., Koyama K., et al., 1983, *PASJ* 35, 531
- Murray S.S., Chappell J.H., Kenter A.T., et al., 1997, In: Siegmund O.H., Gummin M.A. (eds.) *EUV, X-Ray, and Gamma-Ray Instrumentation for Astronomy VIII*, SPIE (Bellingham, WA, USA), Proc. SPIE 3114, p.11
- Nakamura M., Asada K., Hada K., et al., 2018, *ApJ* 868, 146
- Nalewajko K., Giannios D., Begelman M.C., et al., 2011, *MNRAS* 413, 333
- Nalewajko K., Sikora M., 2009, *MNRAS* 392, 1205
- Nalewajko K., Sikora M., Madejski G.M., et al., 2012, *ApJ* 760, 69
- Nan R., Li D., Jin C., et al., 2011, *IJMPD* 20, 989
- Nandra K., Barret D., Barcons X., et al., 2013, submitted in call for White Papers, arXiv:1306.2307
- Nandra K., George I.M., Mushotzky R.F., et al., 1997, *ApJ* 476, 70
- Napier P.J., 1995, In: Zensus J.A., Diamond P.J., Napier P.J. (eds.) *Very Long Baseline Interferometry and the VLBA*, Astron. Soc. Pacific (San Francisco, CA, USA), ASP Conference Series 82, p. 59
- Narayan R., Piran T., 2012, *MNRAS* 420, 604
- Neronov A., Semikoz D., Vovk I., 2010, *ATel* 2617
- Nolan P.L., Abdo A.A., Ackermann M., et al., 2012, *ApJS* 199, 31
- Nowak M.A., 2000, *MNRAS* 318, 361
- Nowak M.A., Vaughan B.A., Wilms J., et al., 1999, *ApJ* 510, 874
- Nowak M.A., Wilms J., Heinz S., et al., 2005, *ApJ* 626, 1006
- O’Dea C.P., Saikia D.J., 2021, *Astron. Astrophys. Rev.* 29, 3
- Offringa A.R., Wayth R.B., Hurley-Walker N., et al., 2015, *Proc. Astron. Soc. Aust.* 32, e008
- Ojha R., Kadler M., Böck M., et al., 2010, *A&A* 519, A45
- Oke J.B., Sargent W.L.W., Neugebauer G., Becklin E.E., 1967, *ApJL* 150, L173
- Olguín-Iglesias A., Kotilainen J., Chavushyan V., 2020, *MNRAS* 492, 1450
- Olguín-Iglesias A., León-Tavares J., Kotilainen J.K., et al., 2016, *MNRAS* 460, 3202
- Orienti M., D’Ammand F., 2011, *ATel* 3808
- Orienti M., D’Ammando F., Giroletti M., et al., 2014, *MNRAS* 444, 3040
- Orienti M., D’Ammando F., Larsson J., et al., 2015, *MNRAS* 453, 4037
- Oshlack A.Y.K.N., Webster R.L., Whiting M.T., 2001, *ApJ* 558, 578
- Osterbrock D.E., 1989, *Astrophysics of gaseous nebulae and active galactic nuclei*, University Science Books, Melville, NY, USA
- Osterbrock D.E., Koski A.T., 1976, *MNRAS* 176, 61P
- Osterbrock D.E., Martel A., 1993, *ApJ* 414, 552
- Osterbrock D.E., Pogge R.W., 1985, *ApJ* 297, 166
- Pacciani L., 2015, *ATel* 7402
- Pacciani L., Donnarumma I., Denney K.D., et al., 2012, *MNRAS* 425, 2015
- Padovani P., 2017, *Nat. Astron.* 1, 0194
- Padovani P., Giommi P., 1995, *ApJ* 444, 567
- Page K.L., Evans P.A., Tohuvavohu A., et al., 2020, *MNRAS* 499, 3459
- Paliya V.S., 2019, *JApA* 40, 39
- Paliya V.S., Ajello M., Rakshit S., et al., 2018, *ApJL* 853, L2
- Paliya V.S., Pérez E., García-Benito R., et al., 2020, *ApJ* 892, 133

- Paliya V.S., Sahayanathan S., Parker M.L., et al., 2014, *ApJ* 789, 143
- Paliya V.S., Sahayanathan S., Stalin C.S., 2015, *ApJ* 803, 15
- Paliya V.S., Stalin C.S., 2016, *ApJ* 820, 52
- Paliya V.S., Stalin C.S., Shukla A., Sahayanathan S., 2013, *ApJ* 768, 52
- Pan H.W., Yuan W., Yao S., et al., 2018, *ApJ* 866, 69
- Panessa F., Bassani L., 2002, *A&A* 394, 435
- Paragi Z., Reynolds C., Biggs A.D., et al., 2005, In: Romney J., Reid M. (eds.) *Future Directions in High Resolution Astronomy*, Astron. Soc. Pacific (San Francisco, CA, USA), ASP Conference Series 340, p. 611
- Park T., Kashyap V.L., Siemiginowska A., et al., 2006, *ApJ* 652, 610
- Pauliny-Toth I.I.K., Kellermann K.I., 1966, *ApJ* 146, 634
- Pauliny-Toth I.I.K., Witzel A., Preuss E., et al., 1978, *AJ* 83, 451
- Pavlidou V., Angelakis E., Myserlis I., et al., 2014, *MNRAS* 442, 1693
- Pavlinisky M., Tkachenko A., Levin V., et al., 2018, *ExA* 45, 315
- Peñil P., Domínguez A., Buson S., et al., 2020, *ApJ* 896, 134
- Peacock A., Andresen R.D., Manzo G., et al., 1981, *SSR* 30, 525
- Pearson T.J., Readhead A.C.S., 1988, *ApJ* 328, 114
- Pélangéon A., Atteia J.L., Nakagawa Y.E., et al., 2008, *A&A* 491, 157
- Penrose R., 1969, *NCimR* 1, 252
- Peterson J.R., Paerels F.B.S., Kaastra J.S., et al., 2001, *A&A* 365, L104
- Petropoulou M., Coenders S., Dimitrakoudis S., 2016, *Aph* 80, 115
- Petropoulou M., Mastichiadis A., 2015, *MNRAS* 447, 36
- Piano G., Cardillo M., Verrecchia F., et al., 2018, *ATel* 12005
- Piner B.G., Pant N., Edwards P.G., 2010, *ApJ* 723, 1150
- Piner B.G., Unwin S.C., Wehrle A.E., et al., 1999, *ApJ* 525, 176
- Plotkin R.M., Anderson S.F., Brandt W.N., et al., 2012, *ApJL* 745, L27
- Pottschmidt K., 2002, Ph.D. thesis, Eberhard-Karls-Universität Tübingen, Germany
- Poutanen J., Stern B., 2010, *ApJL* 717, L118
- Predehl P., Andritschke R., Arefiev V., et al., 2021, *A&A* 647, A1
- Predehl P., Sunyaev R.A., Becker W., et al., 2020, *Nature* 588, 227
- Press W.H., Teukolsky S.A., Vetterling W.T., Flannery B.P., 2007, *Numerical Recipes 3rd Edition: The Art of Scientific Computing*, Cambridge Univ. Press, UK, 3rd edition
- Prestage R.M., Constantikes K.T., Hunter T.R., et al., 2009, *IEEE Proc.* 97, 1382
- Punch M., Akerlof C.W., Cawley M.F., et al., 1992, *Nature* 358, 477
- Pushkarev A.B., Kovalev Y.Y., Lister M.L., Savolainen T., 2017, *MNRAS* 468, 4992
- Pye J.P., McGale P.A., Allan D.J., et al., 1995, *MNRAS* 274, 1165
- Qian Q., Fendt C., Vourellis C., 2018, *ApJ* 859, 28
- Rachen J.P., Mészáros P., 1998, *Phys. Rev. D* 58, 123005
- Raiteri C.M., Villata M., Acosta-Pulido J.A., et al., 2017, *Nature* 552, 374
- Rakshit S., Stalin C.S., Chand H., Zhang X.G., 2017, *ApJS* 229, 39
- Ramakrishnan V., Hovatta T., Nieppola E., et al., 2015, *MNRAS* 452, 1280
- Rao A.R., Singh K.P., Bhattacharya D., 2016, *arXiv:1608.06051*
- Rau A., Meidinger N., Nandra K., et al., 2013, *arXiv:1308.6785*
- Ravasio M., Tagliaferri G., Ghisellini G., Tavecchio F., 2004, *A&A* 424, 841
- Readhead A.C.S., Cohen M.H., Pearson T.J., Wilkinson P.N., 1978, *Nature* 276, 768
- Reber G., 1944, *ApJ* 100, 279
- Rees M.J., 1966, *Nature* 211, 468
- Revnivtsev M., Semena N., Akimov V., et al., 2012, In: Takahashi T., Murray S.S., den Herder J.W.A. (eds.) *Space Telescopes and Instrumentation 2012: Ultraviolet to Gamma Ray*, SPIE (Bellingham, WA, USA), Proc. SPIE 8443, p.279
- Reynolds S.P., 1982, *ApJ* 256, 13

- Ricci C., Loewenstein M., Kara E., et al., 2021, *ApJS* 255, 7
- Richards J.L., Max-Moerbeck W., Pavlidou V., et al., 2011, *ApJS* 194, 29
- Richter S., Spanier F., 2016, *ApJ* 829, 56
- Ricker G.R., Atteia J.L., Crew G.B., et al., 2003, In: Ricker G.R., Vanderspek R.K. (eds.) *Gamma-Ray Burst and Afterglow Astronomy 2001: A Workshop Celebrating the 1st Year of the HETE Mission*, AIP Publishing (Melville, NY, USA), AIP Conf. Proc. 662, p.3
- Rieger F.M., Volpe F., 2010, *A&A* 520, A23
- Rodrigues X., Garrappa S., Gao S., et al., 2021, *ApJ* 912, 54
- Röken C., Schuppan F., Proksch K., Schöneberg S., 2018, *A&A* 616, A172
- Romano P., Vercellone S., Foschini L., et al., 2018, *MNRAS* 481, 5046
- Roming P.W.A., Kennedy T.E., Mason K.O., et al., 2005, *Space Sci. Rev.* 120, 95
- Roques J.P., Paul J., Mandrou P., Lebrun F., 1990, *AdSpR* 10, 223
- Rothschild R.E., Blanco P.R., Gruber D.E., et al., 1998, *ApJ* 496, 538
- Rout S.K., Méndez M., Belloni T.M., Vadawale S., 2021, *MNRAS* 505, 1213
- Rutledge R.E., 1998, *PASP* 110, 754
- Rybicki G.B., Lightman A.P., 1979, *Radiative processes in astrophysics*, Wiley-Interscience, New York, USA
- Ryle M., Hewish A., 1960, *MNRAS* 120, 220
- Ryle M., Neville A.C., 1962, *MNRAS* 125, 39
- Ryle M., Smith F.G., Elsmore B., 1950, *MNRAS* 110, 508
- Sahu S., López Fortín C.E., Valadez Polanco I.A., Rajpoot S., 2021, *ApJ* in press
- Saito S., Stawarz Ł., Tanaka Y.T., et al., 2013, *ApJL* 766, L11
- Salomé Q., Longinotti A.L., Krongold Y., et al., 2021, *MNRAS* 501, 219
- Salpeter E.E., 1964, *ApJ* 140, 796
- Sandage A., 1964, *ApJ* 139, 416
- Sandage A., 1965, *ApJ* 141, 1560
- Sandage A., 1967, *ApJL* 150, L177
- Sanders W.T., Edgar R.J., Juda M., et al., 1992, In: Siegmund O.H.W. (ed.) *EUV, X-Ray, and Gamma-Ray Instrumentation for Astronomy III*, SPIE (Bellingham, WA, USA), Proc. SPIE 1743, p.60
- Sanders W.T., Edgar R.J., Liedahl D.A., Morgenthaler J.P., 1998, In: Breitschwerdt D., Freyberg M.J., Truemper J. (eds.) *IAU Colloq. 166: The Local Bubble and Beyond*, Springer Verlag Berlin Heidelberg New York, Lecture Notes in Physics 506, p.83
- Sanford P.W., 1974, *RSPSA* 340, 411
- Santangelo A., Madonia R., 2014, *Aph* 53, 130
- Satalecka K., Bernardini E., Dorner D., et al., 2021, In: Keilhauer B., Kappes A. (eds.) *37th International Cosmic Ray Conference, PoS(ICRC2021)* 960
- Savage R.D., Booth J.A., Gebhardt K., et al., 2008, In: Stepp L.M., Gilmozzi R. (eds.) *Ground-based and Airborne Telescopes II*, SPIE (Bellingham, WA, USA), Proc. SPIE 7012, p.119
- Savitzky A., Golay M.J.E., 1964, *Analytical Chemistry* 36, 1627
- Scargle J.D., Norris J.P., Jackson B., Chiang J., 2013, *ApJ* 764, 167
- Scheuer P.A.G., Readhead A.C.S., 1979, *Nature* 277, 182
- Schmidt M., 1963, *Nature* 197, 1040
- Schmitt J.L., 1968, *Nature* 218, 663
- Schönfelder V., Aarts H., Bennett K., et al., 1993, *ApJS* 86, 657
- Schönfelder V., Bennett K., Blom J.J., et al., 2000, *A&AS* 143, 145
- Schreier E.J., Gorenstein P., Feigelson E.D., 1982, *ApJ* 261, 42
- Schulz R., Kreikenbohm A., Kadler M., et al., 2016, *A&A* 588, A146
- Schwartz D.A., Hudson H.S., Peterson L.E., 1970, *ApJ* 162, 431
- Schwinger J., 1949, *Phys. Rev.* 75, 1912
- Seielstad G.A., Cohen M.H., Linfield R.P., et al., 1979, *ApJ* 229, 53
- Serlemitsos P.J., Petre R., Glasser C., Birsa F., 1984, *ITNS* 31, 786
- Serlemitsos P.J., Smith B.W., Boldt E.A., et al., 1977, *ApJL* 211, L63
- Seyfert C.K., 1943, *ApJ* 97, 28
- Shah Z., Mankuzhiyil N., Sinha A., et al., 2018, *RAA* 18, 141

- Shakeshaft J.R., Ryle M., Baldwin J.E., et al., 1955, *Mem. R. Astron. Soc.* 67, 106
- Shakura N.I., Sunyaev R.A., 1973, *A&A* 24, 337
- Shapley H., Curtis H.D., 1921, *Bul. of the Nat. Res. Council* 2, 171
- Sharov A.S., Efremov Y.N., 1963, *IBVS* 23, 1
- Shen Y., Richards G.T., Strauss M.A., et al., 2011, *ApJS* 194, 45
- Shukla A., Mannheim K., 2020, *Nat. Commun.* 11, 4176
- Shukla A., Mannheim K., Patel S.R., et al., 2018, *ApJL* 854, L26
- Siemiginowska A., Smith R.K., Aldcroft T.L., et al., 2003, *ApJL* 598, L15
- Sikora M., Begelman M.C., Rees M.J., 1994, *ApJ* 421, 153
- Sikora M., Stawarz Ł., Lasota J.P., 2007, *ApJ* 658, 815
- Sikora M., Stawarz Ł., Moderski R., et al., 2009, *ApJ* 704, 38
- Simionescu A., Werner N., Urban O., et al., 2015, *ApJL* 811, L25
- Singh K.K., Meintjes P.J., 2020, *AN* 341, 713
- Singh K.P., Kushwaha P., Sinha A., et al., 2021, *MNRAS*
- Singh V., Chand H., 2018, *MNRAS* 480, 1796
- Sinha A., Khatoon R., Misra R., et al., 2018, *MNRAS* 480, L116
- Sinha A., Shukla A., Misra R., et al., 2015, *A&A* 580, A100
- Sironi L., Giannios D., Petropoulou M., 2016, *MNRAS* 462, 48
- Sironi L., Spitkovsky A., 2014, *ApJL* 783, L21
- Siuniae R.A., Babichenko S.I., Goganov D.A., et al., 1990, *AdSpR* 10, 233
- Sizemore W., 1991, In: Crawford D.L. (ed.) *IAU Colloq. 112: Light Pollution, Radio Interference, and Space Debris*, *Astron. Soc. Pacific* (San Francisco, CA, USA), *ASP Conference Series* 17, p. 176
- Smith A.J., HAWC Collaboration 2015, In: 34th International Cosmic Ray Conference, *PoS(ICRC2015)* 966
- Smith J.F., Courtier G.M., 1976, *RSPSA* 350, 421
- Smith P.S., Montiel E., Rightley S., et al., 2009, In: 2nd International Fermi Symposium, *eConf Proceedings* C0911022, arXiv:0912.3621
- Soffitta P., Attinà P., Baldini L., et al., 2020, In: *Society of Photo-Optical Instrumentation Engineers (SPIE) Conference Series*, SPIE (Bellingham, WA, USA), *Proc. SPIE* 11444, p.1017
- Sol H., Zech A., Boisson C., et al., 2013, *APh* 43, 215
- Sood R.K., Thomas J.A., Waldron L., et al., 1988a, *MNRAS* 234, 73P
- Sood R.K., Thomas J.A., Waldron L., et al., 1988b, *Proc. Astron. Soc. Aust.* 7, 486
- Sowards-Emmerd D., Romani R.W., Michelson P.F., et al., 2005, *ApJ* 626, 95
- Spada M., Ghisellini G., Lazzati D., Celotti A., 2001, *MNRAS* 325, 1559
- Stein W.A., O'Dell S.L., Strittmatter P.A., 1976, *ARA&A* 14, 173
- Stella L., 1988, *Mem. Soc. Astron. It.* 59, 185
- Stocke J.T., Danforth C.W., Perlman E.S., 2011, *ApJ* 732, 113
- Stroh M.C., Falcone A.D., 2013, *ApJS* 207, 28
- Strüder L., Briel U., Dennerl K., et al., 2001, *A&A* 365, L18
- Sulentic J.W., Zamfir S., Marziani P., et al., 2003, *ApJL* 597, L17
- Swanenburg B.N., Bennett K., Bignami G.F., et al., 1981, *ApJL* 243, L69
- Swank J.H., Becker R.H., Boldt E.A., et al., 1977, *ApJL* 212, L73
- Takalo L.O., Nilsson K., Lindfors E., et al., 2008, In: Aharonian F.A., Hofmann W., Rieger F. (eds.) *4th International Meeting on High Energy Gamma-Ray Astronomy*, AIP Publishing (Melville, NY, USA), *AIP Conf. Proc.* 1085, p.705
- Takeuchi M., Mineshige S., Negoro H., 1995, *PASJ* 47, 617
- Tamm I.E., Frank I.M., 1934, *Doklady Akad. Nauk SSSR* 14, 107
- Tamura T., Kaastra J.S., Peterson J.R., et al., 2001, *A&A* 365, L87
- Tanaka Y., Fujii M., Inoue H., et al., 1984, *PASJ* 36, 641
- Tanaka Y., Inoue H., Holt S.S., 1994, *PASJ* 46, L37
- Tanaka Y., Nandra K., Fabian A.C., et al., 1995, *Nature* 375, 659

- Tanaka Y.T., Buson S., Kocevski D., 2017, *ATel* 10791
- Tanaka Y.T., Stawarz Ł., Thompson D.J., et al., 2011, *ApJ* 733, 19
- Tavani M., Barbiellini G., Argan A., et al., 2009, *A&A* 502, 995
- Tavecchio F., 2006, In: Novello M., Perez Bergli-
affa S., Ruffini R. (eds.) *The 10th Marcel Gross-
mann Meeting. On recent developments in theo-
retical and experimental general relativity, grav-
itation and relativistic field theories*, World Sci-
entific (Singapore), *Proc. MGC10*, p.512
- Tavecchio F., Becerra-Gonzalez J., Ghisellini G.,
et al., 2011, *A&A* 534, A86
- Tavecchio F., Ghisellini G., Bonnoli G., Ghirlanda
G., 2010, *MNRAS* 405, L94
- Tavecchio F., Maraschi L., Sambruna R.M., Urry
C.M., 2000, *ApJL* 544, L23
- Terasranta H., Tornikoski M., Valtaoja E., et al.,
1992, *A&AS* 94, 121
- Terrell J., Fenimore E.E., Klebesadel R.W., Desai
U.D., 1982, *ApJ* 254, 279
- Terrell, N. James J., 1972, *ApJL* 174, L35
- The Pierre Auger Collaboration, Aab A., Abreu P.,
et al., 2016, *arXiv:1604.03637*
- Thompson A.R., Gergely T.E., vanden Bout P.A.,
1991, *Phys. Today* 44, 41
- Tingay S.J., Goeke R., Bowman J.D., et al., 2013,
Proc. Astron. Soc. Aust. 30, e007
- Tingay S.J., Jauncey D.L., King E.A., et al., 2003,
PASJ 55, 351
- Tombesi F., Sambruna R.M., Reeves J.N., et al.,
2010, *ApJ* 719, 700
- Tomsick J.A., Boggs S.E., Zoglauer A., et al.,
2021, *arXiv:2109.10403*
- Tozzi P., Gilli R., Mainieri V., et al., 2006, *A&A*
451, 457
- Tran H.D., Lyke J.E., Mader J.A., 2011, *ApJL* 726,
L21
- Truemper J., 1982, *AdSpR* 2, 241
- Tsunemi H., Kitamoto S., Manabe M., et al., 1989,
PASJ 41, 391
- Türler M., 2011, *Mem. Soc. Astron. It.* 82, 104
- Türler M., Courvoisier T.J.L., Paltani S., 2000,
A&A 361, 850
- Turner M.J.L., Abbey A., Arnaud M., et al., 2001,
A&A 365, L27
- Turner M.J.L., Smith A., Zimmermann H.U., 1981,
SSR 30, 513
- Turner M.J.L., Thomas H.D., Patchett B.E., et al.,
1989, *PASJ* 41, 345
- Ubertini P., Barbanera L., Bazzano A., et al., 1986,
In: Culhane J.L. (ed.) *X-ray instrumentation in
astronomy*, SPIE (Bellingham, WA, USA), *Proc.
SPIE* 597, p.74
- Ubertini P., Lebrun F., Di Cocco G., et al., 2003,
A&A 411, L131
- Ueda Y., Eguchi S., Terashima Y., et al., 2007,
ApJL 664, L79
- Uhlenbeck G.E., Ornstein L.S., 1930, *Phys. Rev.*
36, 823
- Ulrich M.H., Kinman T.D., Lynds C.R., et al.,
1975, *ApJ* 198, 261
- Ulrich M.H., Maraschi L., Urry C.M., 1997,
ARA&A 35, 445
- Umar R., Abidin Z.Z., Ibrahim Z.A., 2013, In:
*Tropicale C., Tinggi B. (eds.) 2012 National
Physics Conference: (PERFIK 2012)*, AIP Pub-
lishing (Melville, NY, USA), *AIP Conf. Proc.*
1528, p.32
- Unwin S.C., Cohen M.H., Biretta J.A., et al., 1985,
ApJ 289, 109
- Urry C.M., Padovani P., 1995, *PASP* 107, 803
- Uttley P., 2004, *MNRAS* 347, L61
- Uttley P., McHardy I.M., 2001, *MNRAS* 323, L26
- Uttley P., McHardy I.M., Papadakis I.E., 2002,
MNRAS 332, 231
- van den Berg J.P., Böttcher M., Domínguez A.,
López-Moya M., 2019, *ApJ* 874, 47
- van der Klis M., 1989, In: Ögelman H., van
den Heuvel E.P.J. (eds.) *Timing Neutron Stars*,
Kluwer Academic/Plenum Publishers (New
York, NY, USA), *NATO ASI Series C* 262, p. 27
- van Haarlem M.P., Wise M.W., Gunst A.W., et al.,
2013, *A&A* 556, A2
- Vaughan S., Edelson R., Warwick R.S., Uttley P.,
2003, *MNRAS* 345, 1271
- Vaughan S., Reeves J., Warwick R., Edelson R.,
1999, *MNRAS* 309, 113
- Vedrenne G., Roques J.P., Schönfelder V., et al.,
2003, *A&A* 411, L63
- Venturi T., 2010, In: *10th European VLBI Net-
work Symposium and EVN Users Meeting:
VLBI and the New Generation of Radio Arrays*,

- PoS(10th EVN Symposium) 001
- Verner D.A., Ferland G.J., Korista K.T., Yakovlev D.G., 1996, *ApJ* 465, 487
- Vestergaard M., Peterson B.M., 2006, *ApJ* 641, 689
- Villata M., Raiteri C.M., 1999, *A&A* 347, 30
- Villata M., Raiteri C.M., Tosti G., et al., 2002, *Mem. Soc. Astron. It.* 73, 1191
- Vito F., Brandt W.N., Yang G., et al., 2018, *MNRAS* 473, 2378
- Voges W., Aschenbach B., Boller T., et al., 1999, *A&A* 349, 389
- von Montigny C., Bertsch D.L., Chiang J., et al., 1995, *ApJ* 440, 525
- Vovk I., Babić A., 2015, *A&A* 578, A92
- Wagner S., Rani B., H. E. S. S. Collaboration 2021, *ATel* 15020
- Wagner S.J., Witzel A., 1995, *ARA&A* 33, 163
- Wagner S.M., Burd P., Dorner D., et al., 2022, In: Keilhauer B., Kappes A. (eds.) 37th International Cosmic Ray Conference, PoS(ICRC2021) 868
- Wang F., Du P., Hu C., et al., 2016, *ApJ* 824, 149
- Wang J.M., Luo B., Ho L.C., 2004, *ApJ* 615, L9
- Wang Y., Xue Y., Zhu S., Fan J., 2018, *ApJ* 867, 68
- Warwick R.S., Marshall N., Fraser G.W., et al., 1981, *MNRAS* 197, 865
- Weekes T.C., Badran H., Biller S.D., et al., 2002, *Aph* 17, 221
- Weekes T.C., Cawley M.F., Fegan D.J., et al., 1989, *ApJ* 342, 379
- Wehrle A.E., Cohen M.H., Unwin S.C., et al., 1992, *ApJ* 391, 589
- Weidinger M., Spanier F., 2015, *A&A* 573, A7
- Weiler K.W., Johnston K.J., 1980, *MNRAS* 190, 269
- Weisskopf M.C., O'Dell S.L., van Speybroeck L.P., 1996, In: Hoover R.B., Walker A.B. (eds.) *Multilayer and Grazing Incidence X-Ray/EUV Optics III*, SPIE (Bellingham, WA, USA), Proc. SPIE 2805, p.2
- Wendel C., Shukla A., Mannheim K., 2021, *ApJ* 917, 32
- Werner G.R., Uzdensky D.A., Cerutti B., et al., 2016, *ApJL* 816, L8
- White G.J., Ricketts M.J., 1979, *MNRAS* 187, 757
- Williams R.K., 1995, *Phys. Rev. D* 51, 5387
- Wilms J., 2020, *X-ray Astronomy Lecture*, FAU Erlangen-Nürnberg
- Wilms J., Allen A., McCray R., 2000, *ApJ* 542, 914
- Wilson W.E., Ferris R.H., Axtens P., et al., 2011, *MNRAS* 416, 832
- Winkler C., Courvoisier T.J.L., Di Cocco G., et al., 2003, *A&A* 411, L1
- Wittels J.J., Cotton W.D., Counselman, C. C. I., et al., 1976, *ApJL* 206, L75
- Witze A., 2016, *Nature* 533, 18
- Wolter H., 1952, *AnP* 445, 94
- Woltjer L., 1959, *ApJ* 130, 38
- Wood K.S., Meekins J.F., Yentis D.J., et al., 1984, *ApJS* 56, 507
- Wood M., Caputo R., Charles E., et al., 2017, In: Park H.I., Oh S., Lee H.S., Kwak Y.S. (eds.) 35th International Cosmic Ray Conference, PoS(ICRC2017) 824
- Wootten A., Thompson A.R., 2009, *IEEE Proc.* 97, 1463
- Worrall D.M., Giommi P., Tananbaum H., Zamorani G., 1987, *ApJ* 313, 596
- XRISM Science Team 2020, White paper, arXiv:2003.04962
- Xu D., Komossa S., Zhou H., et al., 2012, *AJ* 143, 83
- Yoshida K., Yonetoku D., Arimoto M., et al., 2018, In: den Herder J.W.A., Nikzad S., Nakazawa K. (eds.) *Space Telescopes and Instrumentation 2018: Ultraviolet to Gamma Ray*, SPIE (Bellingham, WA, USA), Proc. SPIE 10699, p.1451
- Yuan W., Fabian A.C., Celotti A., Jonker P.G., 2003, *MNRAS* 346, L7
- Zamorani G., Henry J.P., Maccacaro T., et al., 1981, *ApJ* 245, 357
- Zel'dovich Y.B., Novikov I.D., 1964, *Dokl. Akad. Nauk SSSR* 155, 1033
- Zhang H., Li X., Giannios D., Guo F., 2021, *ApJ* 912, 129
- Zhang Y.H., Bai J.M., Zhang S.N., et al., 2006, *ApJ* 651, 782
- Zhang Y.H., Celotti A., Treves A., et al., 1999, *ApJ* 527, 719
- Zhang Z., Chen D.Y., Wu J., et al., 2019, *RAA* 19, 160

Zheng Y.G., Yang C.Y., Kang S.J., Bai J.M., 2021,
RAA 21, 008
Ziegler H., 1981, Appl. Spectrosc. 35, 88

A.1 *XMM-Newton* observation of Mrk 421 in June 2019

Spectra were extracted from *XMM-Newton* data with exposures of 2 ks for the full duration of the observation, which has been used to create the hysteresis curve. The spectra were fit with an absorbed power law. The results are listed in Table [A.1](#) (see next page) .

Table A.1.: Fit results of the spectra with 2 ks exposure. The time is given for the time since the start of the observation. Due to two changes in the observing mode, two gaps between 8 ks–13 ks, and 45–51 ks exist.

Time [ks]	Flux [10^{-10} erg cm $^{-2}$ s $^{-1}$]	Index	Fit statistic χ^2 /d.o.f.
0.0–2.0	$17.592^{+0.003}_{-0.002}$	2.047 ± 0.016	323.32/359
2.0–4.0	18.239 ± 0.003	$2.036^{+0.016}_{-0.015}$	395.73/369
4.0–6.0	18.041 ± 0.003	2.044 ± 0.18	307.13/325
6.0–8.0	17.508 ± 0.003	2.043 ± 0.18	358.36/320
13.3–15.3	16.615 ± 0.001	2.055 ± 0.005	592.52/618
15.3–17.3	17.110 ± 0.001	2.038 ± 0.005	592.07/619
17.3–19.3	17.317 ± 0.001	2.025 ± 0.005	608.25/625
19.3–21.3	17.853 ± 0.001	2.002 ± 0.005	731.11/640
21.3–23.3	18.464 ± 0.001	1.976 ± 0.005	740.57/644
23.3–25.3	19.118 ± 0.001	1.956 ± 0.005	761.91/653
25.3–27.3	19.743 ± 0.001	1.934 ± 0.005	728.96/662
27.3–29.3	19.911 ± 0.001	1.927 ± 0.005	783.42/669
29.3–31.3	20.113 ± 0.001	1.919 ± 0.005	756.36/675
31.3–33.3	20.738 ± 0.001	1.905 ± 0.005	715.58/673
33.3–35.3	21.198 ± 0.001	$1.890^{+0.004}_{-0.005}$	833.44/689
35.3–37.3	20.936 ± 0.001	$1.898^{+0.004}_{-0.005}$	796.79/680
37.3–39.3	20.608 ± 0.001	1.905 ± 0.005	690.08/681
39.3–41.3	20.430 ± 0.001	$1.920^{+0.005}_{-0.004}$	717.48/667
41.3–43.3	21.011 ± 0.001	1.910 ± 0.005	740.27/668
43.3–45.3	21.154 ± 0.001	$1.910^{+0.004}_{-0.005}$	689.94/671
51.1–53.1	22.712 ± 0.003	1.902 ± 0.014	410.57/428
53.1–55.1	22.672 ± 0.003	$1.912^{+0.015}_{-0.014}$	425.26/421
55.1–57.1	23.837 ± 0.003	$1.879^{+0.013}_{-0.014}$	435.78/445
57.1–59.1	24.992 ± 0.003	$1.858^{+0.014}_{-0.013}$	417.78/450
59.1–61.1	26.127 ± 0.003	1.848 ± 0.013	446.17/457
61.1–63.1	26.539 ± 0.003	$1.845^{+0.013}_{-0.012}$	434.25/455
63.1–65.1	26.345 ± 0.003	1.835 ± 0.013	426.54/460
65.1–67.1	26.558 ± 0.003	1.841 ± 0.013	471.09/460
67.1–69.1	27.491 ± 0.003	$1.822^{+0.013}_{-0.012}$	496.84/472
69.1–71.1	28.720 ± 0.003	1.816 ± 0.012	546.27/483
71.1–73.1	28.795 ± 0.004	1.824 ± 0.012	444.72/481
73.1–75.1	26.833 ± 0.003	$1.860^{+0.012}_{-0.013}$	428.83/458
75.1–77.1	26.068 ± 0.003	1.873 ± 0.013	472.12/456
77.1–79.1	25.599 ± 0.003	1.866 ± 0.013	473.17/458
79.1–81.1	25.694 ± 0.003	1.859 ± 0.013	459.58/455
81.1–83.1	26.255 ± 0.003	1.849 ± 0.013	476.24/460
83.1–85.1	26.642 ± 0.003	1.847 ± 0.013	450.76/468
85.1–87.1	26.643 ± 0.003	$1.849^{+0.013}_{-0.012}$	456.41/463

A.2 *Swift* observations of Mrk 421 in 2019

The observations of Mrk 421 in the first half of 2019 taken with *Swift*, and resulting X-ray and UV fluxes are listed in Table A.2 and A.3.

Table A.2.: Summary of the resulting fluxes at X-ray and UV energies measured with *Swift* XRT and UVOT, respectively. For both instruments, we report the unabsorbed fluxes.

Date	MJD	ObsID	X-ray			UV		
			Flux (0.5–10 keV) [10^{-10} erg cm $^{-2}$ s $^{-1}$]	Index	Fit statistic χ^2 /d.o.f.	Flux W1 [mJy]	Flux W2 [mJy]	Flux M2 [mJy]
2019-01-03	58486.26	00031630020	9.40 ± 0.12	2.080 ± 0.018	350.13/307.00	-	-	-
2019-01-05	58488.13	00031630021	14.25 ± 0.17	1.889 ± 0.015	581.47/367.00	8.80 ± 0.17	-	-
2019-01-07	58490.12	00031630022	8.52 ± 0.12	2.056 ± 0.018	308.64/303.00	-	-	-
2019-01-09	58492.11	00031630023	9.30 ± 0.13	1.997 ± 0.018	357.39/313.00	8.94 ± 0.17	-	-
2019-01-11	58494.10	00031630024	4.35 ± 0.08	2.231 ± 0.026	250.85/214.00	8.60 ± 0.16	-	-
2019-01-13	58496.09	00031630025	6.79 ± 0.10	2.185 ± 0.021	291.09/260.00	-	-	-
2019-01-15	58498.07	00031630026	6.64 ± 0.10	2.223 ± 0.021	304.73/261.00	8.53 ± 0.17	-	-
2019-01-17	58500.14	00031630027	5.67 ± 0.09	2.179 ± 0.023	274.37/250.00	8.28 ± 0.16	-	-
2019-01-19	58502.26	00031630028	3.92 ± 0.10	2.32 ± 0.04	162.39/148.00	-	-	-
2019-01-21	58504.18	00031630029	4.86 ± 0.08	2.334 ± 0.023	301.12/235.00	-	-	-
2019-01-23	58506.17	00031630030	8.21 ± 0.13	2.007 ± 0.020	320.34/283.00	-	-	-
2019-01-25	58508.91	00031630031	5.75 ± 0.08	2.401 ± 0.022	304.84/239.00	-	-	-
2019-01-28	58511.09	00031630032	6.14 ± 0.10	2.296 ± 0.023	267.85/229.00	8.59 ± 0.17	-	-
2019-02-01	58515.21	00031630034	5.72 ± 0.10	2.284 $^{+0.012}_{-0.041}$	279.84/250.00	-	-	-
2019-02-03	58517.20	00031630035	6.98 ± 0.10	2.344 ± 0.021	351.27/248.00	9.91 ± 0.21	-	-
2019-02-05	58519.26	00031630036	6.87 ± 0.10	2.346 ± 0.022	305.97/245.00	-	-	-
2019-02-07	58521.25	00031630037	6.23 ± 0.09	2.434 ± 0.022	290.97/235.00	-	-	-
2019-02-09	58523.20	00031630038	7.42 ± 0.14	2.412 ± 0.028	239.60/191.00	-	-	-
2019-02-12	58526.05	00031630039	6.42 ± 0.10	2.330 ± 0.022	273.89/238.00	-	-	-
2019-02-14	58528.11	00031630040	11.32 ± 0.16	2.192 ± 0.019	355.71/278.00	-	-	-
2019-02-16	58530.17	00031630041	10.73 ± 0.13	2.252 ± 0.017	387.71/296.00	-	-	-
2019-02-24	58538.12	00031630042	12.28 ± 0.14	2.140 ± 0.016	447.74/320.00	11.77 ± 0.22	10.11 ± 0.17	-
2019-02-26	58540.06	00031630043	7.10 ± 0.15	1.583 ± 0.025	478.38/283.00	11.49 ± 0.22	-	-
2019-02-28	58542.17	00031630044	12.89 ± 0.15	2.058 ± 0.016	394.86/334.00	-	-	-
2019-03-02	58544.23	00031630045	13.97 ± 0.15	2.067 ± 0.014	520.72/357.00	9.78 ± 0.19	-	-
2019-03-04	58546.96	00031630046	11.91 ± 0.13	2.029 ± 0.015	444.52/358.00	9.03 ± 0.17	-	-
2019-03-07	58549.95	00031630047	11.83 ± 0.13	2.145 ± 0.015	482.45/340.00	-	-	-
2019-03-09	58551.86	00031630048	15.53 ± 0.16	1.941 ± 0.013	521.26/391.00	9.54 ± 0.18	-	-
2019-03-11	58553.94	00031630049	11.41 ± 0.14	2.099 ± 0.016	443.60/328.00	9.43 ± 0.21	-	-
2019-03-14	58556.05	00031630050	12.73 ± 0.15	2.042 $^{+0.016}_{-0.015}$	465.24/341.00	9.39 ± 0.18	8.20 ± 0.14	-
2019-03-16	58558.11	00031630051	13.49 ± 0.15	2.014 $^{+0.015}_{-0.014}$	491.88/370.00	-	-	-
2019-03-23	58565.96	00031630052	11.83 ± 0.24	1.983 $^{+0.026}_{-0.025}$	287.72/237.00	9.08 ± 0.20	-	-
2019-03-25	58567.95	00031630053	20.03 ± 0.33	1.918 ± 0.021	351.11/278.00	10.30 ± 0.22	-	-
2019-03-28	58570.13	00031630054	17.02 ± 0.21	2.010 ± 0.016	418.53/335.00	9.86 ± 0.19	-	-
2019-03-29	58571.94	00031630055	14.38 ± 0.20	1.940 ± 0.018	375.52/310.00	11.15 ± 0.22	9.54 ± 0.17	-
2019-03-31	58573.93	00031630056	20.73 ± 0.20	2.001 ± 0.013	544.45/405.00	12.09 ± 0.23	-	-
2019-04-03	58576.91	00031630057	10.98 ± 0.13	2.205 ± 0.016	396.59/307.00	13.72 ± 0.26	11.70 ± 0.19	-
2019-04-05	58578.91	00031630058	11.11 ± 0.13	2.063 ± 0.016	431.94/337.00	13.46 ± 0.25	10.84 ± 0.18	-
2019-04-07	58580.90	00031630059	7.45 ± 0.12	2.021 ± 0.021	322.38/286.00	12.52 ± 0.24	10.67 ± 0.18	12.59 ± 0.27
2019-04-09	58582.96	00031630060	9.97 ± 0.12	2.165 ± 0.017	366.19/307.00	12.04 ± 0.23	10.35 ± 0.17	-
2019-04-12	58585.02	00031630061	19.90 ± 0.22	1.765 ± 0.013	515.99/449.00	12.07 ± 0.23	-	-
2019-04-21	58594.30	00095330001	9.39 ± 0.13	2.035 ± 0.018	289.36/314.00	11.57 ± 0.24	9.96 ± 0.18	-
2019-04-24	58597.02	00031630062	10.04 ± 0.14	1.943 ± 0.018	353.70/310.00	9.48 ± 0.18	8.13 ± 0.14	9.31 ± 0.20
2019-04-25	58598.02	00011325001	10.35 ± 0.10	1.987 ± 0.013	517.69/412.00	9.08 ± 0.17	7.72 ± 0.12	-
2019-04-28	58601.08	00031630063	9.46 ± 0.14	2.101 ± 0.021	288.27/269.00	-	-	-
2019-04-30	58603.00	00011325005	2.22 ± 0.47	1.94 $^{+0.26}_{-0.23}$	9.81/3.00	8.38 ± 0.25	-	-

Table A.3.: Table A.2 continued.

Date	MJD	ObsID	X-ray			UV		
			Flux (0.5–10 keV) [10^{-10} erg cm $^{-2}$ s $^{-1}$]	Index	Fit statistic χ^2 /d.o.f.	Flux W1 [mJy]	Flux W2 [mJy]	Flux M2 [mJy]
2019-05-01	58604.93	00031630065	10.83 ± 0.14	1.956 ± 0.017	389.64/336.00	7.68 ± 0.15	-	-
2019-05-03	58606.93	00031630066	10.76 ± 0.14	2.003 ± 0.017	366.72/325.00	8.52 ± 0.16	-	-
2019-05-05	58608.12	00095330002	7.90 ± 0.13	2.035 ± 0.021	287.68/268.00	8.35 ± 0.22	7.18 ± 0.12	-
2019-05-05	58608.91	00031630067	6.31 ± 0.10	2.164 ± 0.022	257.33/253.00	8.16 ± 0.16	-	-
2019-05-07	58610.90	00031630068	10.22 ± 0.12	1.922 ± 0.015	373.63/363.00	7.92 ± 0.15	6.68 ± 0.13	-
2019-05-10	58613.02	00031630069	9.03 ± 0.13	1.887 ± 0.018	403.92/318.00	7.85 ± 0.15	6.51 ± 0.11	-
2019-05-21	58624.05	00031630071	11.85 ± 0.16	1.889 $^{+0.018}_{-0.017}$	326.57/339.00	8.85 ± 0.17	7.53 ± 0.13	-
2019-05-22	58625.97	00031630072	10.26 ± 0.20	2.012 ± 0.025	251.44/235.00	8.26 ± 0.18	6.89 ± 0.14	-
2019-05-24	58627.92	00031630073	7.92 ± 0.12	2.116 ± 0.021	301.14/267.00	8.31 ± 0.17	-	-
2019-05-26	58629.57	00095330005	8.46 ± 0.12	2.036 ± 0.019	287.81/300.00	8.97 ± 0.18	7.62 ± 0.13	-
2019-05-27	58630.95	00031630074	8.62 ± 0.22	1.96 ± 0.04	164.21/195.00	8.92 ± 0.20	-	-
2019-05-30	58633.96	00031630075	7.38 ± 1.37	2.22 $^{+0.29}_{-0.26}$	1.06/4.00	10.59 ± 0.20	9.27 ± 0.15	10.50 ± 0.23
2019-06-02	58636.95	00031630076	7.39 ± 0.11	2.090 ± 0.021	300.10/271.00	9.92 ± 0.19	-	-
2019-06-06	58640.93	00031630078	7.46 ± 0.11	2.187 $^{+0.021}_{-0.018}$	308.55/274.00	10.68 ± 0.20	9.13 ± 0.15	-
2019-06-09	58643.31	00095330006	15.78 ± 0.16	1.929 ± 0.013	639.77/390.00	10.53 ± 0.20	-	-
2019-06-10	58644.38	00095330007	13.16 ± 0.15	2.048 ± 0.015	417.04/354.00	-	-	-
2019-06-11	58645.56	00095330008	25.61 ± 0.26	1.661 ± 0.012	750.37/473.00	-	9.23 ± 0.14	-
2019-06-12	58646.30	00095330009	18.85 ± 0.19	1.823 $^{+0.013}_{-0.012}$	557.48/426.00	-	-	10.72 ± 0.22
2019-06-13	58647.42	00011445001	10.38 ± 0.13	2.044 ± 0.017	429.93/320.00	-	-	-
2019-06-14	58648.03	00011445002	7.02 ± 0.12	2.263 $^{+0.025}_{-0.024}$	248.10/229.00	11.08 ± 0.21	9.25 ± 0.15	-
2019-06-16	58650.01	00011445003	5.23 ± 0.08	2.314 ± 0.024	241.59/225.00	11.51 ± 0.22	9.86 ± 0.16	-
2019-06-18	58652.01	00011445004	5.55 ± 0.08	2.299 ± 0.021	321.65/250.00	10.81 ± 0.20	9.33 ± 0.15	-
2019-06-20	58654.67	00011445005	10.46 ± 0.12	2.167 ± 0.016	495.98/319.00	11.05 ± 0.21	8.84 ± 0.15	-
2019-06-22	58656.79	00011445006	11.48 ± 0.14	2.011 ± 0.016	460.61/329.00	11.21 ± 0.21	8.70 ± 0.15	-
2019-06-24	58658.58	00011445007	11.27 ± 0.15	1.990 ± 0.017	378.79/330.00	11.86 ± 0.23	-	-

A.3 ATCA observations of PKS 2004–447

The radio data in Table A.4 cover ATCA observations from 2010 up to early 2020 of PKS 2004–447 and are taken in three different bands (λ 4-cm, λ 15-mm, and λ 7-mm).

Table A.4.: ATCA flux densities taken in the λ 4-cm (5.5 GHz, 9 GHz), λ 15-mm (16.8 GHz, 17 GHz, 19 GHz, 21.2 GHz), and λ 7-mm band (38 GHz, 40 GHz). Fluxes are given in mJy, and only statistical uncertainties are reported. This table is taken from [Gokus et al. \(2021b\)](#).

Remarks: [†]Observation done at 16.8 GHz. [‡]Observation done at 21.2 GHz

MJD	S _{5.5 GHz}	S _{9 GHz}	S _{17 GHz}	S _{19 GHz}	S _{38 GHz}	S _{40 GHz}
55240	516 ± 10	378 ± 10	–	–	–	–
55698	407 ± 9	294 ± 9	181 ± 6	166 ± 6	–	–
55848	408 ± 5	294 ± 5	176 ± 5	161 ± 5	–	–
55873	397 ± 8	263 ± 8	181 ± 9	164 ± 9	128 ± 12	125 ± 12
55892	373 ± 10	282 ± 10	–	–	–	–
56075	–	–	149 ± 7	136 ± 7	94 ± 9	93 ± 9
56091	412 ± 8	286 ± 8	157 ± 6	140 ± 6	82 ± 9	80 ± 9
56177	–	–	186 ± 7	168 ± 7	–	–
56598	450 ± 6	329 ± 6	–	–	–	–
56606	438 ± 3	308 ± 3	–	–	–	–
56636	450 ± 3	312 ± 3	–	–	–	–
56742	564 ± 4	410 ± 4	281 ± 9	263 ± 9	–	–
56817	525 ± 3	410 ± 3	268 ± 5	248 ± 5	–	–
56827	521 ± 3	406 ± 3	257 ± 5	236 ± 5	160 ± 10	155 ± 10
56859	520 ± 2	375 ± 2	–	–	–	–
56913	536 ± 3	395 ± 3	248 ± 6	227 ± 6	139 ± 9	134 ± 9
56930	–	–	221 ± 9	203 ± 9	–	–
56943	491 ± 6	363 ± 6	241 ± 6	222 ± 6	136 ± 8	131 ± 8
56980	519 ± 4	379 ± 4	253 ± 8	233 ± 8	139 ± 10	133 ± 10
57007	–	–	–	–	144 ± 12	138 ± 12
57036	490 ± 5	372 ± 5	–	–	–	–
57102	450 ± 3	330 ± 3	212 ± 7	192 ± 7	119 ± 11	114 ± 11
57135	429 ± 6	292 ± 6	191 ± 10	176 ± 10	–	–
57202	–	–	216 ± 7	198 ± 7	118 ± 10	115 ± 10
57246	–	–	–	–	122 ± 9	119 ± 9
57327	428 ± 6	293 ± 6	–	–	–	–
57349	426 ± 5	306 ± 5	184 ± 6	167 ± 6	99 ± 8	95 ± 8
57355	–	–	183 ± 6	167 ± 6	–	–
57381	407 ± 4	295 ± 4	–	–	–	–
57410	395 ± 4	268 ± 4	–	–	–	–
57414	405 ± 7	302 ± 7	–	–	–	–
57436	–	–	–	–	116 ± 11	112 ± 11

Table A.5.: Table A.4 continued.

MJD	S _{5.5 GHz}	S _{9 GHz}	S _{17 GHz}	S _{19 GHz}	S _{38 GHz}	S _{40 GHz}
57454	435 ± 4	316 ± 4	189 ± 7	174 ± 7	122 ± 12	121 ± 12
57485	438 ± 5	327 ± 5	211 ± 8	195 ± 8	129 ± 11	126 ± 11
57510	–	–	210 ± 9	198 ± 9	–	–
57535	–	–	202 ± 7	188 ± 7	–	–
57539	471 ± 5	328 ± 5	–	–	203 ± 11	205 ± 11
57555	–	–	296 ± 9	286 ± 9	–	–
57594	–	–	–	–	181 ± 7	176 ± 7
57617	544 ± 4	409 ± 4	258 ± 6	239 ± 6	160 ± 7	157 ± 7
57676	484 ± 4	405 ± 4	282 ± 6	264 ± 6	186 ± 11	184 ± 11
57728	452 ± 5	333 ± 5	–	–	–	–
57774	485 ± 4	362 ± 4	–	–	–	–
57793	476 ± 6	340 ± 6	–	–	–	–
57880	446 ± 5	313 ± 5	183 ± 4	167 ± 4	–	–
57898	427 ± 7	306 ± 7	–	–	149 ± 8	146 ± 8
58073	455 ± 5	358 ± 5	–	–	–	–
58077	483 ± 6	374 ± 6	–	–	–	–
58080	491 ± 3	378 ± 3	–	–	–	–
58092	487 ± 4	398 ± 4	–	–	–	–
58183	392 ± 5	292 ± 5	205 ± 8	193 ± 8	–	–
58227	387 ± 4	297 ± 4	194 ± 7	179 ± 7	121 ± 10	118 ± 10
58229	398 ± 6	312 ± 6	–	–	–	–
58279	392 ± 4	313 ± 4	–	–	116 ± 15	113 ± 15
58377	352 ± 5	293 ± 5	–	–	–	–
58379	354 ± 3	299 ± 3	–	–	–	–
58391	–	–	254 ± 5	239 ± 5	–	–
58462	424 ± 3	299 ± 3	–	–	–	–
58490	414 ± 4	219 ± 4	–	–	–	–
58513	383 ± 4	281 ± 4	–	–	–	–
58562	433 ± 5	317 ± 5	–	–	–	–
58590	408 ± 3	296 ± 3	–	–	–	–
58601	425 ± 7	295 ± 7	–	–	–	–
58715	442 ± 3	358 ± 3	–	–	–	–
58727	–	–	225 ± 12 [†]	192 ± 12 [‡]	–	–
58760	440 ± 2	347 ± 2	244 ± 5	229 ± 5	156 ± 8	152 ± 8
58809	465 ± 3	352 ± 3	252 ± 7	234 ± 7	–	–
58829	459 ± 4	327 ± 4	–	–	–	–
58879	433 ± 4	332 ± 4	–	–	–	–
58923	467 ± 4	362 ± 4	–	–	–	–
58934	479 ± 4	358 ± 4	–	–	–	–
58942	464 ± 7	414 ± 7	–	–	–	–
58958	501 ± 5	359 ± 5	227 ± 10 [†]	184 ± 102 [‡]	–	–

Acknowledgements

First of all, I want to thank my advisors Jörn Wilms and Matthias Kadler for giving me the opportunity to become an astrophysicist. Both of them have been my mentors since my Bachelor's thesis, and I am grateful for all the support and advice that they have given me over the years. Thanks to them, I was able to travel to international conferences to present my work and to meet people from all over the world. Half my time as a graduate student took place during a global pandemic and it was a great challenge for our working groups. I appreciate it very much that Jörn and Matthias made a big effort in staying connected with everyone.

Speaking of staying connected, I want to thank everyone I had the pleasure of working with in the past 4.5 years, in particular my colleagues at the Remeis-Observatory and the Astronomy group at the University of Würzburg. Because I had the privilege of being a member in two research groups at two Universities, I was able to get a broader insight into several Astronomy topics, and learn about things outside of my own research project. Because the work atmosphere at both institutes was usually pleasant and most of you guys have been great colleagues, it was easy to make some friends along the way. For interesting, encouraging, fun, and sincere conversations about topics in- and outside of work, I want to particularly thank Dominic Bernreuther, Thomas Dauser, Sebastian Falkner, Steven Hämmerich, Amy Joyce, and Ole König from the Remeis family, and Paul Burd, Daniela Dorner, Michael Kreter, Bernd Schleicher, Sarah Wagner, and Christoph Wendel from the Astro group at Würzburg. I also had the pleasure of being a part of the TELAMON collaboration from its start in 2020. I want to thank Matthias Kadler, Alex Kraus, Uwe Bach, the operators at the Effelsberg telescope, and my fellow observers Petra Benke, Florian Eppel, Jonas Heßdörfer, Georgios Paraschos, Florian Rösch, Jonas Sinapius, and Philip Weber for the joyful collaboration. One of the first observing shifts was a memorable stay at the Effelsberg telescope with Florian Eppel and Jonas Heßdörfer, during which we were allowed to walk inside the telescope dish thanks to the initiative by Uwe.

Furthermore, I want to thank Jörn Wilms, Manami Sasaki, and Ulrich Heber, as well as Karl Mannheim and Matthias Kadler for their leadership at the Remeis-Observatory and the Institute for Astronomy, respectively. However, it would be hard to keep everything running without the great support and effort of our secretaries, Edith Day and Karin Kuhns. The same holds true for the admins, without whom most of us would not be able to produce cool scientific results. Ingo Kreykenbohm and Philipp Weber, thank you for your tireless dedication to keeping the Remeis cluster, and everything else, up and running. I am very grateful to everyone who contributed to maintaining the infrastructure of *ISIS*, the *ISISscripts*, and the Remeis data extraction pipelines for X-ray data. I also want to acknowledge the continued support by, and interaction with, former members of the Remeis family that increased further when a Slack channel was established (thank you, Thomas!) as a reaction to the home office situation in March 2020. In particular, I want to mention Tobias Beuchert, Felix Fürst, Victoria Grinberg, Natalie Hell, Thomas Kupfer, and Felicia McBride.

Being a part of the Remeis family usually means that it's not only research projects that keep us busy. I was happy to organise the annual FRANCI meetings together with my colleagues Jacky Catalano and Andreas Specovius from ECAP, Dominic Bernreuther and Maximilian Lorenz from the Remeis observatory, and Paul Burd from Würzburg. Furthermore, I had a

lot of fun being a member of the Social Media team of the Remeis observatory together with Dominic, Steven, and Aafia Zainab.

In retrospect, I deem myself lucky that I was able to take part in the many social gatherings and events that were organised outside of work within the Remeis family, before the Covid-pandemic hit. A regular event, which I enjoyed the most, was the annual skiing holiday in Montafon. Thank you very much, Thomas, for organising a fun week in the snow every year. I will always look back with a smile when remembering these weeks, as well as the many barbeque and movie nights at the observatory. The same holds true for the travelling that I was able to do during my time as a graduate student. I want to particularly mention my stay at the US east coast in 2018, where I first attended the Fermi summer school, and then spent two weeks at NASA GSFC. At the summer school, which took place in the cosy town of Lewes (Delaware), I learned a lot about γ -ray astronomy while also meeting lots of great people. On the organiser's side, I want to specifically mention Elizabeth Ferrara, Elizabeth Hays, Jamie Holder, and Marcos Santander for the great interactions with us students. What made this school so special was the great solidarity among all students, as we not only learned everything about the *Fermi* satellite, but also spent a lot of time together during barbeques, trips to the beach, and playing games in the evening. I'm particularly grateful for the companionship of Atreya Acharyya, Angaraj Duara, Connor Duffy, Amar Hekalo, Milena Crnogorcevic, Tyler Parsotan, and Ibrahim Safa. I thank Roopesh Ojha for inviting me to the GSFC to collaborate on blazar projects, and the lovely dinner with his family. During my visit at the GSFC, I had the privilege to stay with Katja Pottschmidt, which I enjoyed very much due to her incredible hospitality. Later that same year, I was also invited to spend a few days at the Asiago Observatory by Roberto Nesci, who taught me the photometry reduction of data taken with the Rapid Eye Mount, for which I am deeply grateful.

I had the pleasure of being a member of the *Fermi* collaboration and I want to thank all of its members for the enjoyable collaboration meetings and the AGN working group, in particular, for interesting discussions about high-energy processes in blazars. A fun opportunity was doing regular shifts for the 'Flare advocates' and reporting on interesting things happening in the γ -ray sky.

Over the last few years, I discovered my enthusiasm for science communication. I am grateful for being able to give many guided tours at the observatory. I also want to thank Markus Pössel and Carolin Liefke for giving me the opportunity to give an online talk for the 'Haus der Astronomie' about my research topic. Furthermore, I very much appreciate being invited by the organisers of 'Astronomy on Tap Bonn' and 'Astronomy on Tap Köln' to give talks about astronomy online.

I am deeply indebted to Jörn, Matthias, Roopesh, and Norbert Schartel for supporting my applications for a PostDoc position, which now permits me to continue working as an astrophysicist. Furthermore, I feel enormous gratitude towards Fe, who has been a mentor for me since my Bachelor's thesis, and always gave me extremely helpful advice and sincere support. Similarly, it has been a pleasure to get input and advice by Vanessa Moss in our regular conversations. I also want to say a big *Thank You* to Sarah, Steven, Dani, Florian E., Basti, Amy, and Marcus Langejahn, who helped me to improve the manuscript of my thesis by proof-reading.

Last, but not least, I want to thank my friends and family, who always supported my endeavours, in particular my parents, Armin and Gabriele. I appreciate the encouragement and support by Gerd and Ute Kauke. Without my dear friends and the adventures that we have together, life would be meaningless. Thank you, Moritz Bednarski, Tobias Hiefer, Rebekka Kretschmann, Katrin Ludwig, Vanessa Pavlek, Bianka Puscher, Lena Streit, and Johannes Veh. Even though he cannot read this, I also want to thank my dog Amos for being hilarious and providing excellent mental health support. Finally, I am deeply grateful to Basti, who is always there for me.

This research has made use of ISIS functions (ISISscripts) provided by ECAP/Remeis observatory and MIT (<http://www.sternwarte.uni-erlangen.de/isis/>). The figures in this work have been produced with the S-Lang module `slxfig`. I acknowledge the use of the data obtained from the High Energy Astrophysics Science Archive Research Center (HEASARC), provided by NASA's Goddard Space Flight Center. This research has also made use of NASA's Astrophysics Data System Bibliographic Services (<http://adsabs.harvard.edu/>). This work has made use of SAOImage DS9, developed by the Smithsonian Astrophysical Observatory (Joye & Mandel 2003). This research has made use of the SIMBAD database, operated at CDS, Strasbourg, France, as well as of the NASA/IPAC Extragalactic Database (NED) which is operated by the Jet Propulsion Laboratory, California Institute of Technology, under contract with the National Aeronautics and Space Administration. This work has made use of the XRT Data Analysis Software (XRTDAS) developed under the responsibility of the ASI Science Data Center (ASDC), Italy. Part of this work is based on observations obtained with *XMM-Newton*, an ESA science mission with instruments and contributions directly funded by ESA Member States and NASA. This work made use of data from the NuSTAR mission, a project led by the California Institute of Technology, managed by the Jet Propulsion Laboratory, and funded by the National Aeronautics and Space Administration. Furthermore, this research has made use of the NuSTAR Data Analysis Software (NuSTARDAS) jointly developed by the ASI Science Data Center (ASDC, Italy) and the California Institute of Technology (USA). I acknowledge the use of public data from *Fermi*/LAT, which was analysed using the *Fermi Science Tools* (<https://github.com/fermi-lat/ScienceTools>) and *fermipy* (Wood et al. 2017). Parts of this work are based on observations with the 100-m telescope of the MPIfR (Max-Planck-Institut für Radioastronomie) at Effelsberg. The colours used for several plots in this thesis (Figs. 2.6, 4.1, 4.2, 4.3, 4.4, 4.5, 4.6, 4.12, 4.13, 4.14, 4.15, 4.16, 4.17, 4.18, 5.1, 5.2, 5.4, and 5.5) are taken from Paul Tol's colour schemes and templates (<https://personal.sron.nl/pault/>). The scientific, sequential colour map `batlow` (Crameri 2018) is used in Figs. 4.7, 4.8, 4.9, 4.10, and 4.11 to prevent visual distortion of the data and exclusion of readers with colourvision deficiencies (Crameri et al. 2020).